FLEXURAL STIFFNESSES OF AND DIMENSIONAL STABILITY IN CIRCULAR QUASI-ISOTROPIC LAMINATE MIRRORS

BY

Kyung-Pyo Kim

Submitted to the graduate degree program in Aerospace Engineering
and the Graduate Faculty of the University of Kansas
in partial fulfillment of the requirements for the degree of
Doctor of Philosophy

Members of the Committee:

Dr. Richard D. Hale, Chairman*
Associate Professor of Aerospace Engineering

Dr. Ray Taghavi
Professor of Aerospace Engineering

Dr. Mark S. Ewing
Associate Professor of Aerospace Engineering

Dr. Ronald M. Barrett-Gonzalez
Associate Professor of Aerospace Engineering

Dr. Bedru Yimer
Professor of Mechanical Engineering

Date dissertation defended: April 2, 2009

The Dissertation Committee for Kyung-Pyo Kim certifies
that this is the approved version of the following dissertation:

FLEXURAL STIFFNESSES OF AND DIMENSIONAL STABILITY IN CIRCULAR QUASI-ISOTROPIC LAMINATE MIRRORS

Members of the Committee:

Dr. Richard D. Hale, Chairman*
Associate Professor of Aerospace Engineering

Dr. Ray Taghavi
Professor of Aerospace Engineering

Dr. Mark S. Ewing
Associate Professor of Aerospace Engineering

Dr. Ronald M. Barrett-Gonzalez
Associate Professor of Aerospace Engineering

Dr. Bedru Yimer
Professor of Mechanical Engineering

Date dissertation defended: April 2, 2009

Abstract

Composite fiber reinforced plastics are being given favorable consideration for emerging applications in large aperture telescopes, such as the Hubble telescope or communication dishes. Many lightweight mirror fabrication concepts are currently being pursued. Presently, the technology is limited because it has an incomplete understanding of the mechanics associated with quasi-isotropic laminates for diffraction-limited displacement constraints, and lack of understanding for effects of resin buffer layers on composite mirrors for high surface smoothness.

In this dissertation document, radial stiffness associated with stacking sequence effects in quasi-isotropic laminates (π/n, where n=3, 4, and 6) and dimensional stability in the composite laminates are investigated numerically. The numerical results show that directional dependency of flexural stiffness in the laminates, which is strongly associated with stacking sequences, is a significant factor causing unfavorable sinusoidal surface waviness. The maximum radial flexural stiffness variation is found as ±12.85% in $\pi/3$ laminate while a minimum of ±5.63% is found in $\pi/4$ laminate. Mechanics of maximum asymmetry by ±2º misorientation based on ideal π/n laminate lay-ups are evaluated and the results are compared with ideal lay-up sequence cases. The calculated extensional and flexural stiffness values from the maximum asymmetric cases are within less than 0.05%. As such, the radial flexural stiffness variations in quasi-isotropic laminates are shown to be more problematic than asymmetry caused by common manufacturing variance.

The types of surface deformations in quasi-isotropic laminates associated with directional dependency of flexural stiffness are evaluated using finite element analyses. Also, fiber print-through in replicated composite mirrors and the effects of the resin

buffer layer present in the mirrors for mitigation of the fiber print-through are investigated and discussed. Numerical results reveal that there will be an unfavorable sinusoidal surface deformation in each ideal π/n laminate and the shapes are strongly associated with principal fiber directions due to stacking sequence effects. The surface deformations in quasi-isotropic laminates are shown to be typical and such surface deformations are inevitable when composite mirrors are fabricated from discrete layers of anisotropic carbon fiber reinforced plastics. Moreover, the use of additional resin layers appears to more adversely influence the composite mirror substrates. The validation of predicted surface deformations and dimensional distortions are achieved by comparing experimental results on a 8-inch-diameter composite mirror sample fabricated at the University of Kansas Dept. of Aerospace Engineering (KUAE) and Bennett Optical Research (BOR).

A study of quasi-homogeneous materials such as short fiber products as alternative composite materials is investigated. Furthermore, the relation between resin property effects and corresponding resin thickness effects is evaluated and discussed. The analyses provide information on alternative types of materials that primarily affect optical performance and thus are most important for precision optics.

Based on the results, locally varying radial surface deformations in quasi-isotropic laminates fabricated from continuous fiber reinforced plastics distort optical performance. These surface deformations might be eliminated by utilizing short fiber materials and a soft resin system with a very low coefficient of thermal expansion compared to conventional resins.

Acknowledgements

I would never have been able to finish my dissertation without the guidance of my committee members, help from friends, and support from my family and wife.

I would like to express my deepest gratitude to my advisor, Dr. Richard D. Hale, for his excellent guidance, financial support, caring, patience, and providing me with an excellent atmosphere for doing research. I would like to thank Drs. Ray Taghavi, Mark S. Ewing, Ronald M. Barrett-Gonzalez, and Bedru Yimer for serving on my program of study committee. I appreciate the time and effort which they gave to ensure the successful completion of my Doctor of Philosophy degree in Aerospace Engineering, and this document.

I would also like to thank Dr. Peter C. Chen, the Catholic University of America, for help and give his best suggestions. A special thank to Hank Blazek, Bennett Optical Research, for providing me a very special and valuable mirror specimen for my dissertation. I could never have been able to finish without the help.

Finally, I would like to thank my wife and my kids (Eunja Kim, Aaron K. Kim, Andrew K. Kim, and my lovely daughter) who have never failed to stand beside me and my decisions. Your faith and support are a constant source of comport and inspiration.

DEDICATION

to my wife Eunja Kim

for understanding

Table of Contents

Table of Contents (Cont.)

Table of Contents (Cont.)

List of Tables

Page

List of Tables (Cont.)

Page

List of Tables (Cont.)

Page

List of Figures

Page

List of Figures (Cont.)

Page

List of Figures (Cont.)

Page

List of Figures (Cont.)

Page

List of Figures (Cont.)

Page

List of Figures (Cont.)

Page

List of Figures (Cont.)

Page

List of Figures (Cont.)

Page

List of Figures (Cont.)

Page

Nomenclatures

$[A]$, A_{ij}	Extensional stiffness of a laminate
$[B]$, B_{ij}	Coupling stiffness of a laminate
$[D]$, D_{ij}	Flexural stiffness of a laminate
E_1, E_2, E_3	Young's moduli in the x_1, x_2, x_3 local coordinate system
E_L, E_T	Young's moduli in longitudinal and transverse direction in a lamina
$[E]$, E_{ij}	Stiffness matrix
$[E]_{\mathrm{OT}}$	Stiffness matrix for an orthotropic lamina
G_{12}, G_{23}, G_{31}	Shear moduli in the x_1, x_2, x_3 local coordinate system
G_{LT}	Shear module in a lamina
h	Lamina thickness
h_k, h_{k-1}	Top and bottom of a k_{th} lamina in a laminate
k	Number of layers in a laminate
M_x, M_y, M_{xy}	Bending and twist moments per unit length acting on a laminate
N_x, N_y, N_{xy}	In-plane forces per unit length acting on a laminate
$[Q]$, Q_{ij}	2D plane stress stiffness matrix in the x_1, x_2 local coordinate system
$[\bar{Q}]$, $\bar{Q}_{ij}$	2D plane stress stiffness matrix in the x, y global coordinate system
$[T]$	2D stress transformation matrix
$[T]^{-1}$	Inverse of transformation matrix
u	Displacement in the x direction
u_0	Displacement of the mid-plane in the x direction
v	Displacement in the y direction
v_0	Displacement of the mid-plane in the y direction
w	Deflection in z direction

Nomenclatures (Cont.)

w_0	Deflection of the mid-plane in the z direction

Greek

α_{ij}	Thermal coefficient of expansion in $x_1,\ x_2,\ x_3$ coordinate system
$\gamma_{23},\ \gamma_{13},\ \gamma_{12}$	Engineering shear strains in $x_1,\ x_2,\ x_3$ coordinate system
$\gamma_{yz},\ \gamma_{xz},\ \gamma_{xy}$	Engineering shear strains in $x,\ y,\ z$ coordinate system
$\varepsilon_1,\ \varepsilon_2$	Engineering normal strains in the $x_1,\ x_2$ coordinate system
$\varepsilon_x,\ \varepsilon_y$	Engineering normal strains in the $x,\ y$ coordinate system
$\varepsilon_x^0,\ \varepsilon_y^0,\ \gamma_{xy}^0$	Strains of the mid-plane
θ_k	Ply orientation
$\kappa_x,\ \kappa_y,\ \kappa_{xy}$	Curvature of the mid-plane
$\nu_{LT},\ \nu_{TL}$	Poisson's ratio in a lamina
ν_{ij}	Poisson's ratio
$\sigma_1,\ \sigma_2,\ \sigma_3$	Normal stress in the $x_1,\ x_2,\ x_3$ coordinate system
$\sigma_x,\ \sigma_y,\ \sigma_z$	Normal stress in the $x,\ y,\ z$ coordinate system
$\tau_{23},\ \tau_{13},\ \tau_{12}$	Shear stress in the $x_1,\ x_2,\ x_3$ coordinate system
$\tau_{yz},\ \tau_{xz},\ \tau_{xy}$	Shear stress in the $x,\ y,\ z$ coordinate system

List of Acronyms

CFRP	Continuous Fiber Reinforced Plastics
CHE	Coefficient of Hygroscopic Expansion
CMA	Composite Mirror Applications
COI	Composite Optics Incorporated
CTE	Coefficient of Thermal Expansion
FPT	Fiber Print-through
GFRC	Graphite Fiber Reinforced Composite
JPL	Jet Propulsion Laboratory
KUAE	University of Kansas Department of Aerospace Engineering
MRI	Major Research Instrumentation
NSF	National Science Foundation
OSC	Optical Science Center
RMS	Root Mean Square
TSC	Thermally Stable Composites
ULTRA	Ultra Lightweight Telescope for Research in Astronomy
UTRC	United Technologies Research Center

1. Introduction

Developmental endeavors in composite technology have included a wide variety of primary and secondary structures in industries ranging from civil structures to high performance aircraft to high precision optical telescopes. In the field of optics, carbon fiber reinforced plastic (CFRP) materials are being considered as next generation material to replace conventional optical material (glass telescope mirror with steel support structure) due to its excellent macroscopic mechanical properties of high stiffness, low strength-to-weight and stiffness-to-weight ratios and low coefficient of thermal expansion (CTE). Optical mirrors have been made primarily from glass, ceramics and/or metals; the most common metal being used is beryllium (Table 1).

Table 1: Mirror Substrate Material Data.

Materials	**Density (ρ)**	**Young's Modulus (E)**	**Specific Stiffness (E/ρ)**	**Thermal Expansion (CTE)**	**Thermal Conductivity (K)**
English (SI)	lb/in^3 (g/cm^3)	Msi (Gpa)	10E8 in	ppm/F (ppm/K)	Btu/hr-ft-F (W/cm-K)
Preferred	Small	Large	Large	Small	Large
Beryllium I-70A	0.067 (1.85)	42 (287)	6.3	6.3 (11.4)	112 (1.93)
SiC RB 30% Si	0.106 (2.92)	45 (310)	4.25	1.47 (2.64)	91 (1.58)
GFRP P75/Epoxy	0.063 (1.63)	14.5 (3.1)	2.3	0.05 (0.09)	22 (0.38)

Although beryllium has a low density and high Young's modulus, it also has a high coefficient of thermal expansion (CTE) and is considered a hazardous material. The design of any mirror system must consider future product liability, cost, weight, and

thermal stability. Therefore, research on composite mirrors for ground and space-borne applications have been increasing. However, a potential problem arises in composite replicated mirrors due to the presence of fiber print-through. It is currently hypothesized that fiber print through occurs during the cure cycle, when the underlying fiber geometry is transposed to the surface causing high frequency surface errors most commonly attributed to thermal and chemical shrinkage [Ref. 1, 2, 3, and 4]. For this reason, most research on composite mirror application has focused on developing mitigation techniques for fiber print-through.

Significant research and development activities have been performed to eliminate such a problem by applying additional resin layers and polishing the composite mirror surface [Ref. 2 and 3]. Figures 1~3 show a typical fabrication process for a composite mirror substrate and telescope structure. Another merit of carbon fiber reinforced plastic (CFRP) material for telescope mirror application is that it has low coefficient of thermal expansion (CTE) characteristics. One of the most important requirements for ground based and space-borne optical mirror applications is that the optical materials must provide exceptional dimensional stability in the presence of thermal gradients and adverse environments. Because the fiber in continuous fiber reinforced plastics has a negative coefficient of thermal expansion along its length direction while the matrix has a uniformly positive CTE, it is commonly believed that zero effective coefficient of thermal expansion of tailored composite mirror can be produced using CFRP composite material [Ref. 5].

However, a difficulty still exists when unidirectional CFRP composite material is used to fabricate a composite mirror substrate. Asymmetric characteristics of composite

laminated mirrors due to added surface resin coating to eliminate fiber print-through in any significantly varying thermal environment would cause more unacceptable surface deformations. In quasi-isotropic laminates, it is well known that in-plane stiffness of the laminates is directionally independent [Ref. 6]. On the other hand, flexural stiffness strongly depends on stacking sequence. Due to the radial variation of flexural stiffness and unbalance characteristics in local radial axes in quasi-isotropic laminates from stacking sequence effects, circular composite mirrors based on quasi-isotropic lay-up with continuous fiber material might not be suitable for applications such as antenna reflectors or primary mirrors for telescopes.

The purpose of this research is to investigate mechanics of quasi-isotropic laminates in the context of diffraction-limited optics applications, by evaluating the in-plane and flexural stiffness and engineering constant ratio of D_{12}/D_{11}, D_{16}/D_{11}, and D_{26}/D_{11} in quasi-isotropic laminates, inevitable surface deformations in symmetric ideal quasi-isotropic composite mirrors, surface deformations in quasi-isotropic laminates with additional resin rich layers and resin thickness effects to mitigate fiber print-through. For each, alternative solutions will be explored to eliminate the inherent problems of utilizing CFRP continuous material for optic applications.

Figure 1: CFRP fabrication sequence from left to right, processing the glass mandrel, CFRP prepreg material, lay-up of prepreg over the glass mandrel, processing and release CFRP mirror from the mandrel, ready for coating. [Ref. 7]

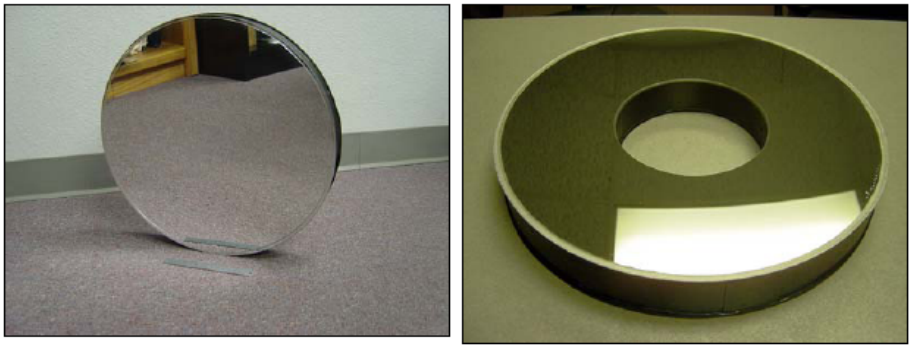

Figure 2: LEFT, Newtonian CFRP 40cm parabolic primary mirror with aluminum + SiO overcoating, RIGHT, A CFRP Cassegrain 40 cm primary mirror with central hole. [Ref. 7]

Figure 3: Left, NRL's Cassegrain 40 cm all CFRP composite telescope, Right Newtonian 40 cm all CFRP composite telescope for astronomical image testing. [Ref. 7]

2. Review of Literature

Optical reflectors or mirrors have traditionally been made of large glass or beryllium with metal support structure. A current requirement in the field is to reduce weight to enable increased scale. However, traditional mirrors are limited due to weight, cost, and reproducibility. Technology utilizing Composite Fiber Reinforced Plastic (CFRP) has been developed and has been successfully used in significant numbers of secondary structure and more recently in increasing numbers of primary structure due to the remarkable strength-to-weight and stiffness-to-weight ratios, and its low coefficient of thermal expansion (CTE) mechanical characteristics. Optical mirrors for ground based and space-borne applications received a spot light in modern composite industries due to weight budgets on space telescopes and the physical limitations on large ground based telescopes. Even though fiber reinforced plastics have achieved great improvement in cost-effective manufacturing and concern about weight, many technical matters still remain in early development stages. In fact, CFRP composite mirror technology is currently one of the most researched areas in the composite field. Requirements for primary optics are as follows:

1. Surface Accuracy ($<\lambda/20$ RMS): λ (623 nm) is the maximum visible (red light) wavelength of light.
2. Surface Roughness ($<\lambda/100$ RMS): most current researchers believe that fiber print-through is typically the limiting factor.
3. Stability (surface displacements and/or deformation $<< \lambda$): this includes long term temporal and thermal stability (CTE) and moisture stability (coefficient of hygroscopic expansion, CHE).

4. Mass (2-20 kg/m^2): high stiffness and low density characteristics on CFRP can lead to this requirement.

Significant previous research and development activities addressed composite application to achieve these requirements. However, the difficulty which often arises with these materials is that they are traditionally orthotropic with varying mechanical properties in the laminate. This is an important factor that could prevent the composite mirror from having diffraction limited performance. A quasi-isotropic laminate exhibits uniform in-plane extensional stiffness. Based on this fact, previous research highlighted in the following sections mainly focused on material selection and successful fabrication for lightweight quasi-isotropic composite mirrors, investigations of dimensionally and thermally stable composite mirrors for space-borne applications, and mitigation technique of induced errors due to fiber print-through in replicated CFRP mirrors. The following sections will discuss what types of research on composite mirror have been done and what significant researches need to be performed for future composite mirror.

2.1. Material Selection and Successful Fabrication for Lightweight Composite Mirrors

Conventional optical telescopes have traditionally been made of large glass mirrors with metal support structure. The fabricating process requires an expensive mandrel and significant polishing time to meet reflectivity and surface accuracy requirements. Even though such exacting efforts in fabricating mirrors are required, traditional mirrors are limited due to weight, cost, durability, and reproducibility. A quick method for generating lightweight optics has been developed for more than a decade ago. Material for primary mirrors deployed in ground based/space-borne applications must meet several criteria: low density, low thermal expansion, and high stiffness. Composite Optics Incorporated (COI) and Optical Science Center (OSC) have surveyed available material for lightweight mirrors for large (1m in diameter) primary mirror [Ref. 8]. After surveying available materials for lightweight mirrors, they tried to combine glass material and composite material to fabricate a new type of lightweight visible quality mirror. The design concept for this mirror allows for the optimal use of each material: glass for the optical surface and composite for supporting structure. After surveying available materials for lightweight mirrors, they concluded that a combination of glass and composite materials might be the best option for precision lightweight mirrors (glass for optical surface and composite for structural support) due to a difficulty in mirror face-sheet fabrication using composite material.

Significant research on composite mirror application has been done at Composite Mirror Applications (CMA). Fabrication technique and testing for very lightweight composite mirrors are performed by Chen, Peter C. and Romeo, Robert C at CMA [Ref.

9, 10, 11, and 12]. The accomplishments include reduction of fiber print-through with polishing, appearance of bond lines, attempts to develop dimensionally stable composite mirrors which allow to fabricate highly smooth surfaces (micro-roughness < 1 nm RMS) with areal density 2 kg/m^2 at 60 cm aperture in small flat or curved composite mirror. Although their works accomplished their purpose for mitigating fiber print-through, the methods were limited by a single temperature (room temperature).

Another research achievement from Peter C. Chen and his colleagues [Ref. 13] has accomplished fabrication of near diffraction limited optical performance ($<\lambda/20$, where λ is wavelength of light 632.8 nm) in replica flats with a mandrel which is a commercial quality optical flat specified as $\lambda/20$ wave rms. However, even though they addressed the success of precision mirror fabrication, this study did not pay attention to potential figure errors in composite replica mirrors such as thermal effect of curing process and cooling process, non-uniform thermal contraction as well as effect of anisotropy from misalignment during fabrication in composite laminate causing internal strains in the laminate as it cools from the cure temperature to room temperature.

The ULTRA program, an NSF Major Research Instrumentation (MRI) at CMA and KUAE, have led to further improvements on CFRP optical mirrors [Ref. 7]. The purpose of the program was to demonstrate the use of continuous fiber reinforced plastic composite materials for optical telescope mirrors and telescope structure. Mirror development under the MRI program has produced a composite mirror surface accuracy up to $\lambda/15$ wave RMS at 632 nm wavelength. The fabricated and polished mirrors which have size from 16 cm to 1m in diameter exhibit fractional wave performance across the visible band.

To summarize the assessment of material selection and composite mirror fabrication techniques: although fabrication technique and surface polishing methods offers unique capabilities for future composite mirror applications, there was no assessment for surface deformation due to stacking sequence effects on composite mirror face-sheets. Precision mirror fabrication could be achieved by applying additional resin layers and polishing the resin surface. However, it might be possible at a single temperature. There will be potential surface deformations due to radial variation of flexural stiffness in quasi-isotropic laminates due to lay-up sequence effects. In this dissertation, the issues associated with potential problems in quasi-isotropic laminates fabricated from continuous fiber materials will be evaluated also thermally induced surface deformations in the laminates due to additional resin layers will be investigated using numerical simulations.

2.2. Dimensionally Stable Composite Mirrors Development for Space-Borne Application

Future large precision reflectors for astrophysical and optical communications satellites lies will require very lightweight mirrors that can be produced at significantly lower cost and faster production times. Composite materials are being considered as the next generation material for space-borne applications due to its excellent mechanical properties such as high stiffness and strength to weight, low CTE, and easy fabrication processes. In the early stage of development of composite mirror, research at United Technologies Research Center (UTRC) has investigated on composite mirror developed and refined graphite fiber reinforced glass composite which is referred to as Thermally Stable Composites (TSC) [Ref. 14]. It was not proposed that this mirror was the optimum mirror for space application; however, it was a first attempt of graphite reinforced glass system which offered significant potential for dimensional stability applications for future composite requirements. In order to develop dimensionally and thermally stable composite mirrors in the space environment, a detailed understanding of coefficient of thermal expansion of composite laminates and the effect of thermal shrinkage of laminated composite mirror in space environment is required. Chris Blair and Jerry Zakrzewski focused on their study on moisture absorption of composite laminates. They pointed out most epoxy resins absorb substantial quantities of water up to 3.5% in room temperature storage environments and this moisture absorption results in substantial expansion in composite mirror structure [Ref. 15]. This research described the mechanical properties and moisture absorption of several new resins, as known as 3M's SP-500, Hexcel F-584 and Toray 3631 for quasi-isotropic composite mirror fabricated

from these new resin systems. However, for a dimensionally stable composite mirror for airborne application, more attention needs to be paid on dimensional stability of composite mirror with thermal variance.

Research at the Jet Propulsion Laboratory (JPL) has taken a balanced, iterative approach that combines analytical simulation, hardware fabrication, and mirror performance testing [Ref. 16]. JPL focused on research activities for material analysis, thermal analysis, and optical analysis using CFRP material for developing and fabricating dimensionally stable composite mirrors. The analytical approach used at JPL for the design of thermally stable, lightweight structural composites has shown only precision mirror development for surface accuracy greater than sub-micron.

Mark K. Pryor at Composite Optics Incorporated (COI) addresses accuracy issues associated with hygrothermal stability of ultra lightweight composite mirror structures [Ref. 17]. Typical composite mirror configurations made from laminated material consist of a thin face-sheet supported by an array of ribs. In his paper, interference problems between the face-sheet/rib resulting in a print-through effect in the presence of thermal load were addressed. Also, Pryor et.al points out adhesive used to bond the ribs to the face-sheet causes additional print-through. The conclusion of this paper is that local deformation in composite mirror surface is induced from local interference between face-sheet and rib, adhesive at the rib and face-sheet interface, and tool mismatch during curing process.

A study to identify key parameters which dominate aberrations of the reflector panel due to thermal loads in space or during the composite mirror manufacturing process was performed using finite element analysis [Ref. 18]. C. P. Kuo and his colleague at JPL

have investigated lightweight composite mirror development with a surface accuracy of a few microns RMS errors. In finite element analysis, the model was used to evaluate the effect of various parameters such as composite mirror geometry, face-sheet lay-up etc. For key parameters in the numerical simulation, the basic elements of a mirror were the composite face-sheets, the composite or aluminum honeycomb core, and the adhesive layers. For high surface accuracy and thermal stability in composite mirror, the major design parameters studied include the coefficient of thermal expansion in facesheets, the rigidity in face-sheet, and the thickness of each of the components. They concluded that many factors influence mirror performance, including face-sheet ply angle errors, uneven application of adhesive at front and back face-sheets, and misalignment of components during assembly. However, the most dominant parameter to control the accuracy of a composite mirror surface based on their research is human error during fabrication. They suggest avoiding misalignment of ply lay-up in manufacturing process to achieve thermally stable high precision composite mirror for space application.

In addition to research on thermally stable composite mirrors, a number of researches [Ref. 5, 19, 20, 21, 22, and 34] focused on benefits of utilizing CFRP material to fabricate for dimensional stability in composite mirror application due to lower coefficient of moisture and thermal expansion characteristics as well as high resistance to micro-cracking due to thermally cyclic loadings. Most of these research concentrated their studies on evaluation of thermal stability in carbon fibers and resins, including toughened epoxies and cyanate esters for composite mirrors. None of this research provided surface deformations in the surface of composite mirrors with a presence of thermal loads.

Remaining activities in the composite mirror area for dimensional stability analysis need to be focused on evaluations of thermally induced deformations in the surface of composite mirrors. Hopefully, this study would be useful for composite optic industry to identify and reduce potential surface undulation problems in composite optics.

2.3. Induced Surface Errors Due to Fiber Print-Through in Replicated Carbon Fiber Reinforced Composite Mirror

The easiest and quickest way to fabricate a lightweight composite optic is to utilize an optical-quality glass or metal tool as a curing mandrel for carbon fiber reinforced plastics [Ref. 7, 9, 10, 11, and 23]. However, the ability to successfully fabricate CFRP mirrors is limited by surface roughness and unacceptable sinusoidal surface variations on replicated composite mirrors. It is currently hypothesized that fiber print through occurs during the cure cycle, when the underlying fiber geometry is transposed to the surface causing high frequency surface errors most commonly attributed to thermal and chemical shrinkage.

In early 1990, Richard Brand and his colleague started investigating fiber print-through effect on replicated composite mirrors [Ref. 24]. They pointed out that although high modulus carbon/epoxy composite structures have been utilized in space structures to take advantage of characteristics of near zero coefficient of thermal expansion and lightweight, their use in optical application has been limited due to high frequency errors in composite mirror surface. Typical mirror application requires a surface finish quality of $\lambda/20$ RMS at 632 nm. Differences between the CTE and CHE of the reinforcing fiber and matrix resin system in composites produce an unstable surface finish throughout the operating temperature as well as in very cold space environment. They concluded that the most significant sinusoidal deformation pattern in composite mirror surface is from fiber print-through and suggested some fiber print-through mitigation techniques such as polymer gel or eutectic coating. Fiber print-through mitigation technique with coating of resin layers might eliminate the problem in composite surface at a single temperature;

however, this technique would result in more serious surface waviness due to asymmetric characteristics with the presence of additional resin layers in composite mirrors.

COI is also one of the pioneers for identifying surface undulation in composite mirrors. In their paper [Ref. 25], they discussed that GFRC (graphite fiber reinforced composite) class of materials can be utilized to meet requirements for large scale space-borne composite mirror application. They pointed out that in order to achieve optimal performance in composite mirrors, the optical elements in a composite mirror system must be dimensionally stable in the space environment. GFRC has low CTE characteristics which meet the requirements. However, they found high frequency errors typically associated with the micro-roughness of an optical surface in composite mirror might be a difficult problem to eliminate and the typical surface micro-roughness of a fabricated composite laminate ranges from 0.5 micron RMS to 1.5 micron RMS. They claim the primary cause of surface roughness in GFRC is the fiber print-through which is induced from curing shrinkage of the resin as results of chemical cross-linking and unmatched shrinkage and expansion of fiber and matrix with changes in temperature due to CTE difference between fiber and matrix.

Hochhalter, J. D. and his colleague also emphasized that fiber print-through is the most important factor causing surface roughness and surface figure errors in composite mirror [Ref. 1, 2, 3, and 4]. They indicated that utilizing composite mirror technique with CFRP might lead to difficulties in improvement in surface roughness and smoothness due to existence of fiber print-through and unmatched shrinkage and expansion of fiber and matrix respectively with changes in temperature [Ref. 1]. To eliminate this problem, the author suggested that by applying an addition of resin rich film to the surface of the

mirror, the effect of fiber print-through is mitigated and any necessary surface correction is made possible. They provided the results of comparison of mirror replication samples that were fabricated using various pressure and resin thickness to indicate that it is evident an elongated scatter pattern is being produced on composite mirror samples with a resin thickness less than 5-mil. As the resin layer thickness increases the roughness due to fiber print-through decreases, also according to the results, 10-mil of resin thickness is required for these materials to fully mitigate the fiber print-through.

In 2005, Hochhalter J. D. and Massarello J. J. etc took a further step for research on fiber print-through in composite mirrors [Ref. 2 and 4]. This time their research activities involved a comparison study in the resin rich layer such as room temperature cure resin layer vs. high temperature cure resin layer and also involve resin thickness effects. They also discussed conventional polishing methods for mitigation of fiber print-through such as polishing resin rich layers. In this research, they concluded that an additional resin layer thickness of more than 10-mil would completely mitigate fiber print-through problem. In addition to the choice of resin rich layer, room temperature cure resins are more effective at replicating tool surfaces. In previous Hochhalter's researches [Ref. 1 and 2], he emphasized that sinusoidal surface distortion caused by fiber print-through are hypothesized to be dominated by chemical and thermal shrinkage and expansion between fiber and matrix during the curing process. His efforts to investigate composite mirrors continued in 2006 [Ref. 3]. The purpose of the research was to identify the dominant causes of fiber print-through to determine whether its sinusoidal presence could be mitigated without an additional resin layer. This research was based on the premise that fiber diameter, cure pressure, and cure temperature are the

dominant factors. A number of CFRP samples with varying fiber type, diameter and cure schemes were fabricated to quantify the causes of fiber print-through. As the results, it was found that the dominant wavelength, defined as fiber print-through, was not influenced by the cure temperature or fiber diameters. The unfavorable surface waviness in composite mirrors as fabricated from elevated curing temperature to room temperature might be producible due to thermal shrinkage between fibers and matrix in laminates. Moreover, it is feasible to reduce the surface waviness by applying smooth resin layers and a polishing technique. However, it is important to observe thermally induced surface deformation from the presence of additional resin layers in composite mirrors. None of this previous research has paid attention to the effects of resin layer and resin thickness on composite mirrors. Thus, particular attention in fiber print-through techniques with additional resin layers must be given for whether the method offers significant advantages or disadvantages over current composite mirror systems. One of the research activities in this dissertation will address this issue.

2.4. Summary of Review of Literature

There is significant activity in many realms of investigation in composite mirror technology, but most of the activities have focused on material assessment of composite fabrication techniques and fiber print-through mitigation method to achieve a precision mirror surface. This dissertation will address several key aspects within the general topic of composite mirror technology: mechanics of π/n quasi-isotropic circular mirrors especially variations of flexural stiffness in the laminates, thermally induced surface deformation in ideal π/n quasi-isotropic laminates with or without additional resin layers for fiber print-through mitigation method, resin thickness effects on the surface of composite mirrors, graded and intermediate resin layers effects on the surface of composite mirrors, possible porosities in the laminates and resulting local surface waviness, additional resin layers in front and back surface of the composite mirrors to eliminate bend-twist effects in fiber print-through method, and analysis on quasi-isotropic laminates using distributed chopped mat.

3. Mechanics of π/n quasi-isotropic circular laminates

In a quasi-isotropic laminate, the in-plane extensional stiffness is associated to directionally uniform, however, the flexural stiffness varies in radial directions due to stacking sequence effects of continuous fiber reinforced material. Surface accuracy requirement for precision mirrors must be less than λ/20 (<31.5nm) which indicates any small changes in mechanics in quasi-isotropic composite laminates either in-plane or through the thickness could affect surface accuracy requirement. Because of this dependency of flexural stiffness induced from stacking sequence, composite mirrors fabricated from continuous fiber reinforced material might not be suitable for future telescope applications. This chapter addresses three different types of quasi-isotropic laminate lay-ups and presents calculations of directionally dependent flexural stiffness contrasting continuous fiber reinforced and other random or distributed homogenous materials. Circular composite quasi-isotropic laminates with distributed homogenous material are shown to provide uniform extensional and flexural stiffness, whereas those with continuous fiber reinforced lamina exhibit variations in flexural stiffness of no less than ±5.63% and no more than ±12.85%. Sensitivity in stiffness of quasi-isotropic laminates is also evaluated, as are bend-twist effects in circular composite mirrors. Homogenous quasi-isotropic lamina materials may be the only practical way to remove variations in flexural stiffness, required for precision composite optics.

3.1. Quasi-Isotropic Laminates Lay-up and Fabrication

When the laminate is constructed by stacking a number of composite plies (orthotropic lamina) in an arbitrary sequence of orientation, the stiffness matrix of the composite will generally be fully populated. However, in many desirable cases, it is possible to specify the stacking sequence such that a number of terms in the individual stiffness term will be eliminated. In a quasi-isotropic laminate, the in-plane (extensional) stiffness matrix [A] is uniform, which means the laminate has elastic coefficients which are associated to be independent of radial orientation in the composite plane. This is a significant reason for usage of composite material and lay-up in composite mirror applications. The typical three types of quasi-isotropic laminates are π/n (where n=3, 4, and 6) with stacking sequence of each laminate being [0, ±60] in $\pi/3$, [±45, 0, 90] in $\pi/4$, and [±60, ±30, 0, 90] in $\pi/6$ laminate.

3.1.1. Fabrication of Composite Replica Mirrors

The University of Kansas Aerospace Engineering Department (KUAE), has worked for many years to build and test the structural characteristics of novel fiber reinforced plastic mirrors, and is currently assessing the theoretical mechanical properties such as extensional and flexural stiffness as well as sensitivity of lay-up errors due to possible angular misalignment. A numerous mirrors have been produced with 8-inches in diameter, 24 layer, and quasi-isotropic laminates in π/n variants: $\pi/3$ which consists of [0, ±60], $\pi/4$ which consists of [±45, 0, 90], and $\pi/6$ which consists of [±30, ±60, 0, 90].

Twenty four layers was initially chosen to minimize variations in flexural stiffness due to stacking sequence, as it is well-known that bend-twist coupling terms becomes small with respect to the primary flexural stiffness terms for laminates with more than sixteen plies. To maintain symmetry, and to ensure reasonable distribution of different lamina orientations through the thickness, the following specific stacking sequences are considered: $\pi/3$ lay-up with $[\pm 60, 0, 60, 0, \pm 60, 0, -60, 0, \pm 60]_s$, $\pi/4$ lay-up with $[\pm 45, 0, 90, 0, 90, \mp 45, 90, 0, \pm 45]_s$, and $\pi/6$ lay-up $[\pm 60, \pm 30, 0, 90, \pm 30, 0, 90, \mp 60]_s$. Figure 4 shows a typical fabrication process for a composite mirror. This approach is based on forming a smooth surface by replicating a polished mandrel surface on composite substrates. The fabrication process starts with a mandrel that has been polished to a shape which is complementary, which is flat, to the desired optical figure.

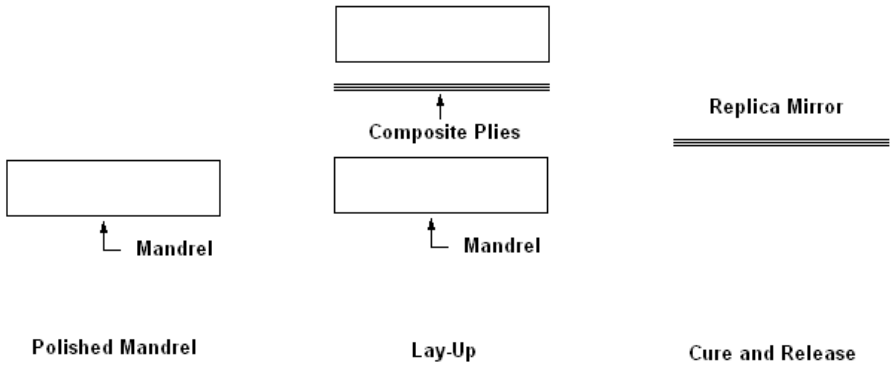

Figure 4: Composite Replica Mirror Fabrication Process

The intended use is to enable evaluations of thermal stability in different environments such as cold or hot working conditions. To characterize the more extreme directional influence functions of thin substrates with flexural stiffness, we also produced 8-inch diameter, 8 layer, quasi-isotropic, $\pi/4$ laminates with two additional veils on the

top and bottom, indicated by a stacking sequence of [**90**, **0**, 45, 0, -45, 90]$_s$, wherein bold indicates veil material. Finally, comparatively thin substrates using chopped mat were produced. This would theoretically reduce bend-twist, coupling, and directional flexural stiffness influence of composite mirrors. Carbon and Kevlar were used to produce 8-inch 12 layer, quasi-isotropic laminates with stacking sequence of [90, 0, 45, 0, -45, 90]$_{s,}$ with chopped veil for both carbon and Kevlar materials. Figure 5 shows various composite mirror samples.

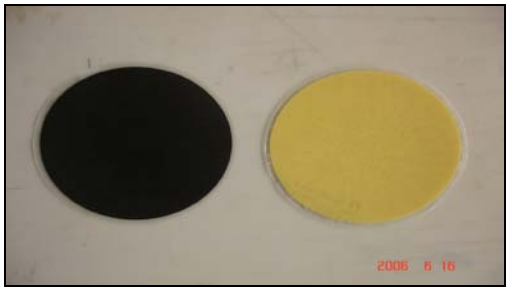

a) 8-inch diameter 12 layer thin composite laminate mirror blank with chopped mat carbon and Kevlar

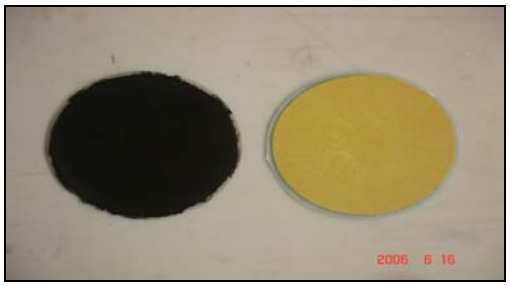

b) 8-inch diameter 8 layer thin composite mirrors with carbon and Kevlar cloth with 2 layer veil top and bottom

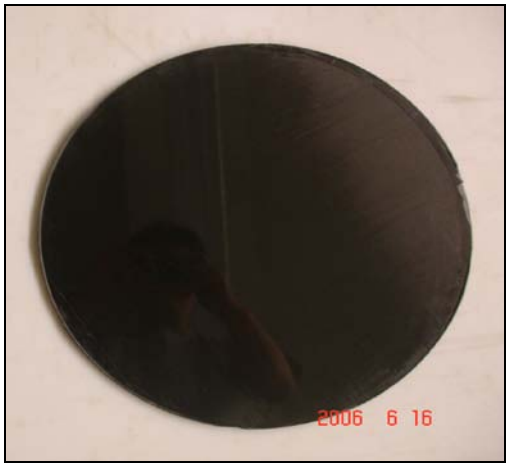

c) 8-inch diameter 24 layer unidirectional carbon composite mirror blank

d)

Figure 5: Fabricated flat composite mirror substrates. a) 8-inch diameter 12 layer thin composite laminate mirror blank with chopped mat carbon and Kevlar, b) 8-inch diameter 8 layer thin composite mirrors with carbon and Kevlar cloth with 2 layer veil top and bottom, c) 8-inch diameter 24 layer unidirectional carbon composite mirror blank

3.2. Analysis of Quasi-Isotropic Laminates

Lightweight composite telescope mirrors hold broad industrial appeal due to cost effectiveness, high strength and stiffness to weight ratios, and low areal density. However, with this cutting edge technology, accurately surfaced, diffraction limited, lightweight composite mirrors remains a challenge because of essential inheritance of directional dependency in unidirectional composite characteristics such as fiber print-though, environmental sensitivity, stability, and material deformation couplings induced by lay-up sequence. It is a common belief that a quasi-isotropic composite laminate plate is suited for future optical applications due to uniform in-plane extensional stiffnesses, and that such plates can replace conventional glass mirrors for future telescopes even in active/adaptive mirror applications. In quasi-isotropic laminates, however, flexural stiffnesses depend strongly on stacking sequence effects. The differences in flexural stiffness in the microscopic scale could cause an unacceptable sinusoidal waviness in composite surface. The purpose of the following section is to evaluate the influence of directionally variant flexural stiffness in mirrors for optical telescopes, including active/adaptive mirror applications. Moreover, mechanical comparisons are made between continuous fiber reinforced material and homogeneous materials such a chopped or short fiber products to see whether continuous fiber material is actually suitable for developing diffraction-limited optical performance, or if instead the industry should pursue alternative composite material product forms to overcome radial variations of flexural stiffness.

For presentation of calculations, the mechanical properties of an ideal laminate are evaluated along the 0 degree axis and the mechanical properties of symmetric-unbalanced laminates, which are the resulting radial properties of a circular composite mirror, are calculated with 5 degree increments for radial direction.

In classical laminated theory [Ref. 34], the strain relationship can be obtained for displacements u and v, plane normal strains (ε_x and ε_y) and shear strain (γ_{xy}) as follows:

$$\varepsilon_x = \frac{\partial u}{\partial x} = \frac{\partial u_0}{\partial x} - z\frac{\partial^2 w_0}{\partial x^2} \tag{1}$$

$$\varepsilon_y = \frac{\partial v}{\partial y} = \frac{\partial v_0}{\partial y} - z\frac{\partial^2 w_0}{\partial y^2} \tag{2}$$

$$\gamma_{xy} = \frac{\partial u}{\partial x} + \frac{\partial v}{\partial y} = \frac{\partial u_0}{\partial y} + \frac{\partial v_0}{\partial x} - 2z\frac{\partial^2 w_0}{\partial x \partial y} \tag{3}$$

The preceding strain-displacement relation can be written in terms of the mid-plane strains and the plate curvature as follows:

$$\begin{Bmatrix} \varepsilon_x \\ \varepsilon_y \\ \gamma_{xy} \end{Bmatrix} = \begin{Bmatrix} \varepsilon_x^0 \\ \varepsilon_y^0 \\ \gamma_{xy}^0 \end{Bmatrix} + z \begin{Bmatrix} \kappa_x \\ \kappa_y \\ \kappa_{xy} \end{Bmatrix} \tag{4}$$

where the mid-plane strains and the curvatures of the plate are:

$$\begin{Bmatrix} \varepsilon_x^0 \\ \varepsilon_y^0 \\ \gamma_{xy}^0 \end{Bmatrix} = \begin{Bmatrix} \dfrac{\partial u_0}{\partial x} \\ \dfrac{\partial v_0}{\partial y} \\ \dfrac{\partial u_0}{\partial y} + \dfrac{\partial v_0}{\partial x} \end{Bmatrix} \tag{5}$$

$$\begin{Bmatrix} \kappa_x \\ \kappa_y \\ \kappa_{xy} \end{Bmatrix} = \begin{Bmatrix} -\dfrac{\partial^2 w_0}{\partial^2 x} \\ -\dfrac{\partial^2 w_0}{\partial^2 y} \\ -2\dfrac{\partial^2 w_0}{\partial x \partial y} \end{Bmatrix} \tag{6}$$

For plane-stress condition the stress-strain relationship for any lamina (e.g., kth) can be as follows:

$$\begin{Bmatrix} \sigma_x \\ \sigma_y \\ \tau_{xy} \end{Bmatrix}_k = \begin{bmatrix} \bar{Q}_{11} & \bar{Q}_{12} & \bar{Q}_{16} \\ \bar{Q}_{12} & \bar{Q}_{22} & \bar{Q}_{26} \\ \bar{Q}_{16} & \bar{Q}_{26} & \bar{Q}_{66} \end{bmatrix}_k \begin{Bmatrix} \varepsilon_x^0 \\ \varepsilon_y^0 \\ \gamma_{xy}^0 \end{Bmatrix} + z \begin{bmatrix} \bar{Q}_{11} & \bar{Q}_{12} & \bar{Q}_{16} \\ \bar{Q}_{12} & \bar{Q}_{22} & \bar{Q}_{26} \\ \bar{Q}_{16} & \bar{Q}_{26} & \bar{Q}_{66} \end{bmatrix}_k \begin{Bmatrix} \kappa_x \\ \kappa_y \\ \kappa_{xy} \end{Bmatrix} \tag{7}$$

where $\begin{bmatrix} \bar{Q}_{11} & \bar{Q}_{12} & \bar{Q}_{16} \\ \bar{Q}_{12} & \bar{Q}_{22} & \bar{Q}_{26} \\ \bar{Q}_{16} & \bar{Q}_{26} & \bar{Q}_{66} \end{bmatrix} = [T]^{-1} \begin{bmatrix} Q_{11} & Q_{12} & Q_{16} \\ Q_{12} & Q_{22} & Q_{26} \\ Q_{16} & Q_{26} & Q_{66} \end{bmatrix} [T]$,

$$Q_{11} = \frac{E_L}{1 - \nu_{LT}\nu_{TL}}$$

$$Q_{22} = \frac{E_T}{1 - \nu_{LT}\nu_{TL}}$$

$$Q_{12} = \frac{\nu_{TL}E_L}{1 - \nu_{LT}\nu_{TL}} = \frac{\nu_{LT}E_T}{1 - \nu_{LT}\nu_{TL}}$$

$$Q_{66} = G_{LT}$$

$Q_{16} = 0$ and $Q_{26} = 0$ for orthotropic material

and the transformation matrix $[T]$ and inverse of $[T]^{-1}$,

$$[T] = \begin{bmatrix} \cos^2\theta & \sin^2\theta & 2\sin\theta\cos\theta \\ \sin^2\theta & \cos^2\theta & -2\sin\theta\cos\theta \\ -\sin\theta\cos\theta & \sin\theta\cos\theta & \cos^2\theta - \sin^2\theta \end{bmatrix}$$

$$[T]^{-1} = \begin{bmatrix} \cos^2\theta & \sin^2\theta & -2\sin\theta\cos\theta \\ \sin^2\theta & \cos^2\theta & 2\sin\theta\cos\theta \\ \sin\theta\cos\theta & -\sin\theta\cos\theta & \cos^2\theta - \sin^2\theta \end{bmatrix}$$

The resultant plane running load and running moment acting on a laminate cross section are derived by integrating the corresponding plane stress through the laminate thickness, h:

$$N_x = \int_{-h/2}^{h/2} \sigma_x dz \qquad N_y = \int_{-h/2}^{h/2} \sigma_y dz \qquad N_{xy} = \int_{-h/2}^{h/2} \tau_{xy} dz \tag{8}$$

$$M_x = \int_{-h/2}^{h/2} z\sigma_x dz \qquad M_y = \int_{-h/2}^{h/2} z\sigma_y dz \qquad M_{xy} = \int_{-h/2}^{h/2} z\tau_{xy} dz \tag{9}$$

where N and M are the in-plane forces and moments (per unit length).

When considering a laminate consisting of n orthotropic lamina, the force-moment system acting at the mid-plane of a laminate can be obtained by summation of force and moment Eqs. (8) and (9) of each layer,

$$\begin{Bmatrix} N_x \\ N_y \\ N_{xy} \end{Bmatrix} = \int_{-h/2}^{h/2} \begin{Bmatrix} \sigma_x \\ \sigma_y \\ \tau_{xy} \end{Bmatrix} dz = \sum_{k=1}^{n} \int_{h_{k-1}}^{h_k} \begin{Bmatrix} \sigma_x \\ \sigma_y \\ \tau_{xy} \end{Bmatrix}_k dz \tag{10}$$

$$\begin{Bmatrix} M_x \\ M_y \\ M_{xy} \end{Bmatrix} = \int_{-h/2}^{h/2} \begin{Bmatrix} \sigma_x \\ \sigma_y \\ \tau_{xy} \end{Bmatrix} z dz = \sum_{k=1}^{n} \int_{h_{k-1}}^{h_k} \begin{Bmatrix} \sigma_x \\ \sigma_y \\ \tau_{xy} \end{Bmatrix}_k z dz \tag{11}$$

The equation (10) and (11) can be written in terms of mid-plane strain and plate curvatures.

$$\begin{Bmatrix} N_x \\ N_y \\ N_{xy} \end{Bmatrix} = \sum_{k=1}^{n} \left\{ \int_{h_{k-1}}^{h_k} \begin{bmatrix} \bar{Q}_{11} & \bar{Q}_{12} & \bar{Q}_{16} \\ \bar{Q}_{12} & \bar{Q}_{22} & \bar{Q}_{26} \\ \bar{Q}_{16} & \bar{Q}_{26} & \bar{Q}_{66} \end{bmatrix}_k \begin{Bmatrix} \varepsilon_x^0 \\ \varepsilon_y^0 \\ \gamma_{xy}^0 \end{Bmatrix} dz + \int_{h_{k-1}}^{h_k} \begin{bmatrix} \bar{Q}_{11} & \bar{Q}_{12} & \bar{Q}_{16} \\ \bar{Q}_{12} & \bar{Q}_{22} & \bar{Q}_{26} \\ \bar{Q}_{16} & \bar{Q}_{26} & \bar{Q}_{66} \end{bmatrix}_k \begin{Bmatrix} \kappa_x \\ \kappa_y \\ \kappa_{xy} \end{Bmatrix} z dz \right\} \tag{12}$$

$$\begin{Bmatrix} M_x \\ M_y \\ M_{xy} \end{Bmatrix} = \sum_{k=1}^{n} \left\{ \int_{h_{k-1}}^{h_k} \begin{bmatrix} \bar{Q}_{11} & \bar{Q}_{12} & \bar{Q}_{16} \\ \bar{Q}_{12} & \bar{Q}_{22} & \bar{Q}_{26} \\ \bar{Q}_{16} & \bar{Q}_{26} & \bar{Q}_{66} \end{bmatrix}_k \begin{Bmatrix} \varepsilon_x^0 \\ \varepsilon_y^0 \\ \gamma_{xy}^0 \end{Bmatrix} z dz + \int_{h_{k-1}}^{h_k} \begin{bmatrix} \bar{Q}_{11} & \bar{Q}_{12} & \bar{Q}_{16} \\ \bar{Q}_{12} & \bar{Q}_{22} & \bar{Q}_{26} \\ \bar{Q}_{16} & \bar{Q}_{26} & \bar{Q}_{66} \end{bmatrix}_k \begin{Bmatrix} \kappa_x \\ \kappa_y \\ \kappa_{xy} \end{Bmatrix} z^2 dz \right\} \tag{13}$$

The equation (12) and (13) can be written as follows:

$$\begin{Bmatrix} N_x \\ N_y \\ N_{xy} \end{Bmatrix} = \left[\sum_{k=1}^{n} \begin{bmatrix} \bar{Q}_{11} & \bar{Q}_{12} & \bar{Q}_{16} \\ \bar{Q}_{12} & \bar{Q}_{22} & \bar{Q}_{26} \\ \bar{Q}_{16} & \bar{Q}_{26} & \bar{Q}_{66} \end{bmatrix}_k \int_{h_{k-1}}^{h_k} dz \right] \begin{Bmatrix} \varepsilon_x^0 \\ \varepsilon_y^0 \\ \gamma_{xy}^0 \end{Bmatrix} + \left[\sum_{k=1}^{n} \begin{bmatrix} \bar{Q}_{11} & \bar{Q}_{12} & \bar{Q}_{16} \\ \bar{Q}_{12} & \bar{Q}_{22} & \bar{Q}_{26} \\ \bar{Q}_{16} & \bar{Q}_{26} & \bar{Q}_{66} \end{bmatrix}_k \int_{h_{k-1}}^{h_k} z dz \right] \begin{Bmatrix} \kappa_x \\ \kappa_y \\ \kappa_{xy} \end{Bmatrix} \tag{14}$$

$$\begin{Bmatrix} M_x \\ M_y \\ M_{xy} \end{Bmatrix} = \left[\sum_{k=1}^{n} \begin{bmatrix} \bar{Q}_{11} & \bar{Q}_{12} & \bar{Q}_{16} \\ \bar{Q}_{12} & \bar{Q}_{22} & \bar{Q}_{26} \\ \bar{Q}_{16} & \bar{Q}_{26} & \bar{Q}_{66} \end{bmatrix}_k \int_{h_{k-1}}^{h_k} z dz \right] \begin{Bmatrix} \varepsilon_x^0 \\ \varepsilon_y^0 \\ \gamma_{xy}^0 \end{Bmatrix} + \left[\sum_{k=1}^{n} \begin{bmatrix} \bar{Q}_{11} & \bar{Q}_{12} & \bar{Q}_{16} \\ \bar{Q}_{12} & \bar{Q}_{22} & \bar{Q}_{26} \\ \bar{Q}_{16} & \bar{Q}_{26} & \bar{Q}_{66} \end{bmatrix}_k \int_{h_{k-1}}^{h_k} z^2 dz \right] \begin{Bmatrix} \kappa_x \\ \kappa_y \\ \kappa_{xy} \end{Bmatrix} \tag{15}$$

With preceding definitions of the stiffness matrices, the above expressions for the in-plane forces and moments become,

$$\begin{Bmatrix} N_x \\ N_y \\ N_{xy} \\ M_x \\ M_y \\ M_{xy} \end{Bmatrix} = \begin{bmatrix} A_{11} & A_{12} & A_{16} & B_{11} & B_{12} & B_{16} \\ A_{12} & A_{22} & A_{26} & B_{12} & B_{22} & B_{26} \\ A_{16} & A_{26} & A_{66} & B_{16} & B_{26} & B_{66} \\ B_{11} & B_{12} & B_{16} & D_{11} & D_{12} & D_{16} \\ B_{12} & B_{22} & B_{26} & D_{12} & D_{22} & D_{26} \\ B_{16} & B_{26} & B_{66} & D_{16} & D_{26} & D_{66} \end{bmatrix} \begin{Bmatrix} \varepsilon_x^0 \\ \varepsilon_y^0 \\ \gamma_{xy}^0 \\ \kappa_x \\ \kappa_y \\ \kappa_{xy} \end{Bmatrix} \tag{16}$$

where

$$\begin{aligned} A_{ij} &= \sum_{k=1}^{n} (\bar{Q}_{ij})_k (h_k - h_{k-1}) \\ B_{ij} &= \frac{1}{2} \sum_{k=1}^{n} (\bar{Q}_{ij})_k (h_k^{\,2} - h_{k-1}^{\,2}) \\ D_{ij} &= \frac{1}{3} \sum_{k=1}^{n} (\bar{Q}_{ij})_k (h_k^{\,3} - h_{k-1}^{\,3}) \end{aligned} \tag{17}$$

$$\begin{Bmatrix} N \\ M \end{Bmatrix} = \begin{bmatrix} A & B \\ B & D \end{bmatrix} \begin{Bmatrix} \varepsilon^\circ \\ \kappa \end{Bmatrix} \tag{18}$$

Where $\bar{Q}_{ij}$ represents the transformed reduced lamina stiffness matrix and the matrices $[A]$, $[B]$, and $[D]$ are called the extensional stiffness matrix, coupling stiffness matrix, and flexural stiffness matrix, respectively.

3.2.1. Ideal Laminate vs. Symmetric-Unbalance Circular Composite Laminate Using Continuous Fiber Reinforced Material vs. Other Homogeneous Materials

3.2.1.1. Continuous Fiber Reinforced Material

In general, the flexural stiffness matrix $[D]$ in a quasi-isotropic laminate is not uniform, but rather depends on orientation and stacking sequence of the laminate. The following results are the calculation and comparison of macro-mechanical stiffness of $[A], [B]$, and $[D]$ matrices for π/n quasi-isotropic circular composite mirror substrate where n=3, 4, 6 using unidirectional and short fiber (chopped mat) material. Table 2 shows the calculation of macro-mechanical stiffness properties of a circular mirror (Symmetric and unbalanced) as a specific example of stacking sequence effects in a π/4 quasi-isotropic laminate with 24 layers.

Table 2: Description of half of stacking sequence for π/4 quasi-isotropic circular composite mirror, Ideal at 0 degree (Symmetric and balance) and radial directions (Off-axis).

Radial axis in mirror (deg.)	Local Stacking Sequence in π/4 Laminate											
On-axis, 0	45	-45	0	90	0	90	-45	45	90	0	45	-45
5	40	-50	-5	85	-5	85	-50	40	85	-5	40	-50
10	35	-55	-10	80	-10	80	-55	35	80	-10	35	-55
15	30	-60	-15	75	-15	75	-60	30	75	-15	30	-60
20	25	-65	-20	70	-20	70	-65	25	70	-20	25	-65
25	20	-70	-25	65	-25	65	-70	20	65	-25	20	-70
30	15	-75	-30	60	-30	60	-75	15	60	-30	15	-75
35	10	-80	-35	55	-35	55	-80	10	55	-35	10	-80
40	5	-85	-40	50	-40	50	-85	5	50	-40	5	-85
45	0	-90	-45	45	-45	45	-90	0	45	-45	0	-90
50	-5	-95	-50	40	-50	40	-95	-5	40	-50	-5	-95
.	.	.	.	.	.	.	.	.	.	.	.	.
.	.	.	.	.	.	.	.	.	.	.	.	.
.	.	.	.	.	.	.	.	.	.	.	.	.
360	45	-45	0	90	0	90	-45	45	90	0	45	-45

Table 3: Variations of [A], [B], and [D] matrices for 24 layer π/n quasi-isotropic laminates using unidirectional material. Note: unit in [A], [B], and [D] are Psi-in, Psi-in^2, and Psi-in^3 respectively.

2.0076E+08	2.0076E+08	**6.2525E+07**	6.2525E+07	**0.0000E+00**	0.0000E+00	**0.0000E+00**	0.0000E+00	**0.0000E+00**	0.0000E+00	**0.0000E+00**	0.0000E+00
	2.0076E+08		6.2525E+07		0.0000E+00		0.0000E+00		0.0000E+00		0.0000E+00
6.2525E+07	6.2525E+07	**2.0076E+08**	2.0076E+08	**0.0000E+00**	0.0000E+00	**0.0000E+00**	0.0000E+00	**0.0000E+00**	0.0000E+00	**0.0000E+00**	0.0000E+00
	6.2525E+07		2.0076E+08		0.0000E+00		0.0000E+00		0.0000E+00		0.0000E+00
0.0000E+00	0.0000E+00	**0.0000E+00**	0.0000E+00	**6.9119E+07**	6.9119E+07	**0.0000E+00**	0.0000E+00	**0.0000E+00**	0.0000E+00	**0.0000E+00**	0.0000E+00
	0.0000E+00		0.0000E+00		6.9119E+07		0.0000E+00		0.0000E+00		0.0000E+00
0.0000E+00	0.0000E+00	**0.0000E+00**	0.0000E+00	**0.0000E+00**	0.0000E+00	**9.0482E+09**	1.1003E+10	**3.1149E+09**	3.2651E+09	**2.6015E+08**	7.3833E+08
	0.0000E+00		0.0000E+00		0.0000E+00		8.7518E+09		2.7373E+09		1.7157E+06
0.0000E+00	0.0000E+00	**0.0000E+00**	0.0000E+00	**0.0000E+00**	0.0000E+00	**3.1149E+09**	3.2651E+09	**9.9977E+09**	1.1003E+10	**7.3833E+08**	7.3833E+08
	0.0000E+00		0.0000E+00		0.0000E+00		2.7373E+09		8.7518E+09		1.7157E+06
0.0000E+00	0.0000E+00	**0.0000E+00**	0.0000E+00	**0.0000E+00**	0.0000E+00	**2.6015E+08**	7.3833E+08	**7.3833E+08**	7.3833E+08	**3.4314E+09**	3.5816E+09
	0.0000E+00		0.0000E+00		0.0000E+00		1.7157E+06		1.7157E+06		3.0538E+09

a) π/3 quasi-isotropic circular laminate from unidirectional material

2.0076E+08	2.0076E+08	**6.2525E+07**	6.2525E+07	**0.0000E+00**	0.0000E+00	**0.0000E+00**	0.0000E+00	**0.0000E+00**	0.0000E+00	**0.0000E+00**	0.0000E+00
	2.0076E+08		6.2525E+07		0.0000E+00		0.0000E+00		0.0000E+00		0.0000E+00
6.2525E+07	6.2525E+07	**2.0076E+08**	2.0076E+08	**0.0000E+00**	0.0000E+00	**0.0000E+00**	0.0000E+00	**0.0000E+00**	0.0000E+00	**0.0000E+00**	0.0000E+00
	6.2525E+07		2.0076E+08		0.0000E+00		0.0000E+00		0.0000E+00		0.0000E+00
0.0000E+00	0.0000E+00	**0.0000E+00**	0.0000E+00	**6.9119E+07**	6.9119E+07	**0.0000E+00**	0.0000E+00	**0.0000E+00**	0.0000E+00	**0.0000E+00**	0.0000E+00
	0.0000E+00		0.0000E+00		6.9119E+07		0.0000E+00		0.0000E+00		0.0000E+00
0.0000E+00	0.0000E+00	**0.0000E+00**	0.0000E+00	**0.0000E+00**	0.0000E+00	**1.0013E+10**	1.0116E+10	**3.0662E+09**	3.0662E+09	**1.1869E+08**	3.0911E+08
	0.0000E+00		0.0000E+00		0.0000E+00		9.0914E+09		2.9362E+09		5.6133E+06
0.0000E+00	0.0000E+00	**0.0000E+00**	0.0000E+00	**0.0000E+00**	0.0000E+00	**3.0662E+09**	3.0662E+09	**9.1308E+09**	1.0116E+10	**1.1869E+08**	3.0911E+08
	0.0000E+00		0.0000E+00		0.0000E+00		2.9362E+09		9.0914E+09		5.6133E+06
0.0000E+00	0.0000E+00	**0.0000E+00**	0.0000E+00	**0.0000E+00**	0.0000E+00	**1.1869E+08**	3.0911E+08	**1.1869E+08**	3.0911E+08	**3.3827E+09**	3.3827E+09
	0.0000E+00		0.0000E+00		0.0000E+00		5.6133E+06		5.6133E+06		3.2527E+09

b) π/4 quasi-isotropic circular laminate from unidirectional material

2.0076E+08	2.0076E+08	**6.2525E+07**	6.2525E+07	**0.0000E+00**	0.0000E+00	**0.0000E+00**	0.0000E+00	**0.0000E+00**	0.0000E+00	**0.0000E+00**	0.0000E+00
	2.0076E+08		6.2525E+07		0.0000E+00		0.0000E+00		0.0000E+00		0.0000E+00
6.2525E+07	6.2525E+07	**2.0076E+08**	2.0076E+08	**0.0000E+00**	0.0000E+00	**0.0000E+00**	0.0000E+00	**0.0000E+00**	0.0000E+00	**0.0000E+00**	0.0000E+00
	6.2525E+07		2.0076E+08		0.0000E+00		0.0000E+00		0.0000E+00		0.0000E+00
0.0000E+00	0.0000E+00	**0.0000E+00**	0.0000E+00	**6.9119E+07**	6.9119E+07	**0.0000E+00**	0.0000E+00	**0.0000E+00**	0.0000E+00	**0.0000E+00**	0.0000E+00
	0.0000E+00		0.0000E+00		6.9119E+07		0.0000E+00		0.0000E+00		0.0000E+00
0.0000E+00	0.0000E+00	**0.0000E+00**	0.0000E+00	**0.0000E+00**	0.0000E+00	**9.2497E+09**	1.0796E+10	**3.4559E+09**	3.4559E+09	**3.8053E+08**	7.3467E+08
	0.0000E+00		0.0000E+00		0.0000E+00		9.0016E+09		2.5465E+09		5.7253E+06
0.0000E+00	0.0000E+00	**0.0000E+00**	0.0000E+00	**0.0000E+00**	0.0000E+00	**3.4559E+09**	3.4559E+09	**9.1141E+09**	1.0796E+10	**3.2428E+08**	7.3467E+08
	0.0000E+00		0.0000E+00		0.0000E+00		2.5465E+09		9.0016E+09		5.7253E+06
0.0000E+00	0.0000E+00	**0.0000E+00**	0.0000E+00	**0.0000E+00**	0.0000E+00	**3.8053E+08**	7.3467E+08	**3.2428E+08**	7.3467E+08	**3.7724E+09**	3.7724E+09
	0.0000E+00		0.0000E+00		0.0000E+00		5.7253E+06		5.7253E+06		2.8630E+09

c) π/6 quasi-isotropic circular laminate from unidirectional material

The numerical results in Table 3 show the extensional, coupling, and flexural stiffness matrices (at on-axis and radial directions) in quasi-isotropic π/n laminates. As shown in Table 3, the laminate properties of extensional stiffness in π/n laminates from unidirectional materials supports the quasi-isotropic characteristic while the coefficients of flexural stiffness in circular mirror plate in each π/n laminates are varying. Such

variation of flexural stiffness in π/n circular mirror substrates due to stacking sequence effects could affect and hinder the mirror substrates from having a dimensionally stable surface mirror configuration for space applications.

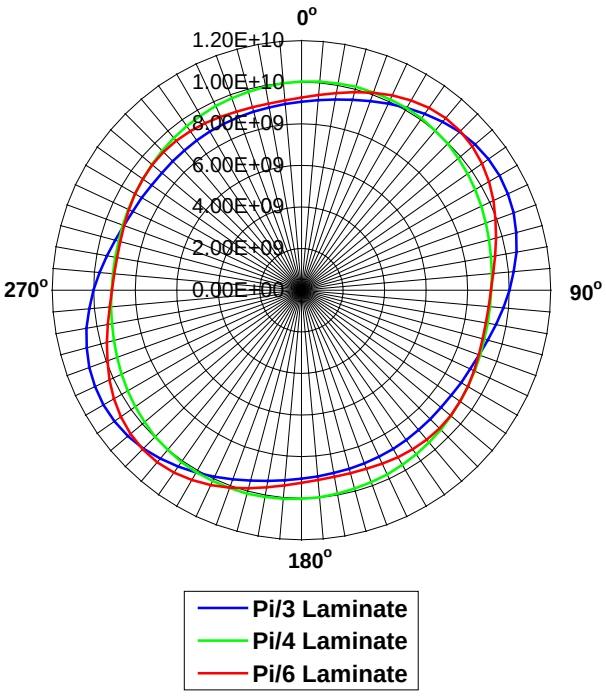

Figure 6: **Maximum and minimum variations of D_{11} in π/n laminates, n=3, 4, and 6. Note: ±12.85% variation of D_{11} in π/3, ±9.95% variation of D_{11} in π/6, and ±5.63% variation of D_{11} in π/4 laminate. Units in psi-in^3**

For this example, the π/3 circular plate has maximum D_{11} variations among the laminates, with maximum radial variation of ±12.85% in D_{11} and D_{22} observed. Similarly, in this example, the least radial variations of ±5.63% in D_{11} and D_{22} observed for the π/4 laminate. Although it is observed that the least flexural stiffness variation is observed in π/4 laminate, the magnitude of variation in flexural stiffness is still large. Thus, it might cause a serious surface deformation when external or internal thermal variance is present in the composite mirror substrates due to the inequality of flexural

stiffness in different radial directions. Consequently, radial flexural stiffness variations due to stacking sequence effects in continuous quasi-isotropic laminates are significant. Figure 6 shows a plot of radial variations of D_{11} in each π/n quasi-isotropic laminate.

3.2.1.2. Other Homogeneous Materials

Such directionally dependent flexural stiffness will be significant in fabricating a precision mirror due to thermal and moisture fluctuations common in cure, directional instabilities in coupling if unsymmetric surface coatings are introduced, and complexity in control of surface aberration and unacceptable surface undulation due to environmental fluctuations for circular composite mirror application and adaptive mirror technology. To eliminate such radial variations of D_{11} in circular quasi-isotropic laminates, one might use other homogenous material (chopped mat, veil…) to produce the circular composite mirrors, resulting in uniform macro-mechanical stiffness in both extensional and flexural stiffness matrices. Table 4 shows the results of macro-mechanical properties of quasi-isotropic circular laminates fabricating from short fiber material. The results clearly indicate that the extensional and flexural stiffness in these quasi-isotropic laminates behave uniformly in any in-plane radial direction. Local variations in extensional stiffness which may be caused by fiber volume or “random” orientation distributions must be considered in these alternate layer materials, but it is believed that sufficient layers of supposedly random orientation will also randomize these local effects.

Table 4: Variations of [A], [B], and [D] matrices for 24 layer π/n quasi-isotropic laminate using chopped mat (Homogenous material). Note: unit in [A], [B], and [D] are Psi-in, Psi-in^2, and Psi-in^3 respectively.

2.0076E+08	2.0076E+08	**6.2517E+07**	6.2517E+07	**0.0000E+00**	0.0000E+00	**0.0000E+00**	0.0000E+00	**0.0000E+00**	0.0000E+00	**0.0000E+00**	0.0000E+00
	2.0076E+08		6.2517E+07		0.0000E+00		0.0000E+00		0.0000E+00		0.0000E+00
6.2517E+07	6.2517E+07	**2.0076E+08**	2.0076E+08	**0.0000E+00**	0.0000E+00	**0.0000E+00**	0.0000E+00	**0.0000E+00**	0.0000E+00	**0.0000E+00**	0.0000E+00
	6.2517E+07		2.0076E+08		0.0000E+00		0.0000E+00		0.0000E+00		0.0000E+00
0.0000E+00	0.0000E+00	**0.0000E+00**	0.0000E+00	**6.9119E+07**	6.9119E+07	**0.0000E+00**	0.0000E+00	**0.0000E+00**	0.0000E+00	**0.0000E+00**	0.0000E+00
	0.0000E+00		0.0000E+00		6.9119E+07		0.0000E+00		0.0000E+00		0.0000E+00
0.0000E+00	0.0000E+00	**0.0000E+00**	0.0000E+00	**0.0000E+00**	0.0000E+00	**9.6362E+09**	9.6362E+09	**3.0008E+09**	3.0008E+09	**6.6973E+03**	7.3825E+03
	0.0000E+00		0.0000E+00		0.0000E+00		9.6362E+09		3.0008E+09		5.9094E+02
0.0000E+00	0.0000E+00	**0.0000E+00**	0.0000E+00	**0.0000E+00**	0.0000E+00	**3.0008E+09**	3.0008E+09	**9.6362E+09**	9.6362E+09	**6.6973E+03**	7.3825E+03
	0.0000E+00		0.0000E+00		0.0000E+00		3.0008E+09		9.6362E+09		5.9094E+02
0.0000E+00	0.0000E+00	**0.0000E+00**	0.0000E+00	**0.0000E+00**	0.0000E+00	**6.6973E+03**	7.3825E+03	**6.6973E+03**	7.3825E+03	**3.3177E+09**	3.3177E+09
	0.0000E+00		0.0000E+00		0.0000E+00		5.9094E+02		5.9094E+02		3.3177E+09

a) π/3 quasi-isotropic circular laminate from homogeneous material.

2.0076E+08	2.0076E+08	**6.2517E+07**	6.2517E+07	**0.0000E+00**	0.0000E+00	**0.0000E+00**	0.0000E+00	**0.0000E+00**	0.0000E+00	**0.0000E+00**	0.0000E+00
	2.0076E+08		6.2517E+07		0.0000E+00		0.0000E+00		0.0000E+00		0.0000E+00
6.2517E+07	6.2517E+07	**2.0076E+08**	2.0076E+08	**0.0000E+00**	0.0000E+00	**0.0000E+00**	0.0000E+00	**0.0000E+00**	0.0000E+00	**0.0000E+00**	0.0000E+00
	6.2517E+07		2.0076E+08		0.0000E+00		0.0000E+00		0.0000E+00		0.0000E+00
0.0000E+00	0.0000E+00	**0.0000E+00**	0.0000E+00	**6.9119E+07**	6.9119E+07	**0.0000E+00**	0.0000E+00	**0.0000E+00**	0.0000E+00	**0.0000E+00**	0.0000E+00
	0.0000E+00		0.0000E+00		6.9119E+07		0.0000E+00		0.0000E+00		0.0000E+00
0.0000E+00	0.0000E+00	**0.0000E+00**	0.0000E+00	**0.0000E+00**	0.0000E+00	**9.6362E+09**	9.6362E+09	**3.0008E+09**	3.0008E+09	**0.0000E+00**	1.7920E+03
	0.0000E+00		0.0000E+00		0.0000E+00		9.6362E+09		3.0008E+09		0.0000E+00
0.0000E+00	0.0000E+00	**0.0000E+00**	0.0000E+00	**0.0000E+00**	0.0000E+00	**3.0008E+09**	3.0008E+09	**9.6362E+09**	9.6362E+09	**0.0000E+00**	1.7920E+03
	0.0000E+00		0.0000E+00		0.0000E+00		3.0008E+09		9.6362E+09		0.0000E+00
0.0000E+00	0.0000E+00	**0.0000E+00**	0.0000E+00	**0.0000E+00**	0.0000E+00	**0.0000E+00**	1.7920E+03	**0.0000E+00**	1.7920E+03	**3.3177E+09**	3.3177E+09
	0.0000E+00		0.0000E+00		0.0000E+00		0.0000E+00		0.0000E+00		3.3177E+09

b) π/4 quasi-isotropic circular laminate from homogeneous material.

2.0076E+08	2.0076E+08	**6.2517E+07**	6.2517E+07	**0.0000E+00**	0.0000E+00	**0.0000E+00**	0.0000E+00	**0.0000E+00**	0.0000E+00	**0.0000E+00**	0.0000E+00
	2.0076E+08		6.2517E+07		0.0000E+00		0.0000E+00		0.0000E+00		0.0000E+00
6.2517E+07	6.2517E+07	**2.0076E+08**	2.0076E+08	**0.0000E+00**	0.0000E+00	**0.0000E+00**	0.0000E+00	**0.0000E+00**	0.0000E+00	**0.0000E+00**	0.0000E+00
	6.2517E+07		2.0076E+08		0.0000E+00		0.0000E+00		0.0000E+00		0.0000E+00
0.0000E+00	0.0000E+00	**0.0000E+00**	0.0000E+00	**6.9119E+07**	6.9119E+07	**0.0000E+00**	0.0000E+00	**0.0000E+00**	0.0000E+00	**0.0000E+00**	0.0000E+00
	0.0000E+00		0.0000E+00		6.9119E+07		0.0000E+00		0.0000E+00		0.0000E+00
0.0000E+00	0.0000E+00	**0.0000E+00**	0.0000E+00	**0.0000E+00**	0.0000E+00	**9.6362E+09**	9.6362E+09	**3.0008E+09**	3.0008E+09	**7.8792E+02**	7.3047E+03
	0.0000E+00		0.0000E+00		0.0000E+00		9.6362E+09		3.0008E+09		7.8792E+02
0.0000E+00	0.0000E+00	**0.0000E+00**	0.0000E+00	**0.0000E+00**	0.0000E+00	**3.0008E+09**	3.0008E+09	**9.6362E+09**	9.6362E+09	**7.8792E+02**	7.3047E+03
	0.0000E+00		0.0000E+00		0.0000E+00		3.0008E+09		9.6362E+09		7.8792E+02
0.0000E+00	0.0000E+00	**0.0000E+00**	0.0000E+00	**0.0000E+00**	0.0000E+00	**7.8792E+02**	7.3047E+03	**7.8792E+02**	7.3047E+03	**3.3177E+09**	3.3177E+09
	0.0000E+00		0.0000E+00		0.0000E+00		7.8792E+02		7.8792E+02		3.3177E+09

c) π/6 quasi-isotropic circular laminate from homogeneous material

3.2.1.3. Bend-Twist Effects in Quasi-Isotropic Laminates

It is also important to evaluate flexural stiffness ratios in quasi-isotropic laminates which might affect local flexural deformation in a circular composite mirror. The following shows the results and comparison studies for bend-twist-coupling ratios between a quasi-isotropic ideal laminate (at 0 degree) for each π/n laminate versus quasi-isotropic circular composite mirrors (symmetric unbalanced laminate). The numerical results shown in Table 5 indicate the bend-twist term D_{16} and D_{26} in all three quasi-isotropic laminates are relatively smaller than the axial flexural stiffness D_{11}. On the other hand, the values of the axial-transverse bend-coupling term D_{12} in the laminates are significant for possible coupling in the laminates. These variations of D_{12}/D_{11} in circular composite mirror might also cause local surface deformations from local coupling due to radial variations in D_{12}/D_{11}.

Table 5: Comparison of bend-bend and bend-twist ratios in π/n quasi-isotropic laminates using unidirectional material. Note: ideal (0 degree).

1. π/3 quasi-isotropic laminate with stacking sequence with [60,-60,0,60,0,-60,60,0,-60,0,-60,60]s

π/3	D_{12}/D_{11}	D_{16}/D_{11}	D_{26}/D_{11}	D_{12}/D_{22}	D_{16}/D_{22}	D_{26}/D_{22}
Ideal	3.4425E-01	2.8752E-02	8.1599E-02	3.1156E-01	2.6021E-02	7.3850E-02
Maximum	3.5898E-01	7.3850E-02	8.1599E-02	3.5898E-01	8.1599E-02	7.3850E-02
Minimum	2.4879E-01	1.9604E-04	1.5962E-04	2.4879E-01	1.5962E-04	1.9604E-04

2. π/4 quasi-isotropic laminate with stacking sequence with [45,-45,0,90,0,90,-45,45,90,0,45,-45]s

π/4	D_{12}/D_{11}	D_{16}/D_{11}	D_{26}/D_{11}	D_{12}/D_{22}	D_{16}/D_{22}	D_{26}/D_{22}
Ideal	3.0623E-01	1.1854E-02	1.1854E-02	3.3580E-01	1.2998E-02	1.2998E-02
Maximum	3.3650E-01	3.2380E-02	3.1705E-02	3.3650E-01	3.1705E-02	3.2380E-02
Minimum	2.9338E-01	6.1743E-04	5.5675E-04	2.9338E-01	5.5675E-04	6.1743E-04

3. π/6 quasi-isotropic laminate with stacking sequence with [60,-60,30,-30,0,90,30,-30,0,90,-60,60]s

π/6	D_{12}/D_{11}	D_{16}/D_{11}	D_{26}/D_{11}	D_{12}/D_{22}	D_{16}/D_{22}	D_{26}/D_{22}
Ideal	3.7362E-01	4.1140E-02	3.5058E-02	3.7918E-01	4.1752E-02	3.5580E-02
Maximum	3.7918E-01	7.3977E-02	8.0478E-02	3.7918E-01	8.0478E-02	7.3977E-02
Minimum	2.3587E-01	6.1602E-04	5.3559E-04	2.3587E-01	5.3559E-04	6.1602E-04

Table 6 indicates the range of values of ratios of D_{12}/D_{11} in quasi-isotropic laminates. The range of D_{12}/D_{11} are varying 14.7~60.76% with least variation in $\pi/4$ and most variation in $\pi/6$ quasi-isotropic laminates.

As indicated and emphasized above, radial variations in flexural stiffness and local coupling due to stacking sequence effects in quasi-isotropic composite mirrors will exist and may prevent the optic industry from fabricating precision mirror surfaces from continuous fiber reinforced plastics.

Table 6: Percentage change in variation of D_{12}/D_{11} in circular composite mirror (first three rows), ideal laminate and quasi-isotropic circular laminates (third row), percentage change in maximum and minimum variation of D_{12}/D_{11} in quasi-isotropic circular composite mirror (last row).

	D_{12}/D_{11} in $\pi/3$ Laminate	D_{12}/D_{11} in $\pi/4$ Laminate	D_{12}/D_{11} in $\pi/6$ Laminate
Ideal laminate of quasi-isotropic laminate (at 0 degree), (1)	0.3443	0.3062	0.3736
Maximum value of quasi-isotropic laminate at all radirections, (2)	0.3590	0.3365	0.3792
Minimum value of quasi-isotropic laminate at all radirections, (3)	0.2488	0.2934	0.2359
% Variations of D_{12}/D_{11} between (1) and (2)	4.28	9.88	1.49
% Variations of D_{12}/D_{11} in values between (2) and (3)	44.29	14.70	60.76

Such bend-twist terms in circular composite mirrors using inherent characteristics of unidirectional materials can be eliminated by utilizing homogenous materials (veil, chopped mat). The results of macro-mechanical stiffness and bend-twist couple ratios in short fiber circular composite mirror plates in Table 4 and 7 show that not only constant flexural stiffness but also constant bend-twist couple ratios can be obtained in all radial directions by using other short fiber materials. Therefore, no bend-twist effects would exist in all three quasi-isotropic laminates using homogeneous materials.

Table 7: Comparison of bend-bend and bend-twist ratios in π/n quasi-isotropic laminates using short fiber material (Homogenous material).

1. π/3 quasi-isotropic laminate with stacking sequence with [60,-60,0,60,0,-60,60,0,-60,0,-60,60]s

π/3	D_{12}/D_{11}	D_{16}/D_{11}	D_{26}/D_{11}	D_{12}/D_{22}	D_{16}/D_{22}	D_{26}/D_{22}
Ideal	3.1141E-01	6.9501E-07	6.9501E-07	3.1141E-01	6.9501E-07	6.9501E-07
Maximum	3.1141E-01	7.6612E-07	7.6612E-07	3.1141E-01	7.6612E-07	7.6612E-07
Minimum	3.1141E-01	6.1324E-08	6.1324E-08	3.1141E-01	6.1324E-08	6.1324E-08

2. π/4 quasi-isotropic laminate with stacking sequence with [45,-45,0,90,0,90,-45,45,90,0,45,-45]s

π/4	D_{12}/D_{11}	D_{16}/D_{11}	D_{26}/D_{11}	D_{12}/D_{22}	D_{16}/D_{22}	D_{26}/D_{22}
Ideal	3.1141E-01	3.0517E-22	3.0517E-22	3.1141E-01	3.0517E-22	3.0517E-22
Maximum	3.1141E-01	1.8596E-07	1.8596E-07	3.1141E-01	1.8596E-07	1.8596E-07
Minimum	3.1141E-01	4.5642E-23	4.5642E-23	3.1141E-01	4.5642E-23	4.5642E-23

3. π/6 quasi-isotropic laminate with stacking sequence with [60,-60,30,-30,0,90,30,-30,0,90,-60,60]s

π/6	D_{12}/D_{11}	D_{16}/D_{11}	D_{26}/D_{11}	D_{12}/D_{22}	D_{16}/D_{22}	D_{26}/D_{22}
Ideal	3.1141E-01	8.1766E-08	8.1766E-08	3.1141E-01	8.1766E-08	8.1766E-08
Maximum	3.1141E-01	7.5804E-07	7.5804E-07	3.1141E-01	7.5804E-07	7.5804E-07
Minimum	3.1141E-01	8.1766E-08	8.1766E-08	3.1141E-01	8.1766E-08	8.1766E-08

3.2.2. Ideal Laminate vs. Maximum Asymmetric-Unbalanced Laminate for Lay-up Sensitivity in Circular Mirror Plate Using Continuous Fiber Reinforced Material and Other Homogenous Materials

It is commonly believed that a precision lay-up is required to fabricate quasi-isotropic composite mirror substrates to get precision surfaces for composite mirrors. In industry standard, human lay-up error in ±2º misalignment is acceptable. Thus, it is interesting to evaluate macro-mechanical stiffness of maximum asymmetric laminates from misalignment by adding +2º to the top half of plies in a quasi-isotropic laminate stacking sequence and -2º to the bottom half stacking sequence. Such an approach illustrates that sensitivity of mechanical properties to degrees of coupling caused by maximum asymmetry for π/n quasi-isotropic laminates. Table 8 provides the details of

asymmetric laminate stacking sequence for this sensitivity study as a specific example based on π/4 quasi-isotropic laminate stacking sequence.

Table 8: Description of stacking sequence of asymmetric and unbalanced circular composite mirror based on π/4 quasi-isotropic lay-up.

Radial axis in mirror (deg.)	Description of stacking sequence of asymmetric π/4 laminated mirror based on π/4 quasi-isotropic lay-up sequence by adding +2 degree misalignment on the top lay-up sequence											
On-axis, 0	43	-47	-2	88	-2	88	-47	43	88	-2	43	-47
5	38	-52	-7	83	-7	83	-52	38	83	-7	38	-52
10	33	-57	-12	78	-12	78	-57	33	78	-12	33	-57
15	28	-62	-17	73	-17	73	-62	28	73	-17	28	-62
20	23	-67	-22	68	-22	68	-67	23	68	-22	23	-67
25	18	-72	-27	63	-27	63	-72	18	63	-27	18	-72
30	13	-77	-32	58	-32	58	-77	13	58	-32	13	-77
35	8	-82	-37	53	-37	53	-82	8	53	-37	8	-82
40	3	-87	-42	48	-42	48	-87	3	48	-42	3	-87
45	-2	-92	-47	43	-47	43	-92	-2	43	-47	-2	-92
50	-7	-97	-52	38	-52	38	-97	-7	38	-52	-7	-97
.	.	.	.	.	.	.	.	.	.	.	.	.
.	.	.	.	.	.	.	.	.	.	.	.	.
.	.	.	.	.	.	.	.	.	.	.	.	.
360	43	-47	-2	88	-2	88	-47	43	88	-2	43	-47

a) Stacking sequence of top half of asymmetric π/4 laminated mirror

Radial axis in mirror (deg.)	Description of stacking sequence of asymmetric π/4 laminated mirror based on π/4 quasi-isotropic lay-up sequence by adding -2 degree misalignment at the bottom lay-up sequence											
On-axis, 0	-43	47	2	92	47	-43	92	2	92	2	-43	47
5	-48	42	-3	87	42	-48	87	-3	87	-3	-48	42
10	-53	37	-8	82	37	-53	82	-8	82	-8	-53	37
15	-58	32	-13	77	32	-58	77	-13	77	-13	-58	32
20	-63	27	-18	72	27	-63	72	-18	72	-18	-63	27
25	-68	22	-23	67	22	-68	67	-23	67	-23	-68	22
30	-73	17	-28	62	17	-73	62	-28	62	-28	-73	17
35	-78	12	-33	57	12	-78	57	-33	57	-33	-78	12
40	-83	7	-38	52	7	-83	52	-38	52	-38	-83	7
45	-88	2	-43	47	2	-88	47	-43	47	-43	-88	2
50	-93	-3	-48	42	-3	-93	42	-48	42	-48	-93	-3
.	.	.	.	.	.	.	.	.	.	.	.	.
.	.	.	.	.	.	.	.	.	.	.	.	.
.	.	.	.	.	.	.	.	.	.	.	.	.
360	-43	47	2	92	47	-43	92	2	92	2	-43	47

b) Stacking sequence of bottom half of asymmetric π/4 laminated mirror

As shown by the results in Table 9, the coefficients of in-plane stiffness in both on-axis and off-axis of such asymmetric π/n laminates are no different compared with stiffness analysis on symmetric π/n laminates. The stiffness matrices from each π/n

laminate are tabulated in Table 9. Similarly, radial variations in flexural stiffness in asymmetric laminates behave almost the same as the properties of π/n laminates.

Table 9: Variations of [A], [B], and [D] matrices for 24 layer asymmetric-unbalanced laminate based on stacking sequence of π/n quasi-isotropic laminate using unidirectional material. Note: unit in [A], [B], and [D] are Psi-in, Psi-in^2, and Psi-in^3 respectively.

2.0076E+08	2.0076E+08	**6.2525E+07**	6.2525E+07	**0.0000E+00**	0.0000E+00	**2.1398E+06**	6.0544E+06	**1.9573E+06**	1.9573E+06	**0.0000E+00**	3.4969E+06
	2.0076E+08		6.2525E+07		0.0000E+00		9.8109E+04		3.3988E+05		0.0000E+00
6.2525E+07	6.2525E+07	**2.0076E+08**	2.0076E+08	**0.0000E+00**	0.0000E+00	**1.9573E+06**	1.9573E+06	**6.0544E+06**	6.0544E+06	**0.0000E+00**	3.4969E+06
	6.2525E+07		2.0076E+08		0.0000E+00		3.3988E+05		9.8109E+04		0.0000E+00
0.0000E+00	0.0000E+00	**0.0000E+00**	0.0000E+00	**6.9119E+07**	6.9119E+07	**0.0000E+00**	3.4969E+06	**0.0000E+00**	3.4969E+06	**1.9573E+06**	1.9573E+06
	0.0000E+00		0.0000E+00		6.9119E+07		0.0000E+00		0.0000E+00		3.3988E+05
2.1398E+06	6.0544E+06	**1.9573E+06**	1.9573E+06	**0.0000E+00**	3.4969E+06	**9.0505E+09**	1.0997E+10	**3.1138E+09**	3.2625E+09	**2.6126E+08**	7.3478E+08
	9.8109E+04		3.3988E+05		0.0000E+00		8.7531E+09		2.7399E+09		3.2870E+04
1.9573E+06	1.9573E+06	**6.0544E+06**	6.0544E+06	**0.0000E+00**	3.4969E+06	**3.1138E+09**	3.2625E+09	**9.9976E+09**	1.0997E+10	**7.3478E+08**	7.3478E+08
	3.3988E+05		9.8109E+04		0.0000E+00		2.7399E+09		8.7531E+09		3.2870E+04
0.0000E+00	3.4969E+06	**0.0000E+00**	3.4969E+06	**1.9573E+06**	1.9573E+06	**2.6126E+08**	7.3478E+08	**7.3478E+08**	7.3478E+08	**3.4303E+09**	3.5790E+09
	0.0000E+00		0.0000E+00		3.3988E+05		3.2870E+04		3.2870E+04		3.0564E+09

a) **Asymmetric-unbalanced circular laminate based on π/3 quasi-isotropic laminate stacking sequence from unidirectional material**

2.0076E+08	2.0076E+08	**6.2525E+07**	6.2525E+07	**0.0000E+00**	0.0000E+00	**1.1827E+06**	3.8920E+06	**0.0000E+00**	2.2258E+06	**2.8515E+06**	2.8515E+06
	2.0076E+08		6.2525E+07		0.0000E+00		6.3139E+04		0.0000E+00		3.1958E+05
6.2525E+07	6.2525E+07	**2.0076E+08**	2.0076E+08	**0.0000E+00**	0.0000E+00	**0.0000E+00**	2.2258E+06	**1.1827E+06**	3.8920E+06	**1.6688E+06**	2.8515E+06
	6.2525E+07		2.0076E+08		0.0000E+00		0.0000E+00		6.3139E+04		3.1958E+05
0.0000E+00	0.0000E+00	**0.0000E+00**	0.0000E+00	**6.9119E+07**	6.9119E+07	**2.8515E+06**	2.8515E+06	**1.6688E+06**	2.8515E+06	**0.0000E+00**	2.2258E+06
	0.0000E+00		0.0000E+00		6.9119E+07		3.1958E+05		3.1958E+05		0.0000E+00
1.1827E+06	3.8920E+06	**0.0000E+00**	2.2258E+06	**2.8515E+06**	2.8515E+06	**1.0012E+10**	1.0115E+10	**3.0655E+09**	3.0655E+09	**1.1840E+08**	3.0789E+08
	6.3139E+04		0.0000E+00		3.1958E+05		9.0931E+09		2.9369E+09		5.2950E+06
0.0000E+00	2.2258E+06	**1.1827E+06**	3.8920E+06	**1.6688E+06**	2.8515E+06	**3.0655E+09**	3.0655E+09	**9.1325E+09**	1.0115E+10	**1.1840E+08**	3.0789E+08
	0.0000E+00		6.3139E+04		3.1958E+05		2.9369E+09		9.0931E+09		5.2950E+06
2.8515E+06	2.8515E+06	**1.6688E+06**	2.8515E+06	**0.0000E+00**	2.2258E+06	**1.1840E+08**	3.0789E+08	**1.1840E+08**	3.0789E+08	**3.3820E+09**	3.3820E+09
	3.1958E+05		3.1958E+05		0.0000E+00		5.2950E+06		5.2950E+06		3.2534E+09

b) **Asymmetric-unbalanced circular laminate based on π/4 quasi-isotropic laminate stacking sequence from unidirectional material**

200763000	200763000	**62525000**	62525000	**0**	0	**3027200**	8546650	**978658**	3508610	**1024720**	5755620
	200763000		62525000		0		626162		239869		343624
62525000	62525000	**200763000**	200763000	**0**	0	**978658**	3508610	**1069880**	8546650	**5755620**	5755620
	62525000		200763000		0		239869		626162		343624
0	0	**0**	0	**69118800**	69118800	**1024720**	5755620	**5755620**	5755620	**978658**	3508610
	0		0		69118800		343624		343624		239869
3027200	8546650	**978658**	3508610	**1024720**	5755620	**9253980000**	10790000000	**3451480000**	3451480000	**379400000**	729649000
	626162		239869		343624		9005520000		2550920000		5973420
978658	3508610	**1069880**	8546650	**5755620**	5755620	**3451480000**	3451480000	**9118670000**	10790000000	**323691000**	729649000
	239869		626162		343624		2550920000		9005520000		5973420
1024720	5755620	**5755620**	5755620	**978658**	3508610	**379400000**	729649000	**323691000**	729649000	**3767980000**	3767980000
	343624		343624		239869		5973420		5973420		2867420000

c) **Asymmetric-unbalanced circular laminate based on π/6 quasi-isotropic laminate stacking sequence from unidirectional material**

Figure 7 represents analytical results of D_{11} in asymmetric laminates derived form π/n stacking sequences radially, for better visualization. As shown, stacking sequence effects are not severe in asymmetric laminates through all radial directions. The extensional stiffness and radial variations in D_{11} between quasi-isotropic laminates and asymmetric-unbalanced laminates are within less than 0.05%.

The only difference between symmetric and asymmetric π/n laminates stiffness analysis is the presence of coupling stiffness in asymmetric laminates due to the asymmetric stacking sequence effects. However, the maximum values of coupling stiffness coefficients of B_{11}, B_{22}, and B_{12} etc… present in coupling stiffness matrix are relatively smaller than A_{11}, A_{22}, A_{12}, D_{11}, and D_{22} in π/n asymmetric laminates.

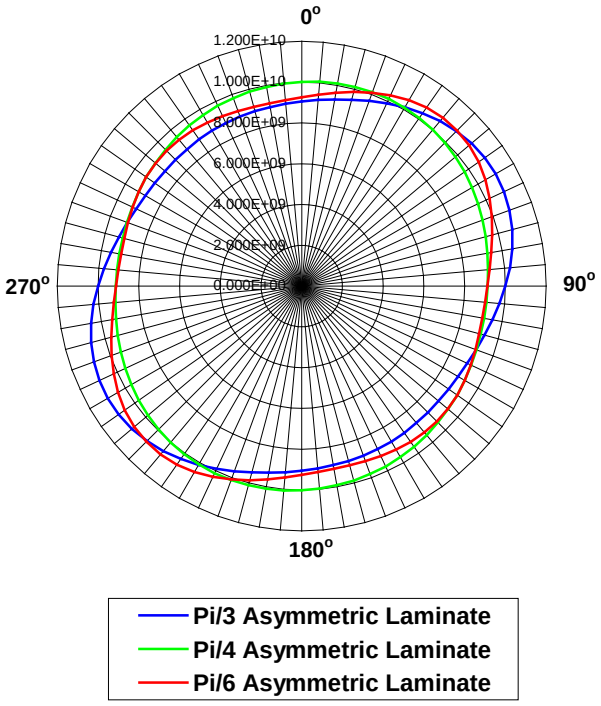

Figure 7: Maximum and minimum variations of D_{11} in asymmetric laminates. Note: ±12.82% variation of D_{11} in $\pi/3$, ±9.9% variation of D_{11} in $\pi/6$, and ±5.62% variation of D_{11} in $\pi/4$ laminate. Unit is in psi-in^3

Bending stiffness ratios in asymmetric laminates behave almost the same as in ideal quasi-isotropic laminates. Tables 10 and 11 show the ranges of ratios of D_{12}/D_{11} in quasi-isotropic laminates are varying 14.62~60.1% with least variation in $\pi/4$ and most variation in $\pi/6$ quasi-isotropic laminates. Also, similar to quasi-isotropic laminates, the bend-twist term D_{16} in all three asymmetric laminates are relatively smaller than axial stiffness D_{11}. Similarly, in asymmetric laminates, the radial values of D_{12} in a circular mirror are significant compared to the values of D_{11}. The asymmetric laminates have almost no differences in values of D_{12} and D_{11} in radial directions as the ideal quasi-isotropic laminates. It is obvious that stacking sequence effects exist for circular mirrors due to directional dependency from unidirectional materials. Again, the existence of coupling stiffness matrix terms in composite mirrors due to asymmetric laminate characteristics are not the dominant factors, since the magnitude of the coefficients are relatively smaller than extensional and flexural stiffness coefficients in the composites. This sensitivity study clearly indicated that although precision lay-up is required to fabricate an accurate surface mirror, small misalignment in quasi-isotropic lay-up do affect mechanical properties in composite mirrors but to a lesser extent than the radial variations alone.

Table 10: Comparison of bend-bend and bend-twist ratios in asymmetric π/n laminates using unidirectional material. Note: ideal (0 degree).

1. π/3 quasi-isotropic laminate with stacking sequence with [60,-60,0,60,0,-60,60,0,-60,0,-60,60]s

π/3	D_{12}/D_{11}	D_{16}/D_{11}	D_{26}/D_{11}	D_{12}/D_{22}	D_{16}/D_{22}	D_{26}/D_{22}
Ideal	3.4425E-01	2.8752E-02	8.1599E-02	3.1156E-01	2.6021E-02	7.3850E-02
Maximum	3.5862E-01	7.3496E-02	8.1187E-02	3.5862E-01	8.1187E-02	7.3496E-02
Minimum	2.4914E-01	3.7552E-06	3.0590E-06	2.4914E-01	3.0590E-06	3.7552E-06

2. π/4 quasi-isotropic laminate with stacking sequence with [45,-45,0,90,0,90,-45,45,90,0,45,-45]s

π/4	D_{12}/D_{11}	D_{16}/D_{11}	D_{26}/D_{11}	D_{12}/D_{22}	D_{16}/D_{22}	D_{26}/D_{22}
Ideal	3.0623E-01	1.1854E-02	1.1854E-02	3.3580E-01	1.2998E-02	1.2998E-02
Maximum	3.3637E-01	3.2252E-02	3.1581E-02	3.3637E-01	3.1581E-02	3.2252E-02
Minimum	2.9347E-01	5.8231E-04	5.2521E-04	2.9347E-01	5.2521E-04	5.8231E-04

3. π/6 quasi-isotropic laminate with stacking sequence with [60,-60,30,-30,0,90,30,-30,0,90,-60,60]s

π/6	D_{12}/D_{11}	D_{16}/D_{11}	D_{26}/D_{11}	D_{12}/D_{22}	D_{16}/D_{22}	D_{26}/D_{22}
Ideal	3.7362E-01	4.1140E-02	3.5058E-02	3.7918E-01	4.1752E-02	3.5580E-02
Maximum	3.7851E-01	7.3471E-02	7.9910E-02	3.7851E-01	7.9910E-02	7.3471E-02
Minimum	2.3642E-01	6.3657E-04	5.5361E-04	2.3642E-01	5.5361E-04	6.3657E-04

Table 11: Percentage change in variation of D_{12}/D_{11} of asymmetric laminates (first three rows), % variation between ideal (at 0 degree) and maximum ratio in circular asymmetric laminate (third row), percentage change in maximum and minimum variation of D_{12}/D_{11} in asymmetric circular mirror (last row).

	D_{12}/D_{11} in π/3 Laminate	D_{12}/D_{11} in π/4 Laminate	D_{12}/D_{11} in π/6 Laminate
Ideal laminate of asymmetric laminate (at 0 degree), (1)	0.3443	0.3062	0.3736
Maximum value of asymmetric laminate at all radirections, (2)	0.3586	0.3364	0.3785
Minimum value of asymmetric laminate at all radirections, (3)	0.2491	0.2935	0.2364
% Variations of D_{12}/D_{11} between (1) and (2)	4.17	9.84	1.31
% Variations of D_{12}/D_{11} in values between (2) and (3)	43.94	14.62	60.10

The evaluation of mechanical stiffness in asymmetric laminates using homogenous material is also calculated to compare with asymmetric laminates stiffness from unidirectional material. The results of $[A]$, $[B]$, and $[D]$ matrices for asymmetric-unbalanced laminates using homogenous material, shown in Tables 12 and 13, indicate uniform directional macro-mechanical stiffness in the laminates extensional and flexural stiffness. The bend-twist-couple ratios in asymmetric laminate using short fiber material are also constant through all radial directions.

Table 12: Variations of [A], [B], and [D] matrices for 24 layer asymmetric-unbalanced laminate based on stacking sequence of π/n quasi-isotropic laminate using chopped mat (Homogenous material). Note: unit in [A], [B], and [D] are Psi-in, Psi-in^2, and Psi-in^3 respectively.

2.0076E+08	2.0076E+08	**6.2517E+07**	6.2517E+07	**0.0000E+00**	0.0000E+00	**5.4828E+01**	5.4828E+01	**5.4828E+01**	5.4828E+01	**0.0000E+00**	5.3995E+01
	2.0076E+08		6.2517E+07		0.0000E+00		9.5208E+00		9.5208E+00		0.0000E+00
6.2517E+07	6.2517E+07	**2.0076E+08**	2.0076E+08	**0.0000E+00**	0.0000E+00	**5.4828E+01**	5.4828E+01	**5.4828E+01**	5.4828E+01	**0.0000E+00**	5.3995E+01
	6.2517E+07		2.0076E+08		0.0000E+00		5.4828E+01		9.5208E+00		0.0000E+00
0.0000E+00	0.0000E+00	**0.0000E+00**	0.0000E+00	**6.9119E+07**	6.9119E+07	**0.0000E+00**	5.3995E+01	**0.0000E+00**	5.3995E+01	**5.4828E+01**	5.4828E+01
	0.0000E+00		0.0000E+00		6.9119E+07		0.0000E+00		0.0000E+00		9.5208E+00
5.4828E+01	5.4828E+01	**5.4828E+01**	5.4828E+01	**0.0000E+00**	5.3995E+01	**9.6362E+09**	9.6362E+09	**3.0008E+09**	3.0008E+09	**6.6321E+03**	7.3106E+03
	9.5208E+00		9.5208E+00		0.0000E+00		9.6362E+09		3.0008E+09		5.8519E+02
5.4828E+01	5.4828E+01	**5.4828E+01**	5.4828E+01	**0.0000E+00**	5.3995E+01	**3.0008E+09**	3.0008E+09	**9.6362E+09**	9.6362E+09	**6.6321E+03**	7.3106E+03
	5.4828E+01		9.5208E+00		0.0000E+00		3.0008E+09		9.6362E+09		5.8519E+02
0.0000E+00	5.3995E+01	**0.0000E+00**	5.3995E+01	**5.4828E+01**	5.4828E+01	**6.6321E+03**	7.3106E+03	**6.6321E+03**	7.3106E+03	**3.3177E+09**	3.3177E+09
	0.0000E+00		0.0000E+00		9.5208E+00		5.8519E+02		5.8519E+02		3.3177E+09

a) **Asymmetric-unbalanced circular laminate based on π/3 quasi-isotropic laminate stacking sequence from homogeneous material.**

2.0076E+08	2.0076E+08	**6.2517E+07**	6.2517E+07	**0.0000E+00**	0.0000E+00	**0.0000E+00**	6.2349E+01	**0.0000E+00**	6.2349E+01	**6.3310E+01**	6.3310E+01
	2.0076E+08		6.2517E+07		0.0000E+00		0.0000E+00		0.0000E+00		1.0994E+01
6.2517E+07	6.2517E+07	**2.0076E+08**	2.0076E+08	**0.0000E+00**	0.0000E+00	**0.0000E+00**	6.2349E+01	**0.0000E+00**	6.2349E+01	**6.3310E+01**	6.3310E+01
	6.2517E+07		2.0076E+08		0.0000E+00		0.0000E+00		0.0000E+00		1.0994E+01
0.0000E+00	0.0000E+00	**0.0000E+00**	0.0000E+00	**6.9119E+07**	6.9119E+07	**6.3310E+01**	6.3310E+01	**6.3310E+01**	6.3310E+01	**0.0000E+00**	6.2349E+01
	0.0000E+00		0.0000E+00		6.9119E+07		1.0994E+01		1.0994E+01		0.0000E+00
0.0000E+00	6.2349E+01	**0.0000E+00**	6.2349E+01	**6.3310E+01**	6.3310E+01	**9.6362E+09**	9.6362E+09	**3.0008E+09**	3.0008E+09	**0.0000E+00**	1.7745E+03
	0.0000E+00		0.0000E+00		1.0994E+01		9.6362E+09		3.0008E+09		0.0000E+00
0.0000E+00	6.2349E+01	**0.0000E+00**	6.2349E+01	**6.3310E+01**	6.3310E+01	**3.0008E+09**	3.0008E+09	**9.6362E+09**	9.6362E+09	**0.0000E+00**	1.7745E+03
	0.0000E+00		0.0000E+00		1.0994E+01		3.0008E+09		9.6362E+09		0.0000E+00
6.3310E+01	6.3310E+01	**6.3310E+01**	6.3310E+01	**0.0000E+00**	6.2349E+01	**0.0000E+00**	1.7745E+03	**0.0000E+00**	1.7745E+03	**3.3177E+09**	3.3177E+09
	1.0994E+01		1.0994E+01		0.0000E+00		0.0000E+00		0.0000E+00		3.3177E+09

b) **Asymmetric-unbalanced circular laminate based on π/4 quasi-isotropic laminate stacking sequence from homogeneous material.**

2.0076E+08	2.0076E+08	**6.2517E+07**	6.2517E+07	**0.0000E+00**	0.0000E+00	**0.0000E+00**	0.0000E+00	**0.0000E+00**	0.0000E+00	**0.0000E+00**	0.0000E+00
	2.0076E+08		6.2517E+07		0.0000E+00		0.0000E+00		0.0000E+00		0.0000E+00
6.2517E+07	6.2517E+07	**2.0076E+08**	2.0076E+08	**0.0000E+00**	0.0000E+00	**0.0000E+00**	0.0000E+00	**0.0000E+00**	0.0000E+00	**0.0000E+00**	0.0000E+00
	6.2517E+07		2.0076E+08		0.0000E+00		0.0000E+00		0.0000E+00		0.0000E+00
0.0000E+00	0.0000E+00	**0.0000E+00**	0.0000E+00	**6.9119E+07**	6.9119E+07	**0.0000E+00**	0.0000E+00	**0.0000E+00**	0.0000E+00	**0.0000E+00**	0.0000E+00
	0.0000E+00		0.0000E+00		6.9119E+07		0.0000E+00		0.0000E+00		0.0000E+00
0.0000E+00	0.0000E+00	**0.0000E+00**	0.0000E+00	**0.0000E+00**	0.0000E+00	**9.6362E+09**	9.6362E+09	**3.0008E+09**	3.0008E+09	**7.8025E+02**	7.2336E+03
	0.0000E+00		0.0000E+00		0.0000E+00		9.6362E+09		3.0008E+09		7.8025E+02
0.0000E+00	0.0000E+00	**0.0000E+00**	0.0000E+00	**0.0000E+00**	0.0000E+00	**3.0008E+09**	3.0008E+09	**9.6362E+09**	9.6362E+09	**7.8025E+02**	7.2336E+03
	0.0000E+00		0.0000E+00		0.0000E+00		3.0008E+09		9.6362E+09		7.8025E+02
0.0000E+00	0.0000E+00	**0.0000E+00**	0.0000E+00	**0.0000E+00**	0.0000E+00	**7.8025E+02**	7.2336E+03	**7.8025E+02**	7.2336E+03	**3.3177E+09**	3.3177E+09
	0.0000E+00		0.0000E+00		0.0000E+00		7.8025E+02		7.8025E+02		3.3177E+09

c) **Asymmetric-unbalanced circular laminate based on π/6 quasi-isotropic laminate stacking sequence from homogeneous material.**

Table 13: Comparison of bend-bend and bend-twist ratios in asymmetric π/n laminates using short fiber material (Homogenous material).

1. π/3 quasi-isotropic laminate with stacking sequence with [60,-60,0,60,0,-60,60,0,-60,0,-60,60]s

π/3	D_{12}/D_{11}	D_{16}/D_{11}	D_{26}/D_{11}	D_{12}/D_{22}	D_{16}/D_{22}	D_{26}/D_{22}
Ideal	3.1141E-01	6.9501E-07	6.9501E-07	3.1141E-01	6.9501E-07	6.9501E-07
Maximum	3.1141E-01	7.5866E-07	7.5866E-07	3.1141E-01	7.5866E-07	7.5866E-07
Minimum	3.1141E-01	6.0728E-08	6.0728E-08	3.1141E-01	6.0728E-08	6.0728E-08

2. π/4 quasi-isotropic laminate with stacking sequence with [45,-45,0,90,0,90,-45,45,90,0,45,-45]s

π/4	D_{12}/D_{11}	D_{16}/D_{11}	D_{26}/D_{11}	D_{12}/D_{22}	D_{16}/D_{22}	D_{26}/D_{22}
Ideal	3.1141E-01	3.0517E-22	3.0517E-22	3.1141E-01	3.0517E-22	3.0517E-22
Maximum	3.1141E-01	1.8415E-07	1.8415E-07	3.1141E-01	1.8415E-07	1.8415E-07
Minimum	3.1141E-01	1.5730E-23	1.5730E-23	3.1141E-01	1.5730E-23	1.5730E-23

3. π/6 quasi-isotropic laminate with stacking sequence with [60,-60,30,-30,0,90,30,-30,0,90,-60,60]s

π/6	D_{12}/D_{11}	D_{16}/D_{11}	D_{26}/D_{11}	D_{12}/D_{22}	D_{16}/D_{22}	D_{26}/D_{22}
Ideal	3.1141E-01	8.1766E-08	8.1766E-08	3.1141E-01	8.1766E-08	8.1766E-08
Maximum	3.1141E-01	7.5067E-07	7.5067E-07	3.1141E-01	7.5067E-07	7.5067E-07
Minimum	3.1141E-01	8.0970E-08	8.0970E-08	3.1141E-01	8.0970E-08	8.0970E-08

As mentioned above, the stacking sequence affects results in radial variations of flexural stiffness and local bend-twist effects through all radial directions in continuous fiber reinforced quasi-isotropic laminates. Such radial variations in a composite mirror could cause a severe surface deformation in the composite mirror substrate, even in adaptive/active mirror applications. Eliminating stacking sequence effects on flexural stiffness and bend-twist effect is one of the most important issues in the composite mirror industry.

To minimize stacking sequence effects, the analysis on quasi-isotropic laminates in this study suggests two statements: First, variation in transformed reduced lamina stiffness $[\bar{Q}_{ij}]$ terms in the flexural stiffness equation should be minimized; second, variations in ply positional dependency $h_k^3 - h_{k-1}^3$ should be minimized. The former can be accomplished with less directionally dependent materials such as chopped mat or veil instead of unidirectional material, and the latter can be accomplished by increasing the

total number of plies. To accomplish the above statements, requires very thin lamina of homogeneous quasi-isotropic material properties. Often increasing the total number of plies or obtaining very thin lamina materials are not practical, so using more homogenous quasi-isotropic lamina material may be the only practical way to reduce variation in flexural stiffness terms.

3.2.3. Comparison of Flexural Stiffness Matrices in Quasi-isotropic Composite Mirror Fabricated from Continuous Fiber Reinforced Material and Other Homogenous Materials

The following Figure 8 shows the radial plot comparisons for flexural stiffness variations between continuous fibers reinforced material and homogenous material.

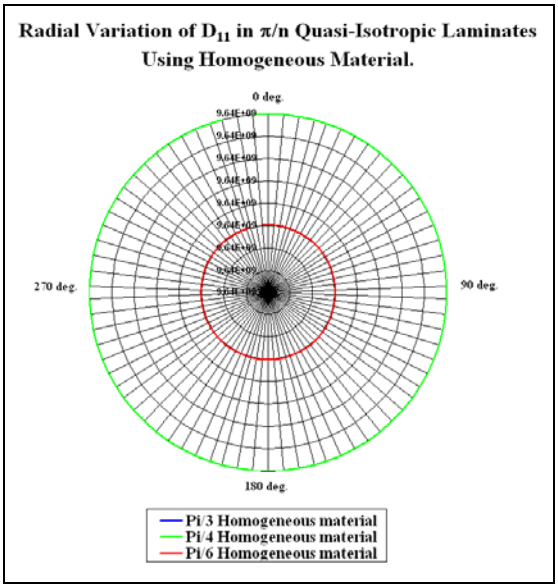

a) π/n laminates using homogeneous material

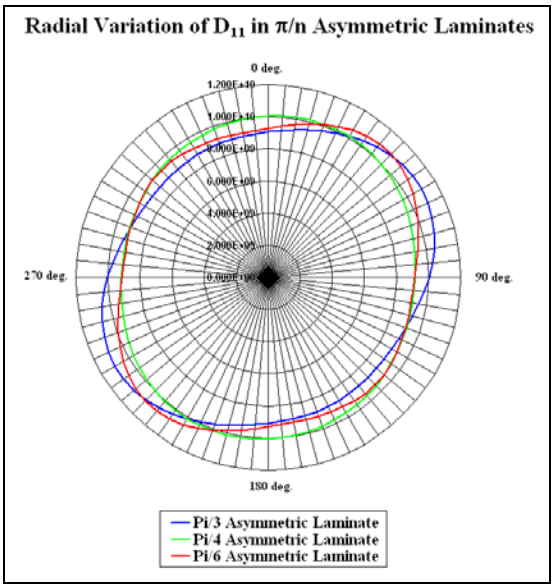

b) π/n laminates using continuous material

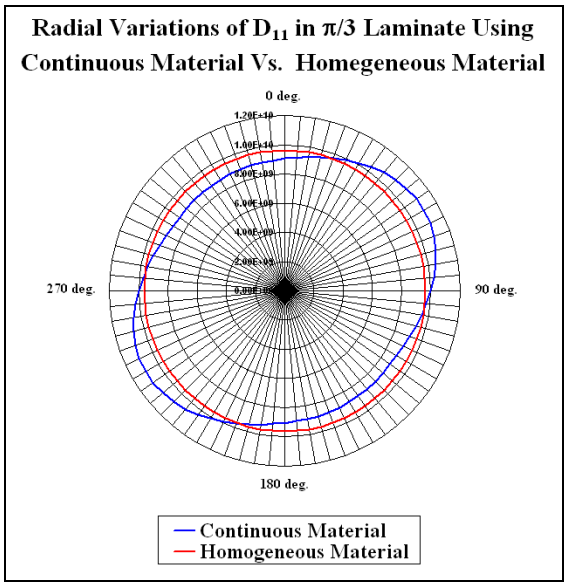

c) π/3 laminate

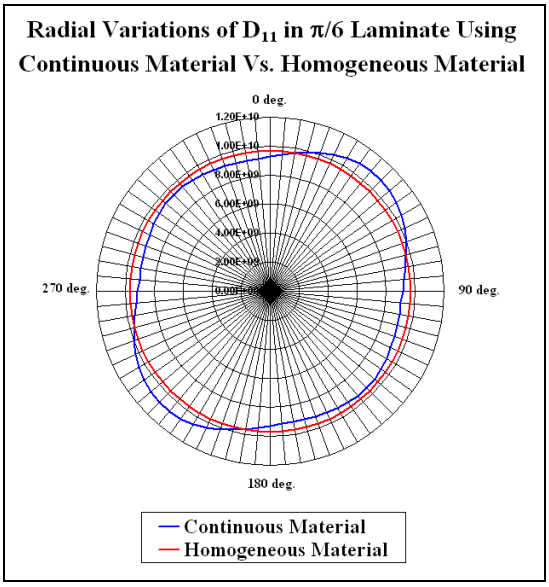

d) π/6 laminate

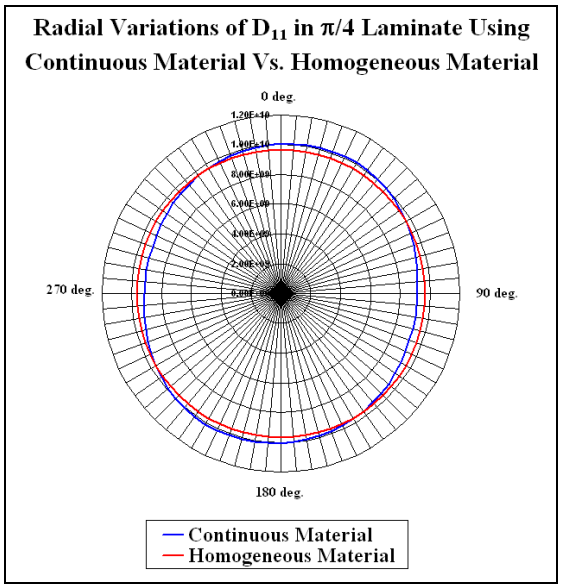

e) π/4 laminate

Figure 8: a) and b) are plots of radial variation of D_{11} in circular π/n quasi-isotropic laminates using chopped mat (Homogenous material) and continuous fiber material, Comparison of radial variations of D_{11} in unidirectional material and chopped mat for π/n quasi-isotropic laminates, c) π/3, d) π/6, and e) π/4 laminate.

The π/3 continuous quasi-isotropic laminate has the most severe variation (±12.85 %) while π/4 laminate has the least variation (±5.63 %). On the other hand, there is no radial variation in flexural stiffness for circular composite laminates fabricated with homogeneous material. Circular composite mirrors using homogeneous material contain uniform properties in both extensional and flexural stiffness, and thus will eliminate the radial variations in flexural stiffness due to stacking sequence effect of circular mirrors from unidirectional materials.

Although it is well known that quasi-isotropic laminate mirrors fabricated using continuous composite material are suited for future composite mirror applications due to the uniform mechanical properties with respect to extensional stiffness, radial variations in flexural stiffness are inevitable. On the basis of work shown in this study, radial variation of flexural stiffness in circular composite mirror due to stacking sequence

effects is significant even though it is well known that bend-twist effects become small with respect to the primary flexural stiffness terms for laminates with more than sixteen plies. Thus, homogenous or distributed reinforcement materials might be superior to continuous fiber reinforced material for applications such as circular antenna reflectors or optical mirrors. Veil, mat, and other chopped fiber products may not be appropriately homogenous, and may demonstrate spatially varying mechanical properties. Generally, these exhibit a preferential direction. Laminates with sufficient numbers of oriented layers of such material may exhibit effectively homogenous properties in extensional and flexural stiffness, particularly if lamina product forms are as thin as possible. The circular composite mirror substrate using short fiber materials will thus exhibit more uniform extension and flexural stiffness, and thus is better suited for composite mirror applications.

4. Numerical Methodology

This chapter comprises the details of numerical methodology on circular quasi-isotropic composite mirror substrate. To capture surface deformations induced by thermal variance on circular composite mirror substrate, a numerical discretization that reflects close to the true physical composite mirror is required. The following sections consist of the details of mesh creations, including the numerical domain of composite mirror, boundary conditions for numerical simulations, and mesh convergence.

4.1. Discretization and Convergence

Finite element methods are used for numerical simulation on dimensional stability (with thermal variance of $\Delta T=30^{o}$ F from room temperature to 100^{o} F) of a circular composite mirror substrate using MSC.Patran 2007 rla and Nastran 2006.0 software. To capture theoretical variations and the shape of surface deformations in a circular composite mirror, 3D radial sliced domains are considered as a proper numerical model.

The assumed laminated composite mirror consists of multiple layers of orthotropic composite material, thus the mechanics in composite mirror substrate are complex. Although a quasi-isotropic circular composite mirror substrate possesses uniform in-plane extensional stiffnesses, it contains non-uniform flexural stiffness as well as non-uniformities which are associated with the distribution of resin and carbon fibers in a composite mirror substrate. Because of the anisotropic flexural stiffnesses and those inconsistencies related to the resin and fibers, quasi-isotropic circular composite mirror substrates may not be suitable for telescope and antenna dish structures, which are most

often loaded normal to the plane. When the composite mirror experiences fluctuations in environmental condition (e.g. a thermal variance is applied to a circular composite mirror), the deformations induced by the load are not uniform through out the entire surface and are highly unpredictable due to the complex mechanical characteristics in the composite mirror substrate. Similarly, the surface deformations due to thermal load on the mirror substrate would not also be uniform. Thus, it is not easy to predict surface deformations in terms of surface location using only a 2D numerical model. In the 3D Nastran/Patran model, three dimensional elements, commonly referred to as solid elements, are used to model structures for accurate numerical results. The 3D element used in this study is called CHEXA elements.

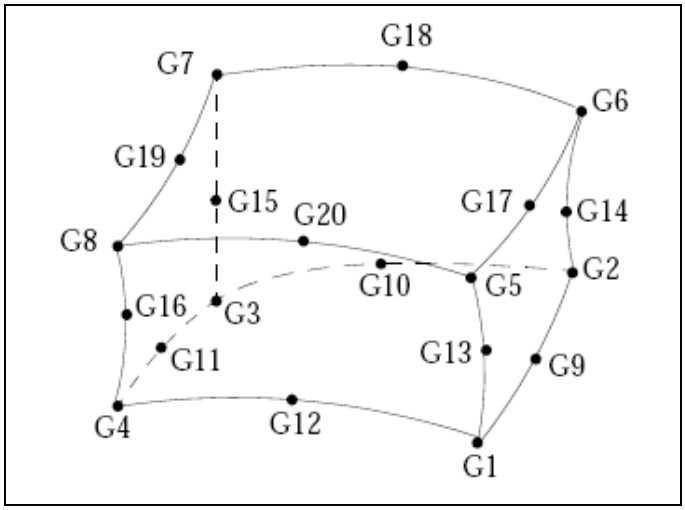

Figure 9: CHEXA element connection in MSC Nastran/Patran

As shown above Figure 9, the CHEXA element is defined by eight corner grid points and up to twelve optional mid-side grid points. Thus, it will be beneficial to use the element in this composite mirror study for more accurate computational results. However, in this numerical computation only 8 nodes CHEXA element is used for numerical evaluation on circular composite mirror model.

To capture the complex radial surface deformation on a composite mirror, it is required to break the composite mirror into small pieces to evaluate its complex surface deformation and subsequently integrate them to evaluate an entire surface deformation rather than use of the entire circular mirror as a computational model. The details of the numerical domain for a 3D sliced mirror substrate and the schematic diagram for the numerical domain are shown in Figure 10.

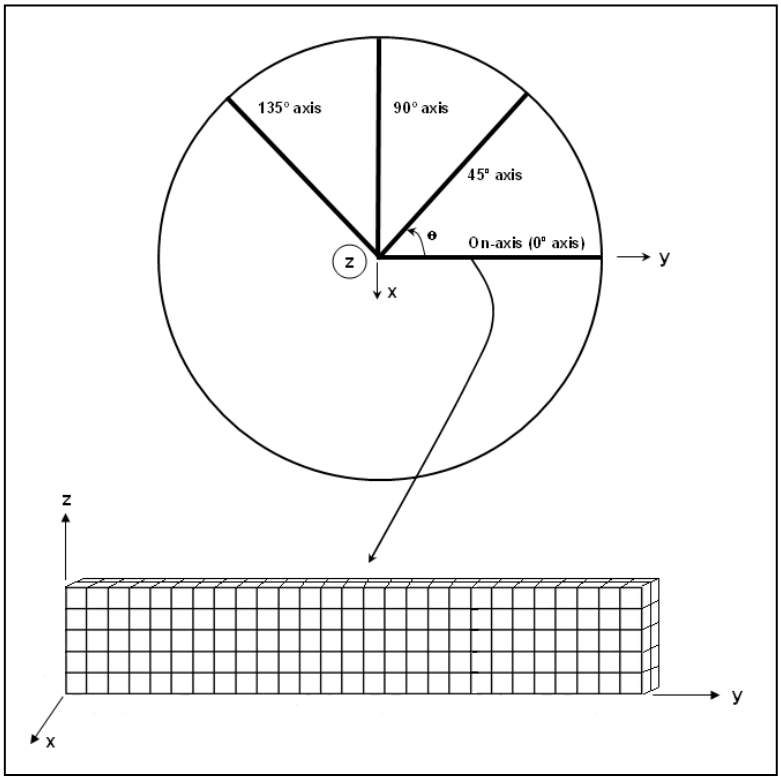

Figure 10: Schematic diagram of numerical domain in 2D view (on-axis, 45, 90, and 135 degree axis, top) and 3D sliced view for numerical domain (on-axis, bottom)

For details of computations, a total of 72 cases (0 degree to 360 degree by 5 degree increments) of 3D sliced models around a circular mirror are performed to capture surface deformations in a circular composite mirror. A thickness of 0.0052 inch is used for both composite lamina and the additional surface layer of pure epoxy (used later for fiber print through mitigation technique). To obtain accurate results, the true size of

physical domain is used for numerical simulation even though the size of the domain is too small. Thus, the size of physical domain is 8” x 0.0416” in the direction of x and z respectively. However, to reduce the computational load, only half of plane of x and z is considered as a case of numerical domain because of the approximate plane of symmetry of the composite mirror in x and y. Therefore, an actual computational domain of the 3D sliced strip has a coordinate starting from x=0 for center of the mirror to x=4 (inch) for the edge of the circular mirror.

The simulations results are often strongly dependent on the strategy of the element discretization generation. Furthermore, identifying the number and distribution of elements in the numerical domain, required to measure nano-scale of deformation is crucial for the results. Therefore, 4 different mesh sizes, (coarse, medium coarse, medium fine, and fine) are examined to see their effects on small surface deformations due to changes in thermal loads. For final fine mesh, mesh seeds of 4600 in the lateral direction and of 32 (4 elements in each layer) in the transverse direction are assigned after mesh sensitivity study for mesh optimization. Figure 11 and 12 shows the mesh convergence study result for maximum displacement on the 3D model vs. total number of degrees of freedom in the numerical domain and the 3D radial slice model discretization for the composite mirror substrate respectively.

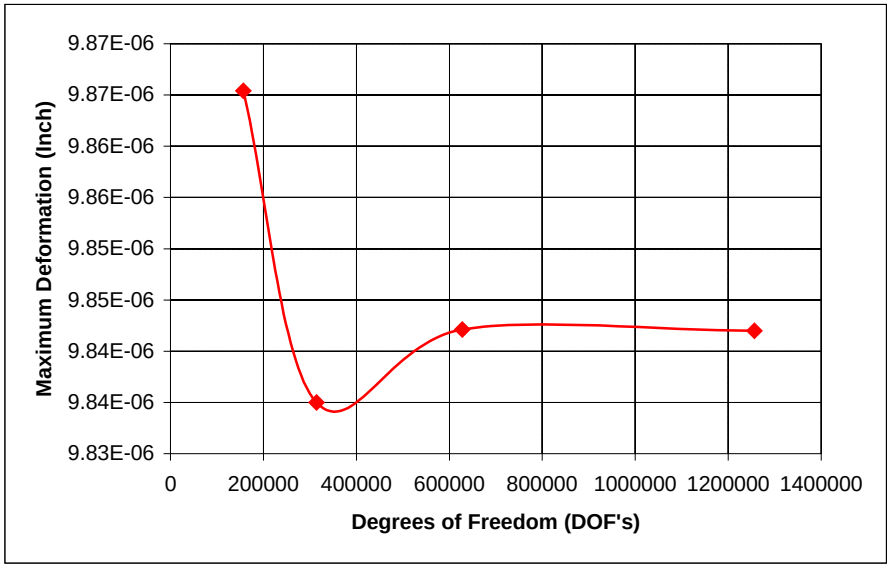

Figure 11: Result of mesh convergence, Maximum displacement (inch) vs. Degrees of freedom

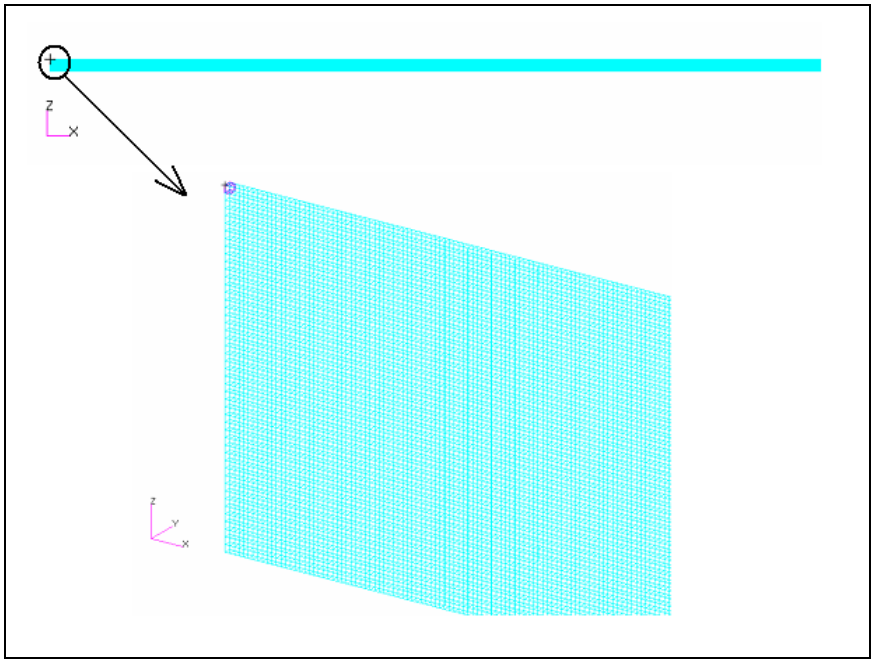

Figure 12: Numerical mesh for 3D radial sliced model for 4-inch radius (due to symmetry, as an example of an ideal 8-layer π/4 quasi-isotropic laminate) circular composite mirror with size of domain of 4"x0.0468"x0.0013" and element size of 0.00087"x0.0013"x0.0013", from MSC.Patran 2007rla

Thus, the model has 538,407 nodes and 353600 CHEXA elements where each element size of 0.00087in x 0.0013in x 0.0013in, representing 1,256,074 degrees of freedom.

4.2. Boundary Conditions

The boundary conditions used for the numerical simulations are determined based on the geometry of composite mirror substrate. In this research, a composite mirror substrate which is called primary mirror is subjected to only a thermal variance ($\Delta T=30°$ F). Thus, there is no external constraint on the composite but only internal thermal variance is applied to the composite mirror substrate. The purpose of this study is focused on how the surface of a composite mirror responds to environmental conditions and to see if the quasi-isotropic laminated composite mirror meets the diffraction limited requirement for space-borne optic application. Displacement boundary conditions include those to simulate symmetric planes and the necessary rigid body constraints. When internal thermal variance is presented to a circular composite mirror, the displacement at the center of the composite must be zero due to its geometric symmetric characteristics. In addition, in 3D sliced domain, some nodes in the numerical domain need to be constrained with zero displacement because of planes of symmetry on a circular composite mirror. Schematic diagrams of boundary condition in 3D model are shown in Figure 13.

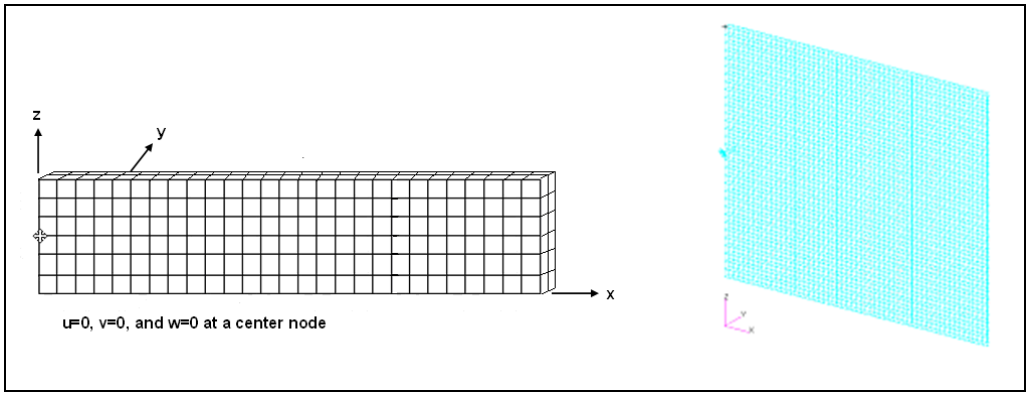

a) Boundary condition at center of composite mirror

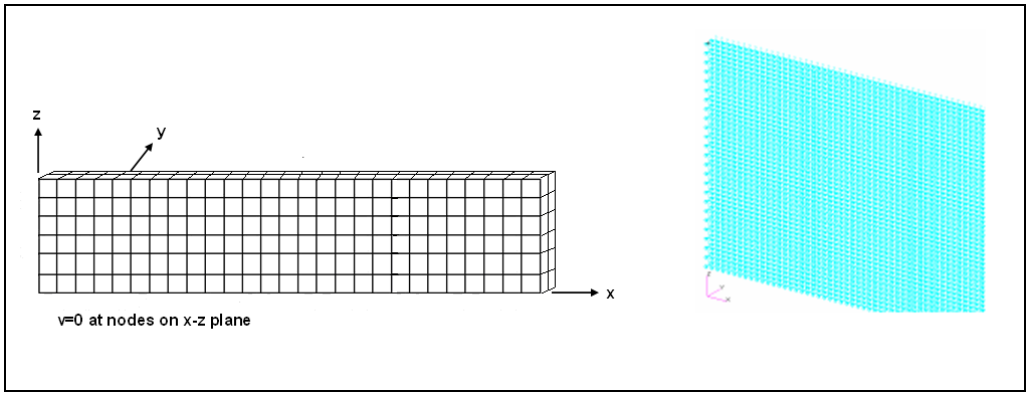

b) Boundary condition on x-z plane of symmetry in composite mirror

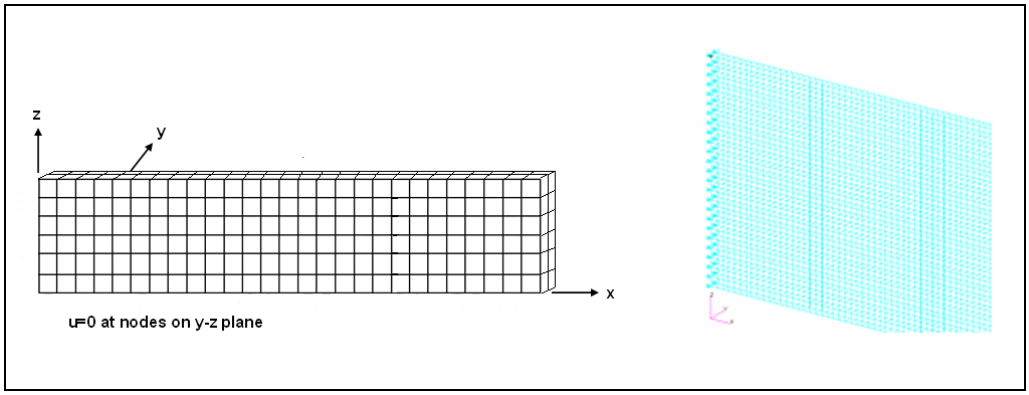

c) Boundary condition on center of y-z plane of symmetry in composite mirror

Figure 13: Descriptions of boundary conditions for numerical simulation, constraint for a center node (up), constraint v=0 on x-z plane (middle), constraint u=0 at left edge nodes on y-z plane (bottom)

4.3. Material Properties of 3D Orthotropic Lamina

Another important step in the setup of the simulation model is specifying the physical properties of each composite layer according to its lay-up sequence. For assigning an appropriate material property on 3D sliced composite domain, a typical 3D orthotropic composite lamina material property is used. A more typical composite analysis uses 2D orthotropic material, and its engineering constants are related only to E_1 for longitudinal stiffness, E_2, transverse stiffness, G_{12} for in-plane shear stiffness, ν_{12} for in-plane Poisson ratio, and α_1 and α_2 coefficient of thermal expansion terms for each principle axis. However, numerical methods using 2D orthotropic material properties might be limited to evaluate surface deformations of the composite mirror only related to in-plane mechanical properties. In this research, evaluating surface deformations induced from in-plane properties but also out of plane properties of the composite is critical. Surface deformation in composite mirror substrate will be affected by both in-plane and out of plane mechanics of composite, and those complex mechanisms would be significant factors to determine accurate surface deformation. For these reasons, the numerical model used in this study uses 3D orthotropic material properties. Figure 14 and Table 14 describe the schematic diagram for 3D orthotropic unidirectional composite material and the details of material properties of lamina and epoxy used in this numerical study respectively.

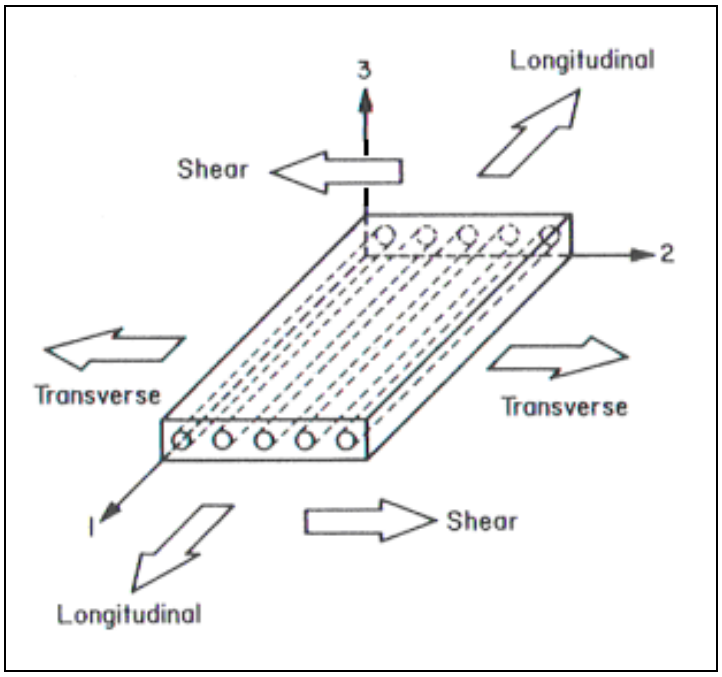

Figure 14: Schematic diagram of 3D orthotropic unidirectional composite material

Table 14: Engineering constants for typical Carbon/Epoxy and resin used in 3D analysis.

Engineering Constant	Typical Carbon/Epoxy	Resin Properties	
E_1 (Msi)	19.1	E_m (Msi)	0.63
E_2 (Msi)	1.36		
E_3 (Msi)	1.34		
G_{12} (Msi)	0.84	G_m (Msi)	0.23
G_{23} (Msi)	0.31		
G_{31} (Msi)	0.67		
ν_{12}	0.3	ν_m	0.36
ν_{23}	0.28		
ν_{31}	0.0238		
α_1 (10^{-6} in/in/°F)	-0.455	α_m (10^{-6} in/in/°F)	16.14
α_2 (10^{-6} in/in/°F)	16.14		
α_3 (10^{-6} in/in/°F)	16.14		

The following section details methods to define 3D orthotropic material property for the CHEXA solid elements in Nastran/Patran program.

A general three dimensional anisotropic material stiffness matrix is defined by equation 4.1.

$$\begin{Bmatrix} \sigma_1 \\ \sigma_2 \\ \sigma_3 \\ \tau_{23} \\ \tau_{13} \\ \tau_{12} \end{Bmatrix} = [E] \left(\begin{Bmatrix} \varepsilon_1 \\ \varepsilon_2 \\ \varepsilon_3 \\ \gamma_{23} \\ \gamma_{13} \\ \gamma_{12} \end{Bmatrix} - (T - T_{REF}) \begin{Bmatrix} \alpha_1 \\ \alpha_2 \\ \alpha_3 \\ \alpha_{23} \\ \alpha_{13} \\ \alpha_{12} \end{Bmatrix} \right) \qquad \text{Equation 4.1}$$

where

$$[E] = \begin{bmatrix} E_{11} & E_{12} & E_{13} & E_{14} & E_{15} & E_{16} \\ E_{21} & E_{22} & E_{23} & E_{24} & E_{25} & E_{26} \\ E_{31} & E_{32} & E_{33} & E_{34} & E_{35} & E_{36} \\ E_{41} & E_{42} & E_{43} & E_{44} & E_{45} & E_{46} \\ E_{51} & E_{52} & E_{53} & E_{54} & E_{55} & E_{56} \\ E_{61} & E_{62} & E_{63} & E_{64} & E_{65} & E_{66} \end{bmatrix}$$

In orthotropic material, as shown in Figure 15, when a normal stress σ_1 is applied, due to the plane of symmetry in coordinate 1 and 2, the out of plane shear strains are zero, ($\gamma_{13} = \gamma_{23} = 0$). Similarly, the plane of symmetry in coordinate 1 and 3 the in-plane shear strain is zero, ($\gamma_{12} = 0$).

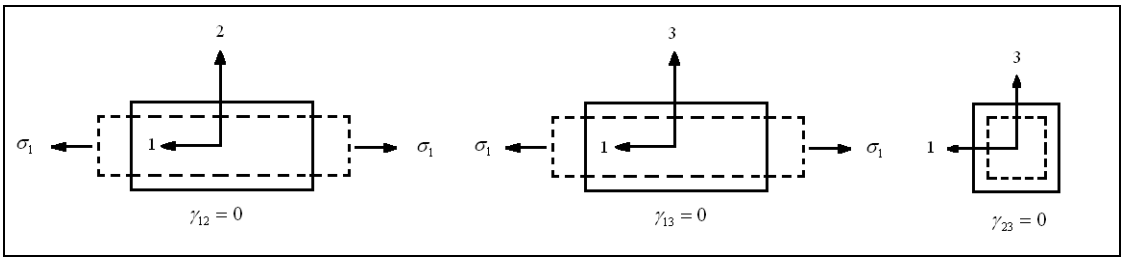

Figure 15: Schematic representation of a normal stress σ_1 applied in the 1-2 and 1-3 symmetric planes of an orthotropic material

This implies that the stiffness constants E_{14}, E_{15}, E_{16} are zero in the stiffness matrix. By similar arguments it can be shown that for an orthotropic material the E_{24}, E_{25}, E_{26}, E_{34}, E_{35}, E_{36}, E_{45}, E_{46}, E_{56} elements are also zero in the stiffness matrix. Thus, the stiffness matrix for orthotropic material is as follows:

$$[E]_{\mathrm{OT}} = \begin{bmatrix} E_{11} & E_{12} & E_{13} & 0 & 0 & 0 \\ E_{21} & E_{22} & E_{23} & 0 & 0 & 0 \\ E_{31} & E_{32} & E_{33} & 0 & 0 & 0 \\ 0 & 0 & 0 & E_{44} & 0 & 0 \\ 0 & 0 & 0 & 0 & E_{55} & 0 \\ 0 & 0 & 0 & 0 & 0 & E_{66} \end{bmatrix}$$

where:

$$E_{11} = \frac{1-\nu_{23}\nu_{32}}{E_2E_3\Delta} \quad E_{12} = E_{21} = \frac{\nu_{21}+\nu_{31}\nu_{23}}{E_2E_3\Delta} \quad E_{13} = E_{31} = \frac{\nu_{31}+\nu_{21}\nu_{32}}{E_2E_3\Delta}$$

$$E_{22} = \frac{1-\nu_{13}\nu_{31}}{E_1E_3\Delta} \qquad E_{23} = E_{32} = \frac{\nu_{32}+\nu_{12}\nu_{31}}{E_1E_3\Delta} \qquad \text{Equation 4.2}$$

$$E_{33} = \frac{1-\nu_{12}\nu_{21}}{E_1E_2\Delta}$$

where:

$[E]_{OT}$ = Stiffness matrix for an orthotropic lamina

ν_{ij} = Poisson's ratios

for orthotropic material,

$$\frac{\nu_{21}}{E_2} = \frac{\nu_{12}}{E_1}$$

$$\frac{\nu_{31}}{E_3} = \frac{\nu_{13}}{E_1}$$

$$\frac{\nu_{23}}{E_2} = \frac{\nu_{32}}{E_3}$$

$E_1,\ E_2,\ E_3$ = Young's modulus in the 1, 2, and 3 directions

$G_{23},\ G_{31},\ G_{12}$ = Shear moduli

$$\Delta = \frac{1-\nu_{12}\nu_{21}-\nu_{23}\nu_{32}-\nu_{13}\nu_{31}-2\nu_{21}\nu_{32}\nu_{13}}{E_1E_2E_3}$$

also

$$E_{44} = G_{23}$$
$$E_{55} = G_{31}$$
$$E_{66} = G_{12}$$

For proper lamina material orientations, which depend on lay-up sequence in the composite laminate, the stiffnesses matrix needs to be converted in global coordinate system for numerical simulations. If θ_k is defined as the angle in the k_{th} lamina in composite, the transformation matrix is defined as following:

$$[T]_k = \begin{bmatrix} \cos^2\theta_k & \sin^2\theta_k & 0 & 0 & 0 & \cos\theta_k \sin\theta_k \\ \sin^2\theta_k & \cos^2\theta_k & 0 & 0 & 0 & -\cos\theta_k \sin\theta_k \\ 0 & 0 & 1 & 0 & 0 & 0 \\ 0 & 0 & 0 & \cos\theta_k & -\sin\theta_k & 0 \\ 0 & 0 & 0 & \sin\theta_k & \cos\theta_k & 0 \\ -2\cos\theta_k \sin\theta_k & 2\cos\theta_k \sin\theta_k & 0 & 0 & 0 & \cos^2\theta_k - \sin^2\theta_k \end{bmatrix}$$

$$[T]_k^{-1} = \begin{bmatrix} \cos^2\theta_k & \sin^2\theta_k & 0 & 0 & 0 & -2\cos\theta_k \sin\theta_k \\ \sin^2\theta_k & \cos^2\theta_k & 0 & 0 & 0 & 2\cos\theta_k \sin\theta_k \\ 0 & 0 & 1 & 0 & 0 & 0 \\ 0 & 0 & 0 & \cos\theta_k & \sin\theta_k & 0 \\ 0 & 0 & 0 & -\sin\theta_k & \cos\theta_k & 0 \\ \cos\theta_k \sin\theta_k & -\cos\theta_k \sin\theta_k & 0 & 0 & 0 & \cos^2\theta_k - \sin^2\theta_k \end{bmatrix}$$

Thus, each angle lamina mechanical properties assigned in Nastran/Patran was transformed according to equation 4.3:

$$[E]_k = [T]_k^{-1} [E]_{\mathrm{OT}} [T]_k \qquad \text{Equation 4.3}$$

Based on laminate stacking sequence, the material properties using above technique are assigned into Nastran/Patran model of the composite.

5. Dimensional Stability in Quasi-Isotropic Laminated Composite Mirror Substrates

This chapter comprises numerical analysis on surface deformations induced by thermal load present in three π/n (where n=3, 4, and 6) circular quasi-isotropic composite mirrors. The analyses involve numerical simulation of ideal quasi-isotropic laminates without (assumed no fiber print-through) or with resin rich layers (to mitigate fiber print-through) on the composite mirror substrates, resin rich thickness effect on quasi-isotropic laminate, and surface deformations on different types of composite material utilizing distributed chopped mat. Finally, analyses compare resin rich layer materials (graded stiffness and coefficient of thermal expansion) to characterize surface deformations caused by stacking sequence effects, anisotropic flexural stiffness, and complex mechanic characteristics of quasi-isotropic laminated composite mirrors.

5.1. Surface Deformations in Ideal π/n Quasi-Isotropic Laminated Composite Mirror Substrates Due to Thermal Load

Lightweight composite replica mirrors fabricated from unidirectional composite fiber reinforced materials must contend with a problem that is inherent in fiber reinforced composite material. A laminated composite is composed of many individual plies. In each individual lamina, stiffness and thermal expansion is highly relative to its orientation. Thus, mechanics in a laminated composite is quite complex in stiffnesses and coefficient of thermal expansion. Such factors would be the dominant reasons which would cause surface deformations which exceed surface accuracy requirement for

precision optics. In a macroscopic scale, small surface deformations in a composite due to the presence of various loads in the substrate might be negligible. However, in a microscopic scale, especially optics, small surface variations in the substrate are critical. One possibility of surface deformations in composite mirror substrate is that surface amplitude variations and sinusoidal surface undulation patterns are strongly dependent on the lay-up sequences in π/n quasi-isotropic laminates, where n= 3, 4, and 6. Variations in flexural stiffnesses in the quasi-isotropic composite substrates are also driven by stacking sequence effects. In the following section, surface deformation patterns in π/n quasi-isotropic laminates and the amplitude of the surface deformations induced from mechanical complexities due to lay-up sequence are identified.

To evaluate dimensional stability of surface deformations and patterns in composite mirror surface, the π/n laminates are considered as exposed to operate in hot environmental conditions. An ideal π/n quasi-isotropic composite laminate (assumed no fiber print-through after fabrication so no resin rich layer) for each π/n laminate where n=3, 4, 6 is considered as a computational model. For dimensional stability analyses, a 30 degree Fahrenheit change from reference temperature is used for this numerical study.

In macroscopic scale, when thermal variance (used $\Delta T=30\ ^\circ$ F from room temperature to 100° F for all computational cases) is applied to 3D ideal composite sliced strip, constant in-plane and through thickness surface deformation in the composite strip is expected due to the symmetric lay-up in the ideal composite strip. The numerical result of surface deformation from MSC.Nastran/Patran for deformation of the model due to thermal load in Figure 16 supports the above statement. The numerical result shows constant in-plane and out of plane deformation due to symmetric laminate characteristic.

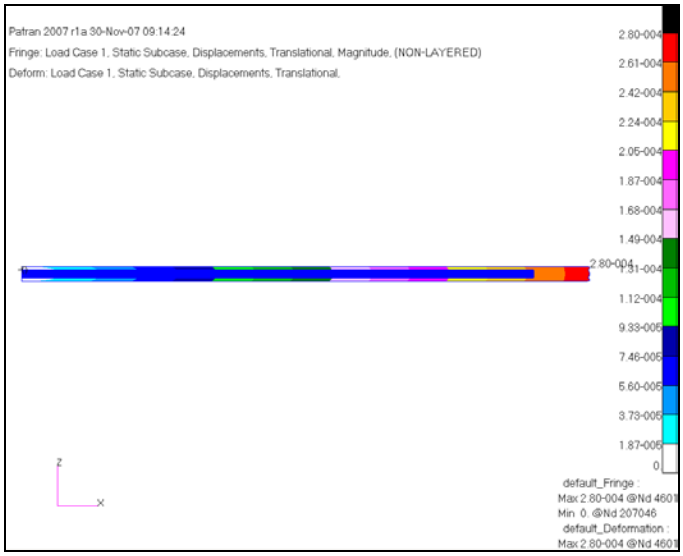

Figure 16: Deformation contour for dz vs. dx (exaggerated deformation view) due to the thermal load ($\Delta T=30°F$) in an ideal $\pi/4$ quasi-isotropic composite mirror at 0 degree

For lay-up sequence of individual radial axis in a circular composite mirror, each radial sliced strip (as a computational model) of laminate has unique stacking sequence which is symmetric and either balanced or unbalanced. For instance, the stacking sequence sliced strip at on-axis (0 degree) is $[45, 0, -45, 90]_s$ which is symmetric and balanced while stacking sequence at 5 degree axis is $[40, -5, -50, 80]_s$ which contains symmetric but different fiber orientations in the strip. Such characteristics at each radial axis of the laminate strip, when thermal load is present in the composite strip, would result in unique constant through thickness deformation according to its symmetric local stacking sequence.

On the other hand, in a quasi-isotropic laminated circular mirror, flexural stiffness varies radially even in the presence of directionally independent constant in-plane stiffness in the quasi-isotropic composite mirror. The radial variations in flexural stiffness due to quasi-isotropic lay-up in ideal π/n laminates are shown in Figure 17. Several factors contribute to the variations. The radial variations in D_{11} originated from stacking

sequence effects throughout the circular composite mirror, complexities of the mechanics and coefficient of thermal expansion in the substrate due to the different ply angles from on-axis (0 degree) to others.

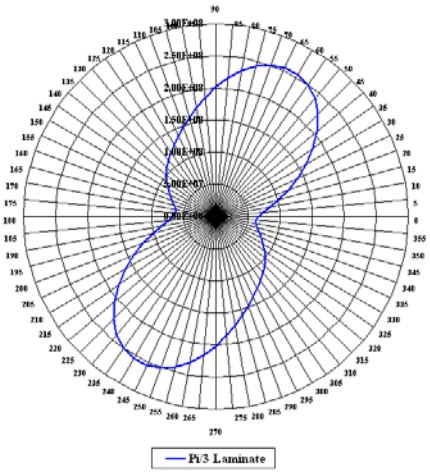

a) In Ideal π/3 Quasi-Isotropic Laminate

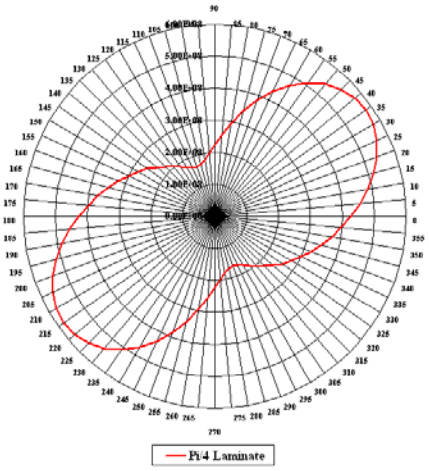

b) In Ideal π/4 Quasi-Isotropic Laminate

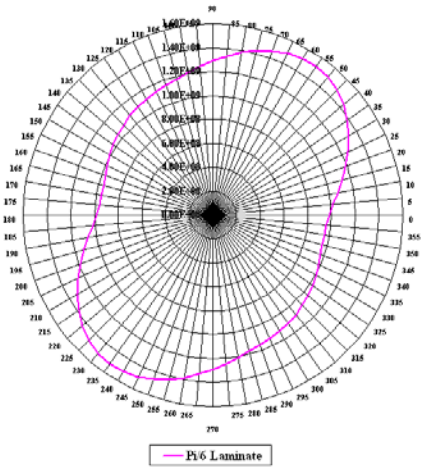

c) In Ideal π/6 Quasi-Isotropic Laminate

Figure 17: Radial variations of D_{11} in π/n quasi-isotropic laminates (n=3, 4, and 6)

Such variations in flexural stiffness shown in Figure 17 and complex mechanics such as coefficient of thermal expansion due to lay-up sequence in quasi-isotropic laminate would result in surface undulations in the entire surface of the mirror.

The following Figure 18 shows the thermally induced in/out of plane deformation plot at different axes (5 degree up to 20 degree) of the sliced strip in π/4 circular composite mirror. As the results shown below, the out of plane deformation in each radial strip has different values.

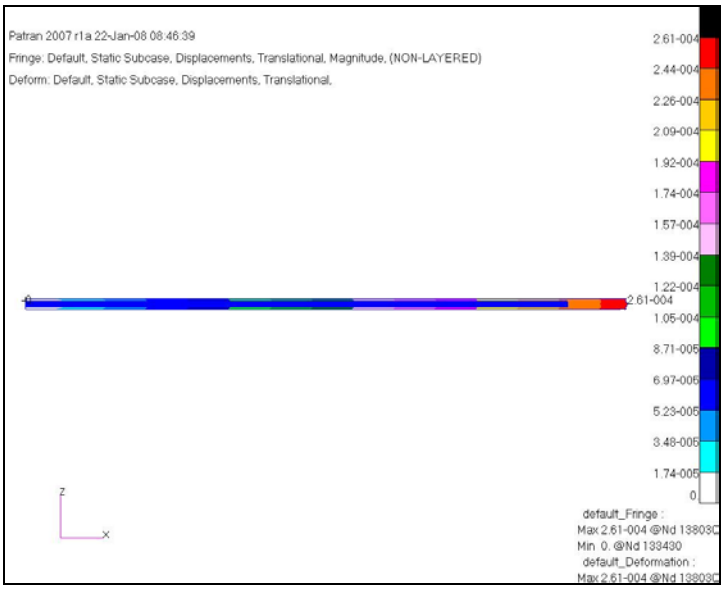

a) Deformation contour for dz vs. dx in ideal π/4 quasi-isotropic composite mirror at 5 degree axis

Figure 18: Deformation contour for dz vs. dx (exaggerated deformation view) due to the thermal load (ΔT=30°F) in an ideal π/4 quasi-isotropic composite mirror at 5 degree up to 20 degree axis

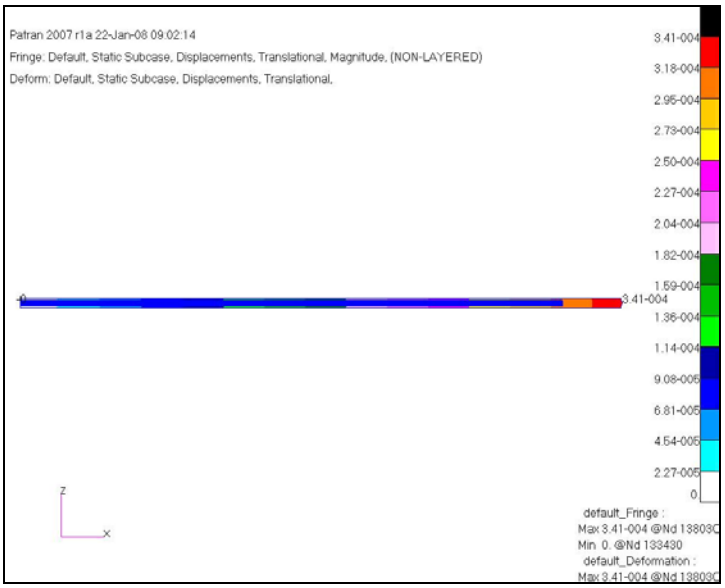

b) Deformation contour for dz vs. dx in ideal π/4 quasi-isotropic composite mirror at 10 degree axis

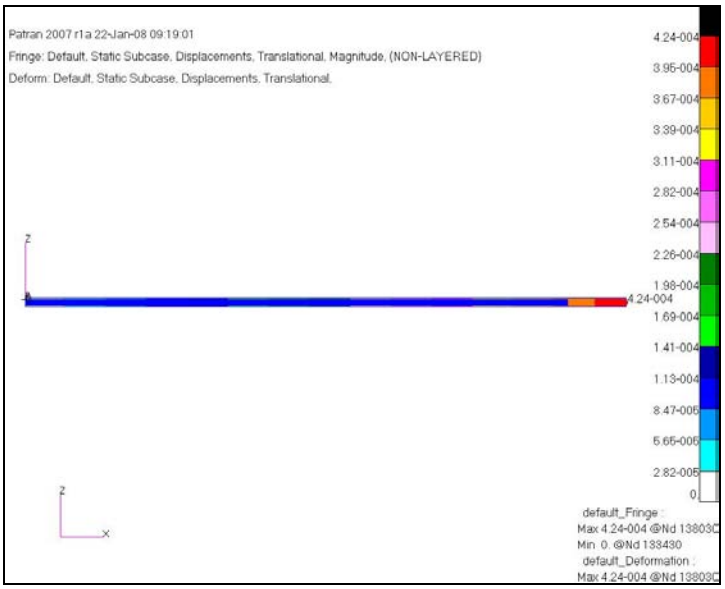

c) Deformation contour for dz vs. dx in ideal π/4 quasi-isotropic composite mirror at 15 degree axis

Figure 18 (Cont.): Deformation contour for dz vs. dx (exaggerated deformation view) due to the thermal load (ΔT=30°F) in an ideal π/4 quasi-isotropic composite mirror at 5 degree up to 20 degree axis

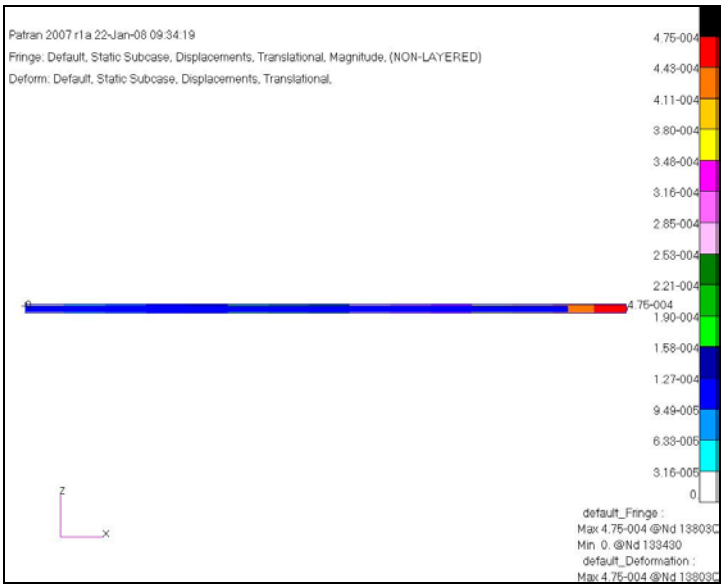

d) Deformation contour for dz vs. dx in ideal π/4 quasi-isotropic composite mirror at 20 degree axis

Figure 18 (Cont.): Deformation contour for dz vs. dx (exaggerated deformation view) due to the thermal load (ΔT=30°F) in an ideal π/4 quasi-isotropic composite mirror at 5 degree up to 20 degree axis

Figure 19 shows the surface deformation plot between out of plane, dz and in-plane, dx from 0 degree axis to 45 degree axis in an ideal π/4 mirror. As shown in the Figure, each radial axis has constant surface deformation, but the magnitude of deformations is changing between the radial directions in the composite. The surface variation between 0 degree axis to 45 degree axis on the surface of the mirror is $0.3x10^{-6}$ inch or 7.62 nm. It was assumed that a composite mirror would be dimensionally stable because of low CTE characteristics. The result shown in Figure 19 clearly indicates that the magnitude of surface deformation at each radial axis is affected by lay-up sequence, flexural stiffness, and mechanics of laminate at each radial direction, and none of the surface deformation meet the diffraction limited requirement for optics when thermal load present in ideal quasi-isotropic laminated composite mirror substrates. From the numerical result, optically large amplitude in surface deformation and optically complex

surface undulation patterns are expected in a composite mirror due to lay-up sequence effects, anisotropic mechanics, and directionally dependent flexural characteristics.

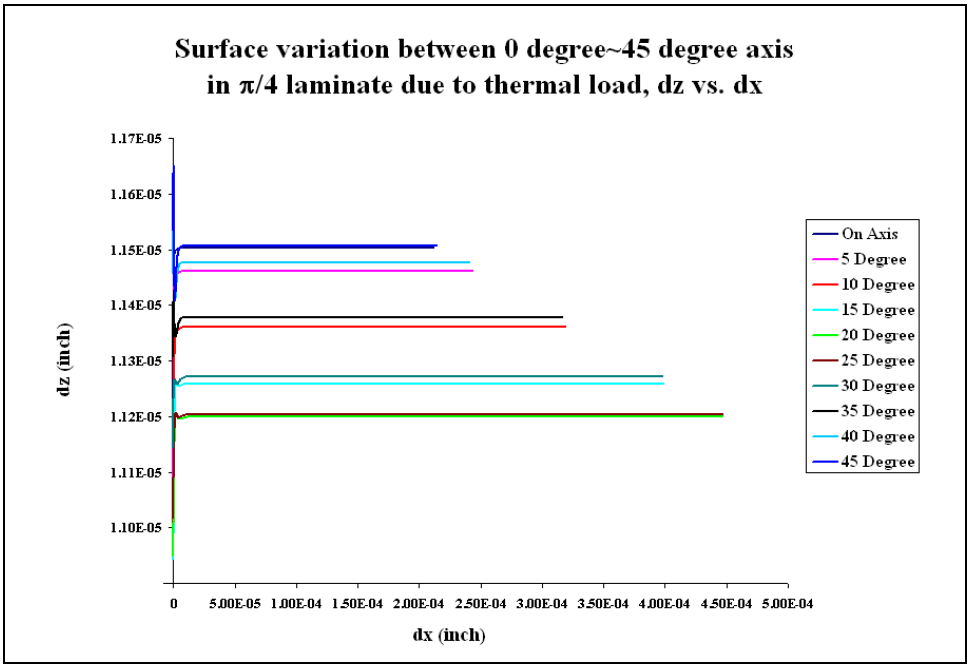

Figure 19: Thermally induced surface variation at axes between 0 degree and 45 degree in ideal π/4 quasi-isotropic laminate substrate with thermal load of $\Delta T=30^{o}$ F

In composite optics, a common assumption is that presence of constant in-plane stiffnesses and very low CTE in quasi-isotropic composite characteristics would provide a dimensionally stable composite mirror. For these reasons, continuous fiber reinforced composite material is commonly used to fabricate a communication reflector or a primary mirror for telescopes. However, in cold and hot working environments such surface deformations in the composite substrates are predictable and inevitable.

Complete normalized 3D surface deformation contours for π/n mirrors are shown in Figures 20~22. The numerical data from each quasi-isotropic laminate was normalized for plotting 3D surface deformation contours in π/n mirrors. For details of normalization,

an example of π/3 laminate, all surface deformations calculated in 72 slices were evaluated to find a maximum dx and dz, then normalized all the rest of dx and dz values to the maximum values ($D_z/D_{z,max}$ vs. $D_x/D_{x,max}$).

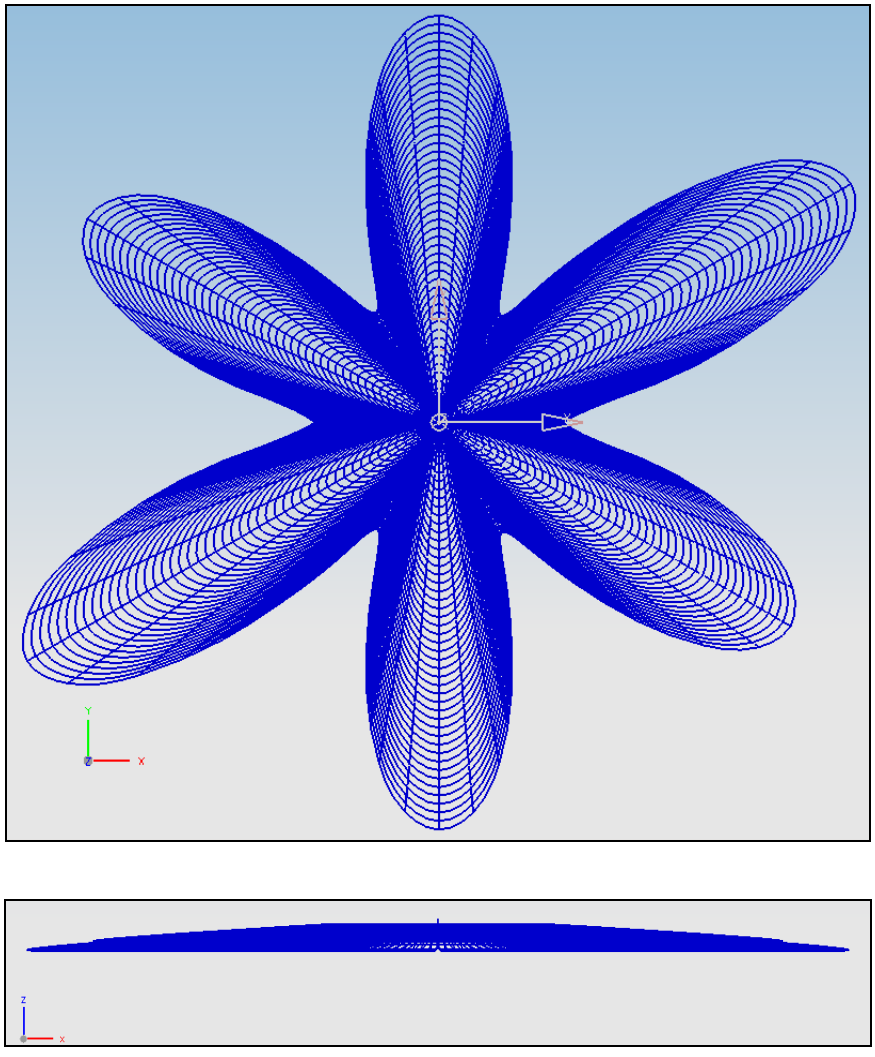

Figure 20: Top and side views of normalized surface contours in π/3 quasi-isotropic laminate

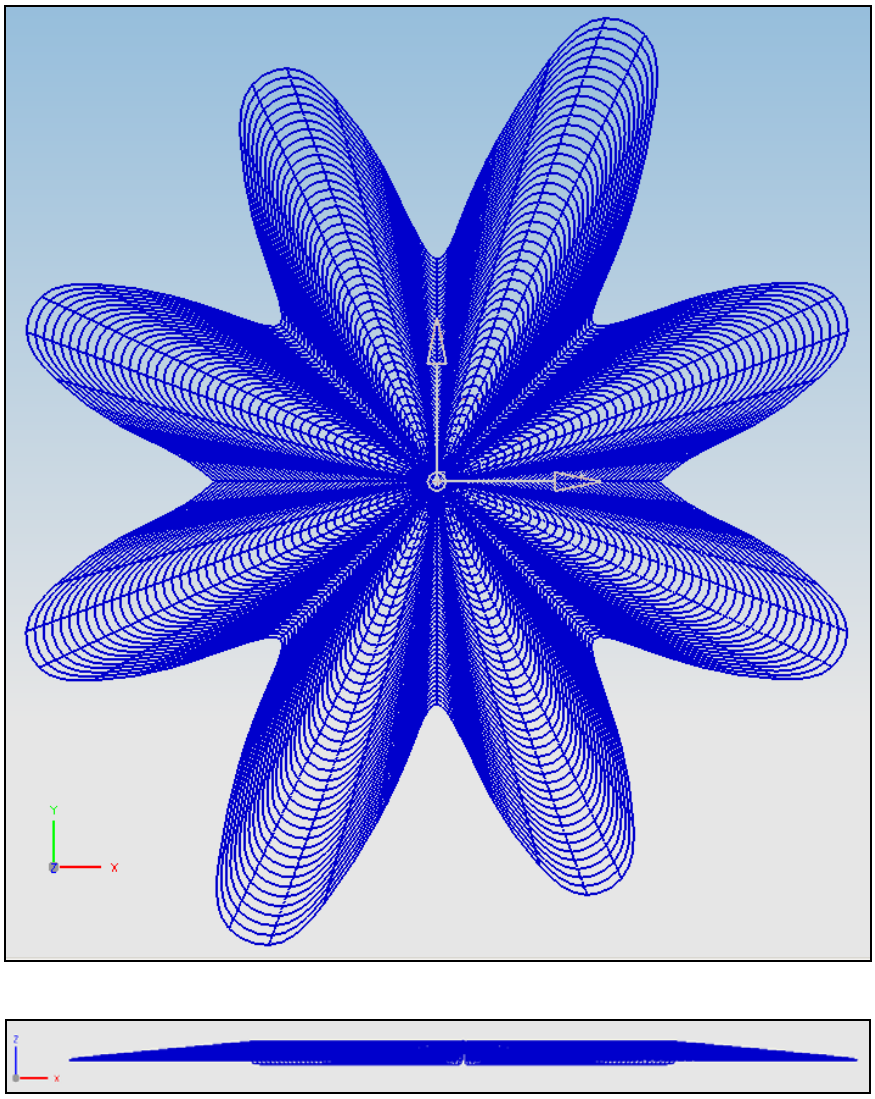

Figure 21: Top and side views of normalized surface contours in π/4 quasi-isotropic laminate

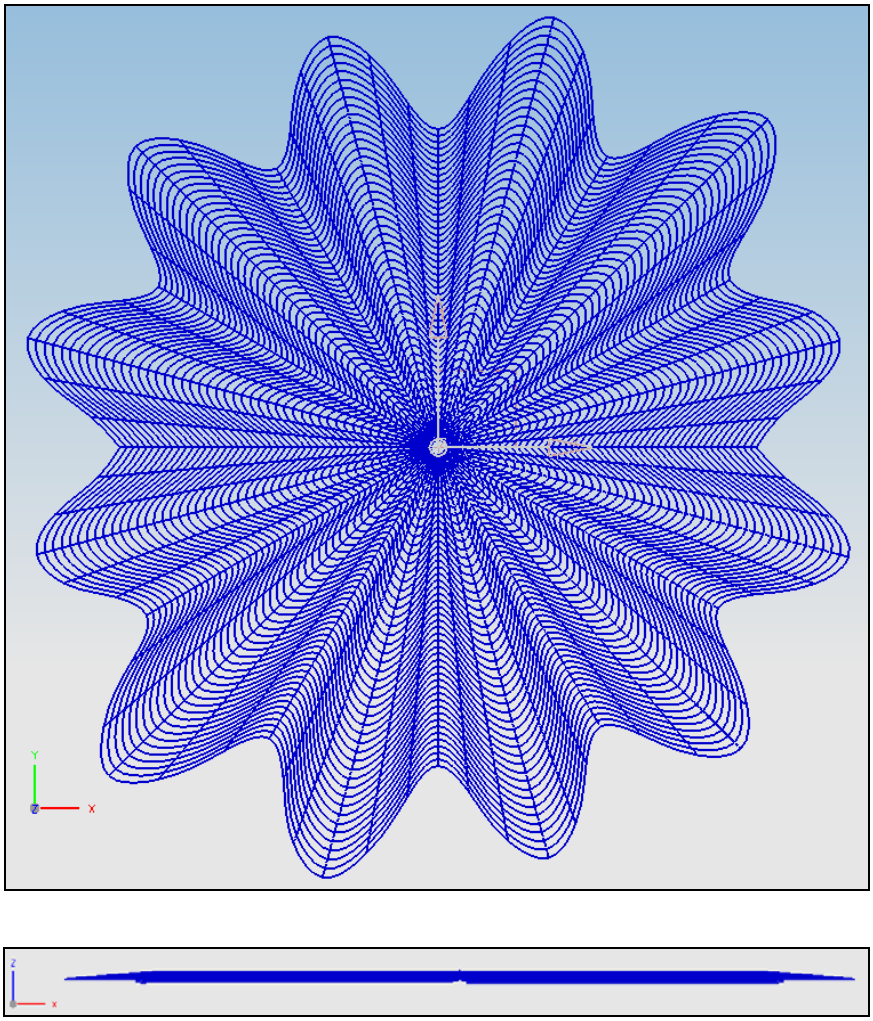

Figure 22: Top and side views of normalized surface contours in π/6 quasi-isotropic laminate

If thermally induced surface deformation shape is first order in curvature, the surface error from the response could be readily corrected in most optic systems. However, the results illustrated in Figures 20~22 reveal that the surface of each π/n mirror has higher order curvature characteristics which are not symmetrical. Such differential geometry is not readily correctable in most optic systems. Controlling these sinusoidal surface undulations is critical to obtain surface accuracy requirement for optics.

It is important to note that sinusoidal undulation patterns in each π/n laminate have unique shapes. For comparison of surface deformation shape in each π/n case, the surface deformation shape in π/3 has three dominant spikes as the result of three principal fiber directions contained in the mirror. Its shape is also more remarkable than π/4 and π/6. That is because there are only three strong principal fiber directions present in π/3, and the strong energy contained at the axes have less displacement in the radial direction. Similarly, as increased principal fiber axes are present in π/4 and π/6 the mirrors result in less dramatic surface deformation with increased fiber directions. In terms of sinusoidal surface undulation pattern, the π/6 laminate has higher order surface undulation characteristics among these three quasi-isotropic laminates. This may lead one to conclude that application of π/n quasi-isotropic laminate composite mirrors for telescopes or optics would be problematic due to significant sinusoidal surface waviness patterns which are difficult to optically correct.

Along with surface undulation patterns in ideal π/n quasi-isotropic laminates, the amplitude of undulation among the composite mirrors would be an important factor for precision composite optics. Figure 23 illustrates a plot between maximum surface

amplitude vs. ideal π/n quasi-isotropic laminates. For a precision optical mirror, the diffraction limited surface accuracy requirement is < λ/20 (31.5nm) RMS where λ is the maximum visible wavelength of light (623nm). None of the above three ideal (assumption of no fiber print-through) π/n laminates meet this requirement when the thermal load of $\Delta T=30\ ^{\circ}F$ is applied. In fact, maximum surface amplitude values found in each ideal laminate are $9.972x10^{-6}$ inch or 253 nm (λ/2.462) in π/3, $9.854x10^{-6}$ inch or 250 nm (λ/2.492) in π/4, and $9.769x10^{-6}$ inch or 248 nm (λ/2.512) in π/6. Although more critical higher frequency surface pattern is presented in π/6 laminate, π/6 laminate has better surface accuracy among the three ideal laminates. This is because more principal fiber directions in circular space in the composite laminate share more energy from thermal load between the axes and adjacent radial axes of the composite substance.

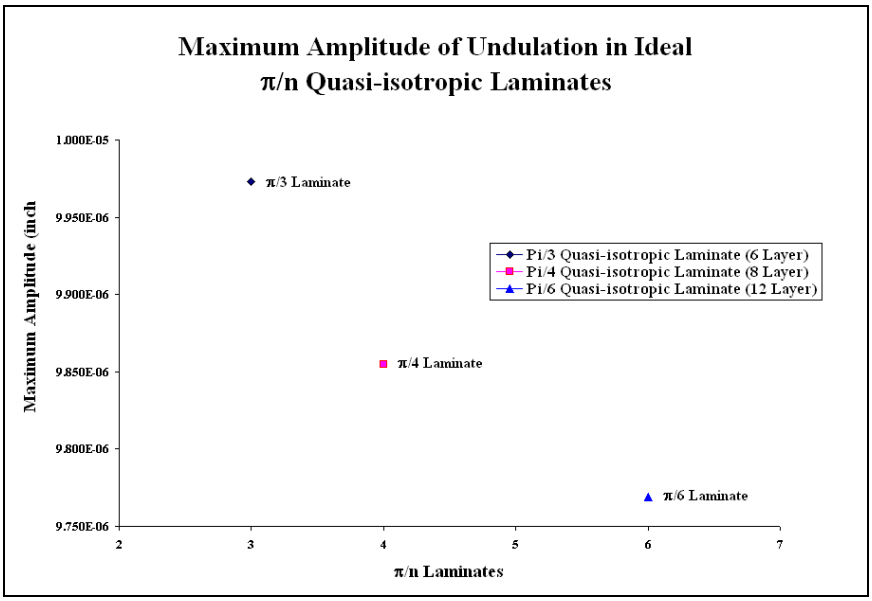

Figure 23: Plot between maximum surface amplitude vs. ideal π/n quasi-isotropic laminates, (unit in inch)

This leads one to hypothesize that relief of surface waviness patterns and reduction of surface deformation amplitude in quasi-isotropic laminates might be possible to meet diffraction limits in optics if a π/∞ lay-up sequence was used to fabricate a circular mirror. However, this hypothesis will encounter the critical problem that more plies are needed which will affect weight budgets or initial material cost (for development of thin layers) to fabricate a circular composite mirror for reduction of surface deformation amplitude. Moreover, in applications for space-borne composite mirrors, the maximum out of thickness deformation due to complex mechanics in composites will increase due to the larger fluctuations in temperature and the larger difference between cure temperature and application temperature.

To conclude, it is believed that composite mirror application may replace conventional glass mirrors which are limited due to weight, durability, and reproducibility, however, lightweight composite replica mirrors must contend with problems that are inherent in continuous fiber reinforced composite material. Distributed media may have more success than continuous fiber materials.

5.2. Fiber Print-Through (FPT) in Quasi-Isotropic Composite Mirrors

In order to achieve optimal performance, elements in an optical system must have acceptable values (<λ/20) of surface roughness over a broad range of spatial frequencies. High frequency error, as known fiber print-through in the process of fabrication, is typically associated with the micro-roughness of an optical surface. Scattering incoming energy and diffusion of reflectivity could occur from this type of error, which could hinder optical performance significantly. This has been one of the challenge areas in precision composite optics. This is called fiber print-through effects.

The primary cause of surface roughness (FPT) is directly related to the fiber and matrix and can be attributed to the following.

1. Curing shrinkage of the resin as a result of chemical cross-linking.
2. Unmatched coefficient of thermal expansion of fiber and matrix with changes in temperature resulting in sinusoidal surface distortion due to chemical and thermal shrinkage during curing.

The following Figure 24 illustrates fiber print-through from fabrication process of composite mirror.

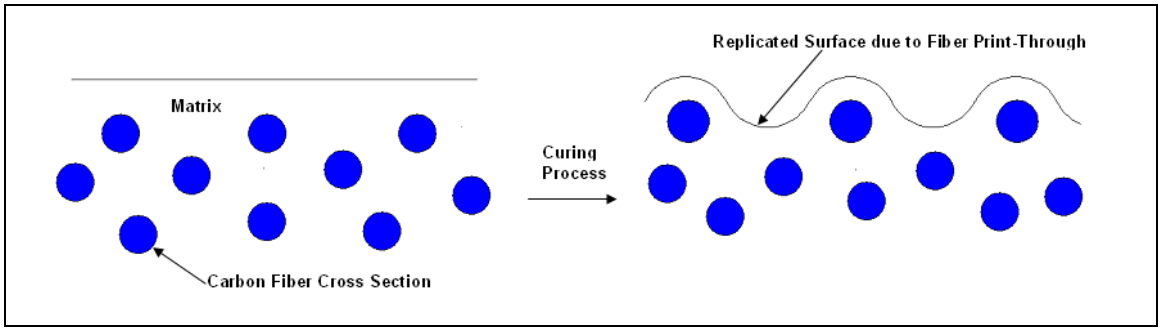

Figure 24: Fiber print-through phenomenon in a replicated composite mirror

The Figure 25 shows fringe images obtained with apparatus. The fringe pattern due to fiber print-through therefore shows, not surprisingly, fairly strong astigmatism.

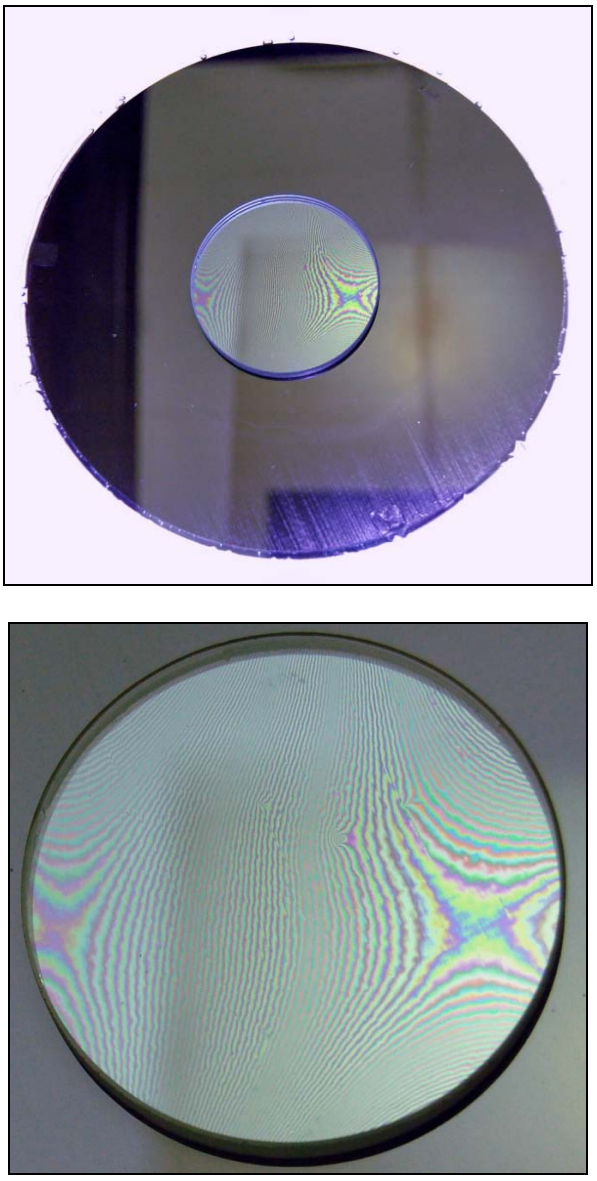

Figure 25: Fringe patterns in composite mirror from fiber print-through (from BOR)

The purpose of this section is to quantify the magnitude of surface roughness from fiber print-through as a function of curing temperature. In order to quantify the cause of fiber print-through from chemical and thermal shrinkage between fiber and matrix, we considered several fibers and matrix materials in unit cell numerical models to evaluate the magnitude of the sinusoidal undulation. The detail of the numerical model is shown in Figure 26. 3D CHEXA elements and the boundary conditions described in Chapter 4 were used. In the model, the volume fraction of fiber and matrix were considered as 60% and 40% respectively.

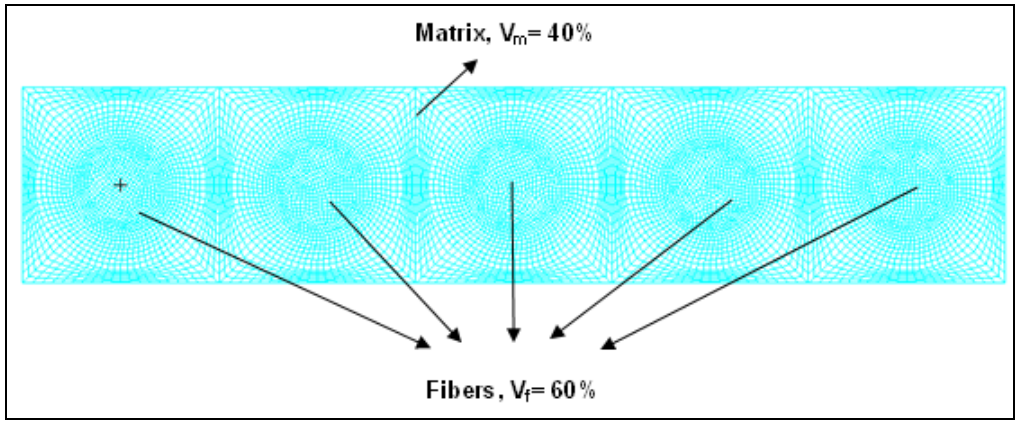

Figure 26: 3D numerical model for fiber print-through analysis, υ_f=60% and υ_m=40%

The material used in this analysis was AS/3501-6 unidirectional carbon prepreg. The simulation followed a normal curing process, where the model was heated at various curing temperatures from 350° F~70° F and cooled down to room temperature (70° F). As shown in Figure 27, the magnitude of fiber print-through results in higher order frequency surface deformation due to the chemical and thermal shrinkage from fiber and matrix in the lamina when the lamina was heated and cooled down to room temperature.

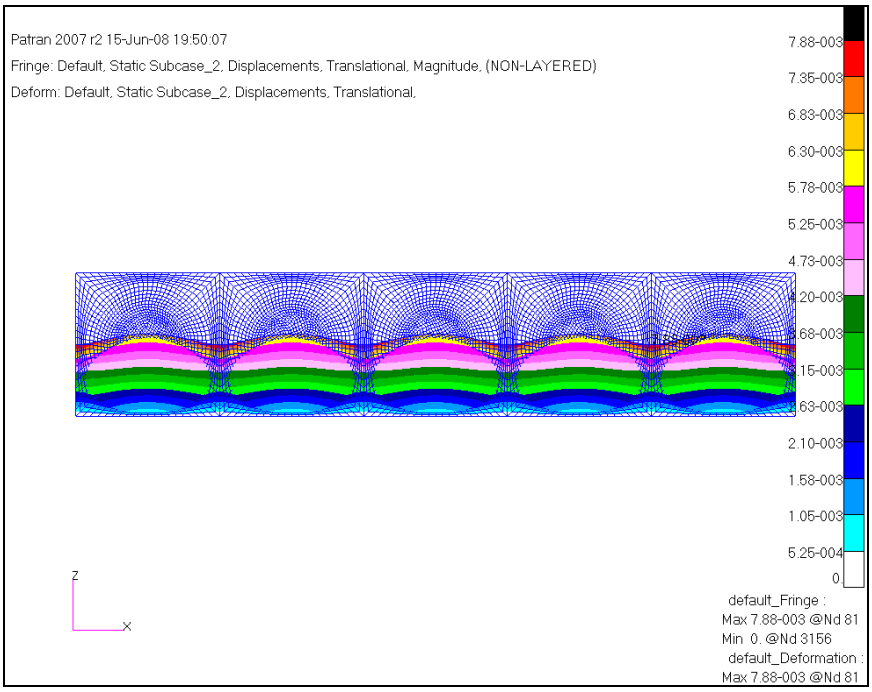

Figure 27: Fiber print-through effect in a lamina from MSC.Patron/Nastran

Carbon fiber reinforced plastics provide many of the properties that meet mirror requirements. However, one of critical problems that plagues composite mirror is the presence of fiber print-through. It is currently hypothesized that fiber print-through occurs during the cure cycle, when the underlying fiber geometry is transposed to the surface causing high frequency surface errors due to thermal and chemical shrinkage in fiber and matrix. The numerical simulation validated the hypothesis that fiber print-through does exist when fabricating composite mirrors with a high temperature curing process.

If the cause of the fiber print-through is due to the laminate curing cycle, one can hypothesize that the fiber print-through can be mitigated by using room temperature curing resin system for precision composite mirror fabrication. The following Figure 28

and Table 15 illustrated the numerical results on the magnitude of fiber print-through effect at different curing temperatures.

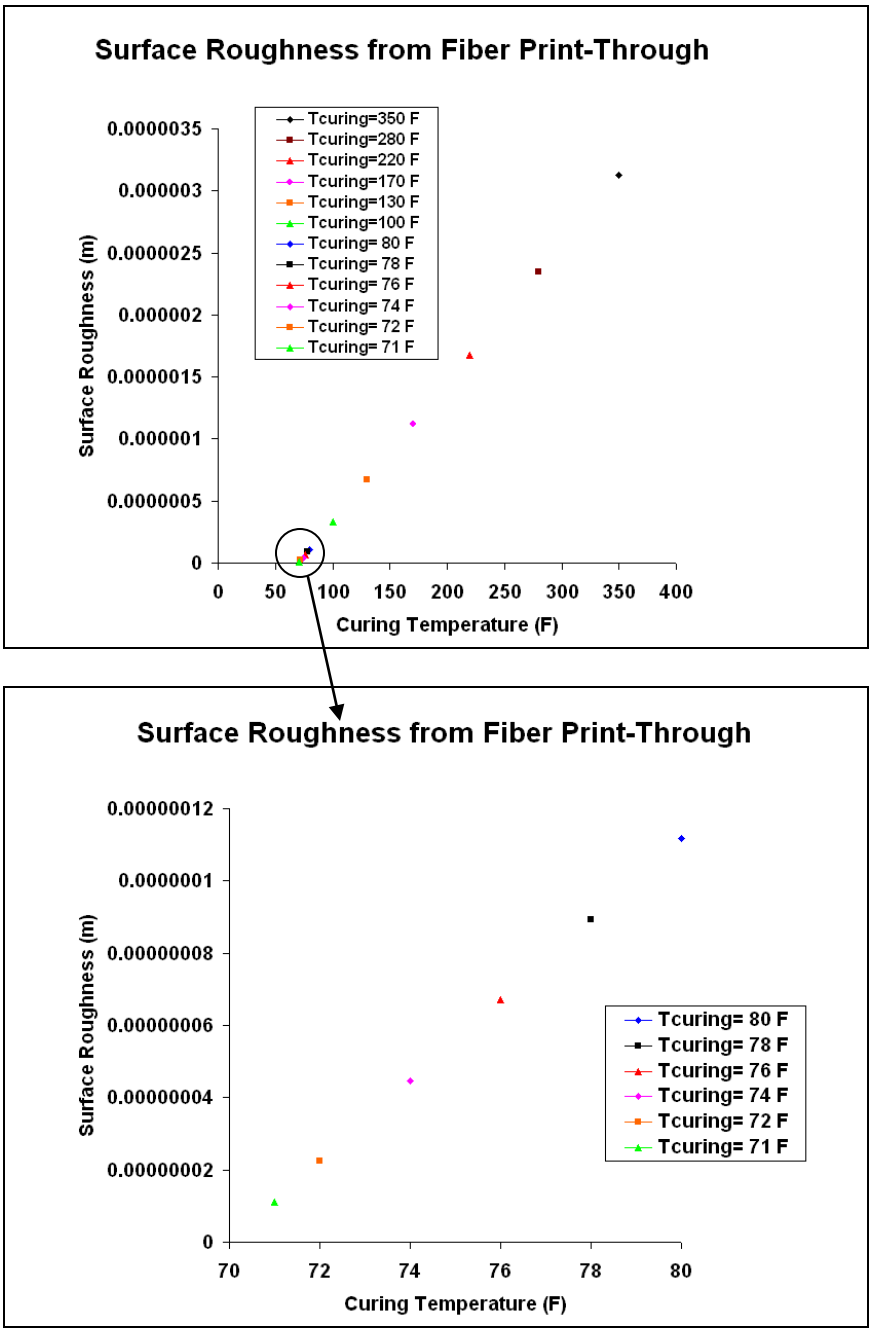

Figure 28: Surface roughness due to fiber print-through as a function of curing temperature

Table 15: Magnitude of surface roughness from fiber print-through as a function of curing temperature.

Curing Temperature (F)	Surface Roughness (inch)	Surface Roughness (nm)	λ/n
350	3.12943E-06	3129.43	0.20
280	2.34707E-06	2347.07	0.27
220	1.67648E-06	1676.48	0.38
170	1.11765E-06	1117.65	0.56
130	6.70592E-07	670.59	0.94
100	3.35296E-07	335.30	1.88
80	1.11765E-07	111.77	5.64
78	8.94123E-08	89.41	7.05
76	6.70592E-08	67.06	9.39
74	4.47062E-08	44.71	14.09
72	2.23531E-08	22.35	28.18
71	1.11765E-08	11.18	56.37

With 350 degree F curing system in composite material, surface roughness due to chemical and thermal shrinkages in fiber and matrix was found as 3129 nm (λ/0.2). The magnitude of surface roughness in 350° F resin curing system are not acceptable for precision diffraction limited mirror requirement (<λ/20=31.5nm). On the other hand, it was notable to see that the surface roughness decreased as we decreased curing temperatures. It may not be possible to eliminate the higher order surface undulation due to shrinkage of fiber and matrix, but it may be possible to reduce the magnitude of fiber print-through to the diffraction limited requirement for precision optics by utilizing room temperature resin system in composite material. The higher order surface roughness in a resin with near room temperature curing system was found as λ/56.37 (11.18 nm), and it met the diffraction limited requirement. As indicated, fiber print-through effects fade away as we used low temperature curing resin system.

To conclude, if higher order surface roughness due to fiber print-through during composite mirror fabrication process is inevitable and it hinders precision optical performance, utilizing room temperature curing system is one possible way to mitigate the fiber print-through effects in precision composite mirror. One can expect to deviate from this recommendation if environmental fluctuations are expected in service.

5.3. Surface Deformations on π/n Quasi-Isotropic Laminated Composite Mirror Substrates with Additional Resin Rich Layers

Although many suppliers are fabricating composite fiber reinforced mirrors, it is a common belief that precision mirror development utilizing CFRP materials is limited by surface roughness and surface figure error due to fiber print-through inherent in the mirror fabrication process. In general, a CFRP mirror substrate contains one or more resin rich layers on the top surface to mitigate the fiber print-through.

The resin coating is commonly implemented in a composite mirror for several reasons. First, resin coating is used to affect the stress distribution around the fiber matrix interface. Second, resin coating is used to alter the overall composite properties, such as elastic properties and reduction of thermal stresses in the composite with a mismatch in coefficient of thermal expansion (CTE) of fiber and matrix.

In composite optics, even though such additional layers result in slight asymmetry in the composite mirror substrate, it has been assumed that the relatively low energy in the resin rich layer compared to substrate would not affect the entire composite substrate. However, when thermal variance is present, the laminate expands according to a more complex mechanism than an ideal quasi-isotropic symmetric laminate. As shown in Figure 29, the resin-rich surface layer, by contrast, has a low axial stiffness and a fairly high coefficient of thermal expansion compared with the quasi-isotropic laminate.

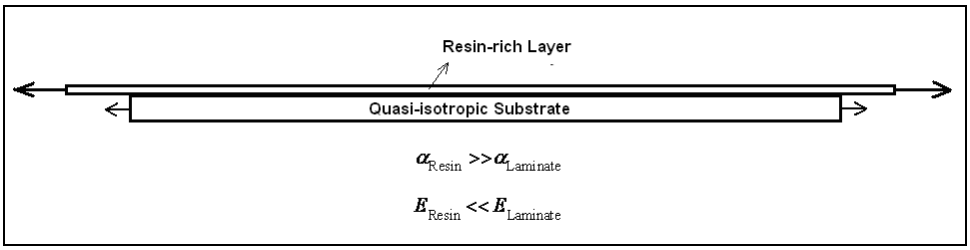

Figure 29: Schematic diagram for physical behavior in composite mirror substrate and resin rich layer due to different mechanical properties between the substrate and resin layer.

Due to the fact that the composite substrate has very high in-plane stiffness and very low coefficient of thermal expansion while the resin rich matrix has relatively low axial stiffness and high coefficient of thermal expansion, slight bending and twisting in the substrate due to asymmetry would be expected, and the natural response of surface deformation in a composite mirror would be out of plane deformation in the resin rich layer as shown in Figure 30. This is exactly what is not desired in optical systems.

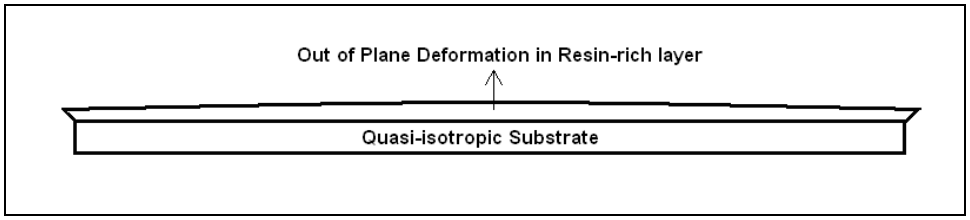

Figure 30: Schematic diagram for out of plane deformation in resin-rich layer

Again, if the response of the out of plane deformation in a composite mirror is radially symmetric, this would be a first order change in curvature which is constant radial out of plane deformation. This problem can be readily corrected within most optical systems. As discussed in section 5.1, constant radial out of plane deformation is not feasible even in an ideal quasi-isotropic laminate. In fact, it is predicted that when thermal gradient is presented to the asymmetric laminate, high energy and sinusoidal

deformation pattern in an ideal laminate plate would reflect through and be magnified by the resin rich matrix resulting in more serious surface deformation because of very low energy and high CTE characteristics in the resin matrix.

Figure 31 is a 2D deformation contour when thermally induced load ($\Delta T=30F^{\circ}$) is applied to quasi-isotropic $\pi/4$ laminate from on-axis (0 degree) to 20 degree axis. As illustrated in Figure 31, a slightly bent global shape occurs throughout the entire numerical model as a consequence of asymmetric characteristics in the composite mirror substrate. Compared to the magnitude of surface deformation in the substrate, the result shows that a slight asymmetric laminate results in larger out of plane surface deformations in a composite plate with a resin rich layer.

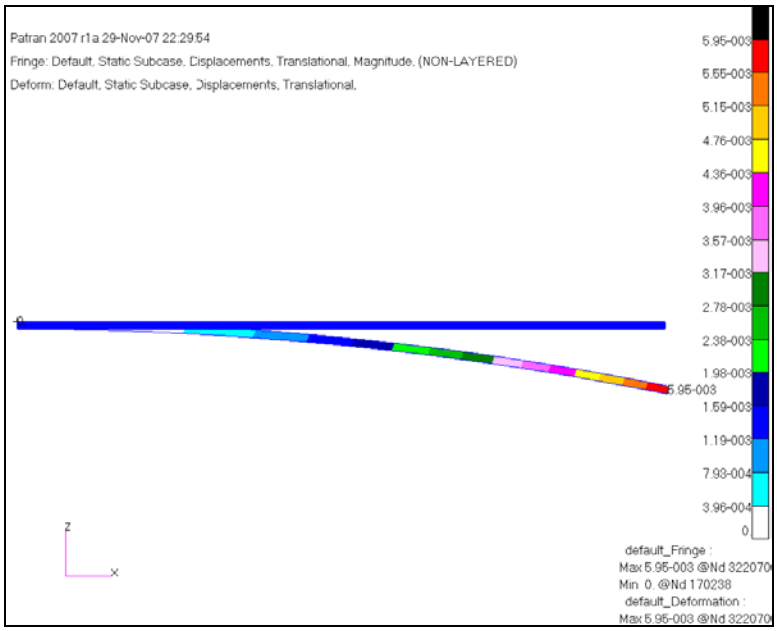

a) Deformation contour in $\pi/4$ quasi-isotropic laminate with additional resin layer. (On-axis)

Figure 31: Deformation contour (exaggerated deformation view) result in Nastran/Patran when thermal load ($\Delta T=30^{o}F$) is applied to quasi-isotropic $\pi/4$ laminate. (At 0 degree up to 20 degree axis)

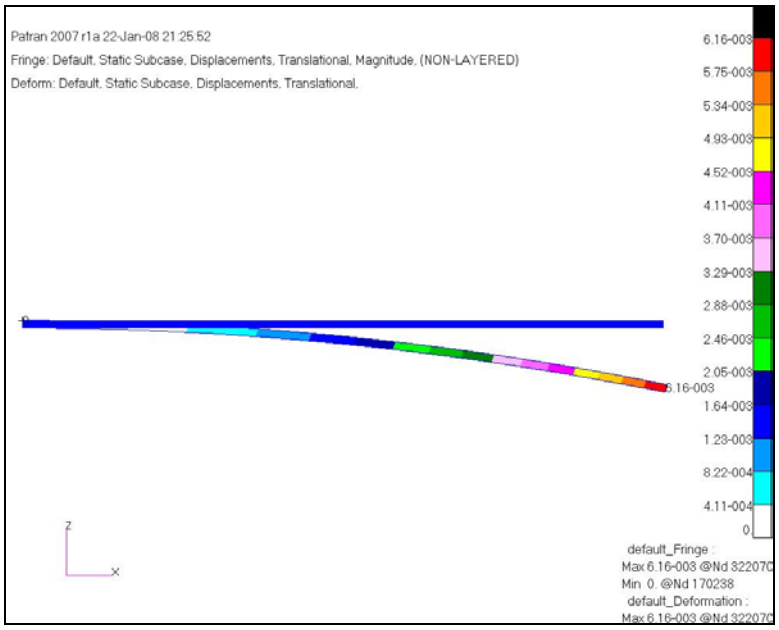

b) Deformation contour in π/4 quasi-isotropic laminate with additional resin layer. (5 degree axis)

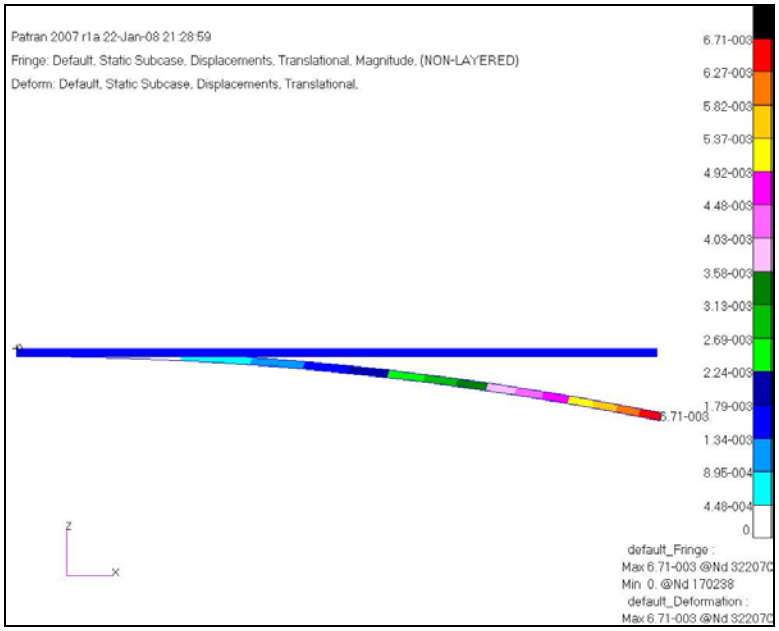

c) Deformation contour in π/4 quasi-isotropic laminate with additional resin layer. (10 degree axis)

Figure 31 (Cont.): Deformation contour (exaggerated deformation view) result in Nastran/Patran when thermal load (ΔT=30°F) is applied to quasi-isotropic π/4 laminate. (At 0 degree up to 20 degree axis)

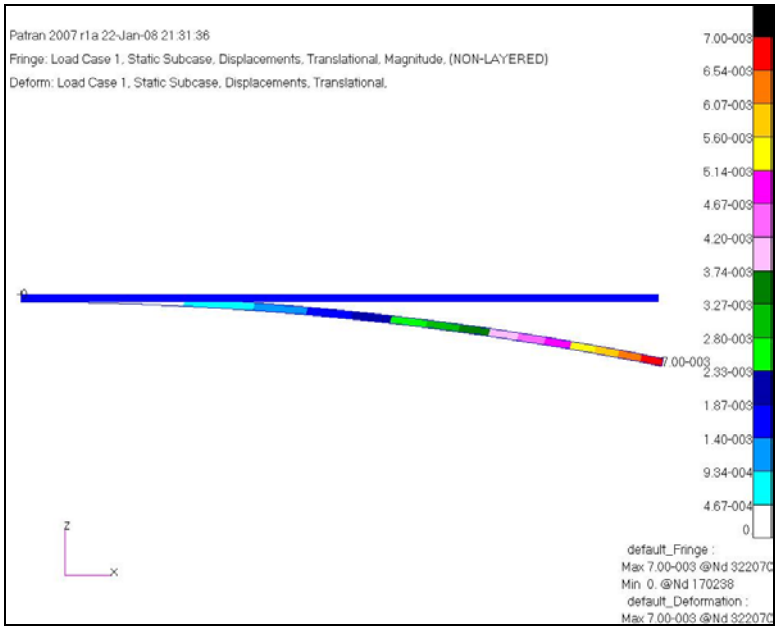

d) Deformation contour in π/4 quasi-isotropic laminate with additional resin layer. (15 degree axis)

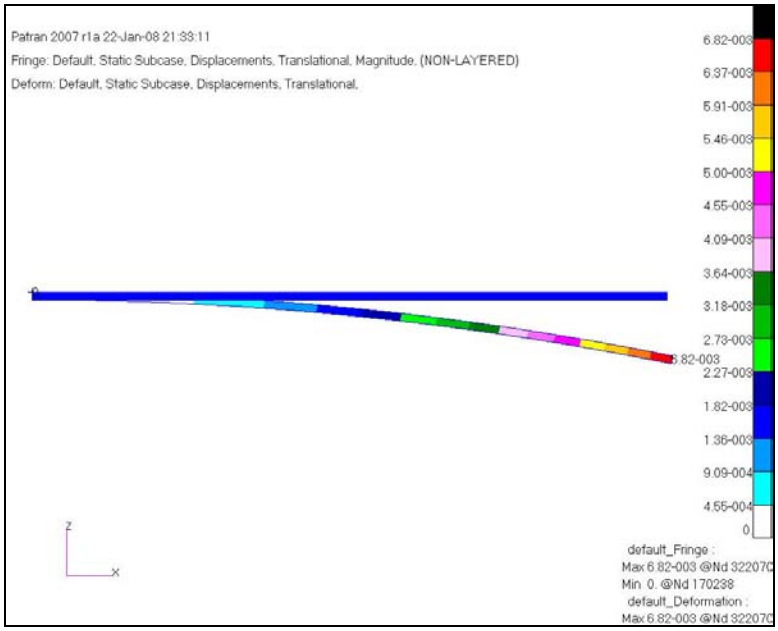

e) Deformation contour in π/4 quasi-isotropic laminate with additional resin layer. (20 degree axis)

Figure 31 (Cont.): Deformation contour (exaggerated deformation view) result in Nastran/Patran when thermal load (ΔT=30ºF) is applied to quasi-isotropic π/4 laminate. (At 0 degree up to 20 degree axis)

Figure 32 illustrates a 2D surface deformation plot between dz/dz_{max} vs. dx/dx_{max} at on-axis up to 45 degree axis in a quasi-isotropic laminate with an additional resin layer. As shown, surface deformation in each radial axis in the slightly asymmetric laminate has more critical surface deformations compared with the ideal laminate.

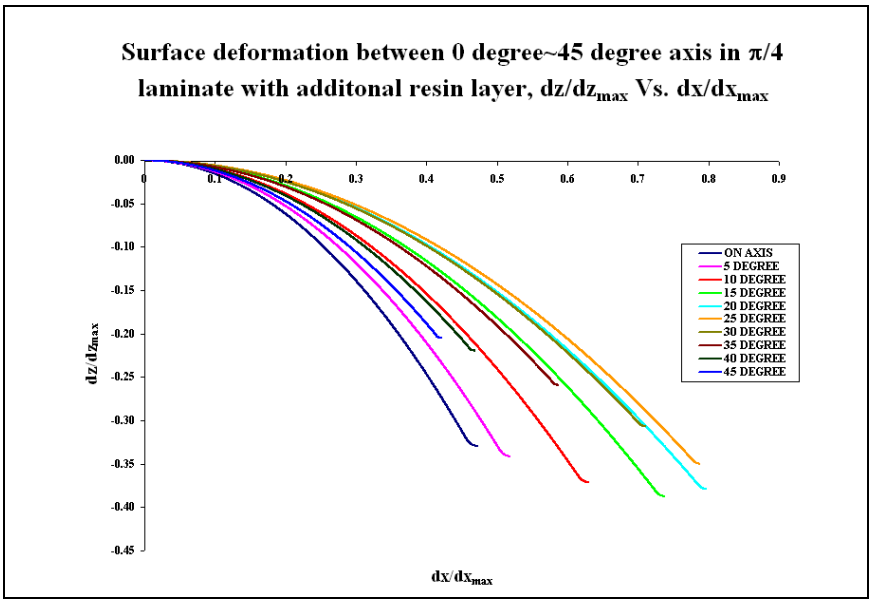

Figure 32: Surface deformation plot for dz/dz_{max} vs. dx/dx_{max} in π/4 quasi-isotropic laminate substrate due to thermal load, (0 degree up to 45 degree)

If fiber print-through is unavoidable and if the resulting surface undulation patterns are not acceptable, it is a common assumption in the composite optics industry that the unacceptable surface from fiber print-through would have to be reduced to an acceptable level by applying resin rich surface layers. The surface undulation characteristics from fiber print-through might be damped out by applying additional resin layers on the top of the quasi-isotropic laminates. This would be effective at a single temperature. However, in cold or hot working environmental conditions, the presence of

the additional resin layer on the composite would result in more severe surface deformations.

Figures 33~35 demonstrate the entire 3D normalized surface deformation contours in π/n laminates with an additional resin layer. As shown in the Figures, the magnitudes of sinusoidal surface deformation in the asymmetric laminates are more severe than in ideal laminates. The presence of the additional resin layer did not damp out the inherent surface waviness and its deformation energy released from ideal quasi-isotropic laminates due to the thermal load. The deformation energies in the ideal laminates reflect through the additional resin layer which contains higher coefficient of thermal expansion, and existence of bending due to slightly asymmetric characteristics in the composite results in more critical surface deformations.

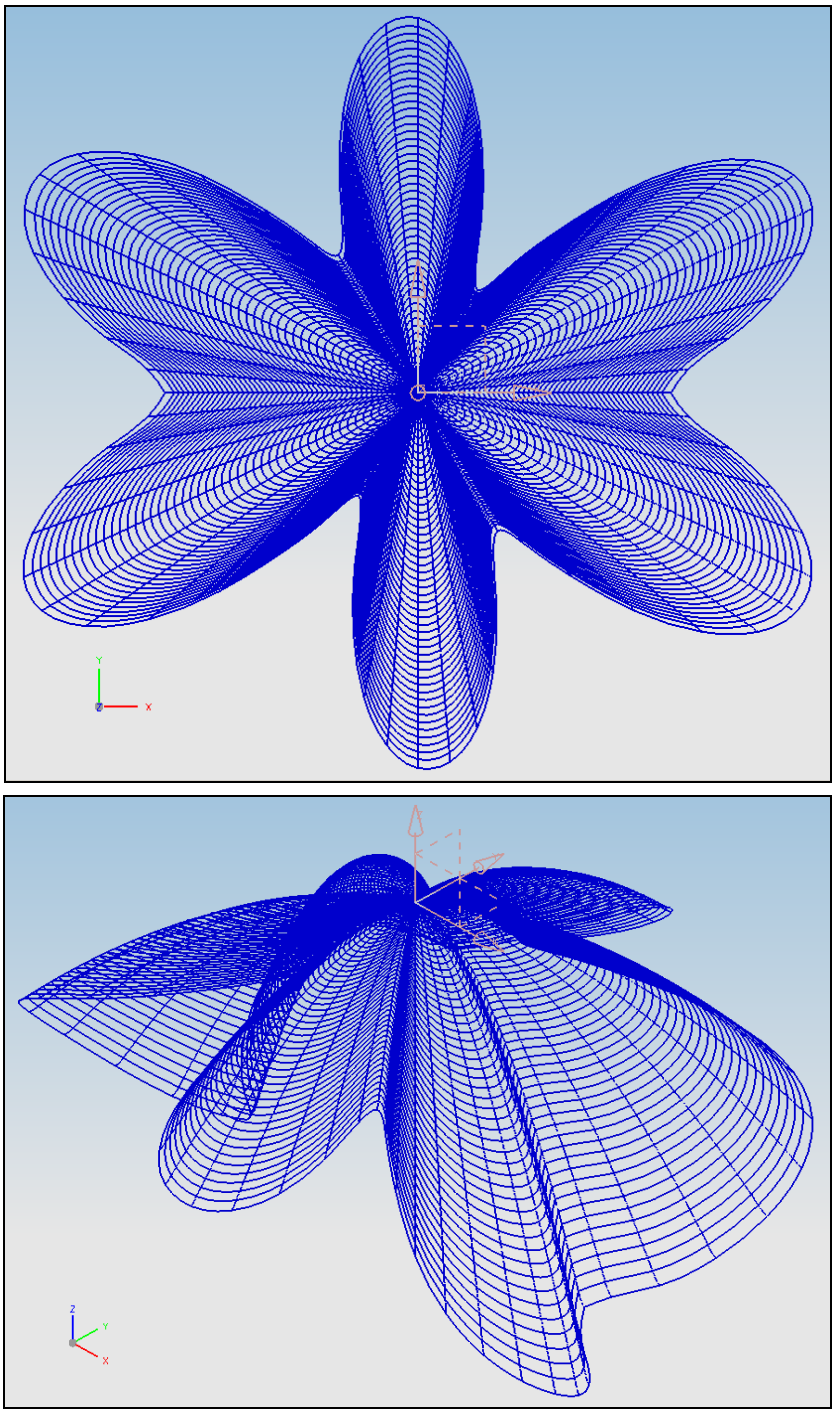

Figure 33: Top and iso-3view of surface deformation contours in π/3 quasi-isotropic laminates with additional resin layer

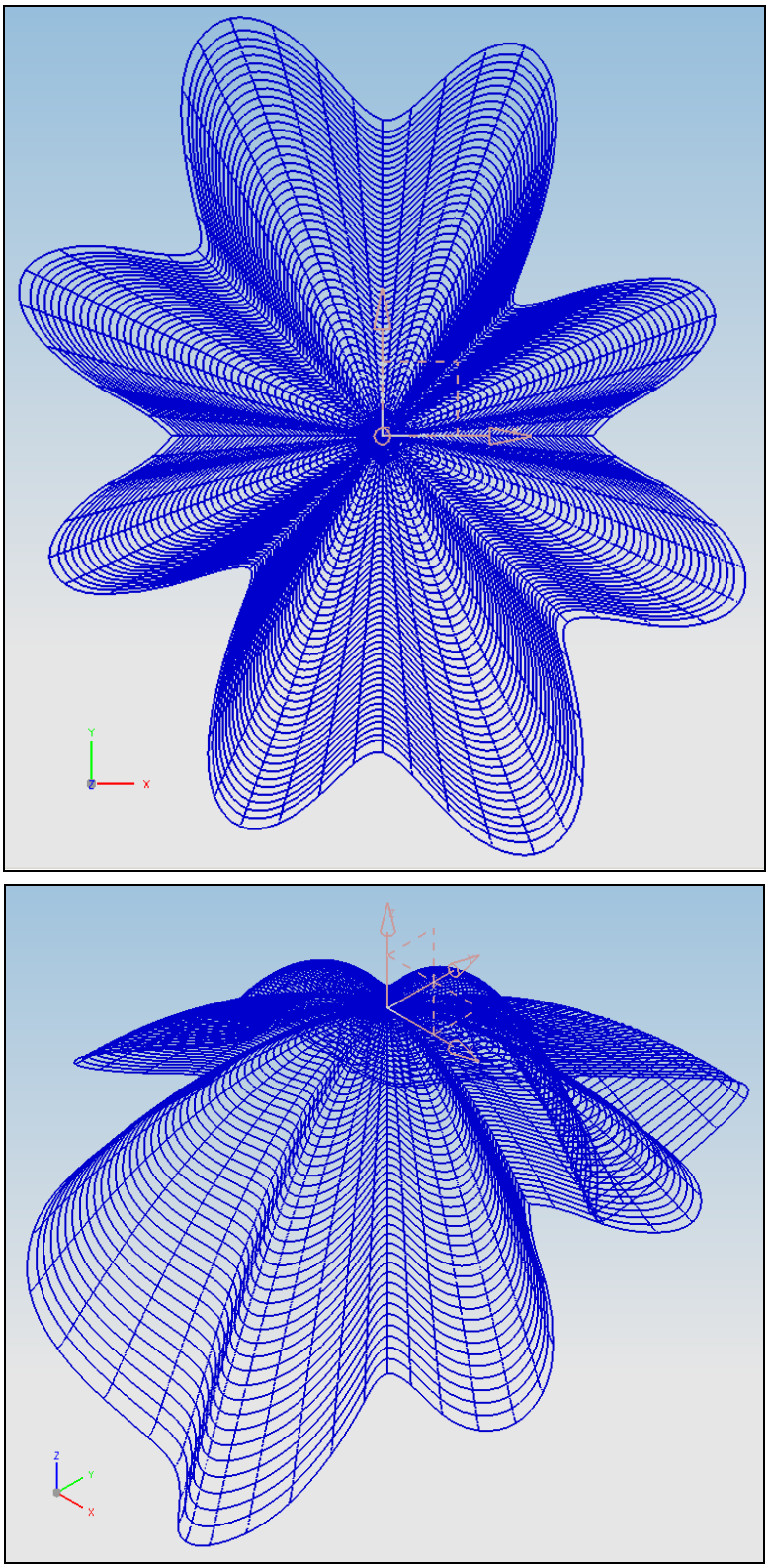

Figure 34: Top and iso-3view of surface deformation contours in π/4 quasi-isotropic laminates with additional resin layer

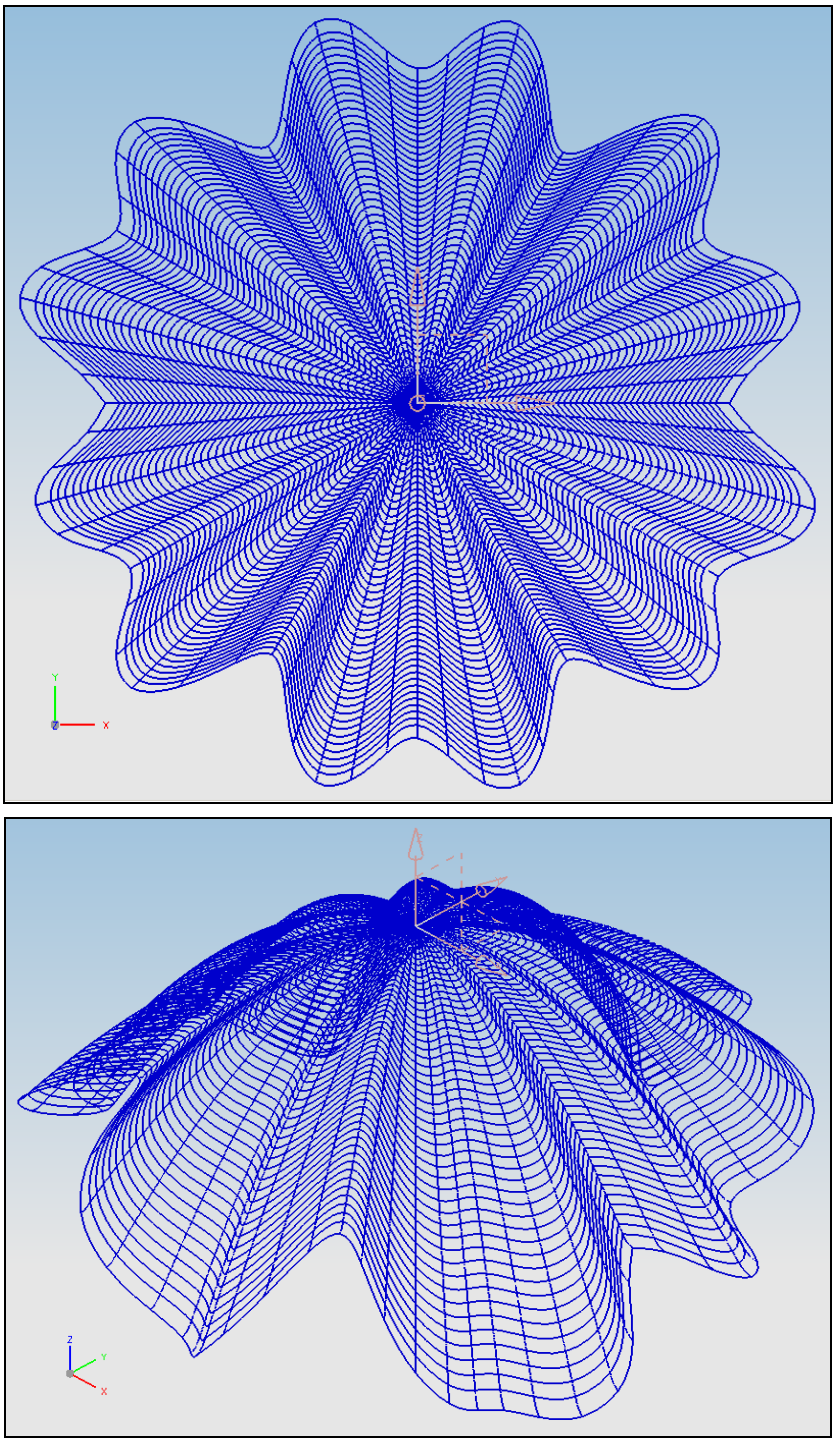

Figure 35: Top and iso-3view of surface deformation contours in π/6 quasi-isotropic laminates with additional resin layer

The numerical results shown in this section demonstrate that the asymmetric characteristics in quasi-isotropic laminate substrates due to use of one or more resin layers for mitigation of fiber print-through problem would result in more serious surface distortions than high frequency surface errors from fiber print-through. The maximum global surface deformation shown in Figures 33~35 for π/n laminates indicate that the additional resin layer applied to the composites are more problematic than surface waviness caused from fiber print-through. These unacceptable deformations and sinusoidal deformation patterns in π/n laminates will be significant factors regardless of the presence of fiber print through in composite mirrors.

Such surface deformations in the quasi-isotropic laminates might be overcome by using homogeneous materials (veil, mat, and other chopped fiber products) for fabricating a circular mirror. By utilizing such a material, constant extensional and flexural stiffness mechanical properties in a circular mirror could be obtained. Homogeneous material properties were used in a similar computational model. Figure 36 illustrates the radial variations of flexural stiffness in ideal π/n laminates (without resin layer), where n=3, 4, 6 and 3D surface deformation contour for π/4 laminate with an additional resin layer.

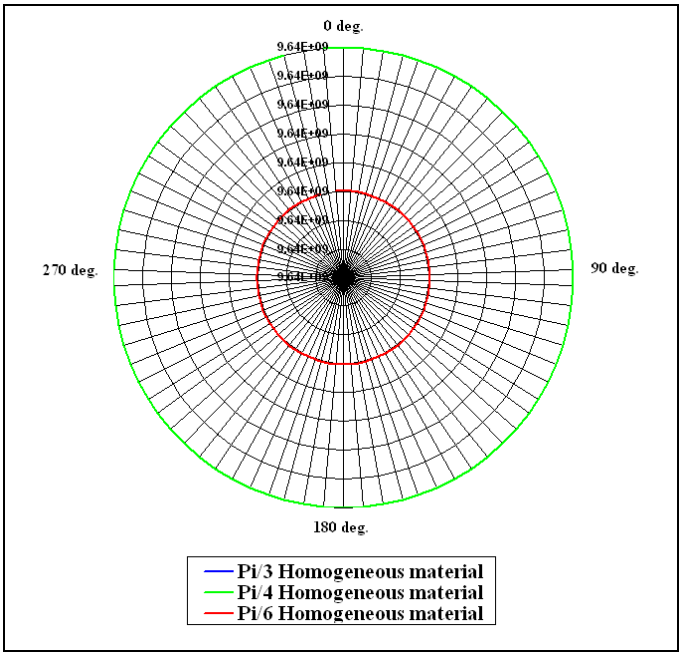

a)

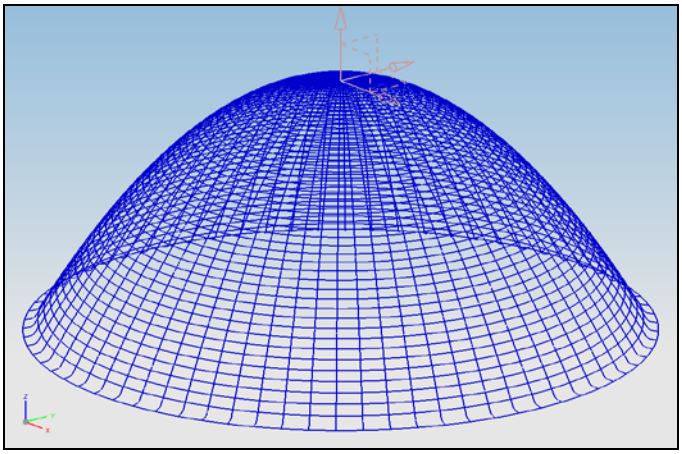

b)

Figure 36: a) Radial variations of D_{11} in ideal π/n quasi-isotropic laminates where n=3, 4, 6 using homogeneous material, b) 3D surface deformation contour in $\pi/4$ laminate (using homogeneous material) with additional resin layer on the top of the composite mirror.

The results show constant radial flexural stiffness in all three ideal laminates and no lay-up sequence effects which can be achieved by using homogeneous material. Also, in the 3D surface deformation contour, the surface deformation shape is first order in curvature, and thus readily correctable with most optic system. Such short fiber or distributed material might be appropriately homogeneous or may display mechanical properties that vary spatially. However, laminates of sufficient layers of such material with sufficient π/n orientations may demonstrate effectively homogeneous mechanical properties in extensional and flexural stiffness.

5.4. Resin Thickness Effects and Graded / Intermediate Resin Layer Effects on a π/4 Quasi-isotropic Mirror Substrate

The previous section discussed the existence of fiber print-through on the surface of a quasi-isotropic laminated mirror which creates unfavorable surface waviness as a result of fabrication process. The problem of the fiber print-through comes from mostly chemical and thermal shrinkage between fiber and matrix when the composite is cooled from highly elevated curing temperature. The purpose of this section is to investigate and quantify the magnitude of surface deformations and its contribution to the total surface roughness in a π/4 quasi-isotropic composite mirror substrate due to presence of additional resin layers for reduction of high frequency surface quality from fiber print-through. The effects of surface waviness by use of additional resin layers are evaluated for function of resin thickness as well as function of mechanical property of resin.

A commonly known fiber print-through mitigation technique is to add additional resin rich layers on the surface of the composite mirror. Numerous investigations have addressed fiber print-through mitigation techniques [Ref. 1, 2, 3, and 4]. These studies showed that high frequency surface undulation on replicated composite mirrors due to fiber print-through rapidly decrease with additional surface resin layers of the composite mirrors with polishing. They found that the surface qualities were getting better when they increased the thickness of resin layers.

The additional resin layer coating and polishing techniques might mitigate the fiber print-through at a single temperature (e.g. the room temperature tests performed). However, as discussed in previous section 5.2, in cold or/and hot working environmental conditions, the presence of the additional resin rich layers on composite mirror surface

would have more adverse effect on the surface deformation than fiber print-through effects. In this section, the effects of resin thickness of 5-mil up to 20-mil on the surface of a π/4 mirror were evaluated to quantify the magnitude of surface undulations. Also, the applicability of various graded and intermediate resin material properties are performed to determine which variables have most positive influence on the surface deformations and to see feasibility of various mitigation techniques for fiber print-through.

5.4.1. Resin Thickness Effects on the Surface of a Quasi-isotropic Mirror

The effects of different thickness of resin layers are examined by finite element analysis. An ideal π/4 quasi-isotropic mirror substrate is considered as a based numerical model. For this study, the AS4/3501-6 Carbon/Epoxy prepreg is used. The numerical models are created such that the laminate has 8 layers with lay-up sequence of $[45, 0, -45, 90]_s$ with different resin thickness of 5 ~20-mil (by increment of 5-mil) respectively. The numerical models are simulated as the mirror was placed under hot environment with temperature change from room temperature to 100° F for evaluation of the magnitude of surface deformations.

Numerical results shown in Figures 37~40 illustrate the amplitude of surface undulation at different thickness of resin layer at each radial axis (0 degree to 165 degree). As predicted, additional resin layer present in composite mirror substrate for fiber print-through mitigation technique did not play a role of damping the high frequency surface patterns emitting from the composite mirror substrate due to stacking

sequence effects. As the numerical results show, adding resin layers for alleviating high frequency surface deformation from fiber print-through stated in Ref. 4 is not practical when mirrors may be expected to experience thermal fluctuations. On the other hand, the presence of more resin layers as buffer layer for the high frequency surface cause adverse effects on surface of the mirror.

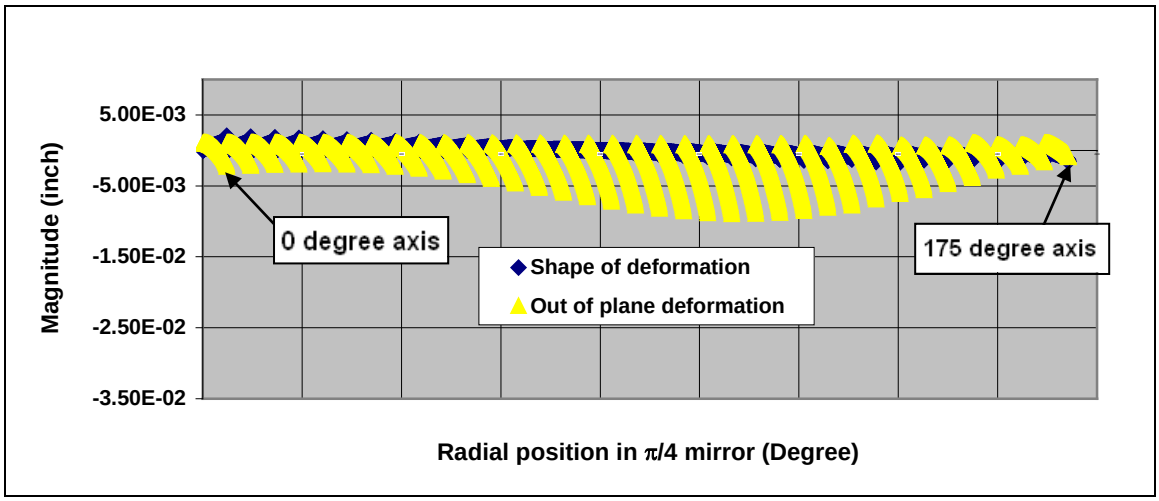

Figure 37: Magnitude and shape of surface deformations in π/4 composite mirror with 5-mil resin surface layer

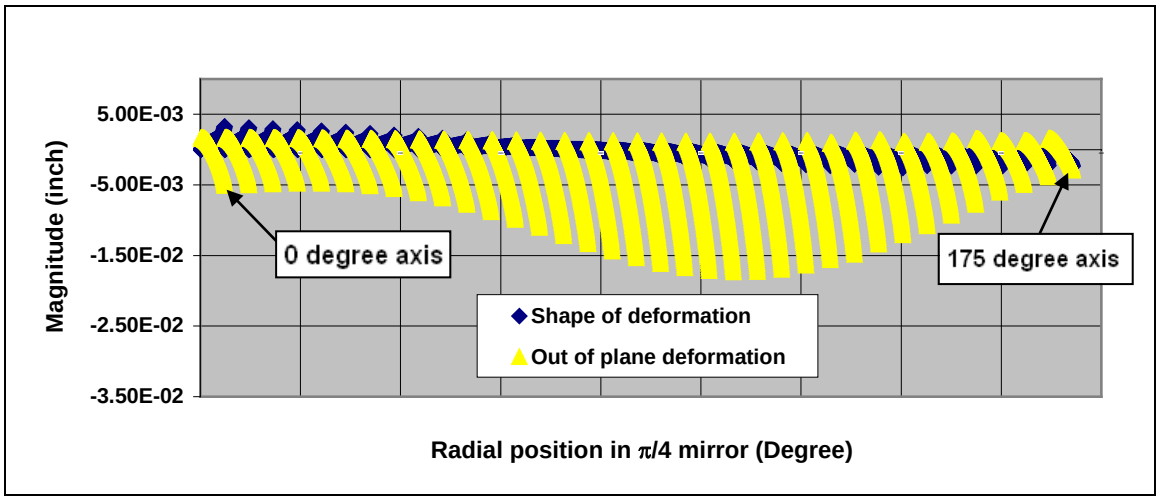

Figure 38: Magnitude and shape of surface deformations in π/4 composite mirror 10-mil resin surface layer

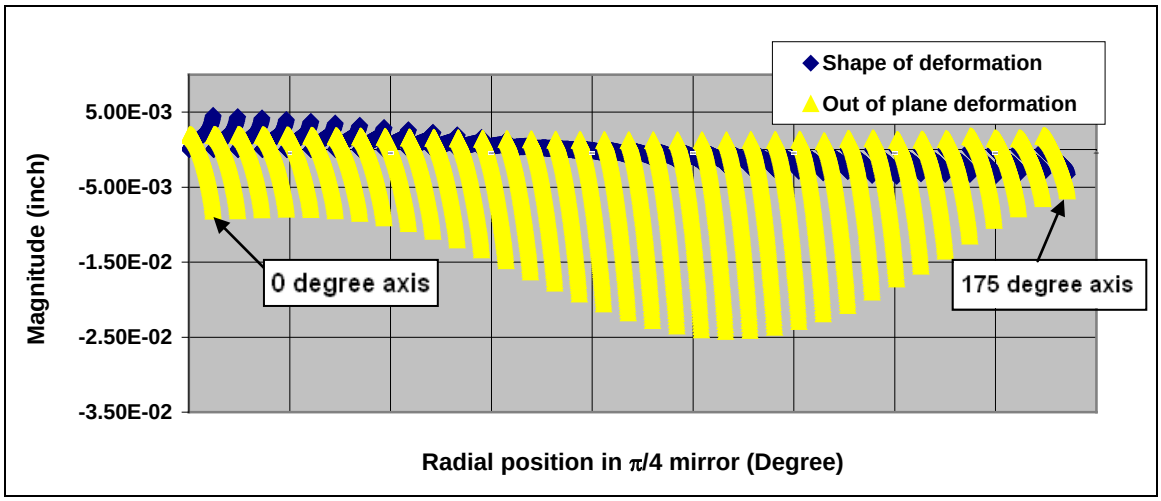

Figure 39: Magnitude and shape of surface deformations in π/4 composite mirror with 15-mil resin surface layer

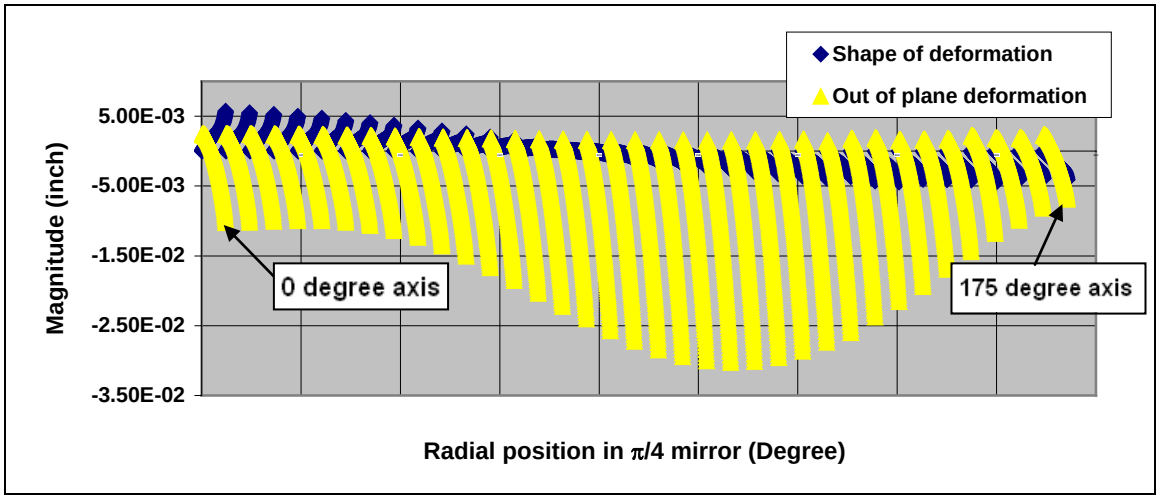

Figure 40: Magnitude and shape of surface deformations in π/4 composite mirror with 20-mil resin surface layer

From the above Figures 37~40 it can be seen that reduction of the surface waviness can not be achieved by increment of resin thickness. The numerical results clearly show that the severity of surface undulation causing great concern in composite optics become greater than before increasing thickness of resin rich layer. It appears that

local bending in the mirror due to asymmetric characteristics introduced by use of additional resin layers and the variations of flexural stiffness from stacking sequence effects cause the global and local sinusoidal surface undulations. The increased asymmetry of the mirror by adding more resin layers is an important factor causing larger global deflections in the laminate as seen in Figures 37~40. It is because of the resin layers on a constant composite substrate adds more asymmetric characteristics in the laminate as their thickness increased. The sinusoidal surface deformation energy emitted due to lay-up sequence and complexity of mechanics in quasi-isotropic composite mirror reflects to the additional resin layer which contains low energy and high coefficient of thermal expansion compared to laminate substrate. Moreover, the increased resin layer applied on surface of the composite mirror resulted in more surface swelling in the additional resin layer due to its increased thickness (because of the relatively high coefficient of thermal expansion of the unreinforced plastic). Thus, the unfavorable consequences on the surface undulation caused by radial variations in flexural stiffness and stacking sequence effects in the quasi-isotropic laminate can not be suppressed even though the laminate was covered with a sufficiently thick resin layer applied on its surface. In fact, the magnitudes of surface waviness in the composite mirror become worse than the value of surface roughness due to fiber print-through. Therefore, the numerical results lead one to conclude that fiber print-through mitigation technique utilizing resin buffer layer creates more uncontrollable sinusoidal surface deformation when thermal load is presented in a composite mirror.

5.4.2. Graded / Intermediate Resin Layer Effects

In previous section 5.4.1, resin thickness effects on surface of composite mirror substrate were investigated. As the results indicate, there is no alleviation of surface waviness on replicated CFRP mirror by use of additional buffer resin layer for mitigation of fiber print-through. In fact, the sinusoidal surface roughness has been increased with presence of thermal load as the thickness of resin rich layer increased. The purpose of this section is to examine the influence of different hypothetical coating materials (graded resin and intermediate resin) and to quantify the amplitude of sinusoidal waviness on surface of the composite mirror due to the different coating materials when the composite mirror was subjected to a uniform temperature change $\Delta T=30°F$ difference between operating temperature and the curing temperature. To investigate the effects of graded resin and intermediate resin on the resulting CFRP carbon composite mirror surface roughness, a total of forty-two cases were analyzed (21 cases each for graded and intermediate resin). The following Figure 41 illustrates the schematic diagram for graded/intermediate resin layer models in finite element analyses. For composite material used in this simulation, AS4/3501-6 prepreg was used to model composite mirror, and the mechanical properties of epoxy 3501-6 contains $E_m=0.638x10^6$ psi, $G_m=0.232x10^6$ psi, $\nu=0.36$, and $\alpha_m=1.64x10^{-5}$ in./in./ºF.

In previous research of fiber print-through mitigation techniques, Massarello et.al. claimed that fiber print-through effects can be eliminated with sufficient resin thickness of greater than 10/1000 inch (10-mil) [Ref. 4]. Thus, 10-mil of resin thickness is used in this study based on the previous research. As shown in Figure 41, for details of numerical

models, two resin buffer layers (each layer has thickness of 5-mil) are considered as applied resin layers on the composite mirror for the numerical simulation.

For graded resin study, two layers (total of 10-mil) of gradually increased or decreased resin property are considered to observe the magnitude of surface waviness from the use of buffer layers. As Table 16 illustrates, seven different graded resin cases for Young's modulus ($E_m/6 \sim 6E_m$) are evaluated along with three graded resin cases for coefficient of thermal expansion ($\alpha_m=1.64x10^{-5}$ in./in./ºF, $\alpha_m/2$, and $\alpha_m/4$) which are totally twenty-one cases for graded resin study.

For the intermediate resin layer study, an intermediate resin layer (which resin property has either lower or higher than original resin material) is added between the surface of composite mirror substrate and a fixed original 3501-6 resin layer. Similar to the graded resin study, twenty-one cases of intermediate resin study are evaluated such that seven different intermediate resin layers are used at three different CTEs. The details of different hypothetical resin coating materials and their respective mechanical properties and coefficient of thermal expansion used in this study are shown in Figure 41 and Table 16. All numerical simulations for resin coating study were performed on a 8 layer stacking sequence of $[45, 0, -45, 90]_s$ $\pi/4$ quasi-isotropic laminate as a base mirror substrate with a constant thermal load of $\Delta T=30^{\circ}$ F.

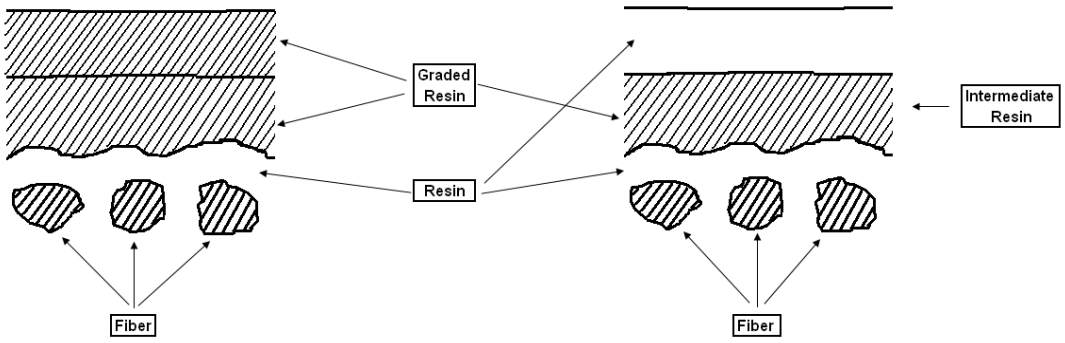

a) Graded resin case b) Intermediate resin case

Figure 41: Schematic diagram for graded resin and intermediate resin cases

Table 16: Resin properties for buffer layer study, a) CTE=α_m, b) CTE= $\alpha_m/2$, and c) CTE= $\alpha_m/4$

	$E_m/6$ $G_m/6$	$E_m/4$ $G_m/4$	$E_m/2$ $G_m/2$	E_m (3501-6) G_m (3501-6)	$2E_m$ $2G_m$	$4E_m$ $4G_m$	$6E_m$ $6G_m$
$E_{m\ (Psi)}$	1.06E+05	1.60E+05	3.19E+05	6.38E+05	1.28E+06	2.55E+06	3.83E+06
$G_{m(Psi)}$	3.91E+04	5.87E+04	1.17E+05	2.32E+05	4.69E+05	9.38E+05	1.41E+06
$\alpha_{m\ (in/in/°F)}$	1.64E-05	1.64E-05	1.64E-05	1.64E-05	1.64E-05	1.64E-05	1.64E-05

a) Graded E and G (Increased from left to right) with CTE=α_m

	$E_m/6$ $G_m/6$	$E_m/4$ $G_m/4$	$E_m/2$ $G_m/2$	E_m (3501-6) G_m (3501-6)	$2E_m$ $2G_m$	$4E_m$ $4G_m$	$6E_m$ $6G_m$
$E_{m\ (Psi)}$	1.06E+05	1.60E+05	3.19E+05	6.38E+05	1.28E+06	2.55E+06	3.83E+06
$G_{m(Psi)}$	3.91E+04	5.87E+04	1.17E+05	2.32E+05	4.69E+05	9.38E+05	1.41E+06
$\alpha_{m\ (in/in/°F)}$	8.20E-06	8.20E-06	8.20E-06	8.20E-06	8.20E-06	8.20E-06	8.20E-06

b) Graded E and G (Increased from left to right) with CTE=$\alpha_m/2$

	$E_m/6$ $G_m/6$	$E_m/4$ $G_m/4$	$E_m/2$ $G_m/2$	E_m (3501-6) G_m (3501-6)	$2E_m$ $2G_m$	$4E_m$ $4G_m$	$6E_m$ $6G_m$
$E_{m\ (Psi)}$	1.06E+05	1.60E+05	3.19E+05	6.38E+05	1.28E+06	2.55E+06	3.83E+06
$G_{m(Psi)}$	3.91E+04	5.87E+04	1.17E+05	2.32E+05	4.69E+05	9.38E+05	1.41E+06
$\alpha_{m\ (in/in/°F)}$	4.10E-06	4.10E-06	4.10E-06	4.10E-06	4.10E-06	4.10E-06	4.10E-06

c) Graded E and G (Increased from left to right) with CTE=$\alpha_m/4$

5.4.3. Results for Two Layer of Graded Resin Coating Study

The numerical results were plotted in Figure 42 to compare the maximum surface deformations calculated from the graded resin layers. As seen in the Figure, for the same coating thickness, a soft material with a low coefficient of thermal expansion helps in reducing the surface deformation. Also, the results indicate that even softer coating material is required for damping out surface deformation energy emitted from composite mirror substrate due to stacking sequence effects. By observing the numerical results it could be concluded that to alleviate the surface deformation in composite mirror in cold or/and hot environmental working conditions or in case of fiber print-through, the most important need for mechanical properties the for the resin buffer layer is a low coefficient of thermal expansion and low material stiffness (Young's modulus and shear modulus).

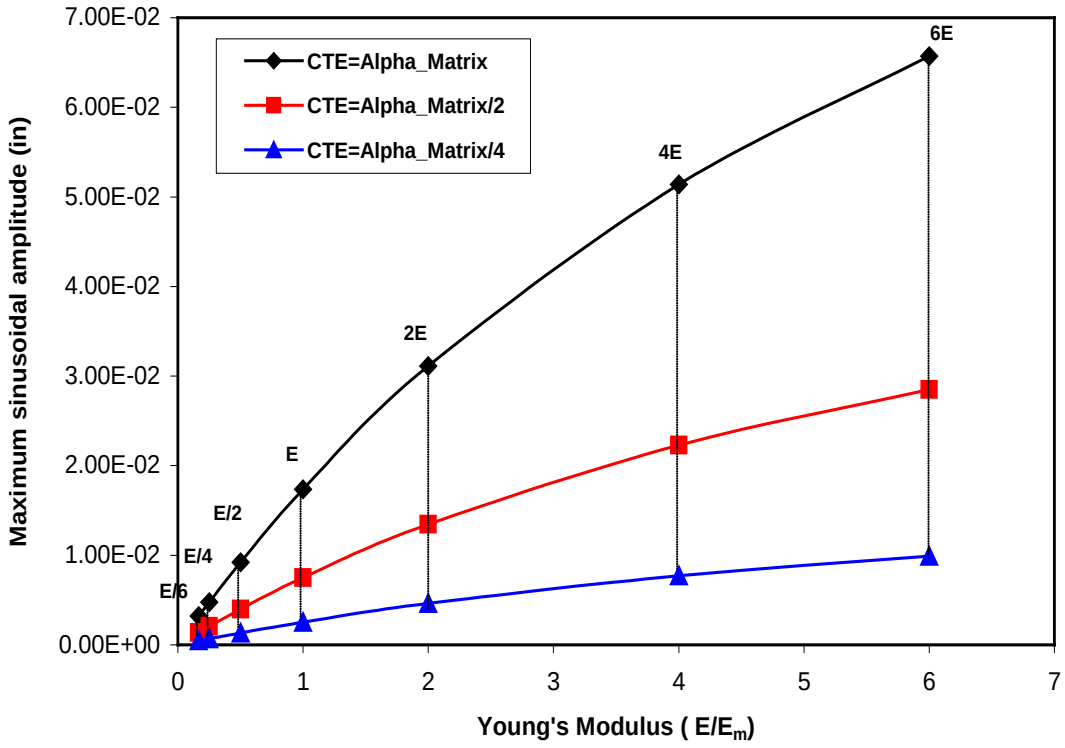

Figure 42: Maximum surface deformation calculated in π/4 quasi-isotropic laminate substrate with graded resin system at different coefficient of thermal expansion.

5.4.4. Results for Intermediate Resin Coating Layer Study (one layer of original resin on the top and one intermediate layer below)

The plotted Figure 43 indicates the results from the intermediate layer study. As seen in the Figure, the response of maximum sinusoidal amplitude in the composite substrate behavior roughly resembles the behavior of the graded resin cases. Again, from the results it can be concluded that it is better to use softer surface coating material with lower CTE to reduce the response of surface waviness in the composite mirror.

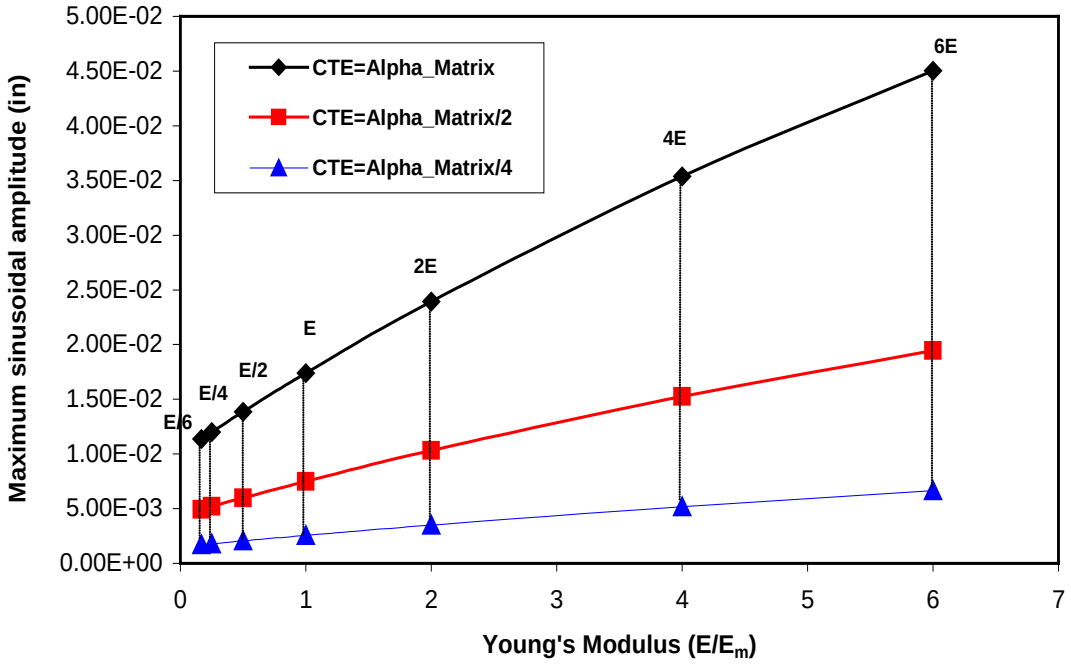

Figure 43: Maximum surface deformation calculated in π/4 quasi-isotropic laminate substrate with intermediate resin system at different coefficient of thermal expansion.

The plotted Figure 44 illustrates the comparison of resin types analysis for alleviation of sinusoidal surface waviness in a typical quasi-isotropic laminate composite substrate.

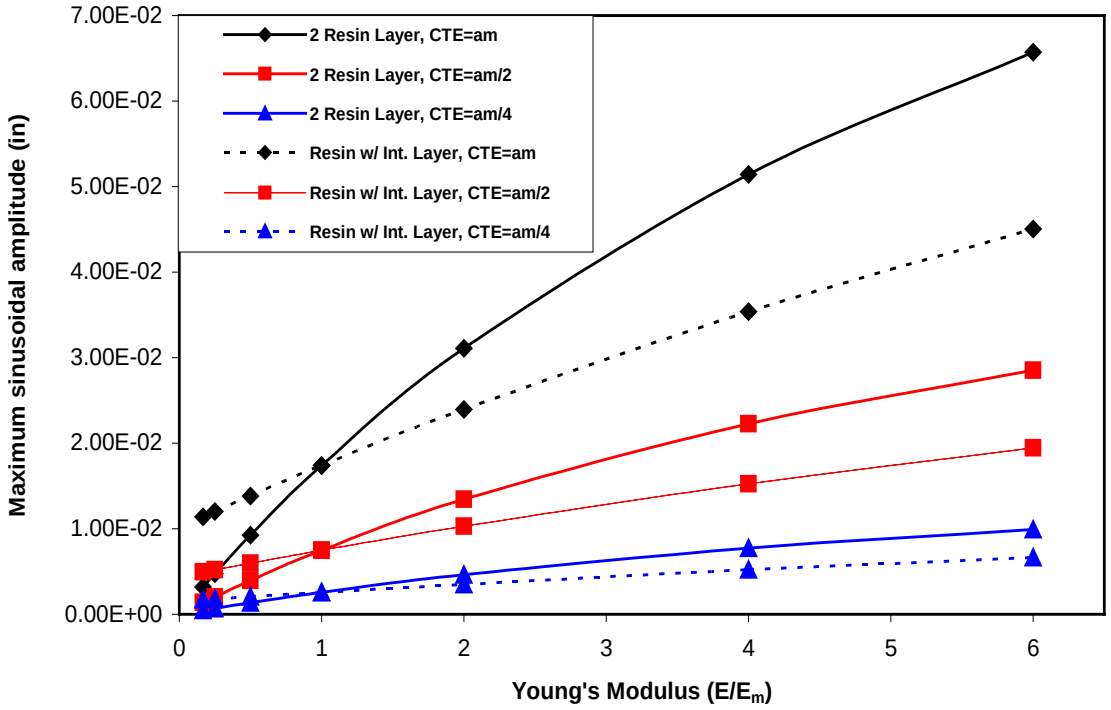

Figure 44: Comparison results between two resin layer and intermediate layer study.

From the numerical results, it is observed that when a quasi-isotropic laminate is placed under hot or cold working environments, the response of the magnitude of surface deformation is greatly influenced by stiffness and CTE in resin system. For the same coefficient of thermal expansion value, the softer surface coating materials helped to reduce the severity of surface waviness. From the results it is observed that the stress concentration at the boundary between composite and resin was relieved utilizing a coating resin with soft mechanical properties with a low thermal coefficient expansion. Thus, to alleviate surface undulations the CTE in resin system has to be as low as

possible. For complete mitigation of fiber print through, even softer coating material for resin with very low coefficient of thermal expansion are required. A very low CTE characteristic in the resin system can be achieved by utilizing carbon nano-tube, however, at the same time the use of the carbon nano-tube also will increase the Young's modulus in the resin system. There is some merit in deriving this, since CTE appears to be the dominant material property. Again, to relieve sinusoidal amplitude from fiber print-through, the resin coating with a soft material with a low coefficient of thermal expansion helps in reducing sinusoidal undulation on composite mirror. Thus, development of a resin such that has very low mechanical properties (soft) with very low CTE will be required to mitigate fiber print through problem and to get dimensional stability of composite mirror.

5.4.5. Surface Layer Conclusion

In general, it is well known that the dominating cause of sinusoidal surface undulation is from fiber print-through, and the fiber print-through is considered an important factor hindering fabricating precision mirrors (< λ/20). To alleviate such surface roughness, it is believed that additional resin layers should be applied on the surface of composite mirror, and that the thickness of resin must be thick enough to achieve the desired surface roughness requirement for diffraction limited mirror (< λ/20). However, this mitigation technique of utilizing additional resin layers will create more severe surface deformations than fiber print-through when the composite mirror is subjected to cold or/and hot environments, even with relatively modest thermal fluctuations which might be expected in practice. As such, composite mirrors with conventional surface resin layers will require appropriate environmental controls (Temperature and likely humidity, as moisture fluctuations will be compatible to those addressed here for thermal). If higher order surface roughness due to fiber print-through during composite mirror fabrication process is inevitable and it hinders precision optical performance, and if additional resin layers need to be added to the surface of composite mirrors, the resin system for buffer layer has to be as soft as possible as well as the coefficient of thermal expansion of the resin system must be as low as possible for reduction of high frequency surface qualities from fiber print-through.

6. Experimental Validation on Surface Deformation Due to Thermally-Induced Load of π/4 Quasi-Isotropic Composite Mirror

In the previous chapter 5, numerical simulations were performed to identify surface deformations in π/n quasi-isotropic composite mirrors experiencing thermally-induced load. In this chapter, experimental results on surface deformation in π/4 quasi-isotropic composite mirror will be addressed to validate the numerical results by using a commercial surface deformation measurement device called Optino (Shack-Hartmann Wave-front Sensor), Bennett Optical Research's experimental data on 6" composite mirror, and independent repetitions of Bennett's approach at KU.

6.1. Experimental Set-up with Optino

The experimental set-up with Optino was first employed to evaluate surface deformation patterns and statistical measure of the magnitude of a varying quantity of surface deformation on π/4 quasi-isotropic composite mirror.

6.1.1. Testing Equipment Components

The purpose of this section is to document the equipment used in the experimental testing of surface deformation measurement of the composite mirror.

1. Wavefront sensor:

► Aperture (8 mm).

► Focal ratios covered (f/0.5~f/300 standard).

► Diameter of lenslets (d=0.2mm, fl=11mm or could be any size).

► Standard sampling of 30 X 30 spots.

► Repeatability of measurement, <λ/300 rms

► Rms repeatability of wavefront measurement, <λ/200 rms

► Absolute precision, typically λ/10 (for spherical surfaces), λ/40 (flat surfaces)

► Wavelength range, 325-1100 nm with cooled camera

► Tilt measurement accuracy, 4μ rad

2. CCD: cooled CCD from SBIG, model 9XE. It has 512 x 512 pixels, each of 20μ, and has a USB2 connection.
3. Reference Mirror, surface accuracy λ/10
4. Mounting for flat mirror.
5. Light source with optical fiber
6. collimator for testing 8" flat mirror, focal length of 75mm, aperture of 7.5mm
7. Beam expander: BE200, aperture of 203mm, focal length of 2032mm
8. Test mirror: 8 layer with stacking sequence of $[45, 0, -45, 90]_s$ of π/4 quasi-isotropic mirror blank with additional resin rich layer (10/1000 inch) to mitigate fiber print-through
9. Mounting for test mirror.
10. Heat gun. (for applying heat on the composite mirror)
11. Infrared thermometer.

6.1.2. Schematic Diagram for Experimental Set-up

The following Figure 45 indicates schematic diagram of experimental set-up

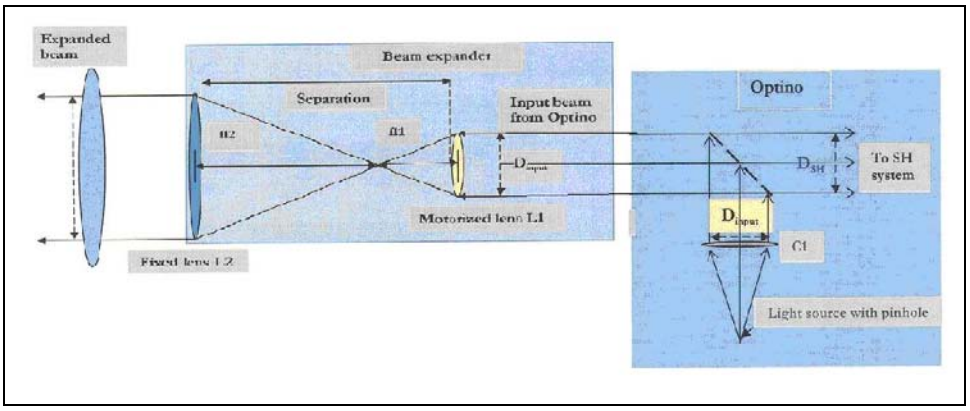

Figure 45: Optino (SH Test) configuration for 8" flat mirror

6.1.3. Configuration and Details of Experimental Set-up

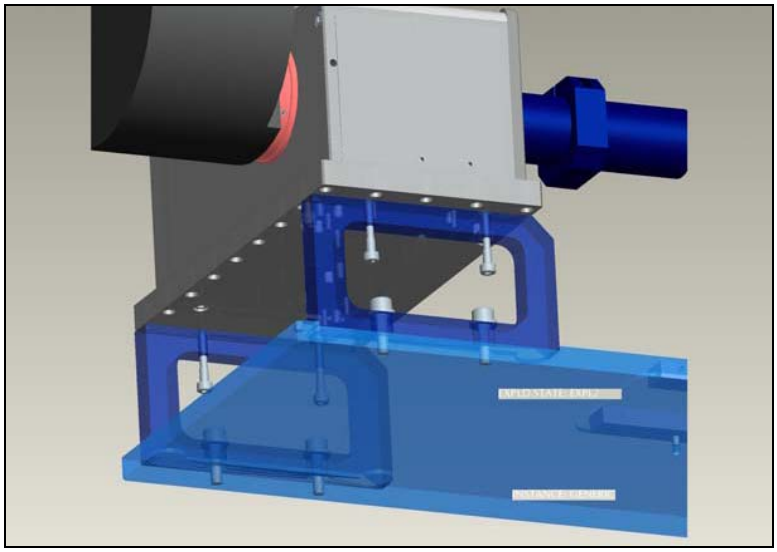

Figure 46: Step 1-Remove Optino and mount it on the spacers to raise its height using 4 M3x30 screws

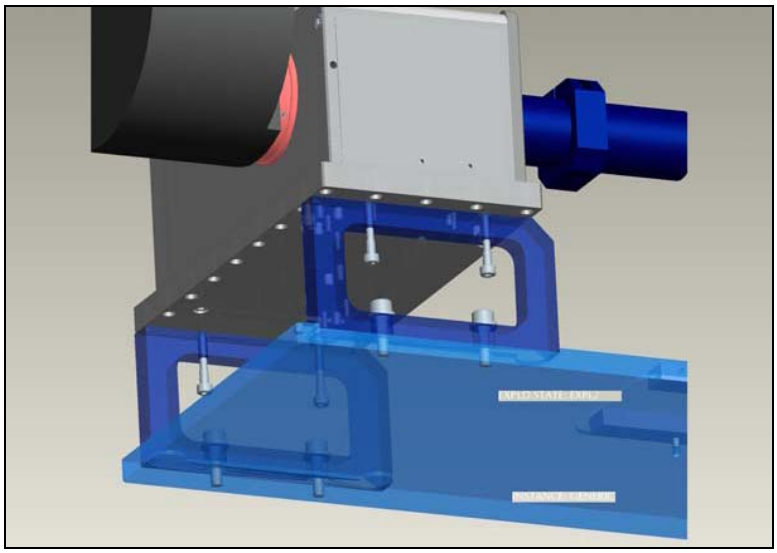

Figure 47: Step 2-Mount Optino and the spacers on the base plate

Setting up Optino for testing flat mirror

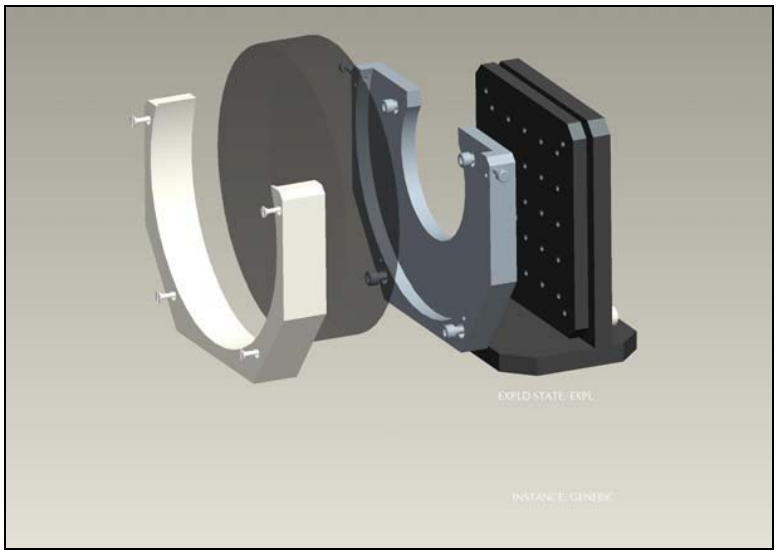

Figure 48: Step 3-Mount the 203 reference flat mirror in its mounting

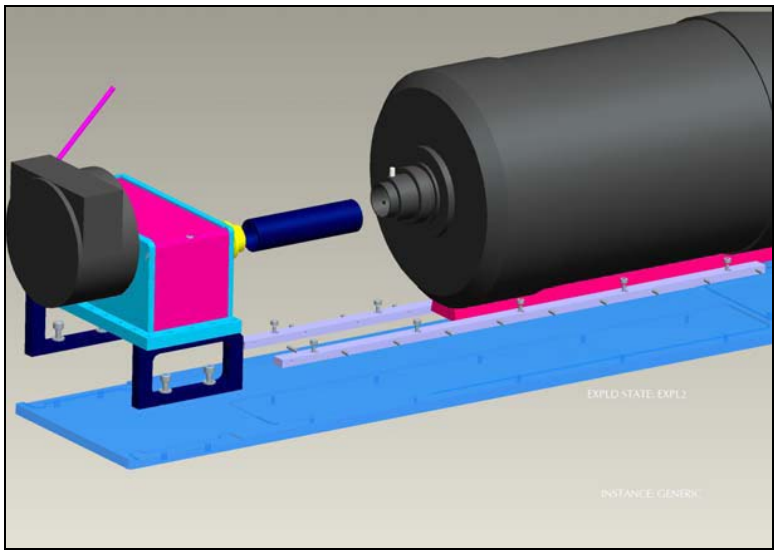

Figure 49: Step 4-Mount the collimator (fl=75mm) on Optino (yellow above). Then screw on the plastic tube onto the collimator. Insert the other end of the tube into the eyepiece end of BE200 and slide it till it reaches the stop shown in Step 1.

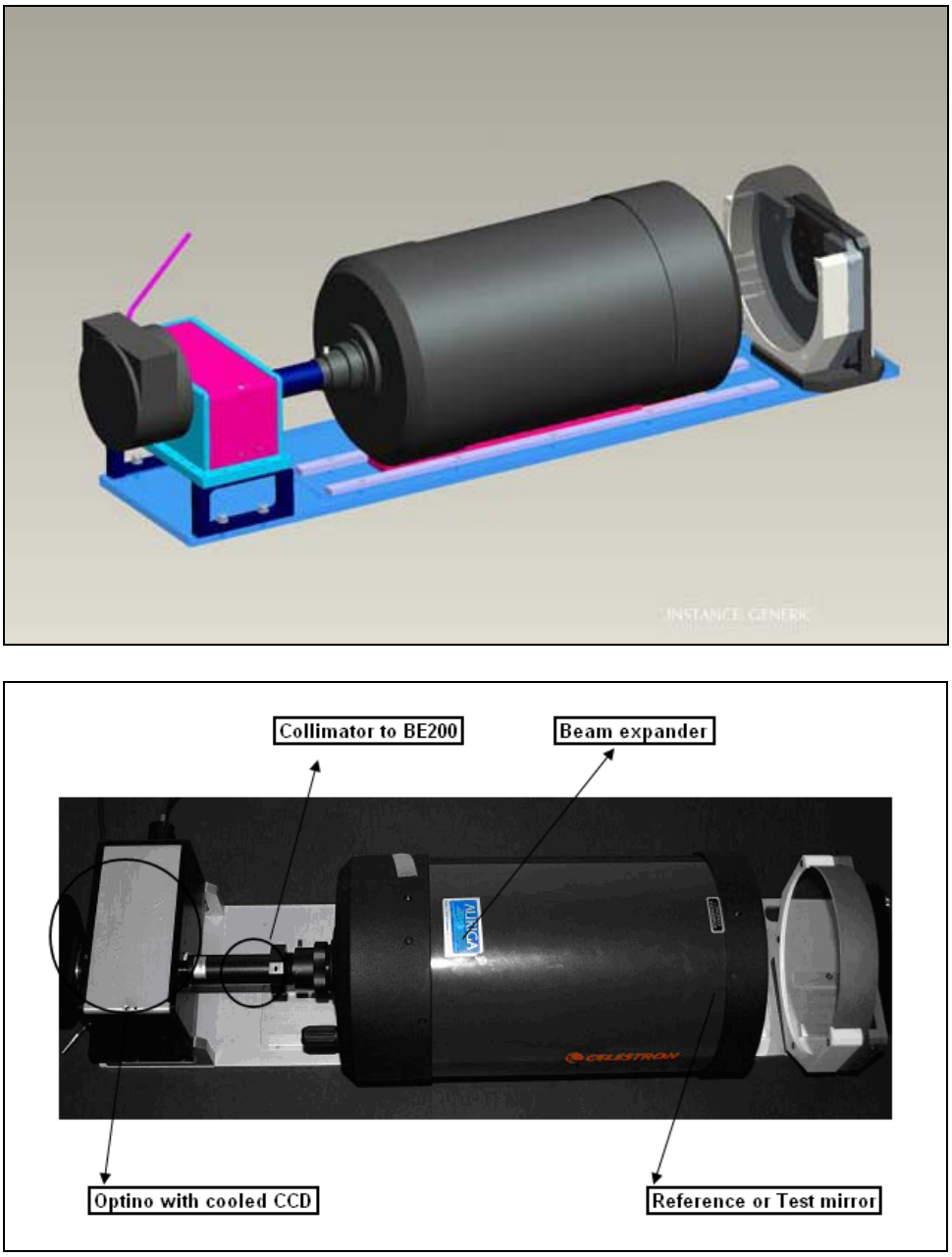

Figure 50: Final system picture of experimental set-up

6.1.4. Experimental Procedure

The purpose of this section is to introduce the reader to the method used for SH image testing of composite mirror.

1. Aligning Optino and BE200 using the projection of an image on a wall.
2. Mount reference mirror and align it to the SH camera using the return image.
3. Take reference image. Note: if any ghost images present, repeat 1 and 2.

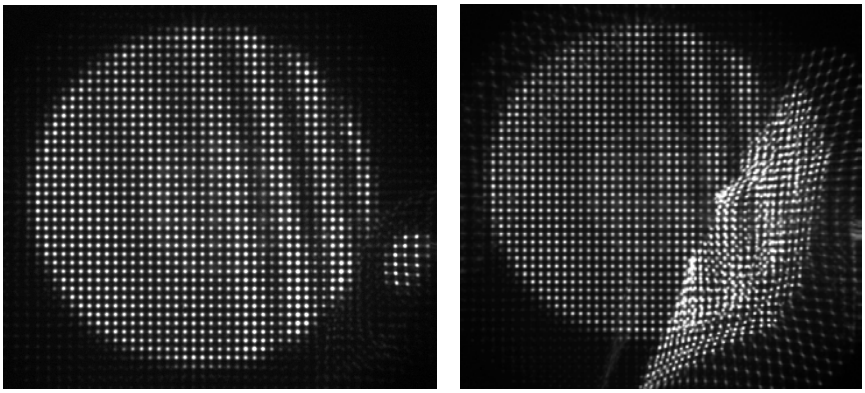

Figure 51: Possible ghost images from light dissipation and misalignments.

4. Replace reference mirror with test mirror.
5. Align the SH image from optical system being tested with respect to the reference image taken in 3.

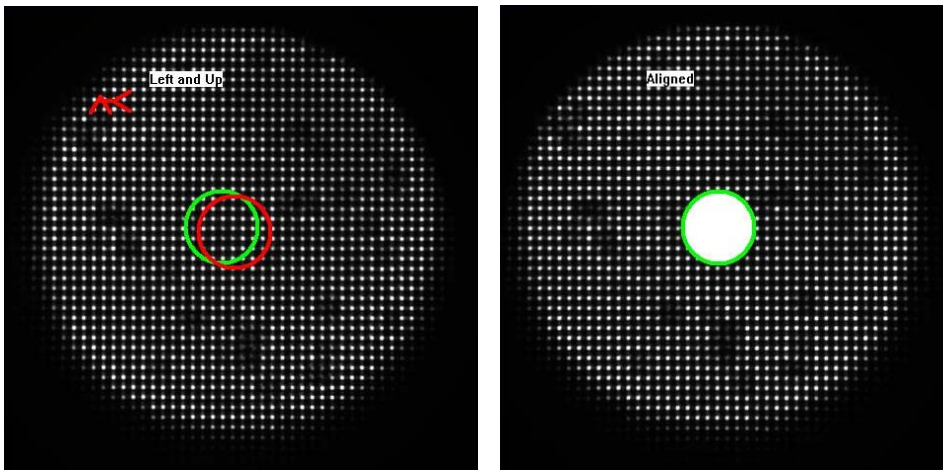

Figure 52: Image of misalignment (left) and aligned image (right)

6. Collimate the light from the optical system being tested.
7. Recheck the alignment
8. Do a test analysis

6.1.5. Experimental Results of Surface Deformation in a Quasi-Isotropic π/4 8” Mirror Using Shack-Hartmann Images from Optino (Wave-front Sensor)

This section comprises the details of experimental methodology to measure surface deformation due to a constant thermal variance ($\Delta T=30^{\circ}$ F) on 8” in diameter π/4 quasi-isotropic laminated mirror. The Shack-Hartmann wave-front sensor (Optino) was intended to capture surface size of 8 mm in diameter, but an additional beam expander (8”) with collimator was used to be able to evaluate the whole 8” surface deformations in the composite mirror. Due to relatively low optical quality of our test mirror, to include low reflectivity, the mirror was coated for better reflectivity as shown in Figure 53.

For details of experimental procedures, the test mirror, which contains 8 layer π/4 lay-up with additional resin layer and thin coating of aluminum, was heated until an elevated temperature of 100̊ Fahrenheit from reference temperature (72° F) to measure thermally induced surface deformation. For external heat source to the test specimen, a heat gun was used for applying desired thermal load. To reach and maintain the desired temperature in the test specimen, the test mirror was overheated beyond the target elevated temperature and was set freely cooling down to reach the desired temperature of 100° F. To detect the temperature of the specimen, an infrared thermometer was used to measure the distributed temperature in the composite mirror. The following Figure 54

shows the experimental set-up on 8” test mirror using a collimator and beam expander in Optino system.

Figure 53: Composite mirror (8 inch π/4 lay-up sequence with resin layers and aluminum coating)

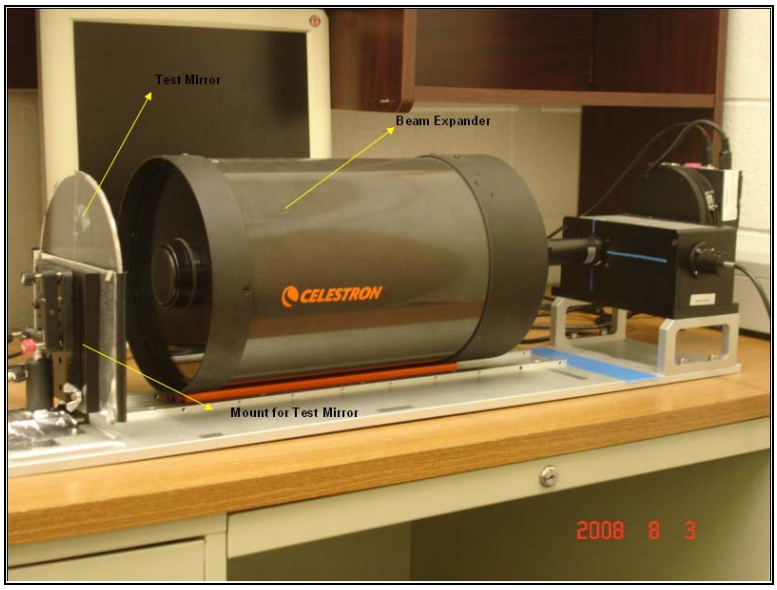

Figure 54: Details of test set-up with a collimator and beam expander

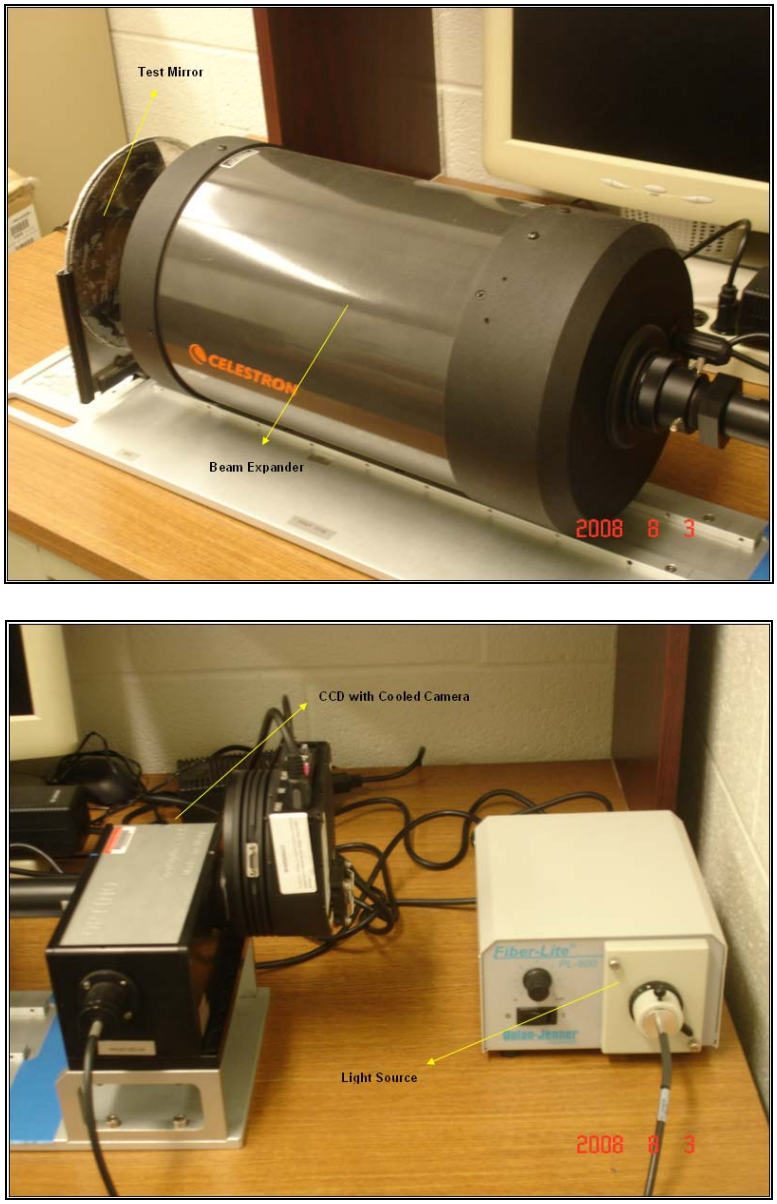

Figure 54 (Cont.): Details of test set-up with a collimator and beam expander

6.1.6. Shack-Hartmann Image Results

The surface deformations in the test mirror were evaluated using the Optino and the results were compared with numerical simulations and predictions from MSC. Nastran/Patran. The mirror model used in both experimental and numerical study is a case of 8 layer with stacking sequence of [45, 0, -45, 90]s of π/4 quasi-isotropic laminate blank with 10 mil of additional resin rich layer on the top of the mirror blank. The composite material used in this study was a unidirectional lamina of AS4/3501-6 composite material.

The Figures 55~60 presented Shack-Hartmann (SH) images of 3D actual quality (AQ) surface and 2D AQ contour from Optino at reference temperature (72 F) and an elevated temperature (100 F). The numerical predicted values were twice larger than the magnitude in surface deformations found in experimental result. This might be derived from optical set-up and testing. For instance, optical system is highly sensitive, thus any unpredictable small changes in experimental set up could give difference results. In this experiment, the possible error sources might be from failing to adequately control heat distribution (difference temperature gradient in the composite mirror) and might be from failing to maintain the constant desired temperature (the specimen could be heated more or less than the desired temperature). These types of errors should be corrected in any subsequent experiment on higher quality mirror samples.

The experimental results tabulated in Table 17 demonstrate that the improved surface finish in the test mirror by applying additional resin layer for mitigation of fiber print-through was not thermally stable for diffraction-limited requirement for precision optics when thermal load is present in the test mirror. In fact, it was observed that surface

accuracy has been rapidly decreased with the thermal load. The surface quality observed at room temperature is highly anisotropic, and the cause of saddle images of surface deformations at temperature of 100˚ F shown in Figures 55~60 indicated the response of surface deformations due to thermal gradient. The cause of the saddle images were explained due to the radial variation of flexural stiffness in the composite mirror and complexity of coefficient of thermal expansion in both matrix and fiber oriented in the composite as results of stacking sequence effects. The surface images evaluated between reference temperature and an elevated temperature (100˚ F) were subtracted to obtain real surface deformation response of the composite mirror due to stacking sequence effects. Figures 61~65 illustrate the actual deformation response in the mirror due to the constant thermal variance ($\Delta T=30^{\circ}$ F).

Table 17: Experimental results (Peak to Valley) of actual surface quality (nm) at reference temperature (72˚ F) and elevated temperature (100˚ F).

Experimental values of actual surface (nm) at elevated temperature (100 F)

Trial	P-V (nm)	λ/n
1	3855.00	0.16
2	3968.00	0.16
3	4049.00	0.16
4	4137.00	0.15
5	4820.00	0.13
AVE.	4165.80	0.15

Subtracted surface (nm) between reference and elevated temperature (100 F)

Trial	P-V (nm)	λ/n
1	3985.40	0.16
2	3718.20	0.17
3	3868.90	0.16
4	4160.00	0.15
5	4422.00	0.14
AVE.	4030.90	0.16

Table 18: Numerical results (Peak to Valley) of surface deformation (nm) at elevated temperature (100º F).

Axis	d_z (in)	Local Δd_z (nm)
0	2.29E-03	3.24E+03
5	2.16E-03	2.59E+03
10	2.06E-03	2.07E+03
15	1.98E-03	9.14E+02
20	1.94E-03	7.87E+02
25	1.97E-03	2.90E+03
30	2.09E-03	5.28E+03
35	2.30E-03	7.74E+03
40	2.60E-03	1.01E+04
45	3.00E-03	1.23E+04
50	3.49E-03	1.42E+04
55	4.04E-03	1.56E+04
60	4.66E-03	1.64E+04
65	5.30E-03	1.67E+04
70	5.96E-03	1.64E+04
75	6.60E-03	1.54E+04
80	7.21E-03	1.39E+04
85	7.76E-03	1.18E+04
90	8.23E-03	9.31E+03
95	8.59E-03	6.38E+03
100	8.84E-03	3.13E+03
105	8.97E-03	3.22E+02
110	8.95E-03	3.87E+03
115	8.80E-03	7.38E+03
120	8.51E-03	1.07E+04
125	8.09E-03	7.68E+03
130	7.79E-03	2.27E+04
135	6.89E-03	1.88E+04
140	6.15E-03	1.44E+04
145	5.58E-03	2.15E+04
150	4.74E-03	2.17E+04
155	3.88E-03	2.67E+04
160	2.83E-03	1.32E+04
165	2.31E-03	1.61E+04
170	1.68E-03	1.79E+04
175	9.71E-04	3.35E+04

Average (nm)
1.18E+04

3D actual surface quality (AQ) and 2D AQ contour images at reference temperature (72º F).

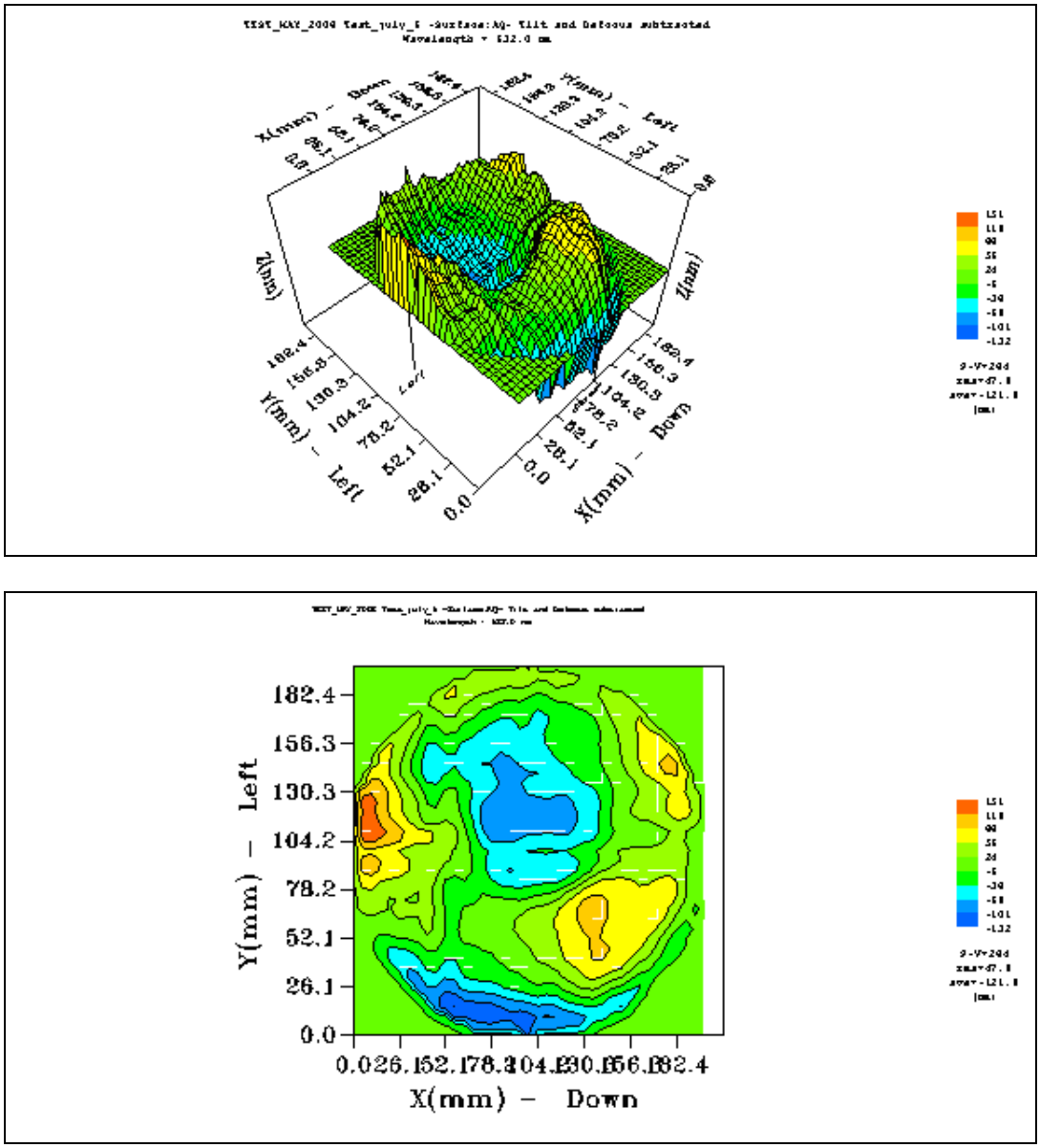

Figure 55: 3D AQ (actual quality) and 2D AQ contour images at reference temperature (72˚ F) from Optino

3D actual surface quality (AQ) and 2D AQ contour images at elevated temperature (100º F).

Surface image at 100 F (Trial 1)

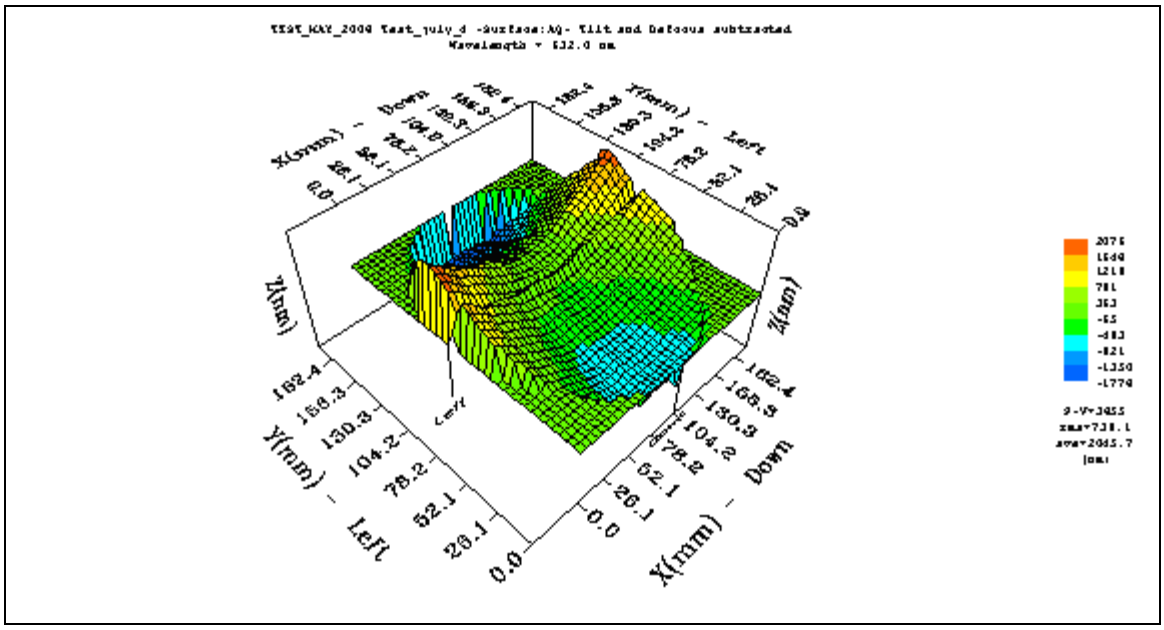

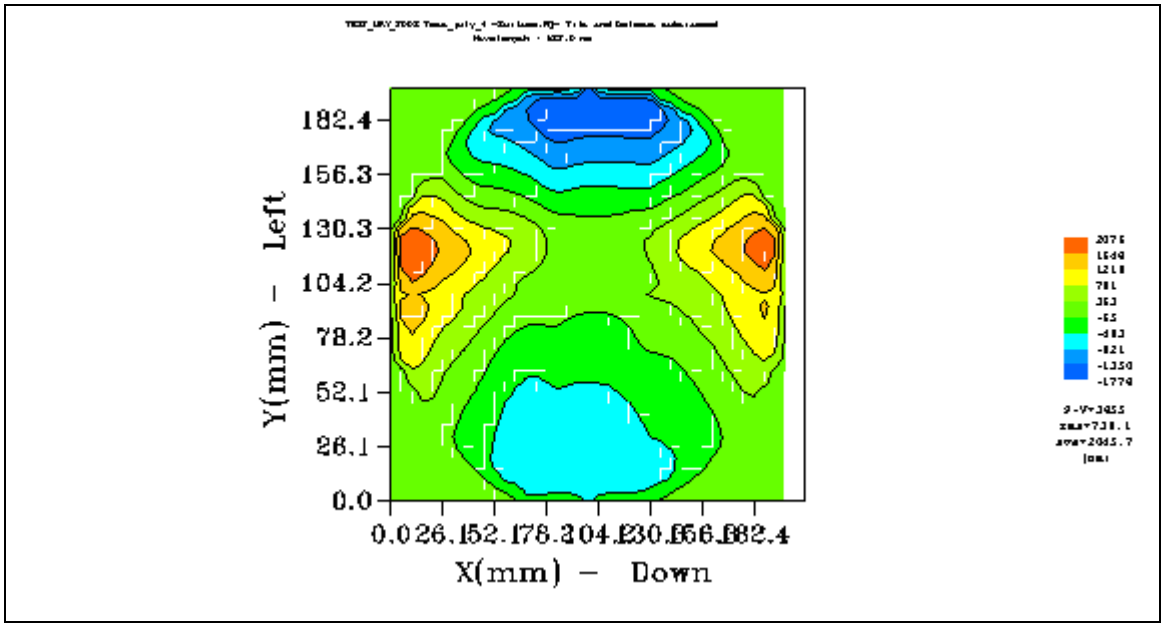

Figure 56: 3D AQ (actual quality) and 2D AQ contour images at elevated temperature (100˚ F) from Optino, Trial 1

Surface image at 100º F (Trial 2)

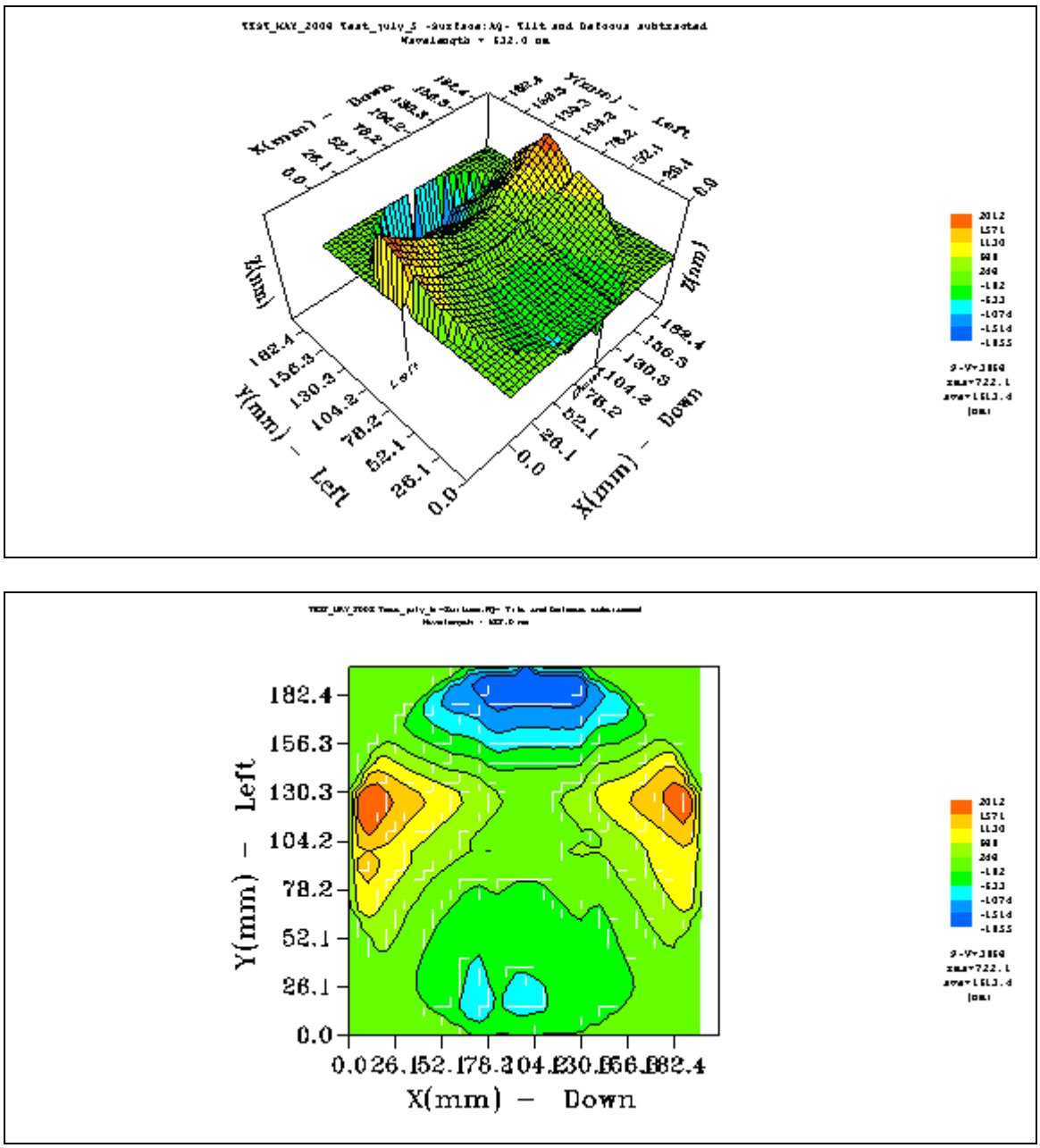

Figure 57: 3D AQ (actual quality) and 2D AQ contour images at elevated temperature (100˚ F) from Optino, Trial 2

Surface image at 100º F (Trial 3)

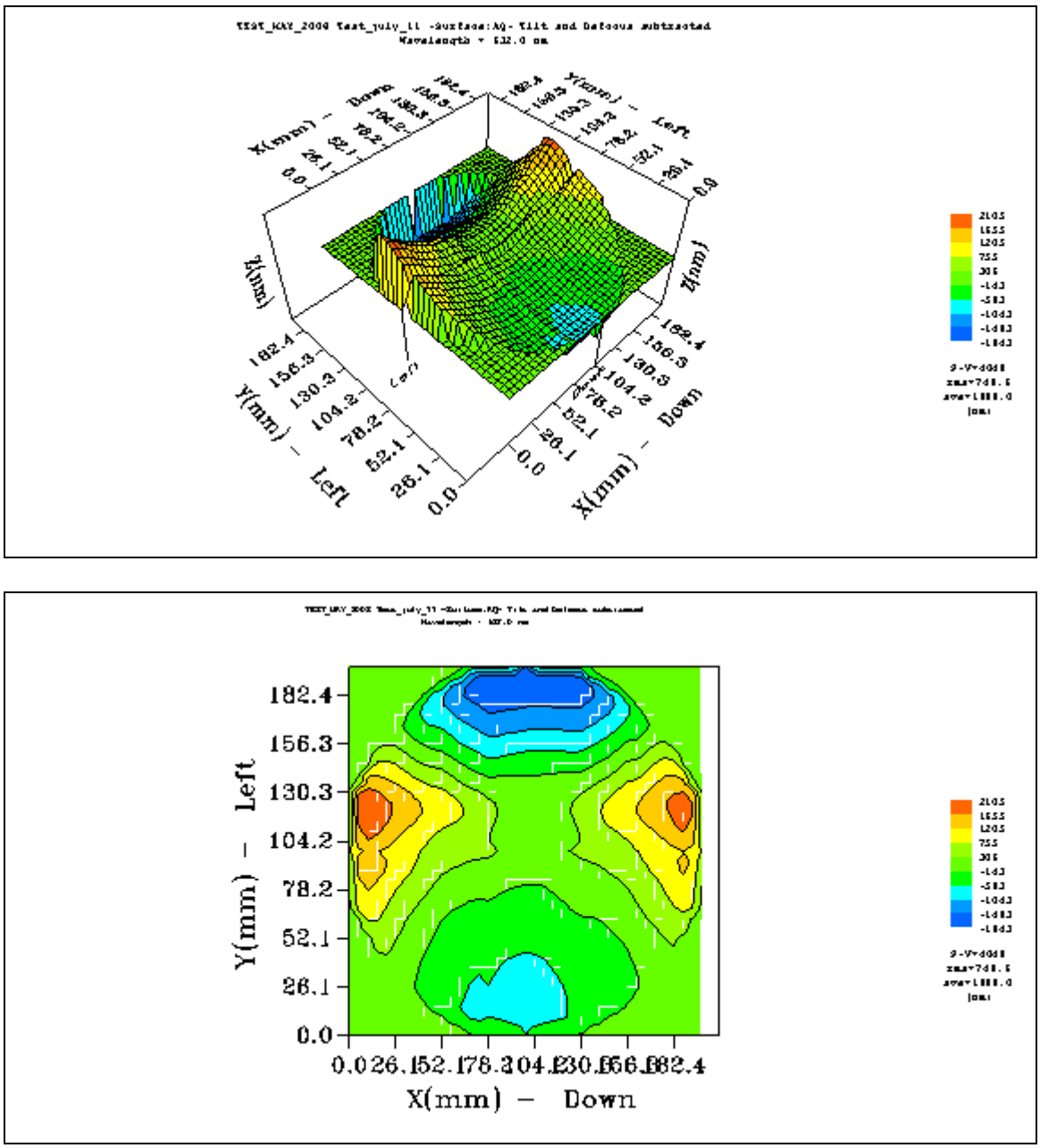

Figure 58: 3D AQ (actual quality) and 2D AQ contour images at elevated temperature (100˚ F) from Optino, Trial 3

Surface image at 100º F (Trial 4)

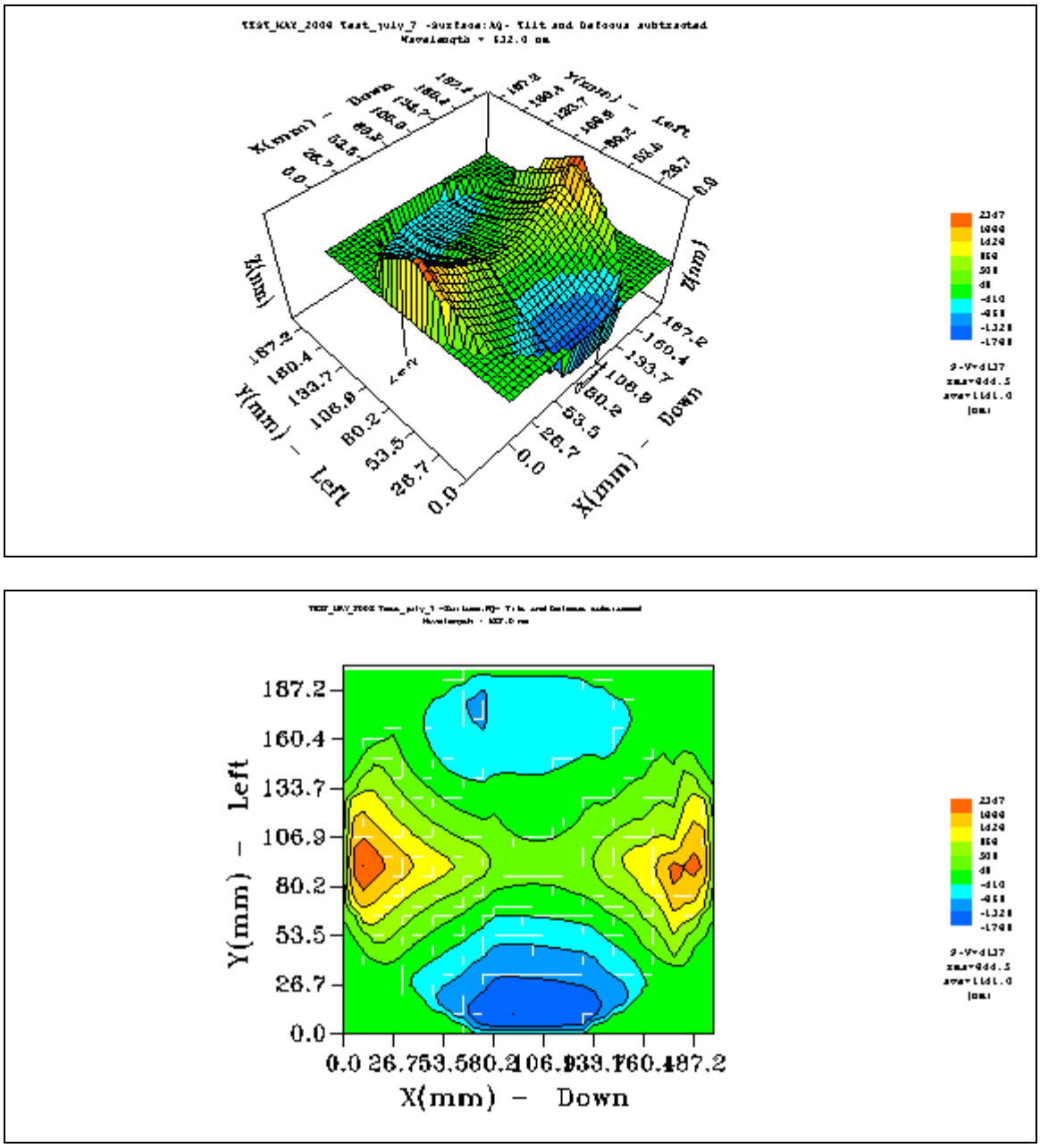

Figure 59: 3D AQ (actual quality) and 2D AQ contour images at elevated temperature (100˚ F) from Optino, Trial 4

Surface image at 100º F (Trial 5)

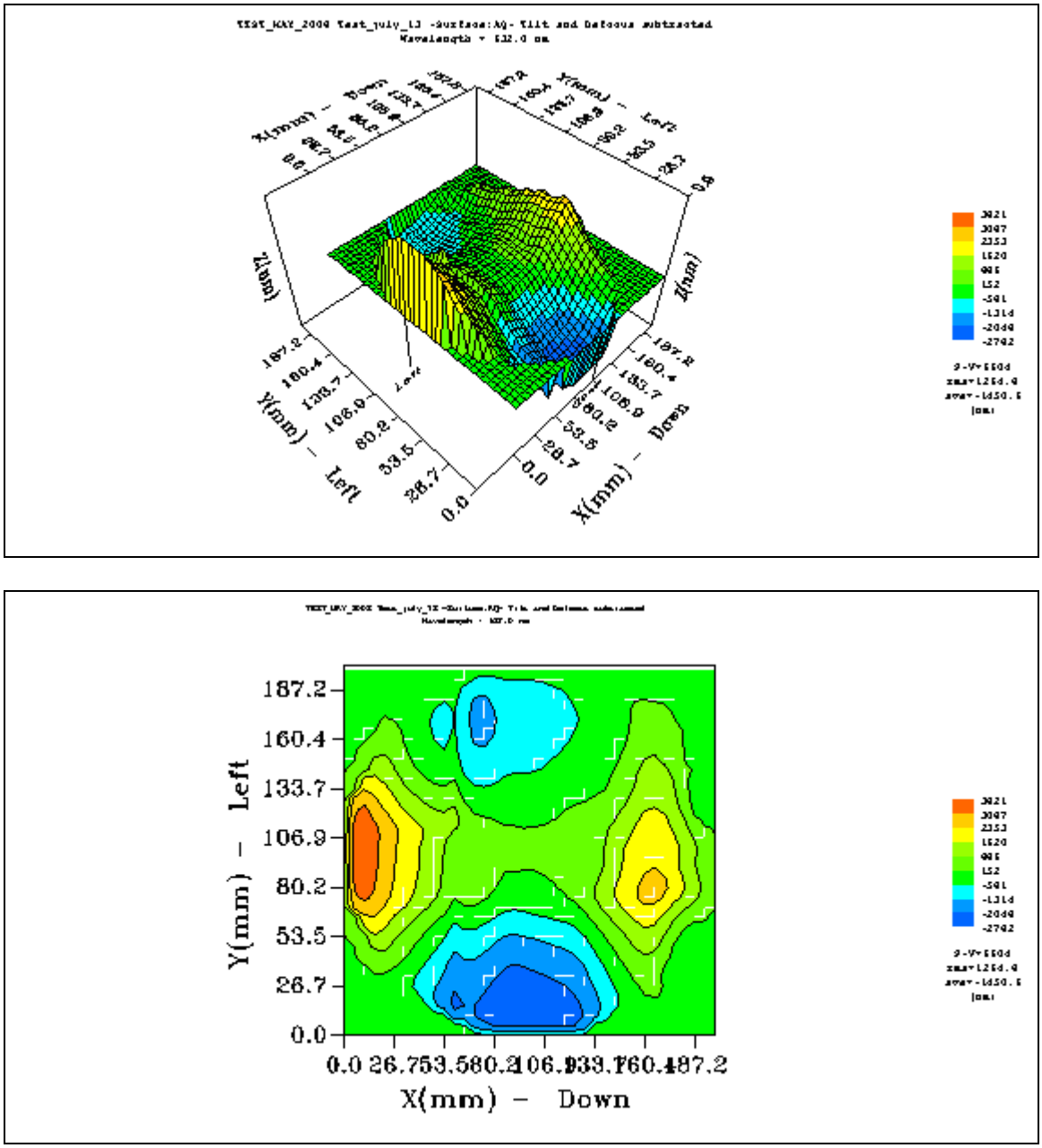

Figure 60: 3D AQ (actual quality) and 2D AQ contour images at elevated temperature (100˚ F) from Optino, Trial 5

Actual response of surface deformation images in π/4 composite mirror evaluated from subtraction between reference temperature surface image and elevated temperature (100º F) surface images.

Subtraction image 1

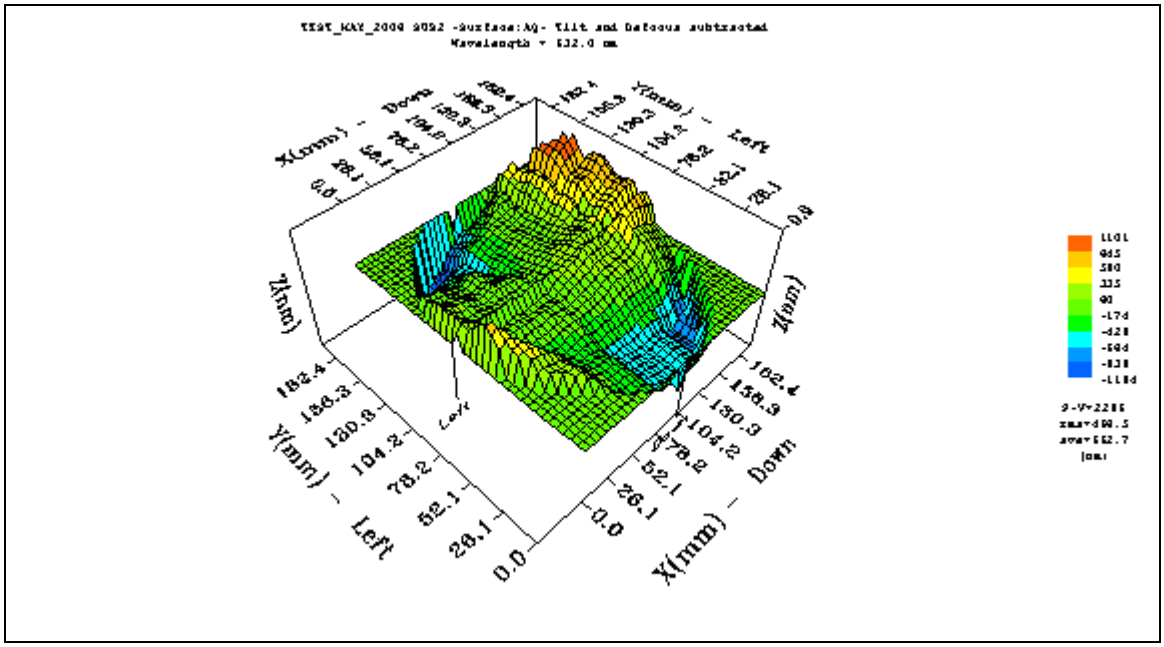

Figure 61: 3D AQ (actual quality) and 2D AQ contour images at elevated temperature (100˚ F) from Optino, Trial 1

Subtraction image 2

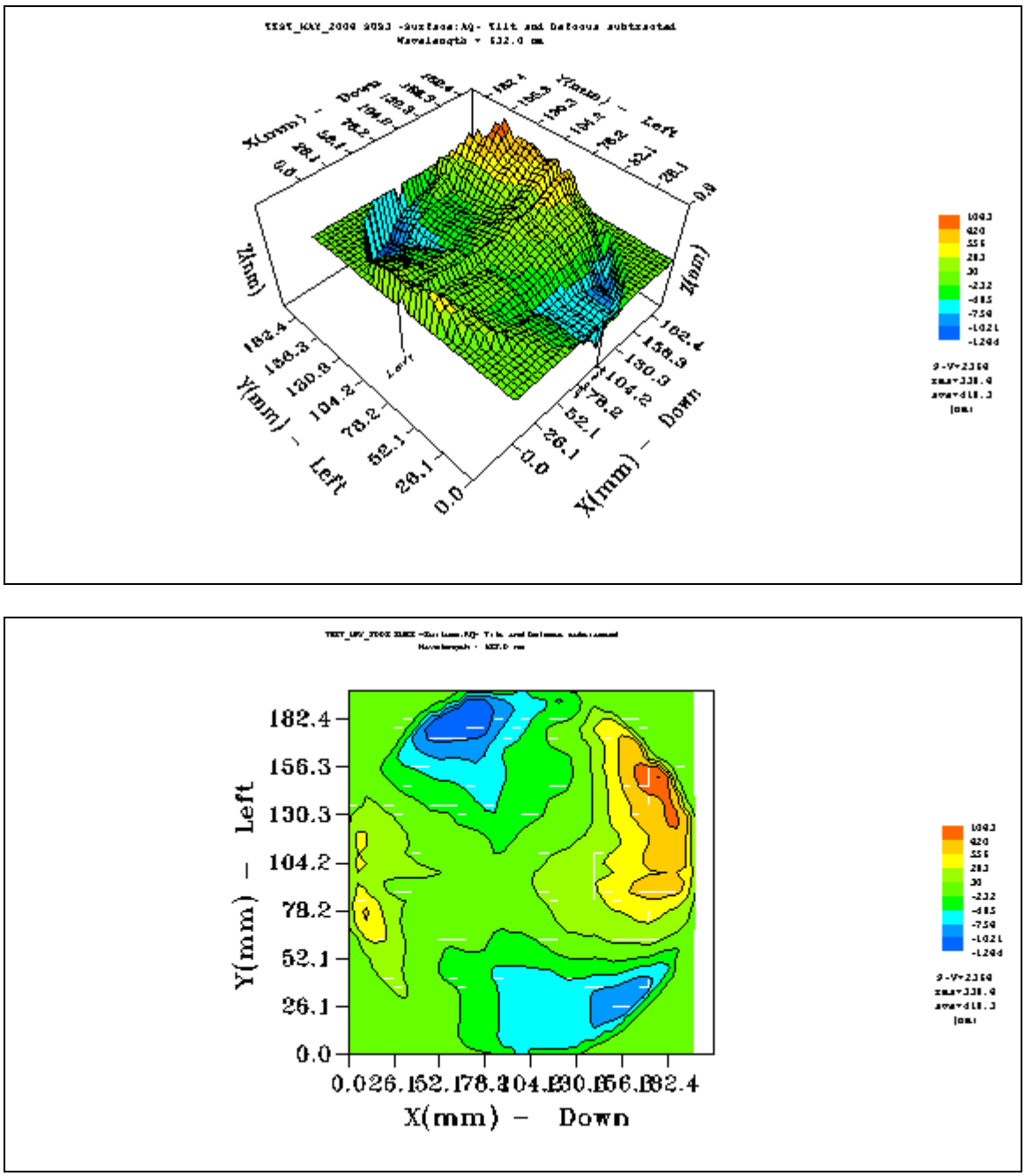

Figure 62: 3D AQ (actual quality) and 2D AQ contour images at elevated temperature (100˚ F) from Optino, Trial 2

Subtraction image 3

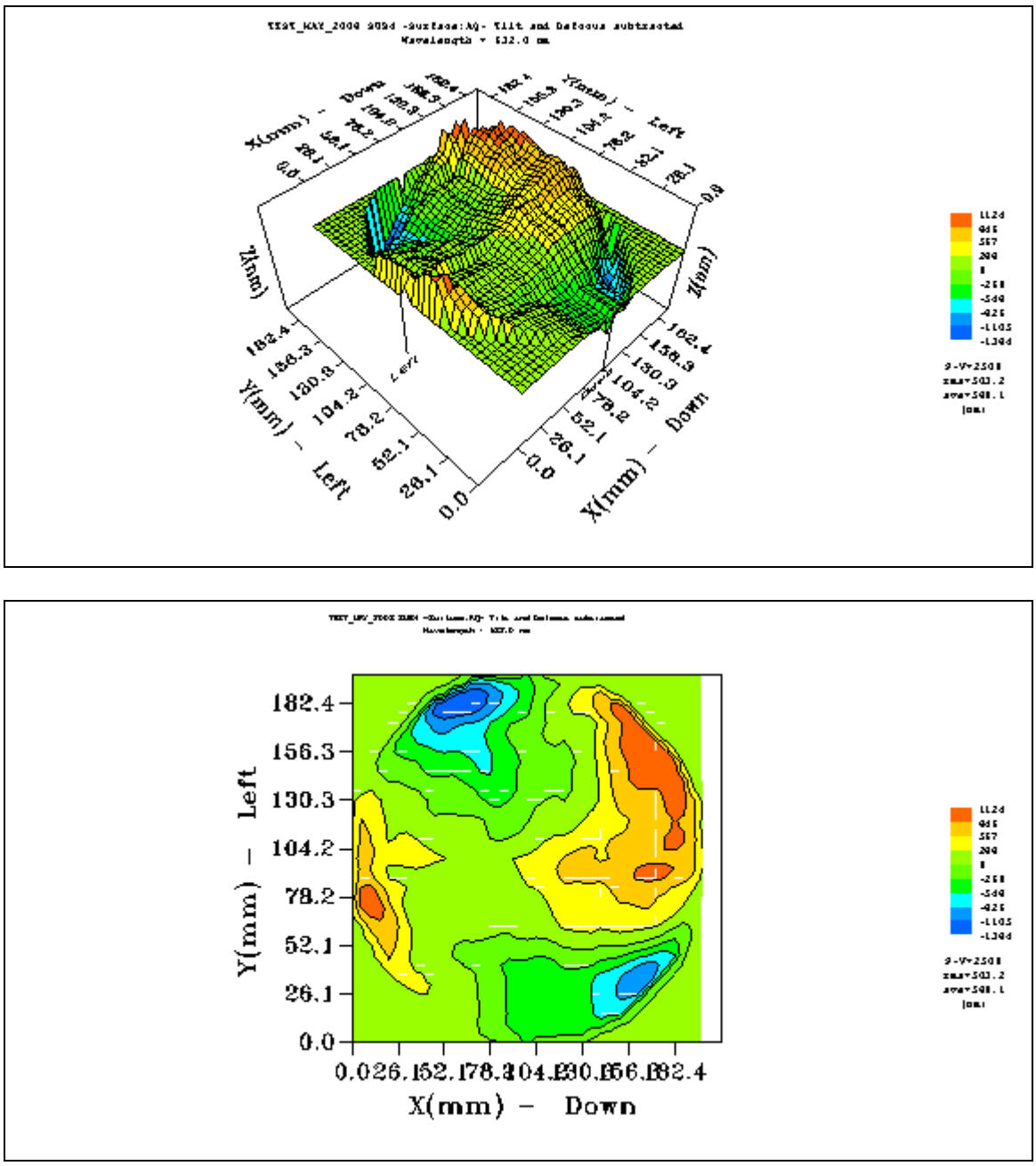

Figure 63: 3D AQ (actual quality) and 2D AQ contour images at elevated temperature (100˚ F) from Optino, Trial 3

Subtraction image 4

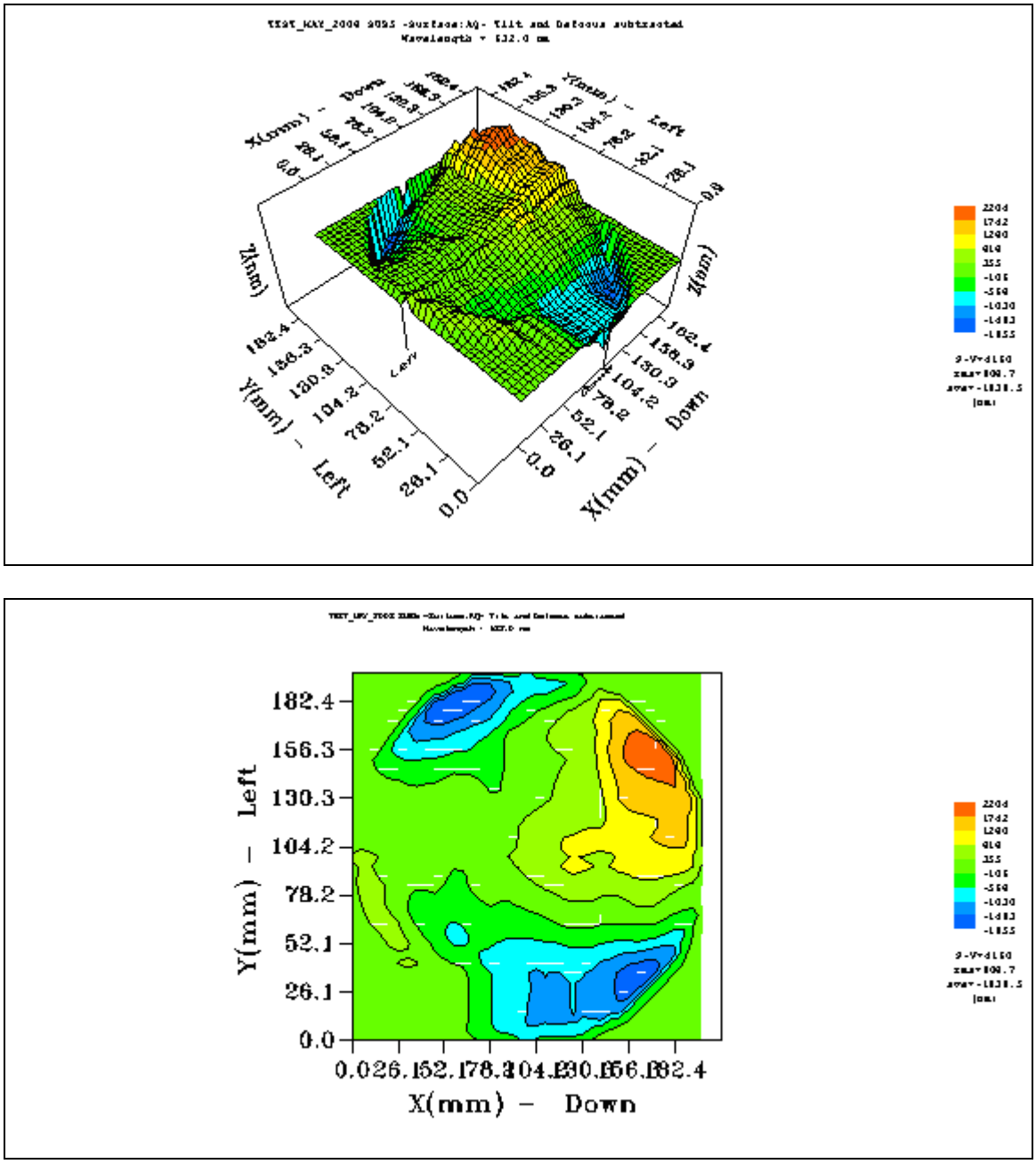

Figure 64: 3D AQ (actual quality) and 2D AQ contour images at elevated temperature (100˚ F) from Optino, Trial 4

Subtraction image 5

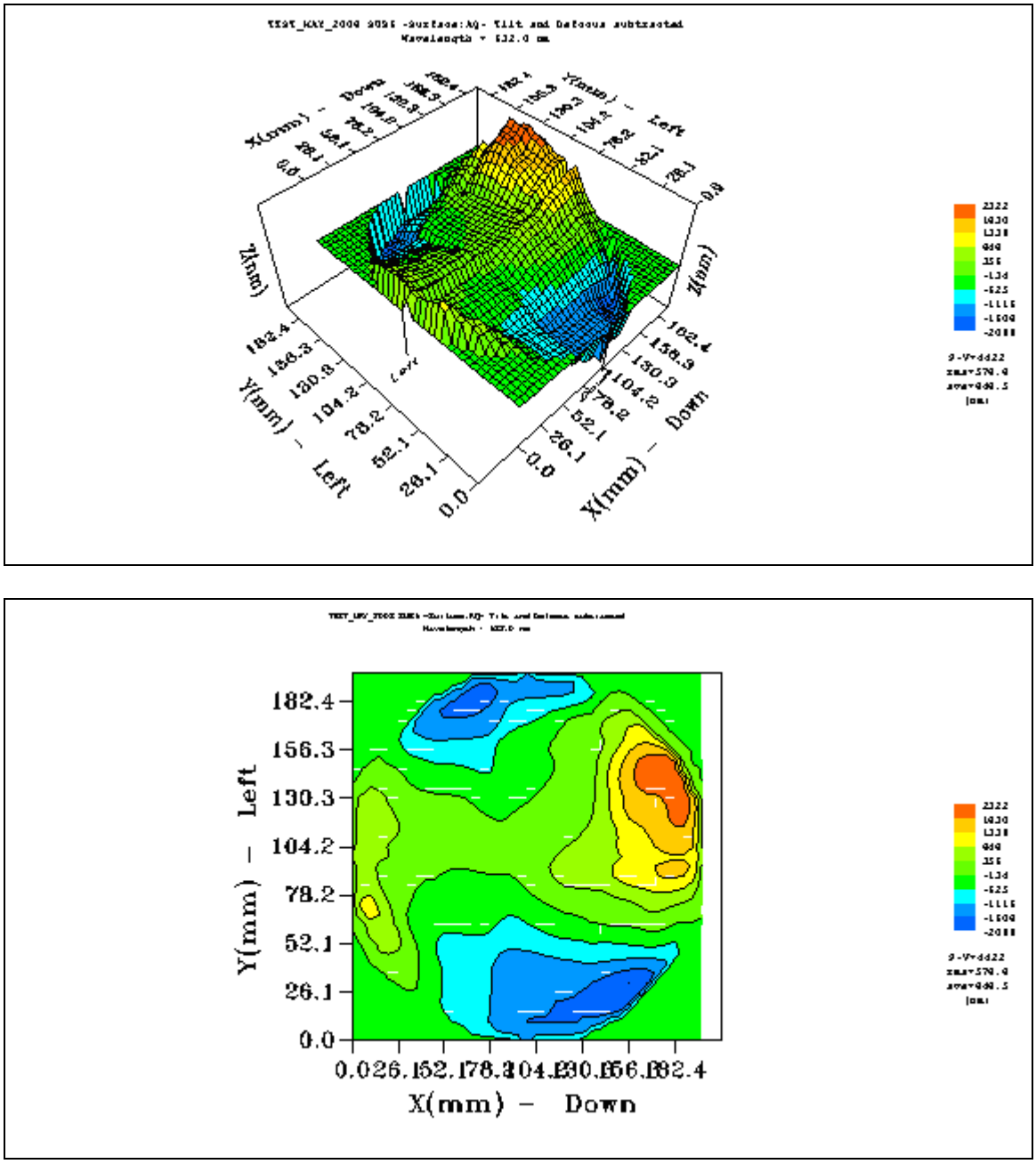

Figure 65: 3D AQ (actual quality) and 2D AQ contour images at elevated temperature (100˚ F) from Optino, Trial 5

The actual global surface deformation patterns due to the thermal variance shown in above Figures 61~65 indicate that the cause of surface pattern is due to differences in flexural stiffness in the mirror due to stacking sequence. The surface is highly distorted and start to move up until 35~40 degree axis from 0 degree axis and the surface deformation patterns move down until 105~110 degree axis. This could be explained that the radial flexural stiffness is varied with the radial direction in the composite. The radial variations of flexural stiffness in quasi-isotropic laminated mirrors were discussed in previous chapter 3. The following Figure 66 illustrates radial variations of flexural stiffness in $\pi/4$ laminate.

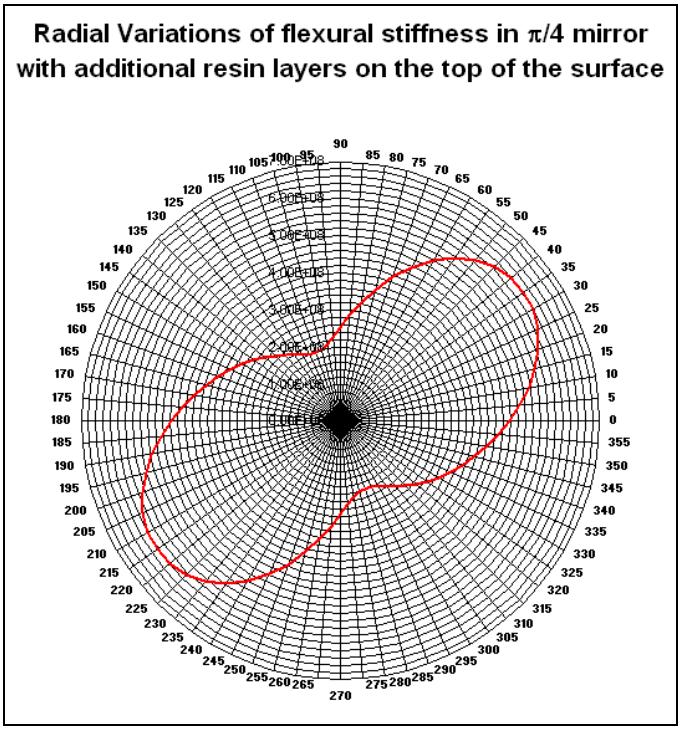

Figure 66: Analytical result for radial variations of flexural stiffness in $\pi/4$ mirror with additional resin layers

6.1.7. Numerical model of π/4 composite mirror

The following section will show that the images from experiment were compared with a numerical simulation created using Nastran/Patran program as shown in Figure 67. The numerical methodology used in this model is identical to described in Chapter 4, but half of entire mirror geometry was considered as numerical model to see the global surface response of the π/4 mirror due to the thermal variance. In this model 324 sub-group were created as representing half of a circular mirror. Each group was assigned unique material property based on stacking sequence. The model contains 498,883 nodes and 466,560 CHEXA elements representing 1,495,432 degrees of freedom. The following Figure 67 shows the details of numerical discretization.

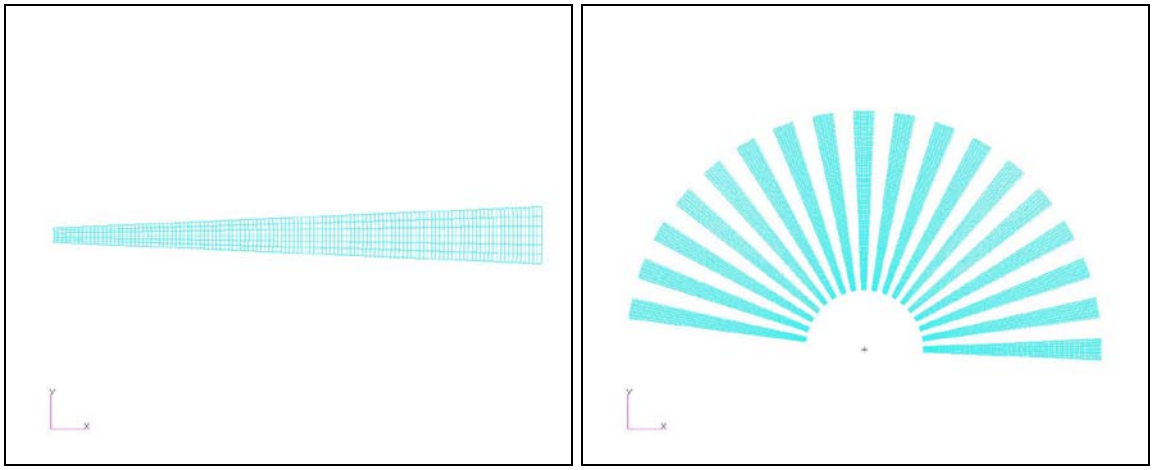

a) 1st layer of 0 degree group

b) 1st layer of 0~ 175 degree groups (shown in even degree axis groups)

Figure 67: Numerical discretization for half of 8" π/4 composite mirror

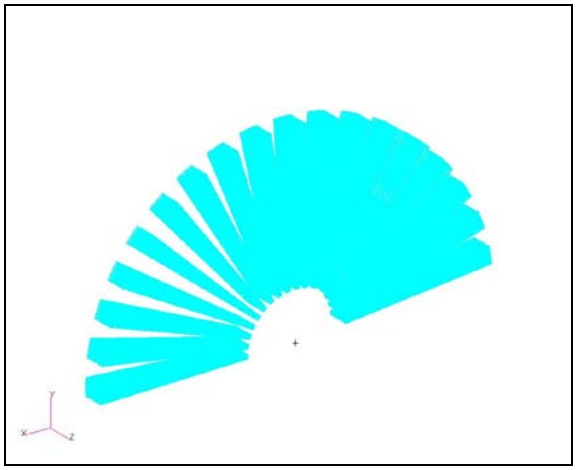

c) 1st ~9th layer of 0~175 degree groups (shown in odd layers in each group)

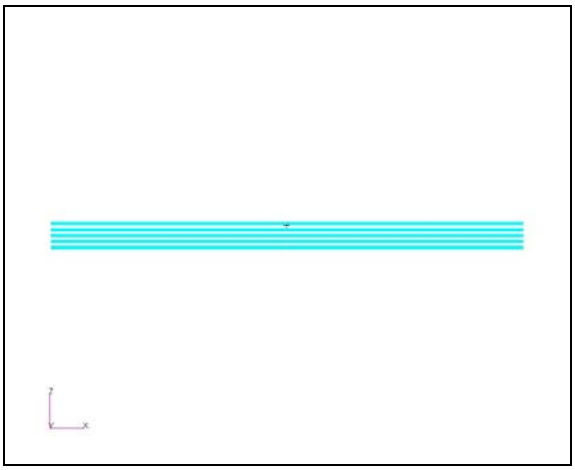

d) 1st ~9th layer from image of c) (shown in odd layers)

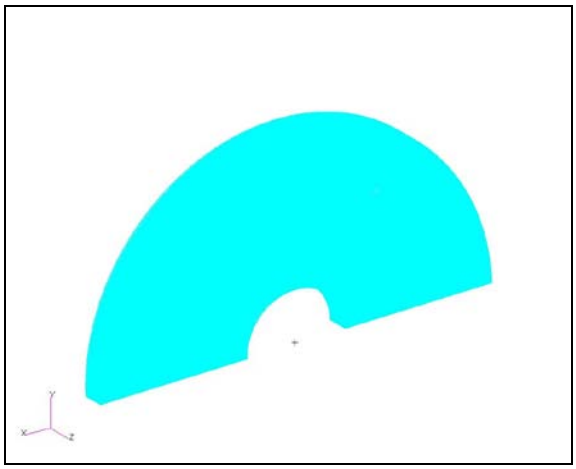

e) Iso-axis view for entire domain

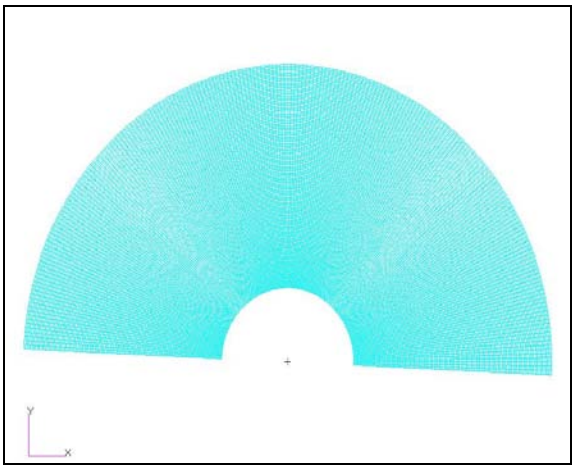

f) Front view for entire domain

Figure 67 (Cont.): Numerical discretization for half of 8" π/4 composite mirror

The numerical results from MSC.Nastran/Patran agree well with the surface deformation results from SH images from Optino. The surface deformation images from experimental test could not display the local surface deformations discussed in Chapter 5. This is because the system ability is limited to capture global response of surface deformation (i.e. the large amplitude global response masks the lower amplitude local response). Figure 68 below show the surface deformation results from numerical simulations and experiment.

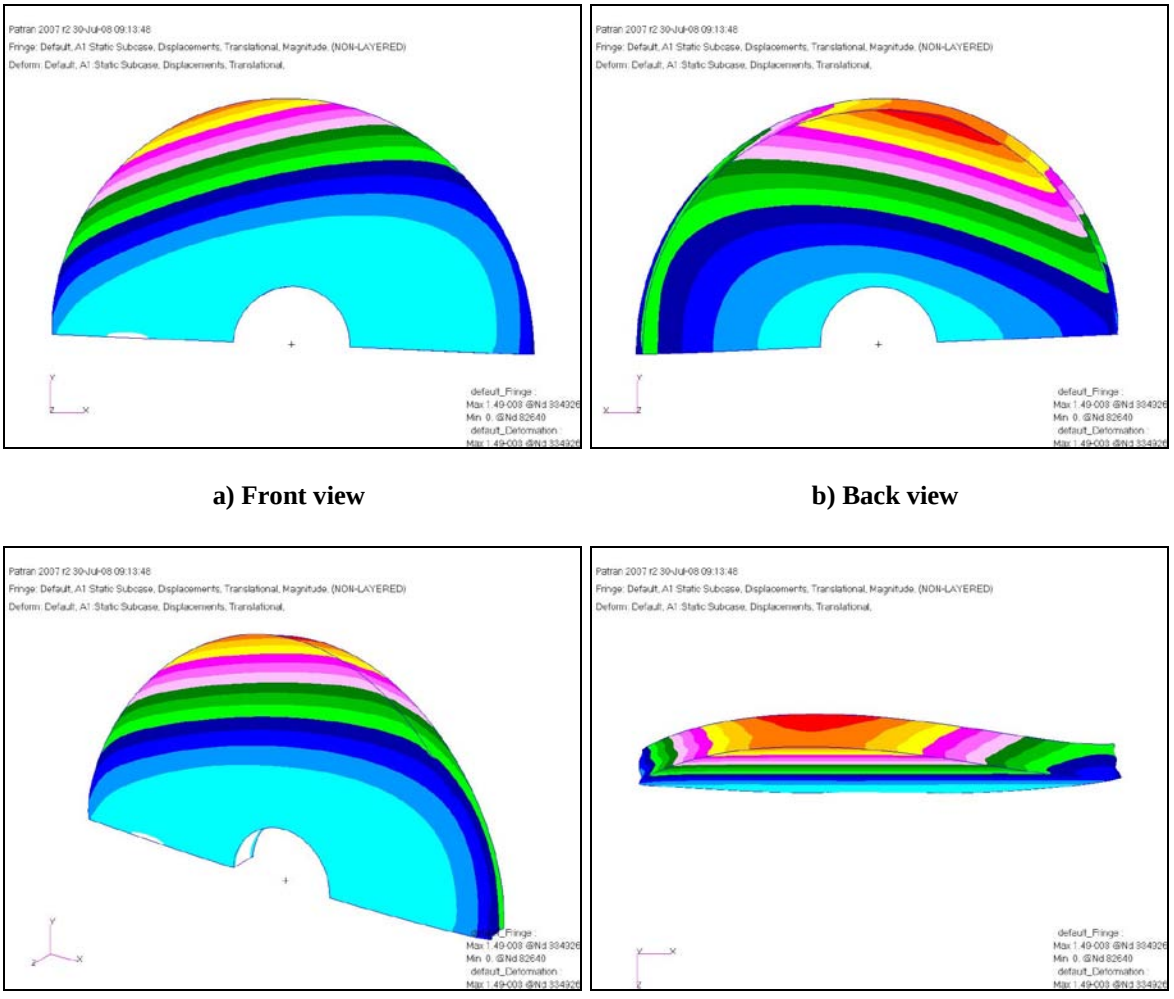

a) Front view **b) Back view**

c) Iso-axis view **d) Top view**

Figure 68: Comparison results between experimental and numerical results for global surface deformation in π/4 laminate. a)~d) numerical results on global surface deformation response in composite mirror

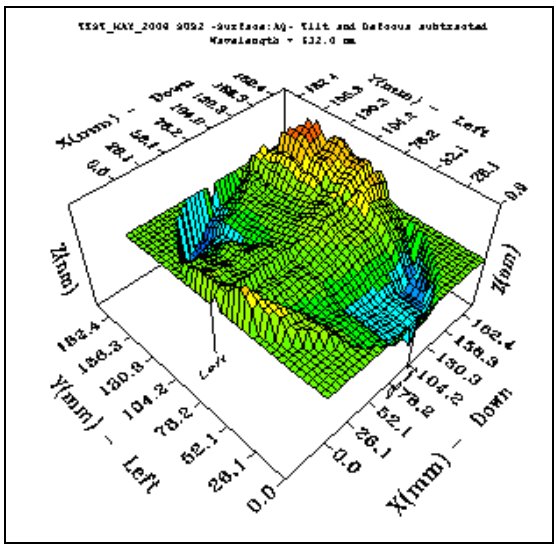

e)

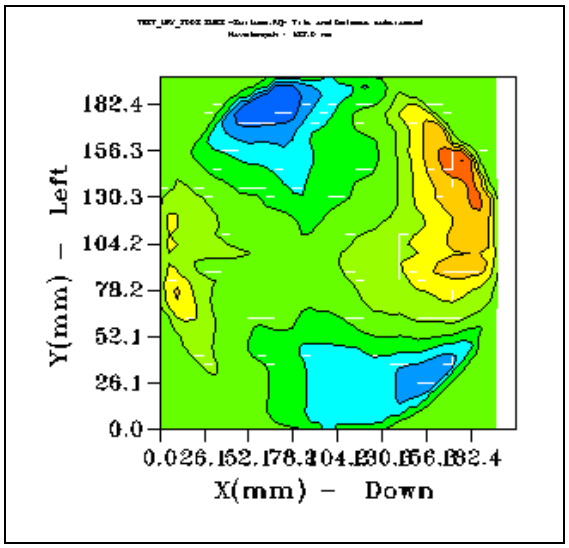

f)

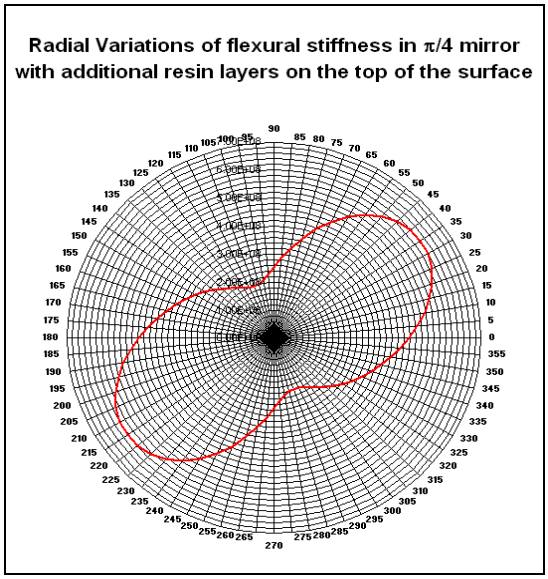

g)

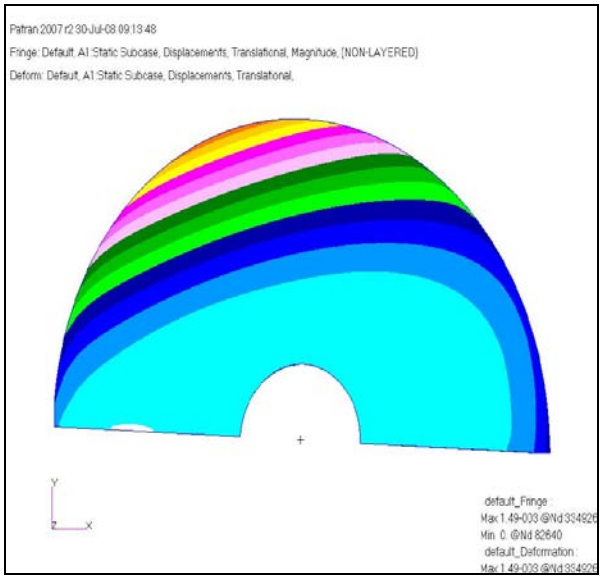

h)

Figure 68 (Cont.): Comparison results between experimental and numerical results for global surface deformation in π/4 laminate. e)~f) experimental result (Optino), g) variation of D11 in the mirror, h) numerical result (Nastran/Patran)

Although experimentally characterized and numerically predicted surface deformation differ in magnitude (twice larger in analytical prediction), the global laminate surface deformation shapes in both numerical and experimental results are well

matched. The relative errors in this study might come during the experiment. In experiment, we are trying to evaluate small surface variations in composite mirror (in nm scale), any small changes while performing the test might give an inaccurate result. There are many manufacturing flaws that need to be fixed for better experimental results. As shown in Figure 53, the test mirror surface has lots of partially blurred spots on the mirror. This might be one of the factors that provide inaccurate experimental results in this section. Higher fidelity experiments require near diffraction-limited mirror samples, which are not available at the time of this writing. Further studies with the wave-front sensor are recommended when mirrors of near diffraction-limited surface conditions (if even at a single reference temperature) are available. Until such time, a more rudimentary experimental technique will be explored in subsequent sections.

6.2. Experimental results from Bennett Optical Research (BOR) on 6” π/4 Quasi-Isotropic Composite Mirror for Preliminary Validation

The purpose of this section is to compare our numerical results to the experimental results performed in Bennett Optical Research (BOR). BOR is a premier business and development laboratory located in Ridgecrest, California. Their specialty is developing large super-polished mandrels for lightweight, low-scatter, astronomical quality composite mirrors employing active or adaptive actuators. This section summarizes BOR experiments for measurement of surface deformation in a 6” composite mirror blank as a function of temperature. The 6” carbon composite mirror blank used in this experiment was fabricated at BOR, and the fabrication process details follow.

6.2.1. Fabrication Process Details on 6” Composite Mirror

1. The material is Lincoln L-930/GT700 prepreg. 16 plies are laid up in the sequence of $[0, 45, -45, 90, 90, -45, 45, 0]_s$. Curing is done with vacuum bagging with 14.7 psi at a final temperature of 260º F.

2. Additional resin layer is added using Epon 828 epoxy with Epicure 3234 curing agent.

3. The neat resin surface is replicated from a polished optical flat made from either Zerodur or Pyrex glass. The replication is done with vacuum bagging and cured at room temperature for 7 days.

4. A release agent is applied to the optical flat prior to the replication.

6.2.2. Experimental Set-up for 6” BOR Composite Mirror

The following Figures 69 and 70 indicate experimental set-up taken in BOR for 6” composite mirror. The mirror was being tested under room temperature (72º F), 114º F, and 150º F to obtain measurement of deflection data on 6” composite mirror blank fabricated at BOR.

Figure 69: Deflection fixturing inside temperature oven (From BOR)

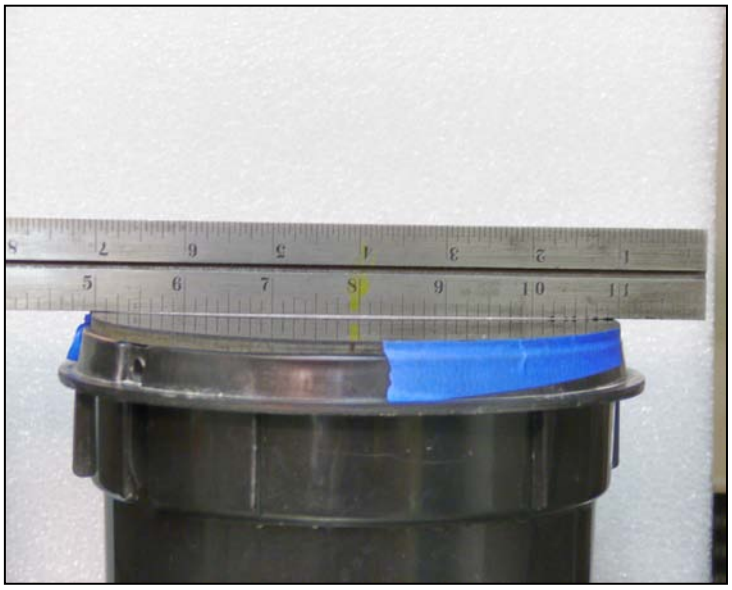

Figure 70: Deflection in 6” composite mirror at room temperature (From BOR)

6.2.3. Experimental Results and Comparison with Finite Element Analysis

The following experimental data was taken at 45 degree off set from fiber orientation for obtaining thermal deflections at temperature of 114° and 150° F at BOR. As shown in the Figures 71~73, the mirror deforms as a function of temperature. The Figure 71 illustrates that initial deflection shape of mirror at room temperature which is first order in curvature. The theoretical surface deflection shape at 45 degree orientation line must be flat due to the details of the mirror fabrication process. The initial surface shape of the mirror might be from their manufacturing process. In our computation model, the same initial deflection shape is also assumed for numerical consistency.

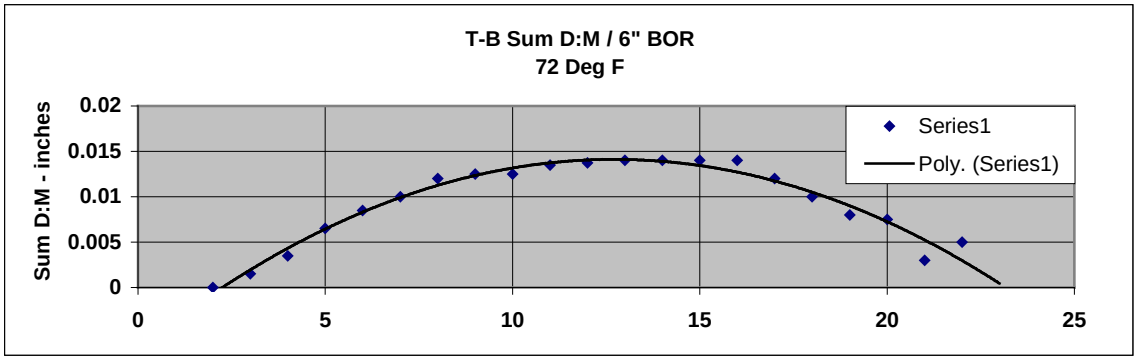

Figure 71: Deflection data found in BOR on 6" mirror at 72º F. (From BOR)

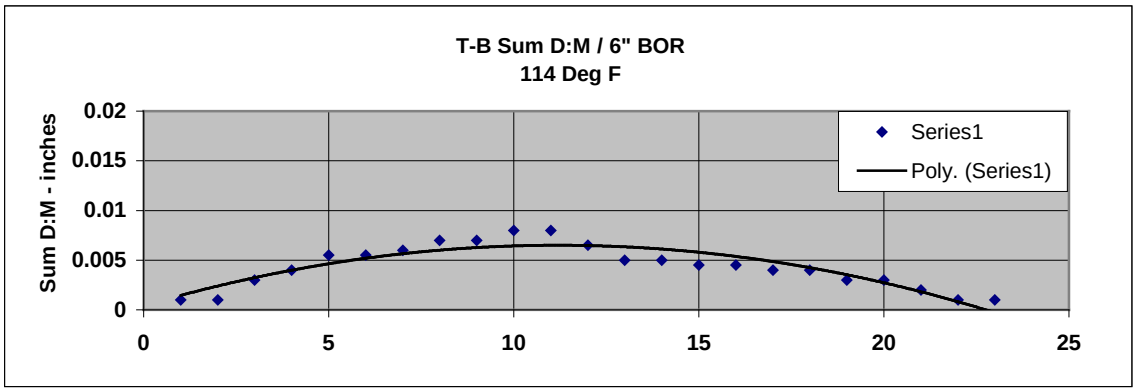

Figure 72: Deflection data found in BOR on 6" mirror at 114º F. (From BOR)

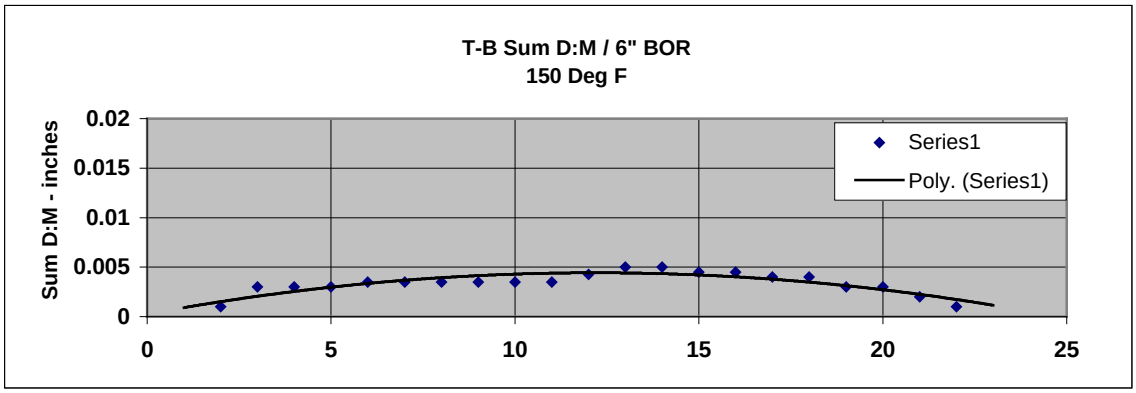

Figure 73: Deflection data found in BOR on 6" mirror at 150° F. (From BOR)

The experimental data shown in Figure 72 illustrates that local deflection data found at 45 degree fiber orientation line were fluctuated at its radial line. It may indicate either experimental error in measurements or a higher order displacement response.

The experimental data from BOR were compared to numerical simulations using finite element analysis, to investigate potential reasons for what appears to be either experimental error in measurements or a higher order displacement response which differs from what we would expect. The numerical simulations do demonstrate a higher order response, but not at the theoretical 45 degree orientation line. The deflection data between experiment and numerical simulations were compared in Figure 74 at elevated temperature of 114° F and 150° F respectively. The numerical deflection data at 45 degree fiber orientation line was first order in curvature as shown, and in some points good agreement is demonstrated. The differences between the experimental results and the predicted values are also shown in Figure 74. It is unclear what causes fluctuation in experimental data at this point, but there is an assumption that the experimental results from BOR may be highly sensitive to the location of the measured line, in either a) angular orientation or b) in position at the theoretical center point origin as described in

Figure 75. Since the mirror was assumed to be ideally quasi-isotropic in these initial experiments, it would not be surprising that little experimental control for position of measurement was exercised.

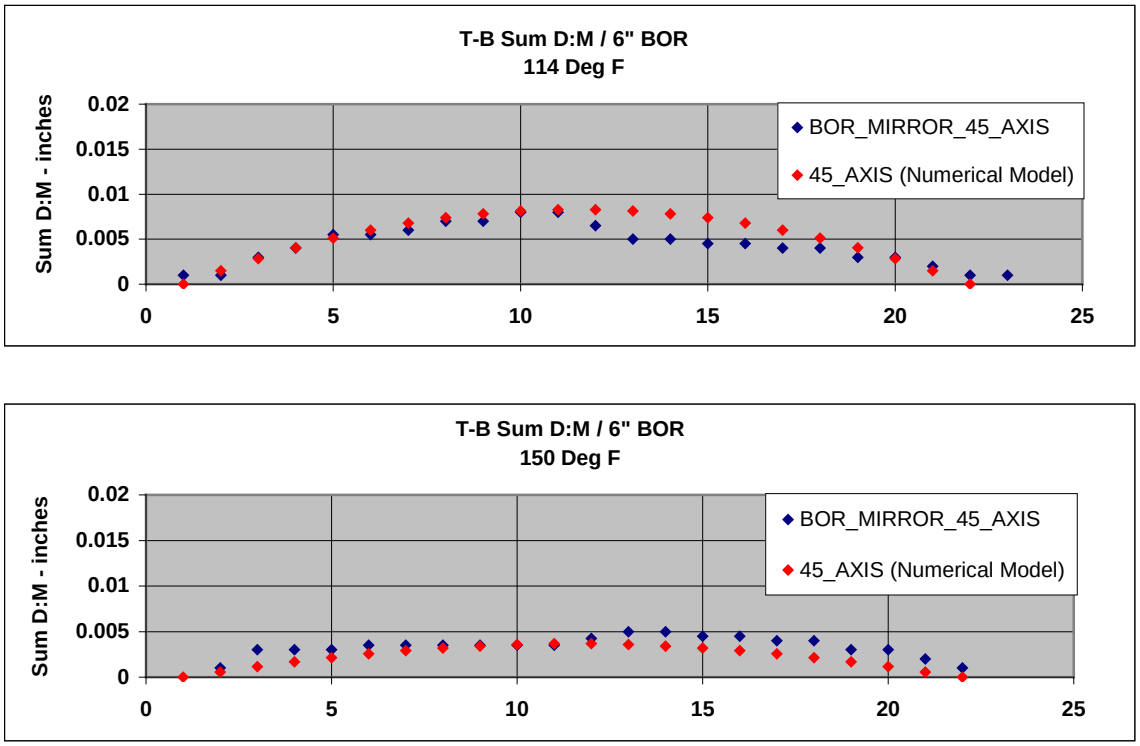

Figure 74: Comparison of deflection data between experiment and numerical simulations at 114º F and 150º F.

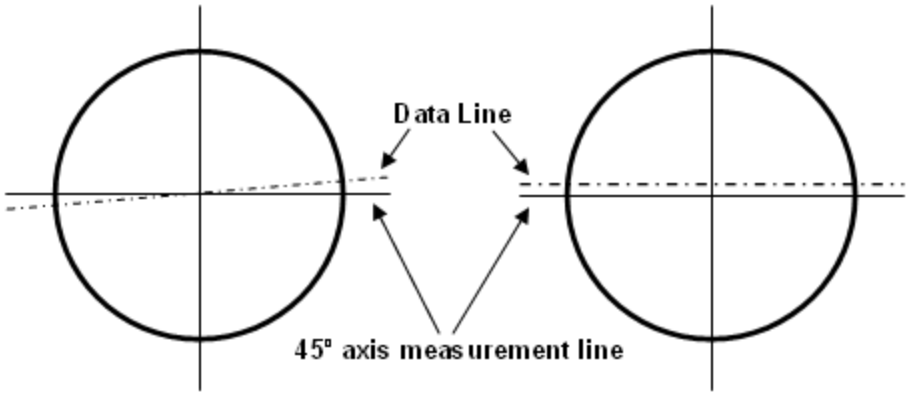

a) **b)**

Figure 75: Possible location of measurement lines in BOR mirror

Angular misalignment could cause magnitude variation, but not the higher order fluctuations which might be evident. As such, the offset is the more interesting scenario. The calculated numerical data was reevaluated to get off-set axis (0.26” either above or below from the 45 degree centerline) measurement based on 45 degree fiber orientation line in BOR mirror to evaluate whether the experimental fluctuation data was taken at off-set axis. The off-set degree measurement may display a higher order displacement response due to stacking sequence in the composite mirror. In Figure 76, 0.26” offset from centerline in our simulated data would suggest that the experimental data measured at 114° F follows our predicted response well. This is a possible evidence of local surface variations in composite mirror due to stacking sequence effects. Even though it is our hypothesis that the mirror surface was evaluated off-axis, the numerical prediction on the surface deformation in the mirror was well matched.

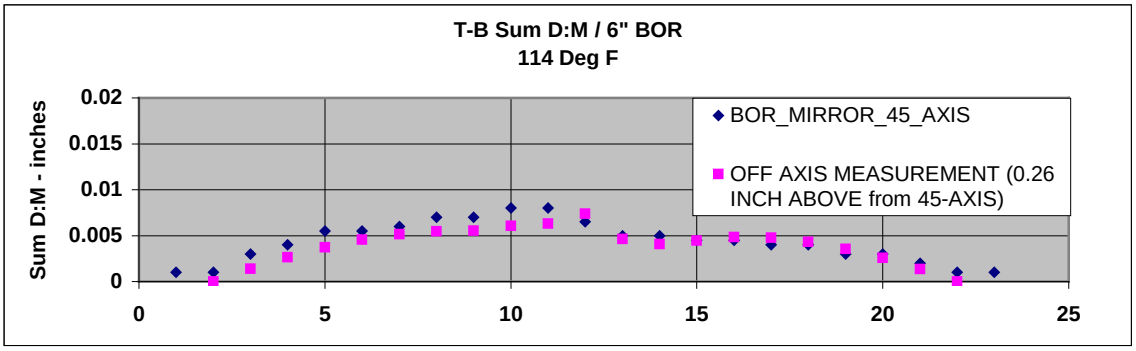

Figure 76: Comparison of deflection data between experimental data (BOR mirror at 45 degree axis) and numerical data (0.26” off-set measurement)

Based on the preliminary experiment on the BOR mirror, the fluctuations in experimental result might be evidence of local surface deformations in the BOR mirror. Such local surface fluctuations in the BOR mirror must come from radial variation in flexural stiffnesses due to stacking sequence effects. The following section address experimental and numerically predicted results on the $\pi/4$ quasi-isotropic mirror fabricated from BOR for further validation.

6.3. Experimental and Numerical Validation on 7" π/4 BOR Mirror

The previous sections 6.1 and 6.2 have discussed and provided preliminary experimental results for the surface deformation on a π/4 quasi-isotropic laminated mirror using wave-front sensor and the experiments performed in Bennett Optical Research (BOR) for local surface deflection at 45 degree axis. This section will provide complete experimental results on a π/4 quasi-isotropic laminate mirror recently fabricated at BOR to explore surface qualities of the BOR mirror, to determine whether the mirror is dimensionally stable, to confirm the dimensional stability issue addressed in previous chapter 5 and to quantify radial surface deformations in the BOR mirror along with numerical simulations. In this section, the validation was achieved by comparing experimental results along with numerical predictions using the finite element method.

6.3.1. Introduction

A wave-front sensor appears to be a good experimental tool for evaluating surface qualities, local deflections or displacements, and the full-field visualization of displacements. Unfortunately, as mentioned in section 6.1.5, high frequency surface distortion due to fiber print-though and global radial undulations in the quasi-isotropic laminate mirror due to flexural stiffness variations presented in the surface of the sample mirror caused dissipation of returning composite mirror surface image during the wave-front experiment. Thus, the surface deflection experimental technique by BOR described in section 6.2 was repeated to investigate surface deformations in a π/4 BOR mirror.

6.3.2. Approach

A determination of surface undulations caused by radial variations in flexural stiffnesses due to stacking sequence effects requires an accurate measure of surface qualities as well as an accurate experimental procedure. The experimental results of this research illustrate the difficulty associated with an accurate determination of out of plane deformations due to lack of capacities in optical test equipment. First, there is large scattered light associated with local variations in surface qualities which hinder us from obtaining accurate optical test data. This deformation, as it becomes severe, causes the light to reflect from the specimen grating at relatively large angles with respect to normal. These high angles of reflection result in a local loss of interference fringes because the emergent light misses the CCD camera lens and thus never arrives at the image point. Second, the wave-front sensor technique described through sections 6.1.1~ 6.1.4 was impractical due to lack of reflectivity and loss of data which occurs at layer interfaces from differential out of plane deformations on the composite mirror surface. Such difficulties also were applied to the newly fabricated BOR mirror. However, surface coating with aluminum material for better reflection on the BOR mirror was not accomplished because BOR strongly recommended against aluminizing the mirror surface of this particular sample to avoid potential contamination of the surface due to surface qualities shown in Figure 77.

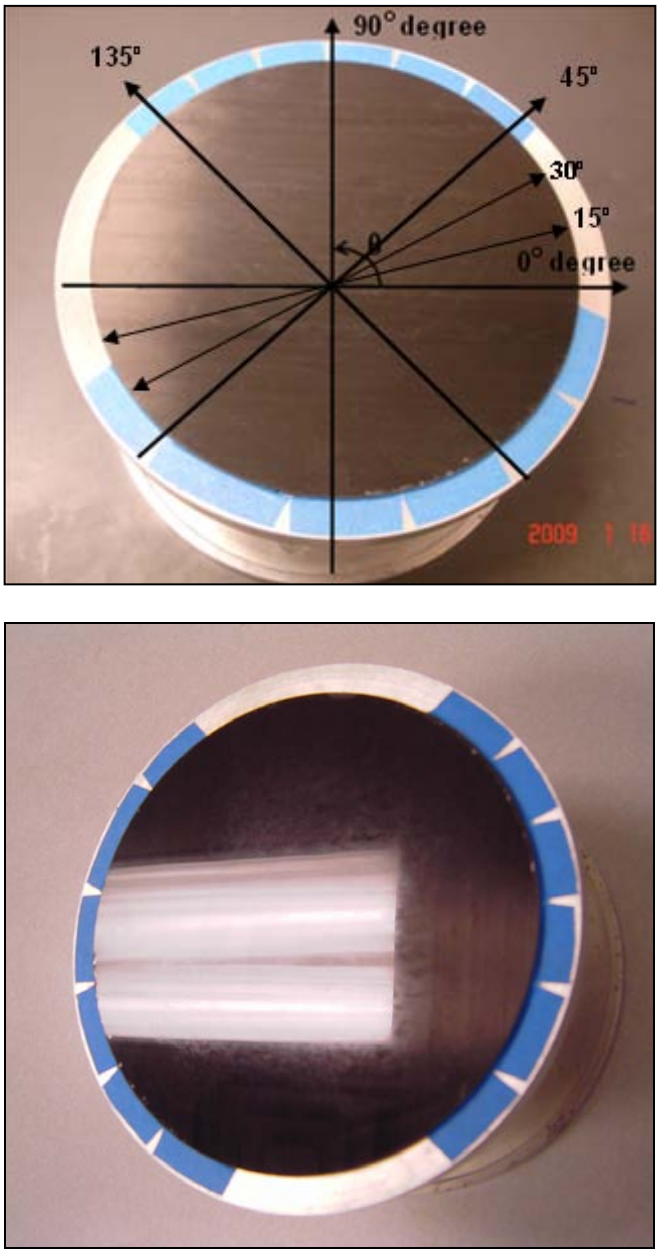

Figure 77: Newly fabricated BOR mirror, π/4 lay-up with additional resin layer

Further, since the focus of this study is to show radial surface deformations associated with stacking sequence effects, the experimental methods showed in section 6.1.5 were repeated for surface evaluation of the new BOR mirror. To investigate surface deformations due to radial flexural stiffnesses and stacking sequence effects in the quasi-isotropic laminated mirror, a π/4 16 layers with a thin film of resin rich layer recently

fabricated from BOR was used (Figure 77). The BOR mirror has the orientation of $[0, \pm 45, 90, 90, \mp 45, 0]_s$. The material used in the composite mirror was Lincoln L-930/GT 700 prepreg. The mechanical properties of the prepreg contains Young's modulus of E_1=14.3x10^6 psi, E_2=1.02x106 psi, E_3=1.01x10^6 psi, and shear modulus of G_{12}=0.63x10^6 psi, G_{23}=0.233x10^6 psi, G_{31}=0.503x10^6 psi. Also, the properties of GT 700 epoxy contains E_m=0.766x10^6 psi, G_m=0.278x10^6 psi. A compression sample of the experimental geometry shown in Figure 78 was prepared. The composite mirror was aligned such that the 0° plies parallel the longitudinal axis of the sample (x-axis) and the 90° plies parallel the y-axis. In the numerical model, the prepared specimen was loaded such that the displacements in z-axis in the back surface nodes of the composite mirror were prescribed as zero, or in other words, the back surface was fully supported. Experimental measurement of the surface deflections in radial directions of the BOR mirror were evaluated at 0 to 360 degree axis with increments of 15 degree. A key feature of this experiment is the incorporation of rotation and translation stages (Figure 78) which allow adjustments in sample orientation for each designated local axes (0, 15, 30 up to 360 degree axis).

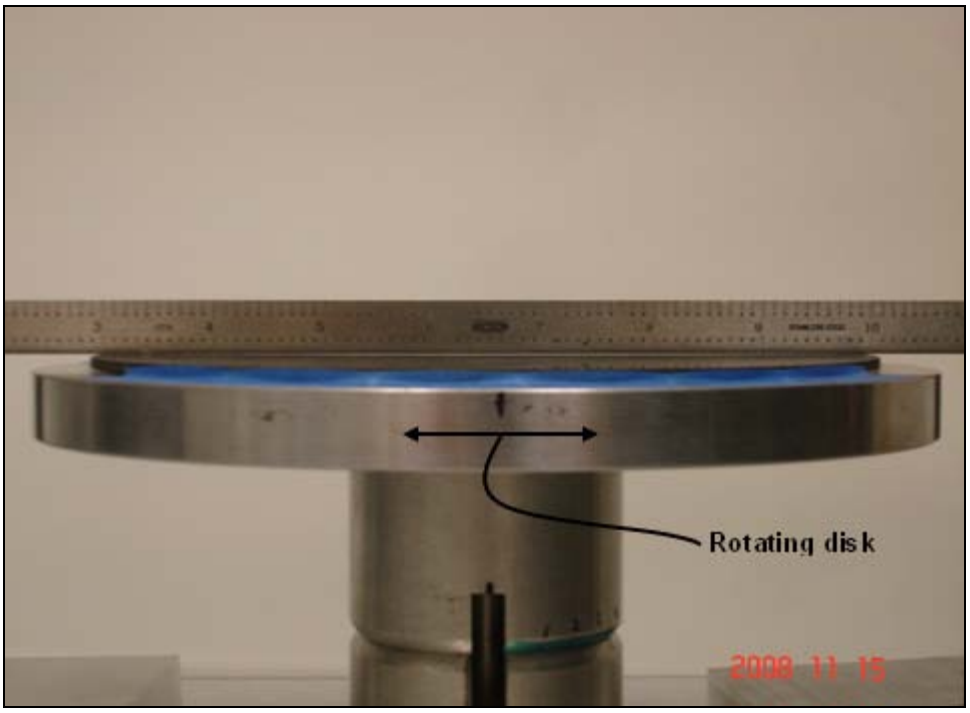

Figure 78: Experimental set-up for 7" BOR mirror at 0 degree axis with room temperature

As shown in Figure 78, the initial deflection shape of the mirror at room temperature was already first order in curvature, as might be expected with a laminate cooled from an elevated temperature cure. The theoretical surface deflection shape in each radial axis direction at room temperature must be flat for ideal condition, but one must account for this initial variation from nominal. Also, in reality, this initial deflection due to bending of the thin composite substrate might be a common phenomenon in a laminate with resin layers on the top surface due to asymmetry. Therefore, the initial deflection shape at each radial line of interest at room temperature was evaluated for developing precise numerical models for accurate numerical validation. For experimental measurements and recording the shapes of local surface deflections, the sample was placed into an oven and heated to designated elevated temperatures. A Sony digital camera with 7.2 Mega pixels was used to record the surface deflections for evaluation.

After recording the image of deflections at each radial axis, the image was evaluated using Image-J software to quantify deflection by counting number of pixels in the image. For all experiments, deflection shape at each radial line was recorded at temperature of 100˚ F and 150˚ F. The absolute deformations were determined by subtracting the room temperature measurements from the elevated temperature measurement. The use of a turn table was particularly important for measurement of deflection fields, in which an accurate determination of radial axis is required. Since some local undulation in deflections occurs in each experiment measurement, a curve fit was used to demonstrate the first order deflection curvature in each radial axis.

Finite element models of the BOR mirror were developed with initial first order curvature at each radial axis using 3-D Hex element with 8 nodes to simulate the surface deflection due to thermal variance. Finite element models of this type have been successful for predicting surface deformation in quasi-isotropic laminates due to thermal gradients as addressed in Chapter 5. Symmetry conditions permit only half of the radial sliced mesh for each local surface deformation line of interest (Figure 79). The displacement function w was prescribed as zero along the bottom of x-y plane in the numerical model and the displacement function v was prescribed as zero along the x-z plane. Finally, the displacement function u was prescribed as zero along the y-z plane in the finite element model.

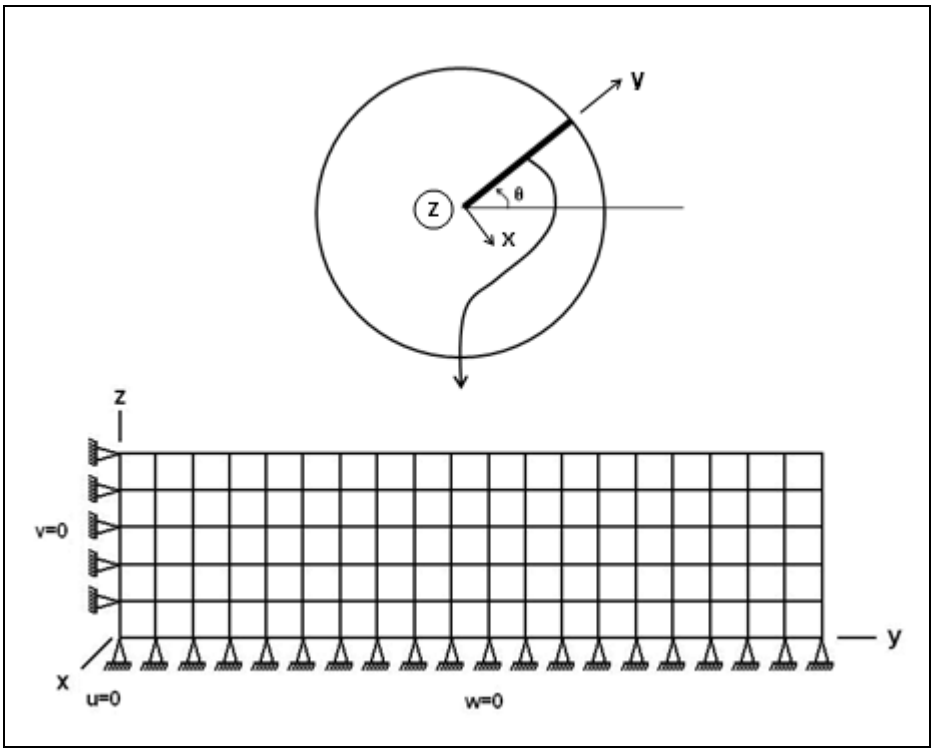

Figure 79: Finite element model for boundary conditions

6.3.3. Results

Radial surface deformations were evaluated from the experimental set-up at temperatures of 100˚ F and 150˚ F. Representative plots of surface deformations at radial directions in 7” BOR mirror at temperature of 100˚ F are shown in Figures 80~81. Note that this includes sets of data, namely the surface deformations at particular radial line of interest in experimental and numerical results. Although the laminate is symmetric about each radial line if the additional resin layer was not counted, there was not only global shape of deflection but also undulating pattern of deflection at each radial measurement. The undulating surface deflection pattern in each radial line might be potential errors

during experiment measurement process or might be high frequency local surface deformation due to fiber print-through. For a precision composite mirror substrate, ideally, the surface variations in these two curves should be within <λ/20 nm. The evaluated surface deformations in either experimental or numerical study support those unfavorable surface deformations due to stacking sequence effects and radial variation in flexural stiffnesses. Table 19 lists the prediction and the experimental values of local surface deflections on the BOR mirror at 100º F.

Table 19: Experimental (trial 1 and 2) and numerical results of surface deflection at local radial axis (0~165 degree axis, 15 degree increment) in BOR mirror at 100º F

	0 deg. Axis	**15 deg. Axis**	**30 deg. Axis**	**45 deg. Axis**	**60 deg. Axis**	**75 deg. Axis**
Predicted (Numerical) δ_z (x 10^{-5} inch)	124.57	171.83	193.97	148.75	230.75	254.76
Experimental δ_z (x 10^{-5} inch) (Trial 2)	123.11 (118.54)	178.85 (161.12)	308.60 (289.94)	152.70 (140.22)	183.73 (180.07)	337.28 (315.51)
Difference, % (Trial 2)	1.17 (4.83)	4.09 (6.23)	59.10 (49.48)	2.66 (5.73)	20.38 (21.96)	32.39 (23.84)

	90 deg. Axis	**105 deg. Axis**	**120 deg. Axis**	**135 deg. Axis**	**150 deg. Axis**	**165 deg. Axis**
Predicted (Numerical) δ_z (x 10^{-5} inch)	183.48	247.74	239.67	170.66	225.32	185.42
Experimental δ_z (x 10^{-5} inch) (Trial 2)	207.47 (198.45)	368.11 (348.87)	199.55 (189.22)	191.39 (186.62)	201.38 (209.98)	181.03 (200.13)
Difference, % (Trial 2)	13.07 (8.16)	48.59 (40.82)	16.74 (21.05)	12.15 (9.35)	10.62 (6.81)	2.37 (7.93)

The differences between the experimental results and the predicted values in percentage are also shown. Good agreement is demonstrated except some local axes have relatively large value of difference between experimental and numerical results. Most of the data from experimental and numerical results are well matched and the values are within 22 % variation except some deviated data between experimental and numerical presented at 30, 75, 105, and 120 degree axis. Also, and of most importance, the deviation from experiment and theory is most dramatic in the angular orientations ± 15º from one of the defined lamina orientations, suggesting that radial variations identified in Chapter 5 are more severe than predicted herein. The maximum difference between experimental and predicted values was 59.1 % while the minimum value was 1.17 % along the BOR mirror. The maximum deviation is found at 30 degree which value has almost 60% difference to numerical result. However, the experimental and predicted numerical results shown in Figures 80~81 clearly indicate the evidence of unfavorable surface deformations present in composite mirror substrate which will hinder precision mirror performance. The focus of this experiment is most notably to validate the reality of the radial variations in surface deformation, and they succeed in that regard. Future high fidelity surface characterizations are recommended to better understand the deviations between experiment and theory.

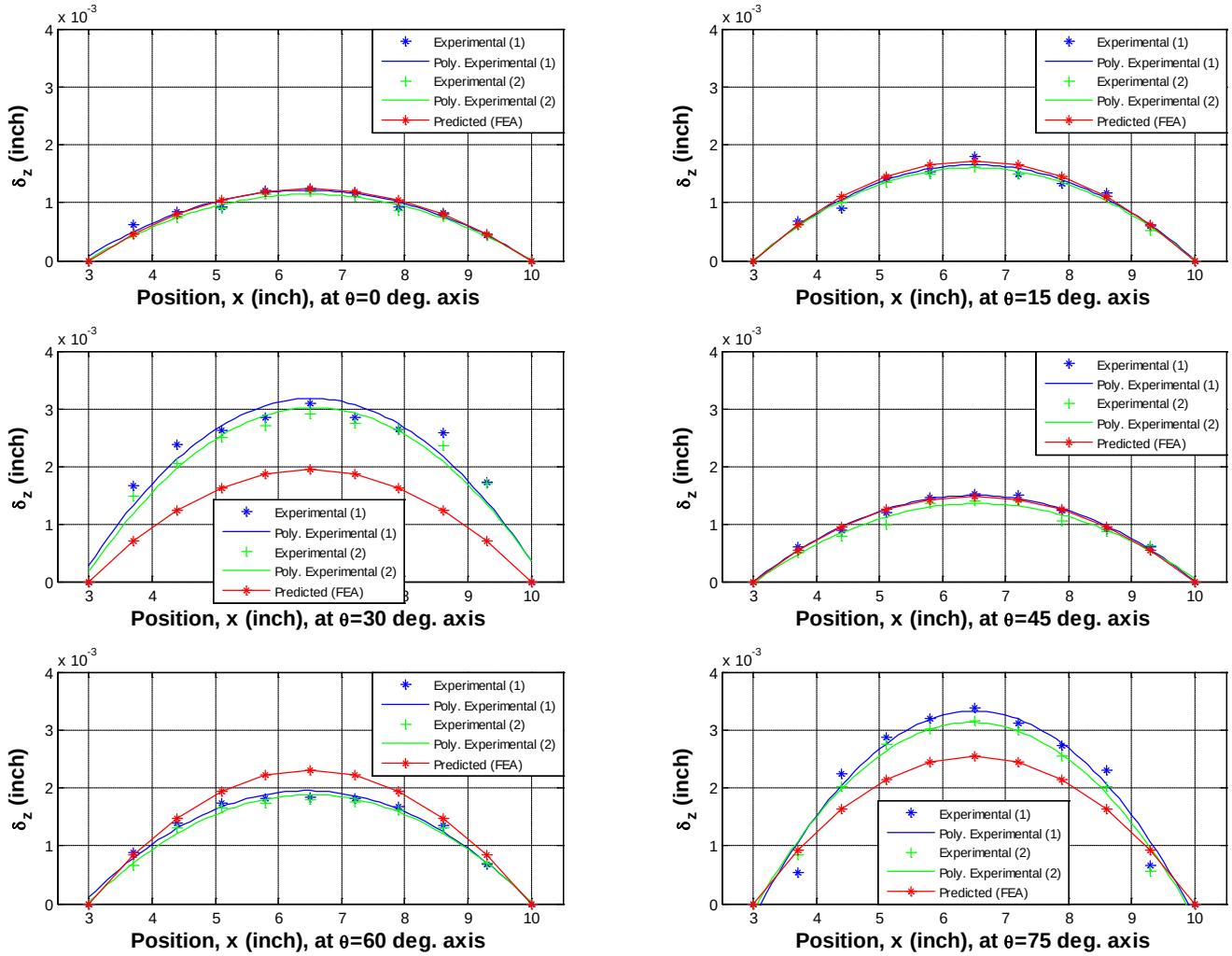

Figure 80: Plots for local surface deformations in BOR mirror from experimental along with predicted (numerical) results-1, at 100° F

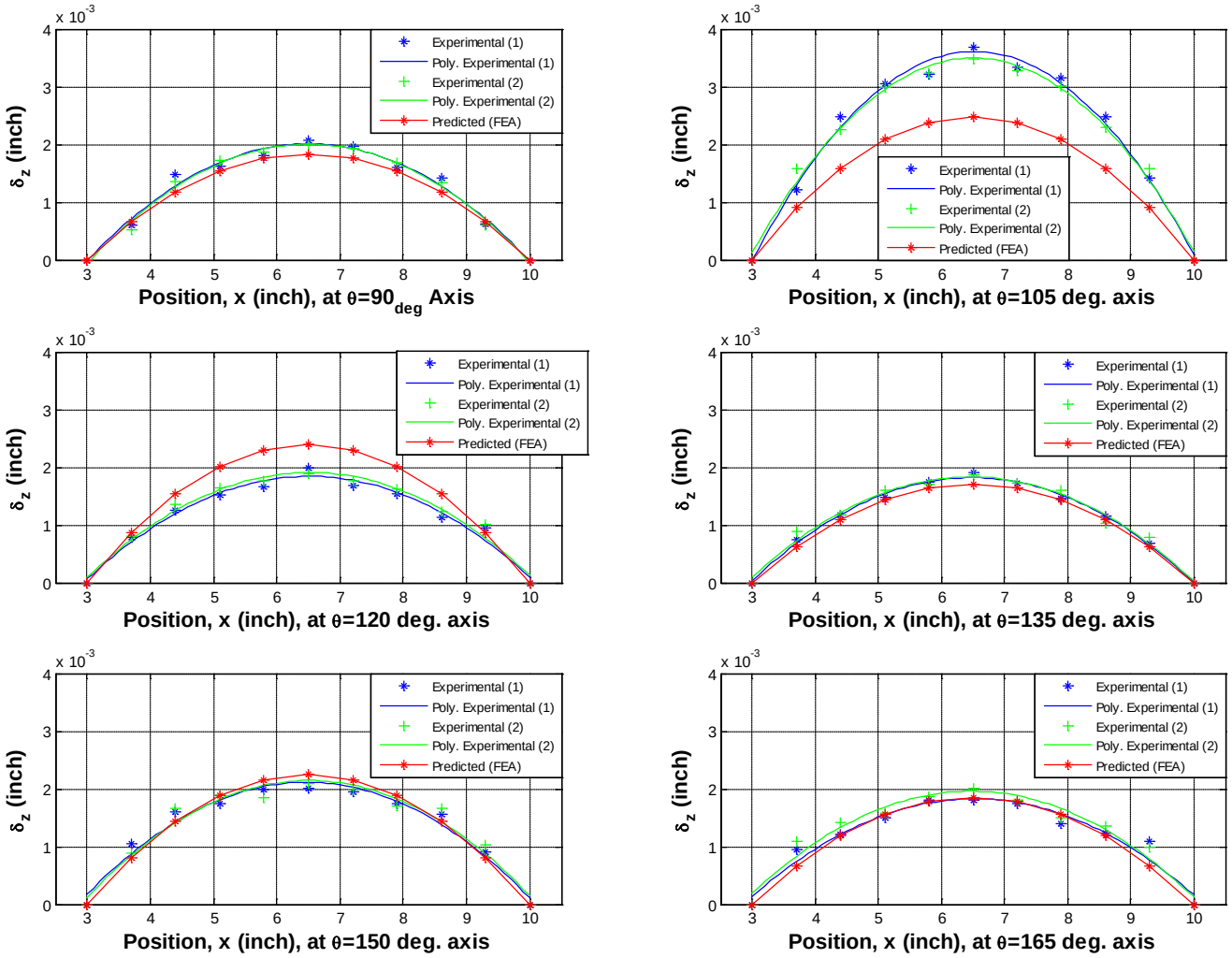

Figure 81: Plots for local surface deformations in BOR mirror from experimental along with predicted (numerical) results-2, at 100° F

Maximum values of surface deformations from experimental result for 7" BOR mirror obtained for each radial direction with presence of thermally-induced load of 100˚ F are plotted in Figure 82, along with finite element predictions. Although the results from experimental and analytical method tend to match, there were some deviations at 30, 75, and 105 degree axis. The maximum error between experimental results is within 11 %. In general, finite element predictions support the experimental data quite well. Moreover, the surface undulation shapes in the mirror sample agree in theory and experiment.

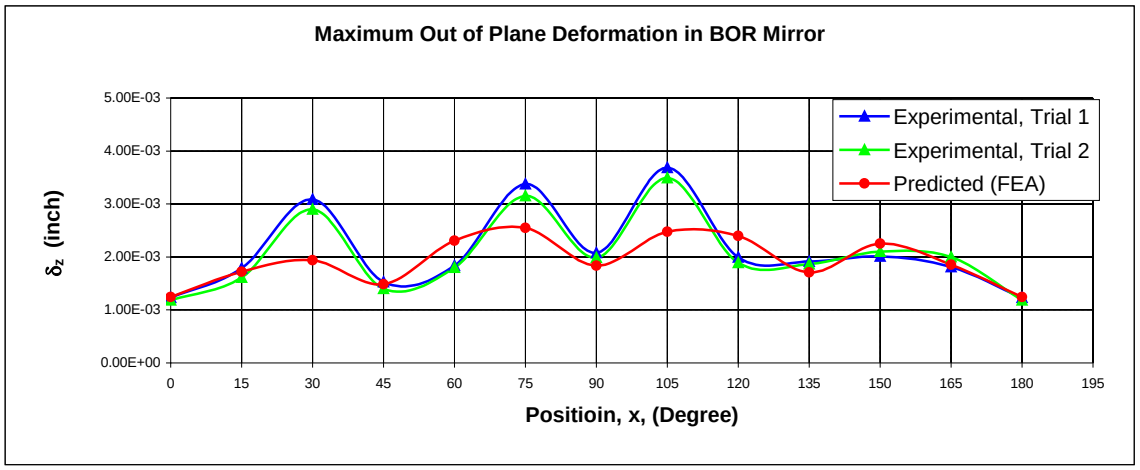

Figure 82: Maximum out of plane deformation in each radial axis in BOR mirror, at 100˚ F

The tendency to over-predict experimentally determined surface deformations in some radial lines (30, 75, and 105 degree axis) might indicate actual surface undulation phenomenon or indicate errors from experimental set-up or errors from instrumental reading. The same experimental procedures were repeated on the 7" BOR mirror with different temperature of 150˚ F. Table 20 illustrates the predicted results from finite element analyses and the experimental results for the BOR mirror at 150º F. The results show that the surface deformation patterns are similar to 100º F case but the agreement between the experimental and numerically predicted values are much closer than in the previous case.

Table 20: Experimental and numerical results of surface deflection at local radial axis (0~165 degree axis, 15º increment) in BOR mirror at 150º F

	0 deg. Axis	**15 deg. Axis**	**30 deg. Axis**	**45 deg. Axis**	**60 deg. Axis**	**75 deg. Axis**
Predicted (Numerical) δ_z (x 10^{-5} inch)	332.18	458.21	517.25	396.66	615.32	679.37
Experimental δ_z (x 10^{-5} inch)	311.15	406.48	571.88	382.72	573.95	776.20
Difference, %	6.33	11.29	10.56	3.51	6.72	14.25

	90 deg. Axis	**105 deg. Axis**	**120 deg. Axis**	**135 deg. Axis**	**150 deg. Axis**	**165 deg. Axis**
Predicted (Numerical) δ_z (x 10^{-5} inch)	489.29	660.64	639.11	455.10	600.85	494.46
Experimental δ_z (x 10^{-5} inch)	430.99	624.41	633.38	439.99	552.13	479.82
Difference, %	11.92	5.48	0.90	3.32	8.11	2.96

All of the experimental and predicted numerical values are well matched. The maximum difference between the experimental and predicted numerical values was within 15% while the minimum difference was 0.90 % along the BOR mirror. Figures 83 and 84 illustrate the radial surface deformations from experimental results along with numerically predicted results for the BOR mirror with temperature of 150º F.

As shown in Figures 83~84, the over-prediction phenomena found in 100˚ F thermal variance case is faded out throughout the radial surface deformation found in experimental results along with predicted numerical results. The maximum deviation between experimental and analytical result has 14.25% at 75 degree axis in the sample. Moreover, the magnitudes of surface deformations in the composite mirror sample are getting larger, making the surface undulation pattern more apparent when more thermally-induced load is present.

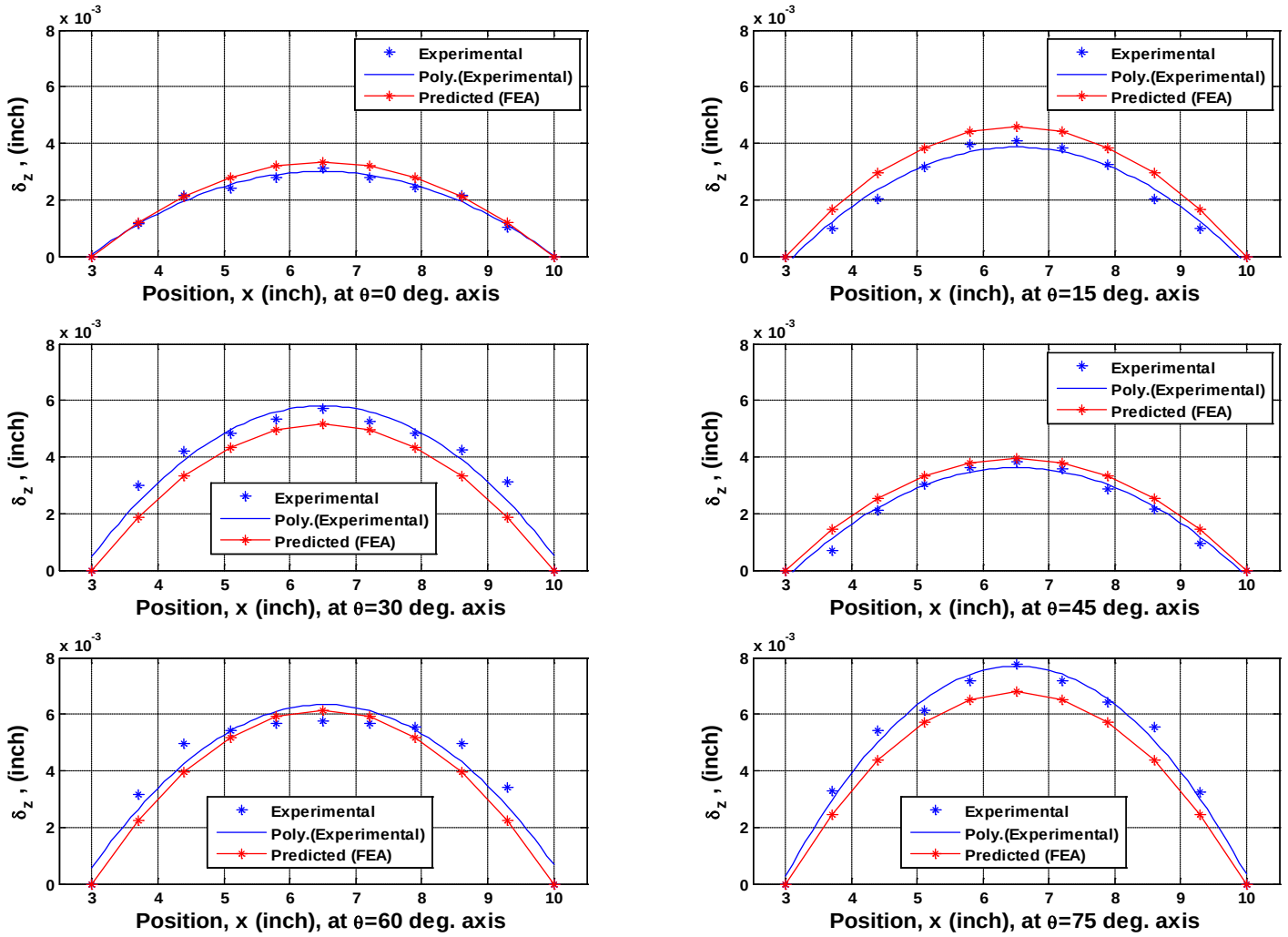

Figure 83: Plots for local surface deformations in BOR mirror from experimental along with predicted (numerical) results-1, at 150° F

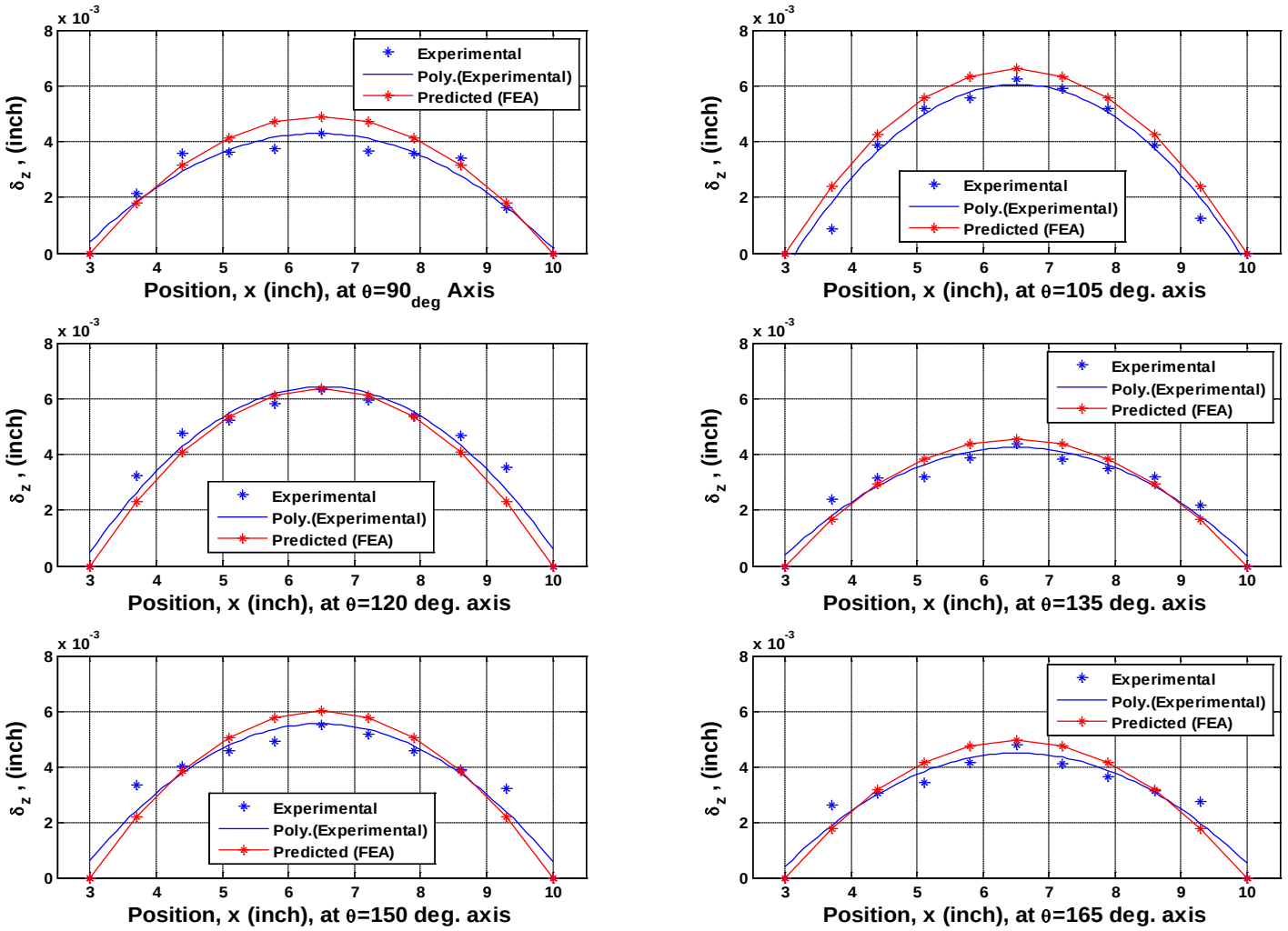

Figure 84: Plots for local surface deformations in BOR mirror from experimental along with predicted (numerical) results-2, at 150° F

Maximum values of surface deformations from experimental result for 7" BOR mirror obtained for each radial direction with presence of thermally-induced load of 150˚ F are plotted in Figure 85, along with finite element predictions just similar to previous case. The maximum error between experimental and results from numerical predictions are within 10 %.

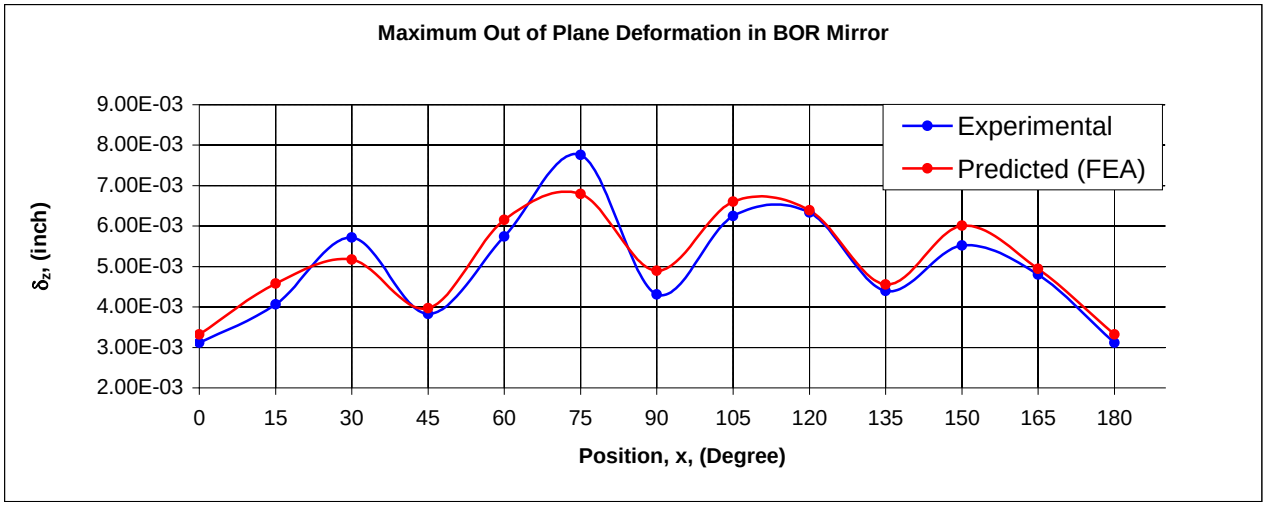

Figure 85: Maximum out of plane deformation in each radial axis in BOR mirror, at 150˚ F

The following Figures 86 and 87 demonstrate the entire 3-D surface deformation contours in the π/4 BOR mirror with an additional resin layer from experimental results and analytical predictions. The surface deformation shapes in the sample mirror in both experimental and FEA results are well matched. As shown in the Figures, the sinusoidal surface deformation in the quasi-isotropic laminates is more severe than high frequency surface quality from curing cycle due to fiber print-through. Once again this suggests that the presence of the additional resin layer should be more problematic in temperature fluctuations, thus hindering optical performance.

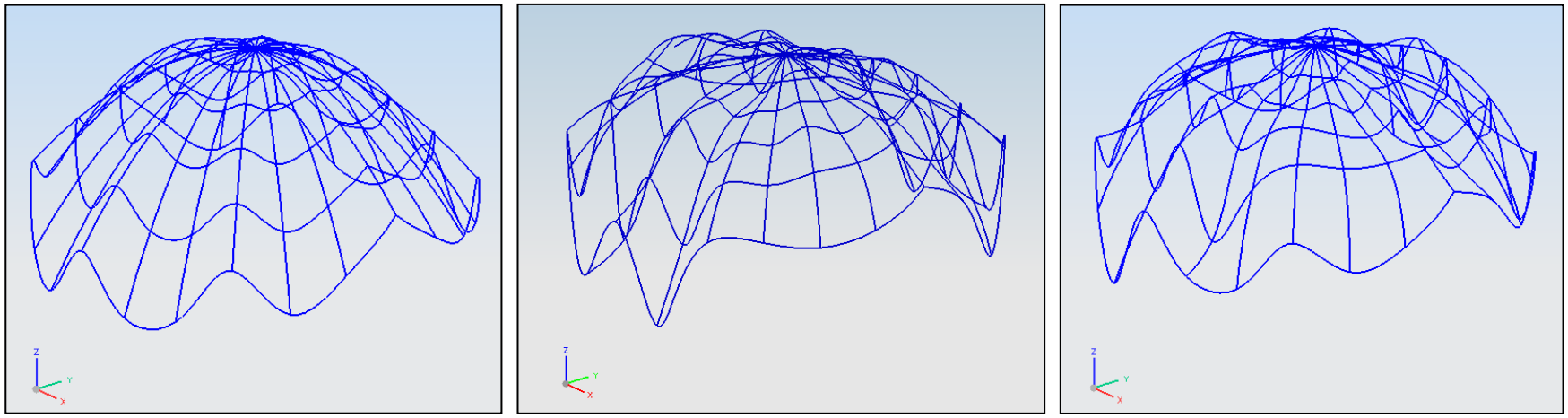

a) Predicted (Numerical) **b) Experimental (100˚ F)** **c) Experimental (150˚ F)**

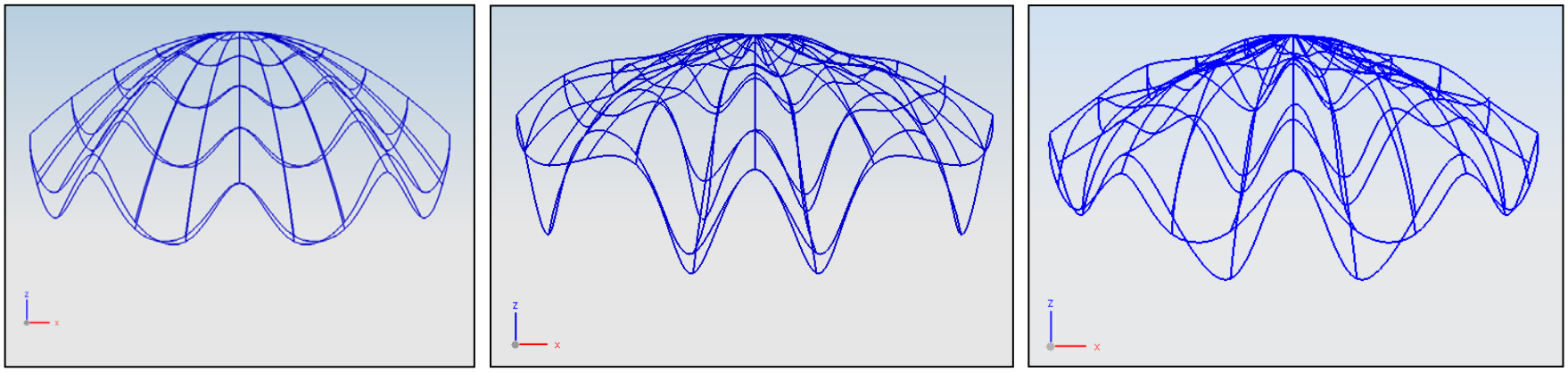

d) Predicted (Numerical) **e) Experimental (100˚ F)** **f) Experimental (150˚ F)**

Figure 86: 3-D surface deformation plots for numerical results (predicted), experimental results-1 (100˚ F and 150˚ F)

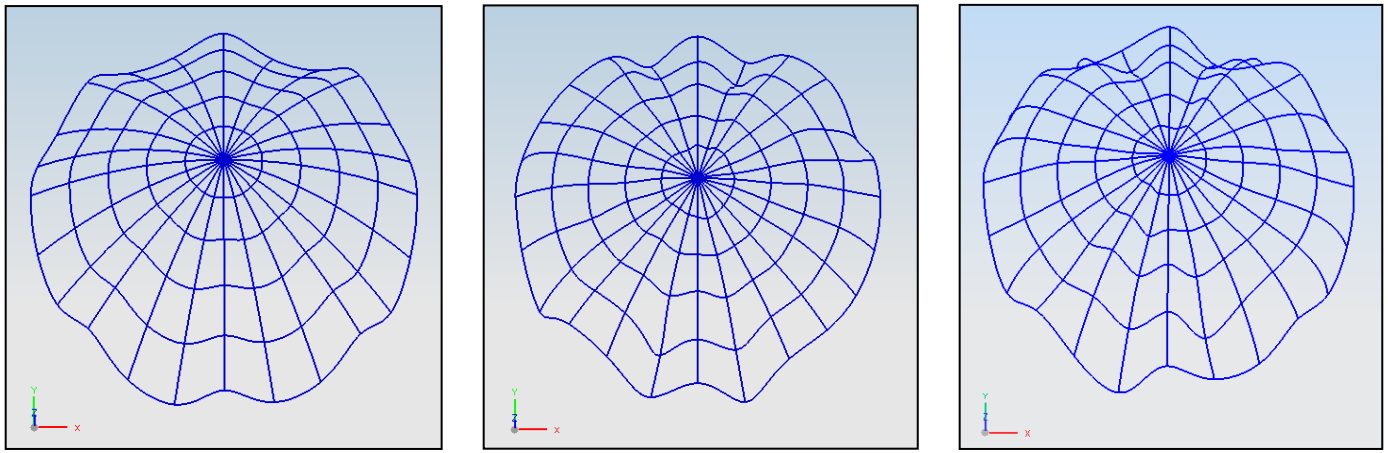

a) Predicted (Numerical) **b) Experimental (100˚ F)** **c) Experimental (150˚ F)**

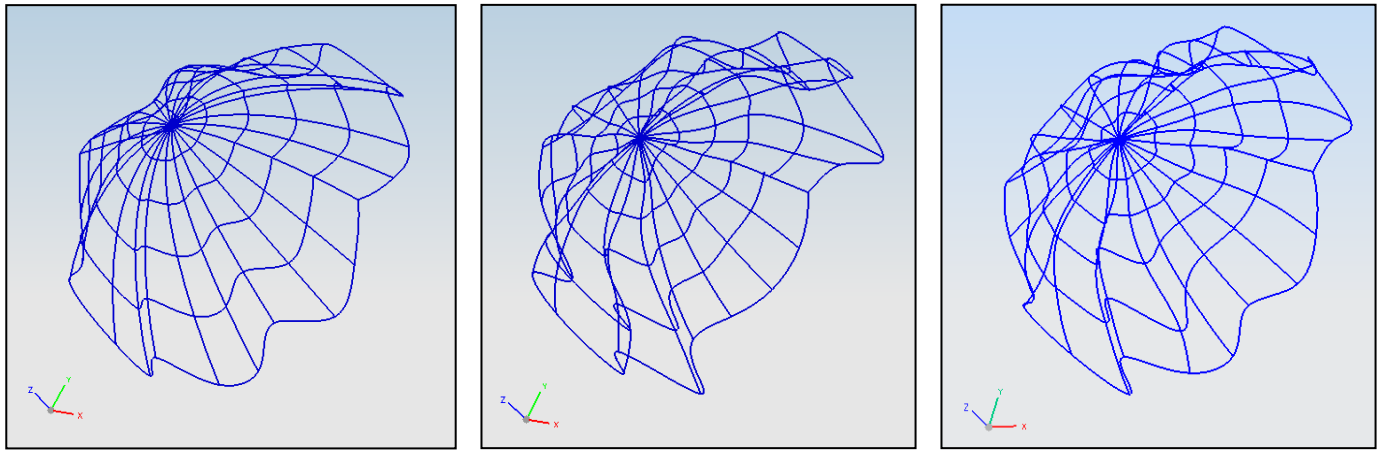

d) Predicted (Numerical) **e) Experimental (100˚ F)** **f) Experimental (150˚ F)**

Figure 87: 3-D surface deformation plots for numerical results (predicted), experimental results-2 (100˚ F and 150˚ F)

In general, in a quasi-isotropic laminate, in-plane stiffnesses in radial directions of the laminate should have no variations due to evenly distributed angle plies in radial directions; however, radial flexural stiffnesses in the laminate are affected by stacking sequence effects. Therefore, surface deformations exhibiting such sinusoidal undulation patterns in the laminate are inevitable. The experimental and analytical results in this document reveal the fact. The existence of radial variations in flexural stiffnesses will have a significant influence on optical performance, especially for composite mirror applications which require high precision performance ($<\lambda/20$). Even laminates fabricated with additional resin layers and polished for mitigating fiber print-through (damping method for high surface frequency), produce more severe surface undulations rather than the laminate without additional resin layers.

These findings suggest that the use of unidirectional materials for fabrication of composite mirrors for ground based and space-borne applications is problematic, as is the use of additional resin layers to damp out fiber print-through. As revealed in this study, quasi-isotropic laminated mirror with more than 16 plies is shown to have significant influence on the surface quality even though it is believed that the bend-twist effect is negligible for a laminate with more than 16 plies. Moreover, the presence of additional resin layers in the composite mirror significantly affects its surface quality. For this reason, investigators must be aware of radial flexural stiffness effects when developing composite mirrors using continuous reinforced fiber plastics.

7. Conclusions and Recommendations

This dissertation has addressed several key aspects within the general topic of carbon fiber reinforced plastic quasi-isotropic laminated mirrors. The main emphases of this dissertation are evaluation of mechanics in quasi-isotropic laminates, surface deformation analyses in ideal quasi-isotropic laminates, and the effects of additional resin layers in the ideal quasi-isotropic laminates. The need for these studies of quasi-isotropic laminates has been established through investigations into the effects of local variations in flexural stiffness in the laminated mirrors. Although recent research has addressed success in fabrication techniques for diffraction-limited composite mirrors, the idealized composite mirrors do exhibit through-the-thickness deformations that hinder them from obtaining precision composite optics stable across a range of environmental conditions.

In this research, the applicability of various quasi-isotropic laminate substrates for precision optics is addressed for discrete layers π/n orientation, where n=3, 4, and 6, in quasi-isotropic laminates. This applicability study includes an assessment and comparison of radial variations of flexural stiffness from continuous fiber rein-forced plastic materials along with homogenous fiber materials.

Surface deformations and distributions in various classes of quasi-isotropic laminates have been determined numerically using finite element models and experimentally using wave-front sensor techniques and direct measurement of radial surface deflection. Experimentally determined surface deformations compare favorably to the results from numerically calculated surface deformations, validating the existence of radially dependent flexural stiffness effects in mirror surface deformations.

7.1. Conclusions

The following summarizes the major conclusions of the numerical and experimental investigations:

a. From analytical results of the mechanics of quasi-isotropic laminates with discrete layers oriented at π/n, where n=3, 4, and 6, flexural stiffnesses depend strongly on direction that corresponds to a circle in the polar stiffness diagram. Among the quasi-isotropic laminates, $\pi/3$ laminate produced most radial flexural stiffness value of ±12.85 %, followed by $\pi/6$ laminate (±9.95%), while the $\pi/4$ laminate produced least value of radial flexural stiffness (±5.63%).

b. The mechanics in maximum asymmetric laminates (±2^o misorientation) in π/n, where n=3, 4, and 6, lay-up sequences were almost the same as in ideal quasi-isotropic laminates cases. The extensional and flexural stiffnesses values are within less than 0.05%. As such, radial variations in flexural stiffness are shown to be more problematic than asymmetry caused by common manufacturing variance.

c. Homogenous carbon fiber materials might be superior to conventional CFRP materials for future composite mirror applications. The analytical results for such homogenous materials (veil, mat, and other short fiber products) indicate that relatively uniform extensional and flexural stiffnesses could be obtained. Spatial variation within lamina is

expected, but global effects should be minimal with distributed layers and orientations of those layers.

d. Results of the surface deformations in π/n laminates using finite element analyses revealed that the presence of surface undulations in the laminates are associated with stacking sequences within the laminates. Analyses assuming a temperature change of 30º F from reference temperature reveal that none of the three quasi-isotropic laminates meet the diffraction-limited surface requirement ($<\lambda/20$) for precision mirrors. Projections of this data further reveal that temperature variations must be maintained within ±3.8º F (±2º C) to expect diffraction-limited performance. Similarly tight control over moisture content will be required.

e. High frequency surface qualities from fiber print-through are one of the most published concerns in the composite optics literature. The numerical simulations on the π/n quasi-isotropic laminates with additional resin layers for mitigation of fiber print-through reveal that the inherent sinusoidal surface undulations from the quasi-isotropic laminates will be more problematic.

f. The numerical simulations on a π/4 quasi-isotropic laminate mirror substrate with additional resin layers show that the more buffer layer present in the mirror substrate, the more adverse sinusoidal surface deformation will get on the quasi-isotropic mirror surface.

g. If additional resin buffer layers need to be added for mitigation of the presence of higher order surface waviness due to fiber print-through, the resin system has to be as soft as possible (low Young's modulus and shear modulus) with a coefficient of thermal expansion as low as possible for alleviation of high frequency surface qualities from fiber print-through. Also, the applied resin buffer layers have to be as thin as possible for better reduction of the high frequency surface quality. Results show that CTE in resin systems is the most dominant factor for reduction of surface waviness in quasi-isotropic laminates.

Based on the results, it can be concluded that when composite with radial flexural stiffness variation are exposed to thermal or hygroscopic environmental variations, the response of the composites are also complex due to lay-up sequence effects. Such effects likely preclude the use of continuous fiber reinforced materials in diffraction-limited optical applications ($<\lambda/20$). This is significant because surface deformations in ideal laminates may be attributed to more severity of surface waviness in the laminates with additional resin layers introduced to correct the more commonly studied fiber print-through problem. The presence of additional resin layers in quasi-isotropic laminates appears to be more problematic than the high frequency surface quality from fiber print-through. Asymmetry caused by the use of one or more resin-rich layers is not believed to be acceptably small. The numerical and experimental results in this document show that there are variations of radial surface deformation in quasi-isotropic laminates that exceed allowable diffraction-limited performance and further show they are locally varied. Such

local surface variations in composite mirrors distort optical performance similar to the surface roughness from fiber print-through, yet the latter has received far more attention. Thus, for composite mirrors, more close attention should be paid to what types of surface deformation might occur when fabricating circular mirrors from continuous fiber reinforced material, particularly with the resin-rich surface layer commonly used to avoid fiber print-through.

7.2. Recommendations

On the basis of work shown in this dissertation, radial variation of flexural stiffness due to lay-up sequence effects is significant, even in instances where bend-twist effects become “small” with respect to the primary flexural stiffness terms for laminates with more than sixteen plies. Thus, large surface deformation and complex sinusoidal surface patterns are inevitable in continuous fiber reinforced composite mirrors under thermal or hygroscopic variances.

There is still room to improve the thermal stability of the composite mirrors from the mechanical complexities and variations of flexural stiffness influence due to stacking sequence. Inevitable surface undulation patterns might be overcome by using alternative homogenous materials such as veils, short fiber (distributed materials), or chopped mat. The short fiber or distributed material might be appropriately homogenous if layered in multiple orientations, and thus it might be better suited for future composite mirror applications. Experimental validations of surface deformations caused by inevitable local variations in the surface plies of such distributed materials are required.

Rudimentary experiments performed herein verify the complex radial variations in surface deformation predicted, and if anything demonstrate more significant local variations. Successful moiré interferometry or wave-front sensor experiments require exceptionally idealized samples (higher quality aluminized mirrors of multiple orientations) for higher fidelity experiments to better characterize the physics of this response.

For alleviation of unfavorable surface waviness from fiber print-through, carbon nano-tube might be a good material, so further research should focus on the applicability of nano-tube as surface deformation reinforcement for characterizing global and local surface deformations in quasi-isotropic composite mirror substrates. This technique could be extraordinarily useful for damping surface waviness, particularly if the composite surface material is needed to contain a very low CTE. Even though it will increase the Young's modulus in resin system that causes adverse effects on the surface waviness, it contains very low CTE characteristics, which is the primary dominant factor for mitigation of surface waviness.

In additions, a study of hygroscopic effects or possible local variations in porosity both inside of laminate and within resin system is needed to further demonstrate the moisture-related expansion or contraction in typical resin matrix composites.

References

1. Hochhalter, J D; Maji, A K; Reicher, D W, *Process Induced Errors in Replicated Carbon Fiber Reinforced Polymer Mirrors*, Proceedings of the Ninth Biennial ASCE Aerospace Division International Conference on Engineering, Construction, and Operations in Challenging Environments; League City/Houston, Texas; USA; 7-10 Mar. 2004. pp. 875-882. 2004

2. Massarello, Jack J; Hochhalter, Jake D; Fuierer, Paul A; Maji, Arup K, *Composite mirror replication*: *curing*, *coating* and *polishing*, Proc. SPIE. Vol. SPIE-5868, pp. 210-219. 2005

3. Hochhalter, Jake D. (Air Force Research Laboratory, Space Vehicles Directorate); Massarello, Jack I.; Maji, Arup K.; Fuierer, Paul A., *The origins of fiber print-through in lightweight composite optics*, Proceedings of SPIE - The International Society for Optical Engineering, v 6289, Novel Optical Systems Design and Optimization IX, 2006, p 628902

4. Massarello, Jack J. (Air Force Research Laboratory, Space Vehicles Directorate); Welsh, Jeffry S.; Hochhalter, Jake D.; Maji, Arup K.; Fuierer, Paul A., *Fiber print-through mitigation technique for composite mirror replication*, Optical Engineering, v 45, n 12, December, 2006, p 123401

5. Bennett, H.E. (Bennett Optical Research Inc.); Blazek, H.F.; Danielson, A.O., *Large lightweight low scatter composite active/adaptive mirror development*, Proceedings of SPIE - The International Society for Optical Engineering, v 6306, Advanced Wavefront Control: Methods, Devices, and Applications IV, 2006, p 63060Q

6. Paradies, Rolf. (Swiss Federal Inst of Technology), *Designing quasi-isotropic laminates with respect to bending*, Composites Science and Technology, v 56, n 4, Apr, 1996, p 461-472

7. Romeo, Robert C. (Composite Mirror Applications, Inc., CMA); Martin, Robert N., *Progress in 1m-class lightweight, CFRP composite mirrors for the ULTRA telescope*, Proceedings of SPIE - The International Society for Optical Engineering, v 6273 I, Optomechanical Technologies for Astronomy, 2006, p 62730S

8. Cantanzaro, Brian; Keane, Dan; Connell, Steve; Baiocchi, Dave; Burge, Jim; Maji, Arup; Powers, Mike, *UltraLITE glass/composite hybrid mirror*, UV, optical, and IR space telescopes and instruments; Proceedings of the Conference, Munich, Germany; UNITED STATES; 29-31 Mar. 2000. pp. 663-671. 2000

9. Chen, Peter C. (Composite Mirror Applications, Inc); Romeo, Robert C., *Ultra lightweight precision optics technology*, Proceedings of SPIE - The International Society for Optical Engineering, v 4003, 2000, p 396-405

10. Chen, Peter C; Romeo, Robert, *Fabrication and testing of very lightweight composite mirrors*, Space telescopes and instruments V; Proceedings of the Conference, Kona, HI; UNITED STATES; 25-28 Mar. 1998. pp. 938-945. 1998

11. Chen, Peter C; Romeo, Robert C, *Ultra lightweight precision optics technology Optical design, materials, fabrication, and maintenance*, Proceedings of the Conference, Munich, Germany; UNITED STATES; 27-29 Mar. 2000. pp. 396-405. 2000

12. Romeo, Robert C, *CFRP composite optical quality mirrors for space applications*, Materials challenge diversification and the future; Proceedings of the 40th International SAMPE Symposium and Exhibition, Anaheim, CA; UNITED STATES; 8-11 May 1995. pp. 1631-1636. 1995

13. Chen, Peter C. (Catholic Univ. of America); Bowers, C.W.; Content, David A.; Marzouk, Marzouk; Romeo, R.C., *Advances in very lightweight composite mirror technology*, Optical Engineering, v 39, n 9, Sep, 2000, p 2320-2329

14. Prewo, K M, *Development of a new dimensionally and thermally stable composite*, Advanced composites - Special topics; Proceedings of the Conference, El Segundo, California, United States; 4-6 Dec. 1979. pp. 1-30. 1979

15. Blair, Chris; Zakrzewski, Jerry, *Coefficient of thermal and moisture expansion and moisture absorption for dimensionally stable quasi-isotropic high modulus graphite fiber/epoxy composites*, Advances in optical structure systems; Proceedings of the Meeting, Orlando, FL; UNITED STATES; 16-19 Apr. 1990. pp. 524-535. 1990

16. Helms, R G; Porter, C P; Wu, Y C; Kuo, C P; Miyake, R N, *Lightweight composite mirror analysis and testing*, Active telescope systems; Proceedings of the Meeting, Orlando, FL; UNITED STATES; 28-31 Mar. 1989. pp. 426-441. 1989

17. Pryor, Mark K, *Hygrothermal stability of laminated CFRP composite mirrors*, UV, optical, and IR space telescopes and instruments; Proceedings of the Conference, Munich, Germany; UNITED STATES; 29-31 Mar. 2000. pp. 655-662. 2000

18. Kuo, C P; Lou, M C; Rapp, D, *Thermal-mechanical behavior of high precision composite mirrors*, AIAA/ASME/ASCE/AHS/ASC Structures, Structural Dynamics, and Materials Conference, 34th and AIAA/ASME Adaptive Structures Forum, La Jolla, CA; UNITED STATES; 19-22 Apr. 1993. pp. 949-958. 1993

19. Abusafieh, A; Federico, D; Connell, S; Cohen, E J; Willis, P B, *Dimensional stability of CFRP composites for space-based reflectors*, Proceedings of SPIE, the International Society for Optical EngineeringProceedings of SPIE, the International Society for Optical Engineering. 2001

20. Bashford, David; Eaton, David, *Microcracking and moisture absorption observed in epoxy and cyanate ester CFRP composites - What are the implications for space payloads?*, ESA International Conference on Spacecraft Structures, Materials and Mechanical Testing, Noordwijk, Netherlands; INTERNATIONAL ORGANIZATION; 27-29 Mar. 1996. pp. 513-520. 1996

21. Woida, Patrick M; Hoffmann, William F; Connell, Steven J; Kasl, Eldon P, *Low temperature figure stability of COI all-composite mirror M4*, Novel optical systems and large-aperture imaging; Proceedings of the Meeting, San Diego, CA; UNITED STATES; 20-21 July 1998. pp. 317-324. 1998

22. Gormican, James P; Kulick, Shell; Kasl, Eldon P; Abplanalp, Laura B, *Dimensionally stable, graphite-fiber reinforced composite mirror technology*, Space astronomical telescopes and instruments II; Proceedings of the Meeting, Orlando, FL; UNITED STATES; 13-14 Apr. 1993. pp. 410-420. 1993

23. Parker, James E, Jr; Lyons, James J, III, *Development of optically flat mirrors using graphite/epoxy laminates*, Current developments in optical design and

engineering V; Proceedings of the Conference, San Diego, CA; UNITED STATES; 12-13 July 1995. pp. 118-124. 1995

24. Brand, Richard; Marks, John, *Composite structures for optical mirror applications*, Advances in optical structure systems; Proceedings of the Meeting, Orlando, FL; UNITED STATES; 16-19 Apr. 1990. pp. 488-496. 1990

25. Connell, S J; Abusafieh, A, *Lightweight space mirrors from carbon fiber composites*, SAMPE Journal (USA). Vol. 38, no. 4, pp. 46-55. July-Aug. 2002

26. Abt, Bernd; Helwig, Gunter; Scheulen, Dietmar, *Composite technology for lightweight optical mirrors*, Advanced *technology optical* telescopes IV; Proceedings of the Meeting, Tucson, AZ; UNITED STATES; 12-16 Feb. 1990. pp. 696-705. 1990

27. Gormican, James P. (Composite Optics Inc., San Diego, CA, USA); Kulick, Shel; Kasl, Eldon P.; Abplanalp, Laura B., *Dimensionally stable graphite-fiber-reinforced composite mirror technology*, Proceedings of SPIE - The International Society for Optical Engineering, v 1945, 1993, p 410-420

28. Romeo, Robert C, *CFRP composite optical quality mirrors for space applications Materials challenge diversification and the future*, Proceedings of the 40th International SAMPE Symposium and Exhibition, Anaheim, CA; UNITED STATES; 8-11 May 1995. pp. 1631-1636. 1995

29. Willis, Paul B. (California Inst of Technology); Dyer, Jack; Dummer, Sam, *Fabrication and thermo-optical properties of the MLS composite primary reflector*, Proceedings of SPIE - The International Society for Optical Engineering, v 3786, 1999, p 200-205

30. Stahl, H. Philip. (Space Optics Mfg. Technology Center, NASA) , *Development of lightweight mirror technology for the next generation space telescope*, Proceedings of SPIE - The International Society for Optical Engineering, v 4451, 2001, p 1-4

31. Tompkins, Stephen S. (NASA Langley Research Cent., Hampton, VA, USA); Funk, Joan G.; Bowles, David E.; Towell, Timothy W.; Connell, John W.,

Composite materials for precision space reflector panels, Proceedings of SPIE - The International Society for Optical Engineering, v 1690, 1992, p 250-26

32. Matson, L E; Mollenhauer, D H, *Advanced Materials and Processes for Large, Lightweight, Space-Based Mirrors,* AMPTIAC Quarterly. Vol. 8, no. 1, pp. 67-74. 2004

33. Takeya, Hajime; Kume, Masami; Hahn, Steven; Ozaki, Tsuyoshi; Kohara, Naoki; Otsubo, Masashi; Tsuneta, Saku, *Development of ultra-light-weight mirror with carbon/carbon composites for optical-IR astronomy*, Proceedings of SPIE. Vol. SPIE-5487, pp. 1084-1091. 2004

34. Robert M. Jones, *Mechanics of composite Materials*, Second Edition

35. Laszlo P. Kollar, George S. Springer, *Mechanics of composite structures*, Cambridge University Press (February 17, 2003)

APPENDIX A: Numerical Calculation of Out of Plane Deformation in a Composite Plate Due to Thermal Variance

Plane Stress and Strain

When a composite plate is under plane stress condition, it is assumed that both out of normal stress and out of shear stresses must be zero.

$$\sigma_z = 0,\ \tau_{xz} = 0,\ \tau_{yz} = 0 \qquad \text{Eqn. (1)}$$

with substitution of eqn. (1) into the equilibrium equations below then,

$$\frac{\partial \sigma_x}{\partial x} + \frac{\partial \tau_{yx}}{\partial y} + \frac{\partial \tau_{zx}}{\partial z} + f_x = 0 \qquad \text{Eqn. (2)}$$

$$\frac{\partial \tau_{xy}}{\partial x} + \frac{\partial \sigma_y}{\partial y} + \frac{\partial \tau_{zy}}{\partial z} + f_y = 0 \qquad \text{Eqn. (3)}$$

$$\frac{\partial \tau_{xz}}{\partial x} + \frac{\partial \tau_{yz}}{\partial y} + \frac{\partial \sigma_z}{\partial z} + f_z = 0 \qquad \text{Eqn. (4)}$$

The above equilibrium equations can be simplified with eqn. (1) as,

$$\frac{\partial \sigma_x}{\partial x} + \frac{\partial \tau_{yx}}{\partial y} + f_x = 0 \qquad \text{Eqn. (5)}$$

$$\frac{\partial \tau_{xy}}{\partial x} + \frac{\partial \sigma_y}{\partial y} + f_y = 0 \qquad \text{Eqn. (6)}$$

Based on the equations (5) and (6), the stress-strain relationships can be expanded as following,

$$\sigma_x = \bar{C}_{11}\varepsilon_x + \bar{C}_{12}\varepsilon_y + \bar{C}_{13}\varepsilon_z + \bar{C}_{14}\gamma_{yz} + \bar{C}_{15}\gamma_{xz} + \bar{C}_{16}\gamma_{xy} \qquad \text{Eqn. (7)}$$

$$\sigma_y = \bar{C}_{21}\varepsilon_x + \bar{C}_{22}\varepsilon_y + \bar{C}_{23}\varepsilon_z + \bar{C}_{24}\gamma_{yz} + \bar{C}_{25}\gamma_{xz} + \bar{C}_{26}\gamma_{xy} \qquad \text{Eqn. (8)}$$

$$\tau_{xy} = \bar{C}_{61}\varepsilon_x + \bar{C}_{62}\varepsilon_y + \bar{C}_{63}\varepsilon_z + \bar{C}_{64}\gamma_{yz} + \bar{C}_{65}\gamma_{xz} + \bar{C}_{66}\gamma_{xy} \quad \text{Eqn. (9)}$$

The equations (7)~(9) can be rewritten as matrix form,

$$\begin{pmatrix} \sigma_x \\ \sigma_y \\ \tau_{xy} \end{pmatrix} = \begin{bmatrix} \bar{C}_{11} & \bar{C}_{12} & \bar{C}_{13} & \bar{C}_{14} & \bar{C}_{15} & \bar{C}_{16} \\ \bar{C}_{21} & \bar{C}_{22} & \bar{C}_{23} & \bar{C}_{24} & \bar{C}_{25} & \bar{C}_{26} \\ \bar{C}_{61} & \bar{C}_{62} & \bar{C}_{63} & \bar{C}_{64} & \bar{C}_{65} & \bar{C}_{66} \end{bmatrix} \begin{pmatrix} \varepsilon_x \\ \varepsilon_y \\ \varepsilon_z \\ \gamma_{yz} \\ \gamma_{xz} \\ \gamma_{xy} \end{pmatrix} \quad \text{Eqn. (10)}$$

The stress-strain and strain-stress relationships due to plane stress and strain condition can be obtained as following,

For stress-strain relationship due to plane stress and strain,

$$\begin{pmatrix} \sigma_x \\ \sigma_y \\ \tau_{xy} \end{pmatrix} = \begin{bmatrix} \bar{C}_{11} & \bar{C}_{12} & \bar{C}_{16} \\ \bar{C}_{12} & \bar{C}_{22} & \bar{C}_{26} \\ \bar{C}_{16} & \bar{C}_{26} & \bar{C}_{66} \end{bmatrix} \begin{pmatrix} \varepsilon_x \\ \varepsilon_y \\ \gamma_{xy} \end{pmatrix} \quad \text{Eqn. (11)}$$

$$\begin{pmatrix} \sigma_x \\ \sigma_y \\ \tau_{xy} \end{pmatrix} = \begin{bmatrix} \bar{C}_{13} & \bar{C}_{23} & \bar{C}_{36} \\ \bar{C}_{14} & \bar{C}_{24} & \bar{C}_{46} \\ \bar{C}_{15} & \bar{C}_{25} & \bar{C}_{56} \end{bmatrix} \begin{pmatrix} \varepsilon_z \\ \gamma_{yz} \\ \gamma_{xz} \end{pmatrix} \quad \text{Eqn. (12)}$$

For strain-stress relationship due to plane stress and strain,

$$\begin{pmatrix} \varepsilon_x \\ \varepsilon_y \\ \gamma_{xy} \end{pmatrix} = \begin{bmatrix} \bar{S}_{11} & \bar{S}_{12} & \bar{S}_{16} \\ \bar{S}_{12} & \bar{S}_{22} & \bar{S}_{26} \\ \bar{S}_{16} & \bar{S}_{26} & \bar{S}_{66} \end{bmatrix} \begin{pmatrix} \sigma_x \\ \sigma_y \\ \tau_{xy} \end{pmatrix} \quad \text{Eqn. (13)}$$

$$\begin{pmatrix} \varepsilon_z \\ \gamma_{yz} \\ \gamma_{xz} \end{pmatrix} = \begin{bmatrix} \bar{S}_{13} & \bar{S}_{23} & \bar{S}_{36} \\ \bar{S}_{14} & \bar{S}_{24} & \bar{S}_{46} \\ \bar{S}_{15} & \bar{S}_{25} & \bar{S}_{56} \end{bmatrix} \begin{pmatrix} \sigma_x \\ \sigma_y \\ \tau_{xy} \end{pmatrix} \quad \text{Eqn. (14)}$$

where $\bar{C}_{ij}$ and $\bar{S}_{ij}$ are the elements of the stiffness matrix $\left[\bar{C}\right]$ and compliance matrix $\left[\bar{S}\right]$ in the global coordinate x, y, z system.

For Carbon Fiber Reinforced Plastic Material

In the presence of plane stress and strain, the equilibrium equations for a CFRP material in local coordinate x_1, x_2, x_3 system follows similar manner for equations (5) and (6).

$$\frac{\partial \sigma_1}{\partial x_1} + \frac{\partial \tau_{12}}{\partial x_2} + f_1 = 0 \qquad \text{Eqn. (15)}$$

$$\frac{\partial \tau_{12}}{\partial x_1} + \frac{\partial \sigma_2}{\partial x_2} + f_2 = 0 \qquad \text{Eqn. (16)}$$

Based on the strain-stress relationships in equations (13) and (14), the strain-stress relationship in the local material coordinate system become,

$$\begin{pmatrix} \varepsilon_1 \\ \varepsilon_2 \\ \gamma_{12} \end{pmatrix} = \begin{bmatrix} S_{11} & S_{12} & S_{16} \\ S_{12} & S_{22} & S_{26} \\ S_{16} & S_{26} & S_{66} \end{bmatrix} \begin{pmatrix} \sigma_1 \\ \sigma_2 \\ \tau_{12} \end{pmatrix} \qquad \text{Eqn. (17)}$$

From eqn. (14), out of plane normal strain in composite material would be obtained as,

$$\varepsilon_3 = \begin{bmatrix} S_{13} & S_{23} & S_{36} \end{bmatrix} \begin{pmatrix} \sigma_1 \\ \sigma_2 \\ \tau_{12} \end{pmatrix} \qquad \text{Eqn. (18)}$$

where S_{ij} are the elements of the compliance matrix $\left[S\right]$ in the local coordinate x_1, x_2, x_3 system.

Out of Plane Deformation in a Composite Plate Due to Thermal variance

The following section is derived from the plane stress condition in a thin reinforced composite plate when the fiber are parallel to the x-y plane and plate is subjected to forces along the edges which are also parallel to the plane of the plate. The plane stress-strain relationship in previous section does not offer the stresses exactly. On the other hands, for composite plates it is an approximation to find change in thickness of composite plate due to thermal variance. The following derivation is based on Ref. [35].

Out of plane thickness variation can be written as following,

$$\delta h = \int_{-h/2}^{h/2} \varepsilon_z \, dz = \sum_{K=1}^{n} \left[\varepsilon_{z_k} (z_k - z_{k-1}) \right] \qquad \text{Eqn. (19)}$$

where k is the ply number, K is the total number of plies in a composite plate, and z is the coordinate of the ply.

The strain relationship under hygrothermal effects can be obtained as following,

$$\varepsilon_i, \ \varepsilon_i - \tilde{\alpha}_i \Delta T - \tilde{\beta}_i c \qquad \text{Eqn. (20)}$$

where $\tilde{\alpha}_i$ and $\tilde{\beta}_i$ are coefficient of thermal expansion and coefficient of moisture expansion in constituents of a composite plate.

Thus, based on eqn. (18) the normal out of strain in a ply in local coordinate system (x_1, x_2, x_3).

$$\varepsilon_3 = \begin{bmatrix} S_{13} & S_{23} & S_{36} \end{bmatrix} \begin{pmatrix} \sigma_1 \\ \sigma_2 \\ \tau_{12} \end{pmatrix} + \Delta T \tilde{\alpha}_3 + c \tilde{\beta}_3 \qquad \text{Eqn. (21)}$$

Stresses in local coordinate (x_1, x_2) in a ply can be written as,

$$\begin{Bmatrix}\sigma_1\\ \sigma_2\\ \tau_{12}\end{Bmatrix}=[T]\begin{Bmatrix}\sigma_x\\ \sigma_y\\ \tau_{xy}\end{Bmatrix} \qquad \text{Eqn. (22)}$$

In global x, y coordinate system, the plane stress-strain relationship in a ply is,

$$\begin{pmatrix}\sigma_x\\ \sigma_y\\ \tau_{xy}\end{pmatrix}=\left[\bar{Q}\right]\left[\begin{Bmatrix}\varepsilon_x\\ \varepsilon_y\\ \gamma_{xy}\end{Bmatrix}-\Delta T\begin{Bmatrix}\tilde{\alpha}_x\\ \tilde{\alpha}_y\\ \tilde{\alpha}_{xy}\end{Bmatrix}-c\begin{Bmatrix}\tilde{\beta}_x\\ \tilde{\beta}_y\\ \tilde{\tilde{\beta}}_{xy}\end{Bmatrix}\right] \qquad \text{Eqn. (23)}$$

where,

$$\begin{Bmatrix}\varepsilon_x\\ \varepsilon_y\\ \gamma_{xy}\end{Bmatrix}=\begin{Bmatrix}\varepsilon_x^{\circ}\\ \varepsilon_y^{\circ}\\ \gamma_{xy}^{\circ}\end{Bmatrix}+z\begin{Bmatrix}\kappa_x\\ \kappa_y\\ \kappa_{xy}\end{Bmatrix} \qquad \text{Eqn. (24)}$$

If a uniform $\Delta T_{\circ}$ is only subjected load, a ply out of normal strain equation can be obtained with substitution of equations (22)~(24) into eqn. (21) those equations may be combined to yield as following,

$$\varepsilon_z=\begin{bmatrix}S_{13} & S_{23} & S_{36}\end{bmatrix}[T]\left[\bar{Q}\right]\left[\begin{Bmatrix}\varepsilon_x^{\circ}\\ \varepsilon_y^{\circ}\\ \gamma_{xy}^{\circ}\end{Bmatrix}+z\begin{Bmatrix}\kappa_x\\ \kappa_y\\ \kappa_{xy}\end{Bmatrix}-\Delta T_{\circ}\begin{Bmatrix}\tilde{\alpha}_x\\ \tilde{\alpha}_y\\ \tilde{\alpha}_{xy}\end{Bmatrix}\right]+\Delta T_{\circ}\left(\tilde{\alpha}_z\right) \qquad \text{Eqn. (25)}$$

With substitution of eqn. (25) into eqn. (19), those equations may be combined to yield,

$$\delta h = \sum_{K=1}^{n} \left[\begin{array}{l} \left[S_{13} \quad S_{23} \quad S_{36} \right] \left[T \right]_k \left(\int_{-h/2}^{h/2} \left[\bar{Q} \right]_k \left\{ \begin{array}{c} \varepsilon_x^\circ \\ \varepsilon_y^\circ \\ \gamma_{xy}^\circ \end{array} \right\} dz + \int_{-h/2}^{h/2} \left[\bar{Q} \right]_k \left\{ \begin{array}{c} \kappa_x \\ \kappa_y \\ \kappa_{xy} \end{array} \right\} z dz - \Delta T_\circ \int_{-h/2}^{h/2} \left[\bar{Q} \right]_k \left\{ \begin{array}{c} \tilde{\alpha}_x \\ \tilde{\alpha}_y \\ \tilde{\alpha}_{xy} \end{array} \right\}_k dz \right) \\ + \Delta T_\circ (\tilde{\alpha}_z)_k \int_{-h/2}^{h/2} dz \end{array} \right]$$

Eqn. (26)

Thus, the equation of out of plane deformation due to thermal load in a composite plate would be as following,

$$\delta h_{Thermal\_effect} = \sum_{K=1}^{n} \left[\begin{array}{l} \left[S_{13} \quad S_{23} \quad S_{36} \right] \left[T \right]_k \left((z_k - z_{k-1}) \left[\bar{Q} \right]_k \left(\left\{ \begin{array}{c} \varepsilon_x^\circ \\ \varepsilon_y^\circ \\ \gamma_{xy}^\circ \end{array} \right\} - \Delta T_\circ \left\{ \begin{array}{c} \tilde{\alpha}_x \\ \tilde{\alpha}_y \\ \tilde{\alpha}_{xy} \end{array} \right\}_k \right) + \frac{(z_k{}^2 - z_{k-1}{}^2)}{2} \left[\bar{Q} \right]_k \left\{ \begin{array}{c} \kappa_x \\ \kappa_y \\ \kappa_{xy} \end{array} \right\} \right) \\ + (z_k - z_{k-1})(\Delta T_\circ (\tilde{\alpha}_z)_k) \end{array} \right]$$

Eqn. (27)

When the thermal load is the only subjected load to a composite plate (Mechanical loads are zero), $N_x = 0$, $N_y = 0$, $N_{xy} = 0$, $M_x = 0$, $M_y = 0$, $M_{xy} = 0$ the mid plane strains and curvatures are equal to the strains and curvatures due to hygrothermal effects in a composite plate.

$$\begin{pmatrix} \varepsilon_x^\circ \\ \varepsilon_y^\circ \\ \gamma_{xy}^\circ \\ k_x \\ k_y \\ k_{xy} \end{pmatrix} = \begin{pmatrix} \varepsilon_x^{\circ,ht} \\ \varepsilon_y^{\circ,ht} \\ \gamma_{xy}^{\circ,ht} \\ k_x^{ht} \\ k_y^{ht} \\ k_{xy}^{ht} \end{pmatrix} \qquad \text{Eqn. (28)}$$

$$\begin{pmatrix} \varepsilon_x^{\circ,ht} \\ \varepsilon_y^{\circ,ht} \\ \gamma_{xy}^{\circ,ht} \\ k_x^{ht} \\ k_y^{ht} \\ k_{xy}^{ht} \end{pmatrix} = \begin{bmatrix} [a] & [b] \\ [b] & [d] \end{bmatrix}_{6x6} \begin{pmatrix} N_x^{ht} \\ N_y^{ht} \\ N_{xy}^{ht} \\ M_x^{ht} \\ M_y^{ht} \\ M_{xy}^{ht} \end{pmatrix} \qquad \text{Eqn. (29)}$$

where, $\begin{bmatrix} [a] & [b] \\ [b] & [d] \end{bmatrix}_{6x6}$ is the inverse of $\begin{bmatrix} [A] & [B] \\ [B] & [D] \end{bmatrix}_{6x6}$ and running load and moment induced from hygrothermal load with constant $\Delta T_{\circ}$ can be calculated using below equations (30) and (31).

$$\begin{pmatrix} N_x^{ht} \\ N_y^{ht} \\ N_{xy}^{ht} \end{pmatrix} = \Delta T_{\circ} \sum_{K=1}^{n} \left((z_k - z_{k-1}) \left[\bar{Q} \right]_k \begin{Bmatrix} \tilde{\alpha}_x \\ \tilde{\alpha}_y \\ \tilde{\alpha}_{xy} \end{Bmatrix}_k \right) \qquad \text{Eqn. (30)}$$

$$\begin{pmatrix} M_x^{ht} \\ M_y^{ht} \\ M_{xy}^{ht} \end{pmatrix} = \frac{\Delta T_{\circ}}{2} \sum_{K=1}^{n} \left((z_k^{\,2} - z_{k-1}^{\,2}) \left[\bar{Q} \right]_k \begin{Bmatrix} \tilde{\alpha}_x \\ \tilde{\alpha}_y \\ \tilde{\alpha}_{xy} \end{Bmatrix}_k \right) \qquad \text{Eqn. (31)}$$